THÈSE

En vue de l'obtention du

DOCTORAT DE L'UNIVERSITÉ DE TOULOUSE

Délivré par :

Institut National Polytechnique de Toulouse (INP Toulouse)

Discipline ou spécialité :

Energétique et Transferts

Présentée et soutenue par :

Mme MELISSA FERAND

le mardi 6 février 2018

Titre :

Outils de prévision du bruit de chambre de combustion de turboréacteurs

---

Ecole doctorale :

Mécanique, Energétique, Génie civil, Procédés (MEGeP)

Unité de recherche :

Centre Européen de Recherche et Formation Avancées en Calcul Scientifique (CERFACS)

Directeur(s) de Thèse :

M. THIERRY POINSOT

M. STÉPHANE MOREAU

Rapporteurs :

M. CHRISTOPHE BAILLY, ECOLE CENTRALE DE LYON

Mme FRANÇOISE BAILLOT, UNIVERSITE DE ROUEN

Membre(s) du jury :

M. CHRISTOPHE BAILLY, ECOLE CENTRALE DE LYON, Président

M. ALEXIS GIAUQUE, ECOLE CENTRALE DE LYON, Membre

M. GUILLAUME DAVILLER, CERFACS, Membre

M. STÉPHANE MOREAU, UNIVERSITE DE SHERBROOKE, Membre

M. THIERRY POINSOT, CNRS TOULOUSE, Membre

Remerciements

Je tiens tout d'abord à remercier particulièrement chaque rapporteur et examinateur de cette thèse, Françoise Baillot, Christophe Bailly et Alexis Giauque qui ont accepté d'évaluer mes travaux de thèse et assisté à ma soutenance. Ce fut un plaisir de répondre à leurs nombreuses questions riches et variées.

Un très grand merci à mes directeurs de thèse, Thierry Poinsot qui m'a permis de réaliser cette thèse au CERFACS et m'a donné un fil conducteur pour orienter ces travaux. Mais également, Stéphane Moreau pour son suivi même à grande distance, ses conseils et son optimisme face à toute situation. Sans oublier Guillaume Daviller, mon encadrant de dernière ligne droite ! Je tiens particulièrement à te remercier pour ton soutien non négligeable et tes nombreux conseils avisés sur cette fin de thèse. Merci à Claude Sensiau qui m'a donné l'opportunité de traiter un si beau sujet depuis mon stage de fin d'étude à SAE et ses nombreuses questions qui m'ont permis de mieux comprendre la problématique d'un point de vue industriel.

Je souhaite également remercier la team COOP que j'ai récemment intégrée, pour leur soutien lors de la préparation de soutenance et pour avoir allégé mes charges de travail juste avant la fin !

Un grand merci à toutes les personnes qui nous facilitent la vie au CERFACS et qui font en sorte que tout se passe bien, Marie Labadens, Chantal Nasri, Michèle Campassens, Lydia Otero et Nicole Boutet. Merci à l'équipe CSG qui est toujours là pour régler tous nos problèmes informatiques en étant toujours de bonne humeur.

Je remercie aussi tous les stagiaires, doctorants, post-doctorants et seniors que j'ai rencontrés durant ces années au CERFACS. Particulièrement merci à la team qui s'est formée à nos débuts de jeunes thésards ! Merci à Majd même s'il est convaincu que le bruit de combustion ne fait toujours pas de bruit, à Dario pour la "particule", à Romain qui même avec ses blagues lourdes a en fait un petit coeur, Carlos, Aïcha, Franchinou, Laura, Christophe, Pierre, Laure, Jarjar, Thomas G., Nico, Pedro, Luc, Luis, sans oublier Doudou, les plus jeunes Félix, Lulu, Maxou

pour tes merveilleux gâteaux, Romain, Quentin, Tastoul, Soizic et tous ceux que j'ai pu oublier. Il y en a tellement ! Un merci spécial à mon cobureau, César, qui a quand-même fait la performance de me supporter pendant toutes ces années.

Enfin, je remercie mes parents, ma soeur et mon frère, ainsi que mon grand-père qui nous a quitté, pour avoir toujours cru en moi et m'avoir soutenue dans mes choix. C'est grâce à vous que je suis ici aujourd'hui. Un grand merci à "Mr. Pineapple" pour nos fous rires, ta patience mise à rude épreuve et ton très grand soutien, merci pour notre complicité !

Contents

List of Figures

List of Tables

Glossary

CFD Computational Fluid Dynamics. 39, 74

CFM CFM International. viii, 90

CMC Conditional Moment Closure. 37

DFT Discrete Fourier Transform. 224

DNS Direct Numerical Simulation. 29, 30

FPDF Filtered Probability Density Functions. 37

FWH Ffowcs Williams and Hawkings. 23, 213, 224, 243

GE General Electric Company. 163

GMRES Generalized Minimum REsidual method. 69

HPT High Pressurized Turbine. 161

HPTS High Pressurized Turbine Stator. 91, 99, 104, 117

IRZ Inner Recirculation Zone. 104, 113

IVM Inlet Velocity Modulation. 76

IWM Inlet Wave Modulation. 76

LES Large Eddy Simulation. 29–31, 37, 39, 76, 85, 99, 113, 121, 160, 169, 227–229

LPT Low Pressurized Turbine. 161

LW Lax-Wendroff. 102

NSCBC Navier-Stokes Characteristic Boundary Conditions. 76, 79, 197, 232

OAPWL Over All Power Level. 160, 163–165, 228

OASPL Over All Sound Pressure Level. 157, 160, 163, 164, 243

ORZ Outer Recirculation Zones. 104

PDF Probability Density Function. 37

PSD Power Spectral Density. x, 120–122

PVC Precessing Vortex Cores. 92

PW Pratt & Whitney. 163

PWL Power Level spectrum. 163, 164

RANS Reynolds Averaged Navier-Stokes Simulation. 29, 30

RMS Root-Mean-Squared. 110

SAE SAFRAN Aircraft Engines. 102, 164

SPL Sound Pressure Level. 164

TEENI Turboshaft Engine Exhaust Noise Identication. 40, 65, 70, 89, 227

TTGC Two-step Taylor-Galerkin numerical Scheme. 99, 102

Notations

c Speed of sound. 10

c_∞ Speed of sound in the far-field. 19

c_p Specific heat capacity at constant pressure. 40

E Total energy per unit mass. 29

γ Heat capacity ratio. 41

He Helmholtz number. 38

$J_{j,k}$ Diffusive flux vector of species k. 29

$J^t_{j,k}$ Turbulent diffusive flux vector of species k. 29

K^+ Dimensionless downstream acoustic wavenumber. 46

K^- Dimensionless upstream acoustic wavenumber. 46

K^ϕ_x Dimensionless axial wavenumber. 42

K^ϕ_y Dimensionless circumferential wavenumber. 42

K^ϕ Dimensionless wavenumber. 42

k^ϕ Wavenumber. 42

K^s Dimensionless entropy wavenumber. 42

K^v Dimensionless vorticity wavenumber. 43

L^{blade}_x Blade axial chord. 38

L_y Blade pitch. 38

m Mode number. 38, 106

M_a Acoustic Mach number. 19

M Mach number. 39

$N_{sectors}$ Number of sectors of the combustion chamber. 106

ν^+ Downstream acoustic wave front angle with respect to the axial direction. 46

ν^- Upstream acoustic wave front angle with respect to the axial direction. 46

ν^ϕ Wave front angle with respect to the axial direction. 42

ν^s Entropy wave front angle with respect to the axial direction. 42

ν^v Vorticity wave front angle with respect to the axial direction. 42

ω Angular frequency. 38

P Pressure. 29

p' Pressure fluctuation. 10

p Mean pressure. 39

$\frac{p'}{\gamma p}$ Dimensionless pressure fluctuation. 39

q_j Total heat flux. 29

q_j^t Turbulent total heat flux. 29

r Mixture gas constant. 29

R Universal gas constant (mass). 29

ρ Density. 10, 39

ρ_k Density of the species k. 29

$\frac{s'}{c_p}$ Dimensionless entropy fluctuation. 40

T Temperature. 29

θ Deviation angle of the velocity vector with respect to the axial direction. 39

θ' Dimensionless velocity deviation angle fluctuation. 40

τ_{ij} Stress tensor. 29

τ_{ij}^{t} Turbulent stress tensor. 29

u Axial velocity. 40

U_j Exhaust velocity. 19

u_i Velocity vector. 29

$\ddot{V}$ Second rate of volume change. 10

v Circumferential velocity. 40

W Molecular weight. 29

w Velocity vector magnitude. 39

w^+ Downstream acoustic wave. 44

w^- Upstream acoustic wave. 44

$\frac{w'}{c}$ Dimensionless velocity modulus fluctuation. 40

W_k Molecular weight of species k. 30

w^s Entropy wave. 42

w^v Vorticity wave. 42

x Axial coordinate. 40

ξ' Vorticity fluctuations. 40

x_i Spatial coordinate (vector). 30

X_k Molar fraction of species k. 30

y Circumferential coordinate. 40

Y_k Mass fraction of species k. 29

Part I

Introduction

Table of Contents

General context

Acoustic regulations

Assessing the performance of an engine is increasingly being driven by environmental considerations. It is no longer a matter of designing engines capable of supplying the required thrust in a reliable and robust manner, but also of limiting the impacts of the engine on the environment. As such, the acoustics of turbojets have become an important issue for engine manufacturers, because noise affects the quality of life, the health and the property value of areas close to airports and flight corridors. In order to limit noise pollution in the vicinity of airports, there is a regulation that airplanes must respect to be allowed to fly. Acoustic certification refers to the total noise generated by the aircraft and not to the noise generated by the engine alone. However, the engine has definitely a significant impact on the total noise of the aircraft. The certification standard is defined by ICAO (International Civil Aviation Organization, ICAO 2006). In consultation with ACARE (Advisory Council for Aeronautics Research in Europe), ICAO intends to reduce aircraft noise by 65% by 2050 compared with 2000 levels (ACARE 2011). However, some airports also have their own regulations. This is the case, for example, with the London airport. The certification is carried out in three points corresponding to the phases of flight which cause an inconvenience for the residents:

- Approach
- Sideline, take-off
- Cutback, fly-over

These certification points are shown in Fig. 1.

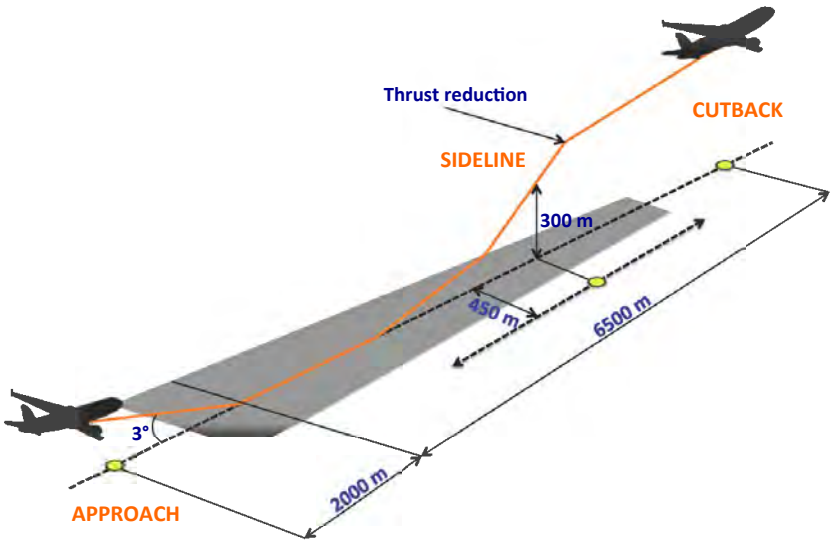

Figure 1: Acoustic certification points

Turbofan-engine acoustic sources

The aircraft noise can be separated into two contributions coming from the airframe and the engine. The airframe noise, typically broadband, is generated by the fuselage, the nacelle, the landing gear and the wings. The engine noise is decomposed into three main sources, cf Fig. 2:

- The noise of rotating parts, typically tonal: fan, compressor, turbine
- The jet noise, due to the mixing of the turbulent structures downstream of the engine exhaust
- The combustion noise, coming from flame unsteadiness in the combustion chamber

The importance of each module in the generation of noise differs according to the regime considered. In addition, each source has a frequency signature and a specific directivity as shown in Fig. 3.

Jet noise and fan noise have long been the dominant noise components. However, the current trend of evolution towards high bypass ratio engines, the use of geared fans coupled to innovative fan blade design and the addition of acoustics liners and other noise attenuators substantially leads to a reduction of jet noise and fan noise. Therefore, combustion noise is thought to become an important

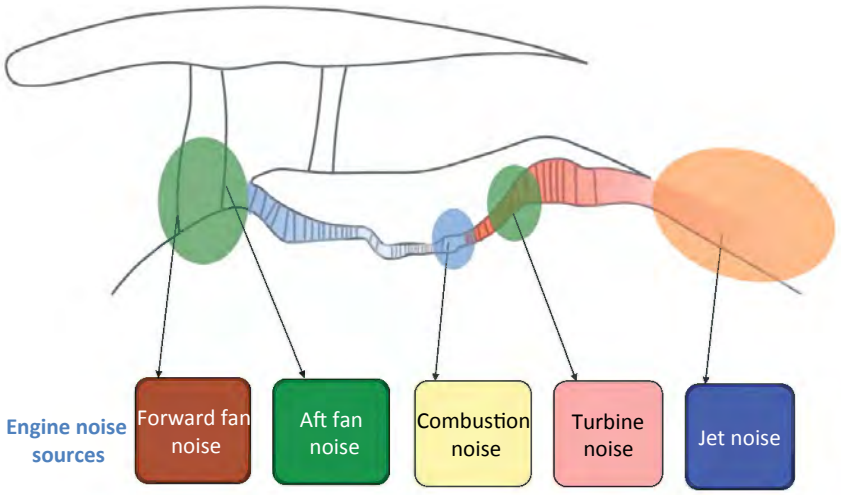

Figure 2: Engine acoustic sources

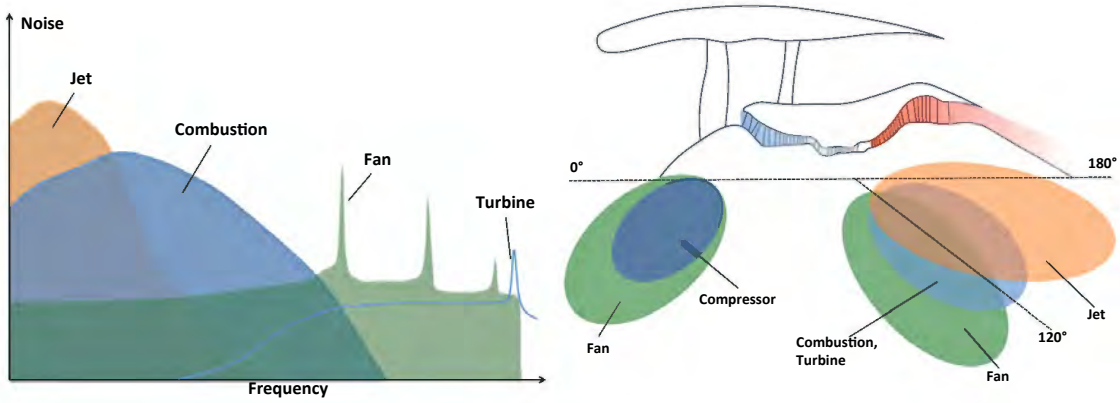

(a) (b)

Figure 3: (a) Total engine spectrum and (b) directivity of the engine acoustic sources

noise contributor of the next generation aircrafts. Moreover, there is a recent motivation to design green engines with high efficiency and low pollutant emission. This requires the development of advanced combustion strategies operating at much higher temperature and at the lean fuel limit, such as lean prevaporized premixed combustion and lean direct injection (Gliebe et al. 2000; Hultgren 21-22

Apr. 2011; Chang et al. 2013). At these conditions, the combustion processes become highly unsteady leading to an increase of combustion noise emission. At these factors can be added the design of engine with higher overall pressure ratios, higher turbine loading and higher power densities (Mongeau et al. 2013).

The significance of combustion noise has been recognized at low power-engine conditions when the aircraft is on the ground or during landing and approach. It is also known to be the dominant source of noise of auxiliary power units (APU, Tam et al. 2005).

Recent renewed interest for combustion noise is guided by ambitious aircraft noise reduction objectives (ACARE 2011). To reduce effectively the combustion noise it is necessary to have a better understanding of its mechanisms. However, a large number of parameters are involved in the complex combustion processes. Although combustion noise has been studied since the 70's, there is still much work to be done to develop a widely accepted theory. Recent advances in experimental diagnostics and in computational modeling could have an important contribution to combustion noise knowledge and prediction. A description of the known characteristic features of combustion noise is proposed in the next section.

Combustion noise

Combustion noise is becoming an increasingly important component of aero-engine exhaust noise, although it is not yet the main source of noise and it is not of major concern for acoustic certification points. The noise generated by combustion itself is not well known and is generally referred as core noise coming from all contributions generated upstream of the nozzle exit. Actually, core noise corresponds to the excess low frequency broadband noise levels at low jet exhaust velocity which cannot be associated with jet noise. Most of the time, it is obtained by source decompositions (subtraction from other known sources: combustion noise = overall engine noise - (fan noise + jet noise + turbine noise). This decomposition supposes that the interactions between these acoustic sources are linear. One of the reasons for using this acoustic decomposition is that it is very difficult to obtain the noise generated only by the combustion chamber. Therefore, this phenomenon is still not well understood. Until now engine manufacturers mainly use empirical methods based on several engine data and operating points to evaluate combustion noise. These prediction methods generally show good agreement with their own engine data but not necessarily with data from other engine manufacturers. Indeed, the empirical or semi-empirical laws are fitted with the burner design of the manufacturer. However, these methods are practical tools and still widely used since the 70's.

In the literature, numerous theoretical and experimental works on combustion

noise exist. To have a better understanding of combustion noise, to have a good knowledge of the combustion processes is required. However, due to the complexity of these processes which involve a large range of scales, kinetic chemistry with multi-steps reactions and complex molecules (hydrocarbon fuel) and the turbulence effects on the transport of species, it is complicated to develop a well-established theory.

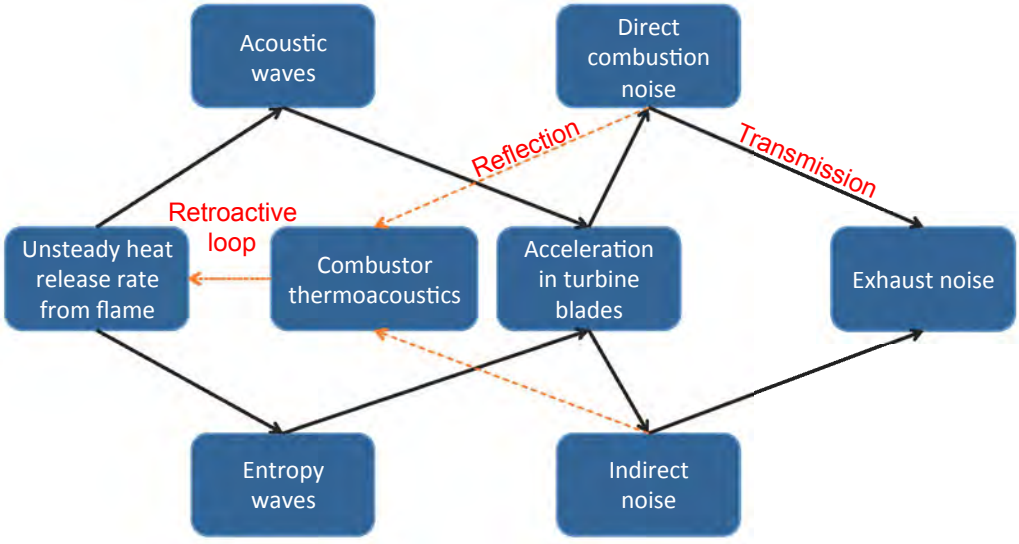

Figure 4: Mechanisms for the generation and propagation of combustion noise

Two mechanisms of generation and propagation of combustion noise, from the combustion chamber to the far field, have been identified since the 1970s (cf Fig. 4):

- Direct combustion noise (Strahle 1971; Candel et al. 2009; Dowling and Mahmoudi 2015): unsteady heat release rate, linked to unsteady fuel combustion, leads to unsteady volume expansion which acts as an acoustic monopole source. The generated acoustic waves propagate upstream and downstream through the stages of the turbojet engine where they are deformed, diffracted and reflected by the solid walls in the diffuser, distributor, turbine and compressor blades.

- Indirect combustion noise (Bake et al. 2009, 2016; Morgans and Duran 2016; Ihme 2017): inhomogeneities in velocity, temperature and also mixture composition, generated in the combustion chamber, propagate downstream and interact with the mean flow and the pressure gradients in the turbine blades and the nozzle. As a result, acoustic waves are generated from convective entropy and vorticity waves. These acoustic waves are partially reflected or transmitted, propagating to the far field.

In confined domains, inhomogeneities in pressure, velocity, temperature and mixture composition entering or being reflected in the combustion chamber are also an important contributor to combustion noise. Indeed, the combustion processes take place in a harsh confined environment. Therefore, compressor and turbine should be considered to take into account all the perturbations. For instance, tonal compressor noise has been identified in combustion chambers at high power levels (Reshotko and Karchmer 1980). Acoustics generated in the first turbine stages can also be reflected at the distributor of the high pressurized turbine and can couple with the combustion chamber acoustics. If the amplitudes of these perturbations coming from the compressor or the turbine are sufficiently high, they can trigger thermoacoustic instabilities with higher acoustic intensities compared to combustion noise (Poinsot 2017). These instabilities can dramatically deteriorate the engine (Lieuwen and Yang 2005). During this phase, the heat release and the pressure perturbations in the combustor are coherent and occur at a discrete tone related to the acoustic resonances of the combustor. This frequency can be shifted slightly by the flame response.

The direct and indirect mechanisms are described in the next sections. For more details one can refer to several recent reviews on combustion noise generation and propagation (Dowling and Mahmoudi 2015; Morgans and Duran 2016; Ihme 2017; Tam et al. 2017).

Direct combustion noise

The direct generation of combustion noise has been studied experimentally since the 1960s for open-flame configurations, starting with turbulent premixed flames investigated by Smith and Kilham [1963]. The direct combustion noise mechanism is often the main source of noise of a free flame and is dependent on the burner geometry, the mass flow-rate and the fuel mixture. Bragg [1963] explained theoretically this observation by relating the volumetric expansion of individual acoustic sources with a characteristic length, proportional to the flame thickness. Indeed, he assumed that the turbulent flame was an assembly of eddies having their own heat release rate and that each eddy acted as a monopole acoustic source statistically independent of the nearby eddies. These conclusions were confirmed experimentally by Thomas and Williams [1966] who showed that for burning bubbles filled with premixed fuel-air mixture, the sound pressure levels are linearly dependent on the flame radius and on the square of the burning velocity. Thus the pressure fluctuations at a distance r from the ignition position can be written as

$$p'(r,t) = \frac{\rho_0}{4\pi r}\ddot{V}\left(t - \frac{r}{c_0}\right), \tag{1}$$

where $\ddot{V}$ is the second rate of change of the bubble volume, ρ_0 the mean air density and c_0 the speed of sound in far field. This equation illustrates that the acoustics is generated by the unsteadiness in the rate of expansion caused by combustion of gas.

Several experiments on premixed and non-premixed flames performed by Hurle et al. [1968]; Price et al. [1968]; Shivashankara et al. [1974] agreed with the monopole characteristic of jet flames and confirmed that the volume expansion can be related to the consumption rate of fuel and oxidant in the flame.

Based on the acoustic analogy of Lighthill [1952], Strahle [1971]; Dowling and Ffowcs Williams [1983] proposed an acoustic analogy for combustion noise radiation which confirms the monopole and low-frequency characteristics of combustion noise. The acoustic pressure in far-field can be modeled as resulting from the superposition of monopole sources due to temporal change of the heat release rate in the combustion region. A more complete propagation equation considering all the thermo-acoustic source terms is given by Crighton et al. [1992]:

$$\begin{aligned}
\frac{1}{c_0^2}\frac{\partial^2 p}{\partial t^2} - \frac{\partial^2 p}{\partial x_i \partial x_i} &= \overbrace{\frac{\partial^2}{\partial x_i \partial x_j}(\rho u_i u_j - \tau_{ij})}^{1} \\
&+ \overbrace{\frac{\partial}{\partial t}\left[\frac{\rho_\infty}{\rho}\frac{(\gamma-1)}{c^2}\left(\dot{\omega_T} + \sum_k h_k \frac{\partial J_k}{\partial x_k} - \frac{\partial q_i}{\partial x_i} + \tau_{ij}\frac{\partial u_i}{\partial x_j} + \dot{Q}\right) + \rho_\infty \frac{D}{Dt}(\ln r)\right]}^{2} \\
&+ \underbrace{\frac{1}{c_\infty}\frac{\partial}{\partial t}\left[\left(1 - \frac{\rho_\infty c_\infty^2}{\rho c^2}\right)\frac{Dp}{Dt} - \frac{p-p_\infty}{\rho}\frac{D\rho}{Dt}\right]}_{3} + \underbrace{\frac{\partial^2}{\partial x_j \partial t}(\rho_e u_j)}_{4}
\end{aligned} \tag{2}$$

where $\rho u_i u_j$ are the non-linear convective forces described by the Reynold stress tensor, τ_{ij} are the viscous forces, γ is the ratio of specific heats, $\dot{\omega_T}$ the heat release, h_k the specific enthalpy for species k, J_k the diffusive molecular flux for species k, q_i the j-th component of the diffusive heat flux and ρ_e is the excess density related to the entropy. This density fluctuation is not associated with acoustic waves and is defined as

$$\rho_e = \rho' - \frac{p'}{\bar{c}^2}. \tag{3}$$

It corresponds to the difference between the overall mass density fluctuation and the one generated by the isentropic transformation such as an acoustic wave (Morfey 1973).

Lighthill's analogy is an inhomogeneous wave equation where the right hand side (RHS) represents the various sources of sound generation. The first term of

the RHS is the quadrupole source of Lighthill's jet noise theory linked to velocity fluctuations. The second source term is of monopole type and describes the sound generated by irreversible flow processes, as combustion and unsteady heat release rate. The third term is related to the variation of specific heats and is often negligible, particularly in combustion chambers where pressure is almost constant. The last term is of dipole nature and describes the effect of momentum changes on density inhomogeneities. This term is the entropy noise source discussed in the next section.

Other acoustic analogies (Phillips [1960]; Lilley [1972]) can be used to describe the combustion noise as presented in the combustion noise investigation of Bailly et al. [2010]. Each analogy yields a different form of the combustion noise source term. Therefore, it can be confusing to determine which acoustic analogy is more appropriate to characterize combustion noise.

Concerning sound generation, differences in the noise characteristics exist between premixed and non-premixed flames: according to Kumar [1976] the noise sources in a premixed flame are related to the unsteady fluctuations in the flame front and are located close to the flame tip (Smith and Kilham 1963; Schuller et al. 2002; Candel et al. 2004). On the contrary, noise sources in non-premixed flames are distributed in the rear region of the reaction zone and related to dilatational effects that are generated by mixing and turbulence-induced strain-rate variations. According to Singh et al. [2003], turbulent non-premixed flames generate higher levels of sound than premixed flames at a similar velocity.

More details for premixed flames are obtained by Kotake and Takamoto [1987] who widely investigated the effects of the equivalence ratio and turbulence on acoustic radiation. They observed that in fuel lean flames, the acoustic source region is mostly located in the upper part of the flame, while in fuel rich flames, this region is located below the maximum temperature of the flame. Moreover, it has been found that higher turbulence levels lead to significant higher noise emissions at lean and stoichiometric conditions, which has also been confirmed by measurements of Kilham and Kirmani [1979].

Meier et al. [2000] and Schneider et al. [2003] performed comparisons between non-reacting jets and premixed flames at same operating conditions and noted that premixed flames increase the Sound Pressure Level (SPL) of jet at all frequencies.

It is known that combustion noise intensity is dependent on various parameters such as the burner size, the flow conditions (velocity, fuel and oxidizer densities, flame temperature and turbulence level), the chemistry, the fuel phase (gaseous or liquid), and the flame type (premixed or non-premixed), as resumed in the review of Tam et al. [2017]. However, it appears that the spectral shape of combustion noise is conserved whatever these parameters. This was confirmed with the parametric studies of Kotake and Takamoto [1987, 1990]; Lieuwen [2002, 2003];

Rajaram and Lieuwen [2004]. This was also corroborated by Tam et al. [2005] analysis on Honeywell APU experiments. It is found that all spectra have a dominant broadband peak and that the spectral shape matches the large structures similarity spectrum obtained with the two sources jet noise model of Tam et al. [2008].

More recently, the sound emitted by a turbulent diffusion flame was numerically solved by Flemming et al. [2007]; Ihme et al. [2009]; Ihme and Pitsch [2012] which combined LES simulations and aeroacoustic calculation methods. Nevertheless, most of these studies concern the propagation of the acoustics of the flame towards a distant free field. In the case of a combustion chamber, another source of noise appears, linked to the confinement of the flame: the entropy noise.

Indirect noise

The indirect combustion noise is associated with the noise generated by the acceleration of entropy and vorticity waves (term 4 in Eq. (2)). But the entropy noise is thought to be more significant than the vorticity noise since important temperature fluctuations, referred as entropy waves, are generated by unsteady combustion, and large scale turbulence downstream from the flame is dissipated by the increasing viscosity due to the high temperature conditions.

The existence of the entropy noise has long been a theoretical concept emerged since the 1970's. Its existence has been experimentally confirmed 40 years later by the experiment of Bake et al. [2009]. The Entropy Wave Generator consists in a tube with an heating device to generate the entropy waves. The entropy waves are then convected though a convergent-divergent nozzle. Experiments show that sound is generated when the entropy pulse passes through the nozzle.

By following the studies of Tsien [1952] and Crocco [1953] with respect to nozzles, Candel [1972] deduced that the entropy spots depending on the unsteady combustion process represent an important source of noise if the expansion of the gases through the turbine stages is taken into account. Indeed, when entropy waves are accelerated, regions of fluid with different densities are contracted, leading to a fluctuating force which acts as an acoustic dipole.

Tam and Parrish [2014] gives a physical explanation for the mechanism of noise generation by convection of entropy wave by performing a numerical simulation of a narrow Gaussian entropy pulse sent throw a convergent-divergent nozzle. In the convergent part of the nozzle, for an adiabatic flow, the mean flow velocity increases towards the throat, so that the pulse width expands. As the mass of the pulse is conserved, the density in the front part of the pulse decreases leading to a decrease of the pressure. To conserve the pressure balance, a rarefaction wave is emitted. In the divergent part of the nozzle, the processes are reversed. That is to say that mean flow velocity decreases leading to the contraction of the pulse

width. This induces an increase of density and pressure leading to a compression wave.

The acceleration of the entropy waves can be provided by a nozzle or a turbine blade row. Due to a rapid increase in Mach number from the combustor exit through the first turbine stator, and thus a strong acceleration, gas turbine configurations have a strong propensity to entropy noise. However, most of the experiments generally concentrate on flow acceleration of entropy waves through a simple nozzle. As for the direct acoustic waves, a part of the indirect acoustic waves generated by the acceleration of entropy waves can propagate upstream toward the flame, contributing to the feedback loop controlling the thermoacoustic instability (Motheau et al. 2014). In the case of an aircraft engine constituted of successive blade rows, acoustic waves and entropy waves propagate downstream and more acoustic waves can be generated by the successive blade row accelerations. Finally, entropy noise will also propagate from the turbine exit, contributing to exhaust noise.

Experimentally, dissociating entropy noise from direct noise was extremely complicated due to the harsh environments, the lack of data post-processing capability and not well adapted configurations. Therefore, a clear identification of entropy noise was not possible (Zukoski and Auerbach 1976; Bohn 1977; Strahle and Muthukrishnanf 1980).

By using coherence function technique, Miles [2009] shows that an important amount of entropy noise is generated in a two-shaft turbofan-engine. It was also highlighted that indirect noise dominates the low frequency band (0-200 Hz), while direct noise was related to the frequency range from 200 to 400 Hz.

Recent studies of Bake et al. [2016] on the generation of entropy noise and vorticity noise in a high pressure turbine show that the dominant noise in the earlier stages of the turbine is vorticity noise. On the contrary, in the latter stages, entropy noise is clearly dominant.

Prediction of indirect noise began with Marble and Candel [1977]. Simple analytical solutions have been found for plane waves in compact nozzles (acoustic wavelength much larger than the characteristic length) as well as in nozzles of finite length considering a linear evolution of the axial velocity. Due to the compact assumption, these solutions concern linear perturbations in the zero-frequency limit. It was this work that first introduced the terms of direct and indirect combustion noise. Then, Cumpsty and Marble [1977] extended the work of Marble and Candel [1977] for two-dimensional cylindrical flows. Some recent work has been focused to extend the assumptions of Marble and Candel to higher frequencies (Stow et al. 2002) and to non-linear perturbations in the compact limit (Huet and Giauque 2013), or to relax the compact assumption (Zinn et al. 1973).

Leyko et al. [2009] showed analytically and numerically with Euler simulations

that the indirect combustion noise can be very important compared to the direct noise for large nozzle accelerations ($M > 0.7$). Duran and Moreau [2013] developed an approach to predict both direct and indirect noise at any frequency, for choked or subcritical nozzles by solving analytically the LEE (Linearized Euler Equations) using Magnus expansions. Recently, Duran and Morgans [2015] extended this approach to propagate circumferential waves through a narrow annular nozzle.

Predicting indirect noise implicitly requires to solve the combustion chamber problem. Solving this complex problem where many processes occur implies to use an accurate simulation method. To overcome the problem, an alternative strategy can be used to replace the combustor with a simplified sinusoidal entropy wave train (Leyko et al. 2014 for a stator, Tam and Parrish 2015, then Papadogiannis et al. 2016; Wang et al. 2016 and Bauerheim et al. 2016 for a stator/rotor). However, it does not take into account the complexity of the combustion noise generation and so can not provide a quantitative result.

Experimental measurements of direct and indirect combustion noise are necessary to validate the models and prediction tools. However few experimental studies exist due to the difficulty of fast temperature measurements. The entropy Wave Generator (EWG) implemented at the German Aerospace Centre (DLR) was dedicated to the generation of indirect noise by the acceleration of entropy waves (Bake et al. 2009). These experiments avoided the harsh environments where combustion occurs by using an electrical heating device that generates pulsed heat release rate fluctuations instead of an unsteady flame. Then, the temperature fluctuations was convected through a convergent-divergent nozzle providing flow acceleration. Both analytical and numerical predictions of the EWG agreed with the measurements. For supersonic conditions, it was found that entropy noise dominates over direct noise (Leyko et al. 2011), while for subsonic conditions, the direct noise mechanisms is dominant (Giauque et al. 2012; Duran et al. 2013b; Howe 2010; Becerril et al. 2016).

The European Turboshaft Engine Exhaust Noise Identification (TEENI) project provided experimental databases for noise inside the engine and radiated far-field noise (Livebardon et al. 2015). Its objective was to develop methods to dissociate spectrally:

- Direct combustion noise
- Indirect combustion noise
- Broadband noise from the high pressure turbine
- Broadband noise from the free turbine

However data on indirect noise could not be achieved due to thermocouple problems.

More recently the European project RECORD was dedicated to the identification of combustion noise mechanisms. It treated the combustion noise from the generation in combustion chamber to the propagation through nozzle or turbine.

While the interactions between entropy, vorticity and acoustics have been widely investigated (Chu and Kovásznay 1958), the relevance of compositional inhomogeneities as a contributor to the indirect combustion noise has not been considered so far. These inhomogeneities are the result of incomplete mixing, mixture stratification or dilution and can become increasingly important with the development of compact and advanced low-emission combustors. Magri et al. [2016]; Ihme [2017] examined theoretically the generation of indirect noise due to compositional inhomogeneities, by rewriting the transfer functions of Marble and Candel [1977] for multi-component gas mixture and introducing a chemical potential function as an additional acoustic source mechanism. They showed that the compositional noise is dependent on the local mixture compositional and can exceed entropy noise for fuel-lean conditions and supersonic nozzle flows. Therefore the compositional indirect noise should be most likely considered with the development of low-emission combustors.

Exhaust noise

Most previous studies on combustion noise were limited to direct and indirect noise propagation up to the turbine exit. However, the effects of perturbations coming from the nozzle upstream as well as flow inhomogeneities on the far-field noise radiation have to be considered. Moreover, the nozzle exhaust flow field and so jet noise are known to be very sensitive to the nozzle exit conditions, the external excitations and the operating conditions. Investigating the contribution of initial conditions and forcing on the jet noise is becoming a crucial point.

The first section is dedicated to the description of jet flow aerodynamic and acoustic characteristics. The second section discusses the temperature effects on jet noise. The last section concerns the effects of acoustic excitation on jet noise.

Jet flow development and noise sources

Preliminary work managed by Mollo-Christensen [1967] on isothermal subsonic jets has shown that a jet flow field is not totally chaotic, but that coherent structures in time and space develop in the initial region of the jet. This observation is corroborated by the work of Crow and Champagne [1971] and Brown and Roshko [1974]. Crow also discovered that the development of the flow field and the turbulent transition are widely controlled by the initial thickness and the initial turbulent or laminar state of the boundary layer, as well as the fluctuating turbulent intensity at the nozzle exit. Indeed, the axisymmetric mixing layer of a jet is a

shear flow with an inflectional axial velocity mean profile. However, such a flow profile is convectively unstable and Kelvin-Helmholtz hydrodynamic instabilities appear. The axisymmetric shear layer results in the formation of vortices close to the nozzle exit. Large-scale vortex pairing appears and leads to the formation of three-dimensional structures, which transition to jet-column instabilities with azimuthal variations.

Upstream of this shear layer, the boundary layer which develops on the walls of the nozzle contains viscous turbulent fluctuations which, at the outlet of the nozzle, excite the Kelvin-Helmholtz instabilities of the shear layer. These excitations to the lips of the nozzle represent initial conditions which are due to the receptivity of the shear layer. The impact of the initial boundary layer on the jet flow development has been experimentally shown by Hussain and Zedan [1978]; Husain and Hussain [1979]; Zaman [1985]. With initial laminar conditions, the turbulent exit conditions are weak, and the shear layer development of nozzle jets is governed by linear instability waves. The length of the potential core is reduced due to a rapid growth of the shear layer, and velocity fluctuations on the lip line peak at the first vortex pairing location, then decrease to reach a steady level. According to the experimental work of Bridges and Hussain [1984] and Zaman [1985], this initial state of the laminar jet results in the presence of strong vorticity pairings generating additional pressure fluctuations.

Aero-engine jet flows are commonly fully turbulent. At these conditions the turbulent transition length is shorter, the growth of the shear layer is more linear and smooth, and the potential core becomes longer. The development of the shear layer is entirely controlled by three-dimensional interactions and the vortex-pairing mode disappears. The peaks in turbulence levels are attenuated and approach a quasi-self-preserving turbulent state.

The development of the shear layer as well as the generation of turbulence, extremely sensitive to the nozzle exit conditions, produce different acoustic sources (Bridges and Hussain 1984; Harper-Bourne 2010). Fine scale turbulence is assimilated to compact noise sources distributed in the shear layer and propagating principally orthogonally to the jet axis. The acoustic propagation of the compact sources is impacted by the turbulent convection and the density stratification of the mean flow, as well as by the acoustic refraction induced by the shear layer. On the contrary, large turbulent structures and vortex pairing evolve in the mixing layer and generate non-compact (coherent) noise sources which propagate strongly in the downstream direction as seen in Fig. 5. As vortex pairing induced additional pressure fluctuations, the acoustic levels are generally overestimated. This additional mechanism of noise generation disappears for jets with a sufficiently turbulent inlet state. Using an empirical approach based on a large database for supersonic simple jets, Tam et al. [2008] proposed a model with two sources which

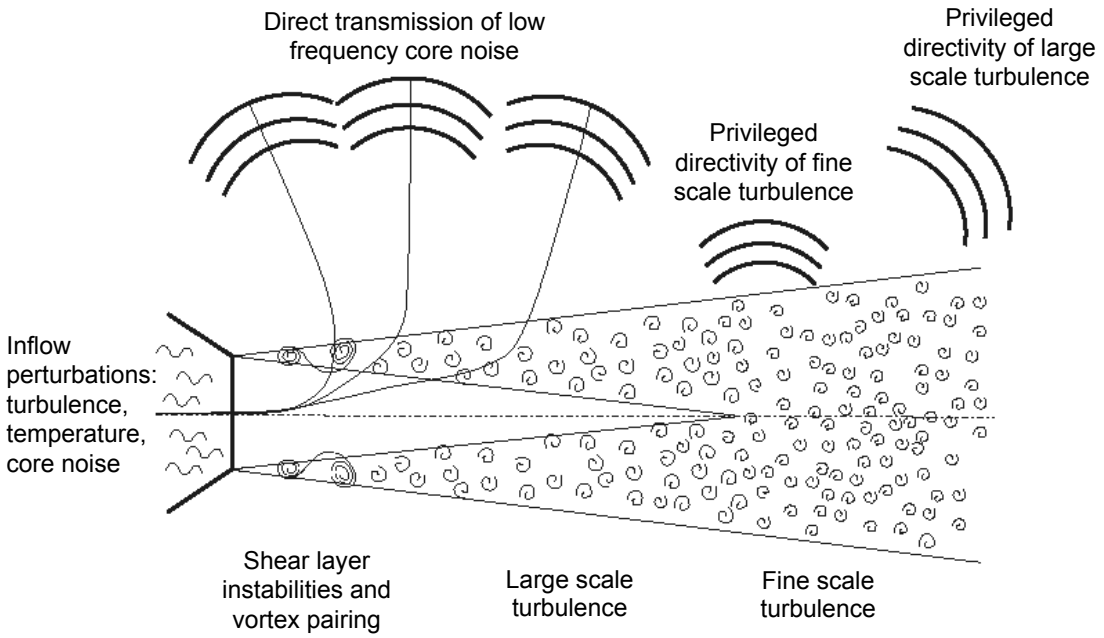

Figure 5: Privileged radiation of core noise, large and fine scale turbulence of a nozzle exhaust

can reproduce experimental jet spectra. This model gives two self-similar spectra LSS (Large Scale Similarity) and FSS (Fine Scale Similarity). The first spectrum, related to the large scale structures, is characterized by a well-marked privileged frequency in a narrow frequency band. The second spectrum, related to the fine scale structures, is more spread in frequency. These two spectra form an envelope in which the jet spectrum can be located.

Numerically, solving the boundary layers of the nozzle is extremely expensive. Consequently, techniques have been developed in order to destabilize the parietal flow and thus to obtain a jet with a turbulent shear layer from the nozzle exit. Bogey et al. [2012] used a spatio-temporal perturbation method to add perturbations to the nozzle inner wall upstream of the ejection. In their study, they tried several levels of excitation allowing to obtain different levels of turbulence at the nozzle exit. They have thus demonstrated the necessity to have a turbulence rate of at least 9% in order to obtain a turbulent jet from the nozzle exit, thus confirming the experimental results of Zaman [1985]. Another method consists in geometric nozzle wall perturbations as used by Fosso-Pouangué et al. [June 4-6 2012] and Sanjose et al. [2014] which obtained sufficiently high turbulence levels.

Zaman [2012] concluded that jets with a tripped boundary layer are less noisy, but that higher turbulence intensity in the nozzle increases the noise propagation.

Bogey et al. [2012]; Bogey and Marsden [2013] performed LES of jets with modulated initial boundary layer state and also observed this noise reduction effect between untripped and tripped boundary layer. A strong reduction of noise due to tripped boundary layer is observed at the 90° sideline angle, but is less important for downstream angles. It has also been noted the presence of large scale structures, meaning that weak vortex pairing noise is still persistent at highly disturbed nozzle exit conditions. This can be justified by the moderate Reynolds number and shear layer thickness.

A lot of studies have been performed for cold jet flow. However, the jet flow of a realistic turbofan-engine configuration is heated as the temperature has been increased during the combustion process. Therefore, it is necessary to investigate the temperature effects on jet noise.

Temperature effects on jet noise

The first to work on the noise of heated jets were Hoch et al. [1973] and Tanna [1977] who tried to investigate the noise mechanisms and the density effects on noise radiation. They observed in particular that at low acoustic Mach number ($M_a = U_j/c_\infty$ with U_j the exhaust velocity and c_∞ the speed of sound in the far-field), the increase in temperature leads to an increase in low frequency acoustic levels. This increase in low frequencies is less and less marked with the increase in Mach number. At high frequencies, the spectral levels decrease with the increase of temperature, whatever the velocity of the jet. At large acoustic Mach, all spectral levels decrease with increasing temperature. Thus, with the increase in temperature, the low and high frequencies are influenced differently according to the jet velocity. Tanna [1977] concluded that for an acoustic Mach number below 0.7, the increase in temperature leads to an overall increase in acoustic levels, due to the increase in low-frequency levels. On the contrary, for an acoustic Mach number above 0.7, acoustic levels decrease with increasing temperature. Their work also showed a peak frequency shift of the sound spectrum which could be attributed to a low Reynolds number effect as observed in the experimentation of Viswanathan [2004]. However, it is now known that it was due to spurious noise originating from the test rig. The density effects and the noise mechanisms in heated jets still remain open questions.

An interesting point to investigate is the combustion noise propagation in heated jet. Indeed, it has been seen that jet flow development and jet noise are sensitive to the nozzle exit conditions (laminar or turbulent boundary layers). High temperatures influence the noise radiation in function of the Mach number. An interesting issue is to know whether acoustic perturbations assimilated to combustion noise will impact the aerodynamic development and the acoustics of the jet flow.

Acoustic excitation of unheated jets

Bechert and Pfizenmaier [1977] and Moore [1977] performed acoustic excitation on isothermal jets and observed a broadband amplification of jet noise through acoustic tonal excitation. This amplification depends on the amplitude level of the tonal excitation and decreases as the jet Mach number increases. At high amplitude levels of excitation, the downstream development of turbulence is modified, implying a non-linear response to the excitation. On the contrary, later studies on low Mach number jets with low Reynolds number, managed by Kibens [1980] and by Hussain and Hasan [1985], showed a reduction of the broadband noise and excitation of subharmonics when forcing at the shear layer instability frequency. Indeed, Crow and Champagne [1971] observed that for a forcing frequency at a Strouhal number of 0.3, which is the privileged frequency of a jet, a perturbation of maximum amplitude is obtained. Moreover, the harmonic forcing organizes the large scale structures of the shear layer, so that the vortex pairing introduces a stationary sound source with strong directivity. Hence, a reduction of the broadband far-field jet noise can be achieved by controlling the excitation of the jet.

Acoustic excitation of heated jets

Although many studies concerning cold jets have been undertaken to reduce jet noise, few studies consider the effects of acoustic excitation on hot jets. Jubelin [June 4-6 1980] found that the broadband amplification in hot jets is lower than in unheated jets, and more localized around the excitation frequency. However, heated jets are more sensitive to upstream excitations, but this sensitivity decreases with increasing temperature. Indeed, the viscosity, which is function of temperature, increases so that fine scale turbulent structures are dissipated and the shear layer is relaminarized.

It is only recently that the full engine-core flow path is considered to take into account the effects of core noise on the far field radiation. See et al. [2012] investigated the jet noise receptivity to the nozzle-upstream entropy perturbations in compressible heated jets. To do so, a model problem is considered, in which a gas-turbine combustor discharges reaction products through a converging nozzle into the ambient environment. Duran et al. [2013a] studied the combustion noise by combining LES of combustion chamber with analytical models for the acoustic propagation across turbine blades. Livebardon et al. [2016] used the same methodology applied to a sector of a turboshaft helicopter engine. O'Brien et al. [2016] performed hybrid simulations of a canonical gas-turbine engine (composed of a combustor, a single-stage turbine, a converging nozzle and jet) and far-field acoustic radiation. It is in this context that the work of this PhD thesis is carried out. This work is in the continuity of the works of Duran and Livebardon and

consists in studying the combustion noise propagation by considering a realistic turbofan-engine core flow path from the combustion chamber to the far field.

Motivations and objectives of the thesis

Combustion noise faces a renewed interest of engine manufacturers as is becoming increasingly important as major contributor in aeroengine noise. This can be explained by two reasons: first, advanced designs have reduced the other sources of noise, notably jet noise which was the dominant source; then, the development of next generation low NOx emission combustors yields more unsteady combustion, resulting in higher thermoacoustic activity and more noise radiation from combustion. Consequently, different prediction methodologies for combustion noise are developed. The challenge is to consider the full engine-core flow path from the combustion chamber to the nozzle exhaust of a complex real turbofan-engine with a double stream jet. First, description of combustion noise requires to consider all the different processes involved in the generation of the sources. Thanks to the growth of High-Performance Computing resources, Computational Fluid Dynamics can be used to simulate the unsteady combustion in a confined chamber, the turbulent flow field, the acoustic source terms, and the transmission and reflexion of acoustic waves through the boundaries of the combustor. In this study, LES of the combustion chamber is performed with AVBP. This LES must accurately capture acoustic, entropy and vorticity waves. Then the generating mechanism of indirect noise in the turbine stages (rotor/stator) is considered with an analytical tool, CHORUS (Duran et al. 2013a; Livebardon et al. 2016), based on the assumptions of Cumpsty and Marble [1977] which allow to consider the conversion of entropy and vorticity modes into acoustic modes by strong acceleration. This tool is fed with the acoustic and convective (entropy and vorticity) waves captured with the LES of combustion chamber and computes the propagation of these waves through the turbine stages. Finally, the computed perturbations at the turbine outlet must be introduced in a simulation of jet noise and propagated to the far-field.

For the hybrid methodology CONOCHAIN (Livebardon 2015), developed at

Cerfacs, the far-field propagation is performed with the Helmholtz acoustic solver, AVSP-f. This computation allows to consider a quiescent flow ($M = 0$) with an heterogeneous sound speed field. However, acoustic refraction effects due to shear layers of jet flow are neglected. Fig. 6 illustrates the CONOCHAIN methodology.

To overcome this limitation and fully determinate the far-field propagation, this last step is replaced by a full resolved LES of dual-stream jets. Combustion noise sources computed at the outlet of the turbine with CHORUS are introduced in the jet simulations. Finally, the Ffowcs Williams and Hawkings (FWH) acoustic analogy is used to far-field propagate the sources extracted in the jet flow.

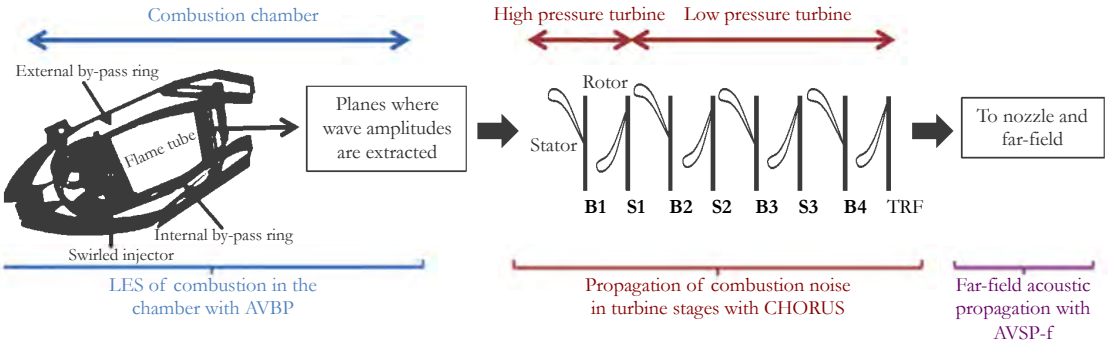

Figure 6: Description of the CONOCHAIN methodology

Figure 7 presents the flowchart of the combustion noise prediction process which guides this manuscript. The first part describes the CONOCHAIN methodology used for the prediction of combustion noise propagation from the combustion chamber to far-field (Chapters 1 to 3). The forcing method to introduce CHORUS combustion noise sources in LES jet simulations is presented in Chapter 4. The last part concerns the application of the two described methodologies to a complex realistic configuration presented in Chapter 5. The capability of the CONOCHAIN methodology will be investigated for different operating points of a turbofan-engine (Chapter 6) and compared to bench data and semi-empirical relations (Chapter 7). Analysis of the CONOCHAIN results will try to give key elements to have a better understanding of combustion noise in real complex configuration. Finally, the exhaust noise is taken into account for the far-field combustion noise propagation in Chapter 8. The influence of combustion noise perturbations on the jet flow development will be investigated. The interaction and contribution of the jet and the combustion to the total downstream engine noise will be discussed.

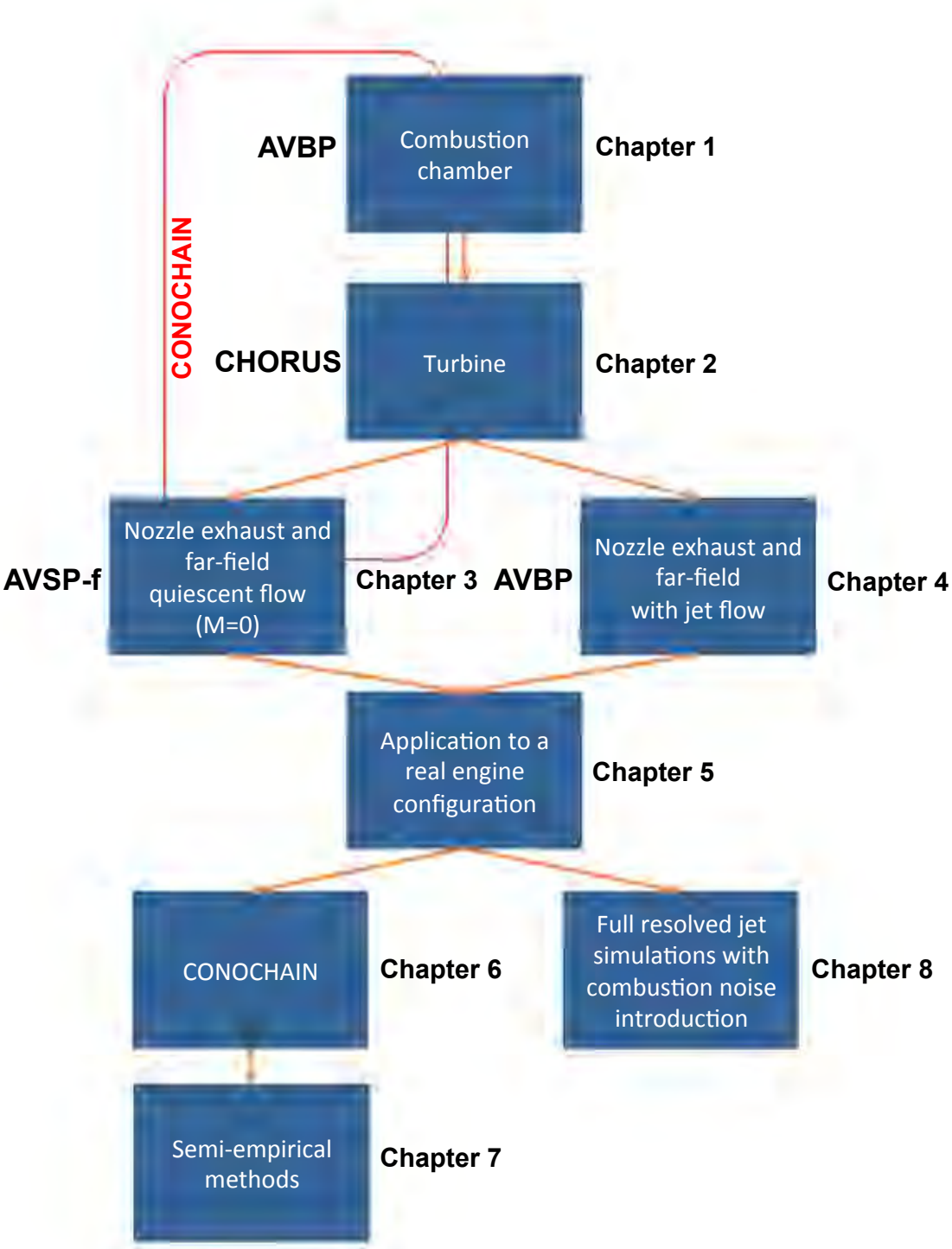

Figure 7: Flowchart of the thesis

Part II

Simulation methods for combustion noise

Table of Contents

Chapter 1

Sources prediction of combustor noise: Large Eddy Simulation of confined reactive flows

Abstract In order to quantitatively describe the combustion noise, multiple physical processes have to be considered. This requires to faithfully reproduce the unsteady combustion, the turbulent flow field and to capture acoustic source terms and their propagation. Combustion noise is a multi-physical and multi-scale problem, that involves a wide range of scales (from largest to smallest characteristic scale): the acoustic wave length, the characteristic flame length, the turbulence integral length scale, the Kolmogorov length scale and finally the flame thickness. The CONOCHAIN methodology first describes the noise generation from the unsteady reacting flow performing Large Eddy Simulation (LES). The advantage of this method is that few models are introduced and the multi-physical coupling between heat release, chemistry, hydrodynamics and acoustics in confined domains is conserved. However, this method faces many challenges regarding numerical discretization, boundary conditions, spatial resolution, transport properties and reaction chemistry. The equations that represent the unsteady reacting flow are presented in this chapter.

1.1 Filtered equations for compressible Large Eddy Simulations

Large Eddy Simulation is an intermediate approach between the Direct Numerical Simulation (DNS) and the Reynolds Averaged Navier-Stokes Simulation (RANS). These methods redefine a system of equations to reproduce the characteristics of turbulent flows. The derivation of the new equations is obtained by introducing operators into the compressible Navier-Stokes equations. Therefore unknown

terms appear and closure models need to be used. The difference between the RANS and the LES comes from the operator used for the derivation. In RANS, a time average is performed. Whereas in LES, a spatial average is chosen. A time-independent filter is defined to separate large scales (larger than the filter size) from small scales (smaller than filter size). Figure 1.1 represents the difference between DNS, LES, and RANS. A quantity a can be decomposed into a resolved

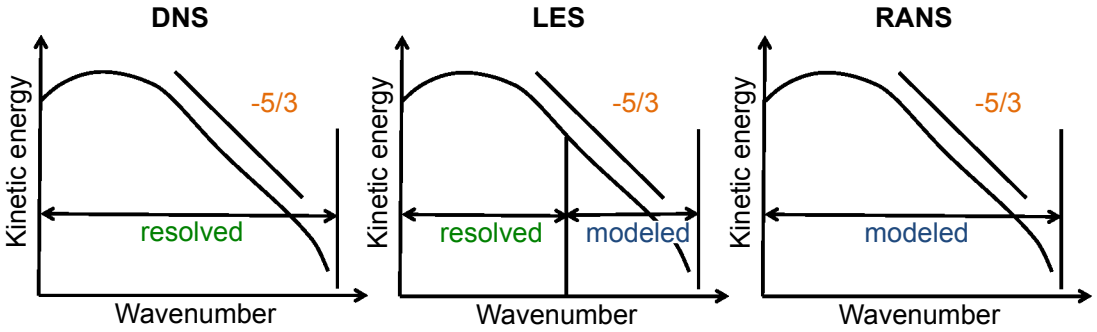

Figure 1.1: Difference of concept between the DNS, the LES and the RANS

part $\bar{a}$ and into a sub-grid part $a' = a - \bar{a}$, due to the unresolved flow. Favre averaging is introduced for the density ρ such that:

$$\tilde{a} = \frac{\overline{\rho a}}{\bar{\rho}} \,. \tag{1.1}$$

The conservation equations for the LES are deduced by filtering the instantaneous conservation equations:

$$\frac{\partial}{\partial t}\left(\bar{\rho}\tilde{u}_i\right) + \frac{\partial}{\partial x_j}\left(\bar{\rho}\tilde{u}_i\tilde{u}_j\right) = -\frac{\partial}{\partial x_j}\left(\bar{P}\delta_{ij} - \bar{\tau}_{ij} - \bar{\tau}^t_{ij}\right) \,, \tag{1.2}$$

$$\frac{\partial}{\partial t}\left(\bar{\rho}\tilde{E}\right) + \frac{\partial}{\partial x_j}\left(\bar{\rho}\tilde{u}_j\tilde{E}\right) = -\frac{\partial}{\partial x_j}\left(\overline{u_i(P\delta_{ij} - \tau_{ij})} + \bar{q}_j + \bar{q}^t_j\right) + \overline{\dot{\omega}_T} + \overline{Q_r} \,, \tag{1.3}$$

$$\frac{\partial}{\partial t}\left(\bar{\rho}\tilde{Y}_k\right) + \frac{\partial}{\partial x_j}\left(\bar{\rho}\tilde{u}_j\tilde{Y}_k\right) = -\frac{\partial}{\partial x_j}\left(\overline{J_{j,k}} + \overline{J_{j,k}}^t\right) + \overline{\dot{\omega}_k} \,, \tag{1.4}$$

where i and j vary discretely between 1 and 3. Unless otherwise stated, the repetition of an index implies a summation on this index (Einstein's notation). The index k refers to the k^{th} species and will not obey this rule. These equations can be reformulated as:

$$\frac{\partial \mathbf{w}}{\partial t} + \nabla.\mathbf{F} = \mathbf{s} \tag{1.5}$$

where $\mathbf{w}$ is the vector of the conservative variables:

$$\mathbf{w} = (\bar{\rho}\tilde{u}_i, \bar{\rho}\tilde{E}, \bar{\rho}_k)^T \tag{1.6}$$

with respectively ρ, u_i, E, ρ_k the density, the three cartesian components of the velocity vector $\mathbf{V} = (u_i)^T$, the energy per unit mass and the K^{th} species $\rho_k = \rho Y_k$ for $k = 1$ to N (N is the total number of species). The source term s is decomposed for convenience into a chemical source term and a radiative source term such that: $\mathbf{s} = \mathbf{s}^C + \mathbf{s}^R$. The flux tensor $\mathbf{F}$ can be decomposed into three parts: non-viscous terms, viscous terms and sub-grid terms. The last part corresponds to unclosed quantities due to the filtering LES and should be modeled. The non-viscous terms are written as

$$\begin{pmatrix} \bar{\rho}\tilde{u}_i\tilde{u}_j + \bar{P}\delta_{ij} \\ \bar{\rho}\tilde{u}_j\tilde{E} + \overline{pu_j}\delta_{ij} \\ \bar{\rho}_k\tilde{u}_j \end{pmatrix}, \tag{1.7}$$

where P, the static pressure, is given by the equation of state for a perfect gas, namely

$$P = \rho r T \text{ with } r = \frac{R}{W}. \tag{1.8}$$

$R = 8.3143$ J.mol^{-1}.K^{-1} is the universal gas constant that depends on the local gas composition through the mean molar mass W and T is the static temperature. The viscous terms of the flux tensor $\mathbf{F}$ are expressed as follows:

$$\begin{pmatrix} -\bar{\tau}_{ij} \\ -\overline{u_i\tau_{ij}} + \bar{q}_j \\ \overline{J_{j,k}} \end{pmatrix} \tag{1.9}$$

where q_j is the total heat flux, $J_{j,k}$ is the flux of the diffusive specie k and τ_{ij} is the viscous stress tensor. Finally the turbulent terms at the sub-grid scale are defined as

$$\begin{pmatrix} -\bar{\tau}^t_{ij} \\ \bar{q}^t_j \\ \overline{J^t_{j,k}} \end{pmatrix} \tag{1.10}$$

where the superscript t refers to the non-resolved terms at the subgrid scale.

1.2 Viscous terms

In AVBP, the terms composing the viscous part of the flux tensor are expressed assuming that the spatial variations of the molecular diffusion fluxes are negligible (Poinsot and Veynante 2011).

The viscous stress tensor τ_{ij} is written in exact formulation and then in its simplified version:

$$\bar{\tau}_{ij} = \overline{2\mu\left(S_{ij} - \frac{1}{3}\delta_{ij}S_{ll}\right)} \approx 2\bar{\mu}\left(\tilde{S}_{ij} - \frac{1}{3}\delta_{ij}\tilde{S}_{ll}\right) , \tag{1.11}$$

$$\text{with } \tilde{S}_{ij} = \frac{1}{2}\left(\frac{\partial \tilde{u}_j}{\partial x_i} + \frac{\partial \tilde{u}_i}{\partial x_j}\right) . \tag{1.12}$$

The molecular viscosity μ is supposed to be independent of the composition of the gas and to be close to that of the air. The classical Sutherland law is then used:

$$\mu = \mu_{ref}\frac{T^{3/2}}{T+S}\frac{T_{ref}+S}{T_{ref}^{3/2}}, \tag{1.13}$$

where for air at $T_{ref} = 273$ K, $\mu_{ref} = 1.7110^{-5}$ kg.m^{-1}.s^{-1} and $S = 110.4$ K.

Alternatively, a second law is available, called power law, for which the expression of the molecular viscosity reads:

$$\mu = \mu_{ref}\left(\frac{T}{T_{ref}}\right)^b , \tag{1.14}$$

with b typically ranging between 0.5 and 1.0. For example $b = 0.76$ for air.

The flux of the diffusive species $J_{j,k}$ based on the Hirschfelder Curtis approximation (Hirschfelder, Curtiss, and Bird 1969) is expressed in the following way:

$$\overline{J_{j,k}} = -\overline{\rho\left(D_k\frac{W_k}{W}\frac{\partial X_k}{\partial x_j} - Y_k V_j^c\right)} \approx -\tilde{\rho}\left(\overline{D_k}\frac{W_k}{W}\frac{\partial \tilde{X}_k}{\partial x_j} - \tilde{Y}_k\tilde{V}_j^c\right) , \tag{1.15}$$

where D_k is the molecular diffusivity coefficient of the species k and $X_k = Y_k W/W_k$ is the k^{th} species mole fraction.

To achieve the equilibrium of the mass balance, a correction speed V_j^c (Poinsot and Veynante 2011) can be written as:

$$V_j^c = \sum_{k=1}^{N}\frac{\bar{\mu}}{\bar{\rho}S_{c,k}}\frac{W_k}{W}\frac{\partial \tilde{X}_k}{\partial x_j} . \tag{1.16}$$

To reduce the numerical costs associated with the transport coefficients computation, a simplified approximation is used in AVBP for D_k. By considering constant Schmidt numbers $S_{c,k}$, the diffusion coefficient of each species k can be expressed as

$$D_k = \frac{\mu}{\rho S_{c,k}}. \tag{1.17}$$

For multi-species flows, an additional heat flux term appears in the diffusive heat flux. This term is due to heat transport by species diffusion. The total filtered heat flux is equivalent to:

$$\bar{q}_j = -\overline{\lambda \frac{\partial T}{\partial x_j}} + \sum_{k=1}^{N} \overline{J_{j,k} h_{s,k}} \approx -\bar{\lambda} \frac{\partial \tilde{T}}{\partial x_j} + \sum_{k=1}^{N} \overline{J_{j,k}} \tilde{h}_{s,k} \ , \tag{1.18}$$

where λ is the thermal conductivity of the mixture and $h_{s,k}$ the sensible mass enthalpies of the specie k.

The thermal conductivity can be simply related to the molecular viscosity by assuming a constant molecular Prandtl number Pr, so that:

$$\lambda = \frac{\mu C_p}{P_r}, \tag{1.19}$$

with the heat capacity of the mixture, $C_p = \sum_{i=1}^{N} C_{p,k} Y_k$.

1.3 Turbulent sub-grid scale terms

Because of the filtering, some terms of the transport equations representing turbulence fluxes at the sub-grid scale remain unknown and prevent complete resolution of the problem. In order to numerically solve the system, closure terms must be added. The models used in AVBP are detailed below (Poinsot and Veynante 2011).

The turbulent Reynolds tensor is expressed in the form:

$$\overline{\tau_{ij}}^t = -\bar{\rho} \left(u_i \tilde{u}_j - \tilde{u}_i \tilde{u}_j \right) \ . \tag{1.20}$$

In AVBP, this tensor is modeled as:

$$\overline{\tau_{ij}}^t = 2 \bar{\rho} \nu_t \left(\tilde{S}_{ij} - \frac{1}{3} \delta_{ij} \tilde{S}_{ll} \right) \ , \tag{1.21}$$

with ν_t the turbulent viscosity whose modeling relies on a turbulent subgrid model presented in the next section 1.4.

The species diffusion flux at the sub-grid scale is written:

$$\overline{J_{j,k}}^t = \bar{\rho}\left(\overline{u_j Y_k} - \tilde{u_j}\tilde{Y_k}\right) \ . \tag{1.22}$$

It is modeled as

$$\overline{J_{j,k}}^t = -\bar{\rho}\left(D_k^t \frac{W_k}{W}\frac{\partial \tilde{X_k}}{\partial x_j} - \tilde{Y_k}\tilde{V_j^{c,t}}\right) \ , \tag{1.23}$$

$$\text{with } D_k^t = \frac{\nu_t}{S_{c,k}^t} \tag{1.24}$$

$$\text{and } V_j^{c,t} = \sum_{k=1}^{N} \frac{\mu_t}{\bar{\rho} S_{c,k}^t}\frac{W_k}{W}\frac{\partial \tilde{X_k}}{\partial x_j} \ , \tag{1.25}$$

where $S_{c,k}^t$ is the constant turbulent Schmidt number of the k^{th} species and is the same for all species, μ_t is the turbulent dynamic viscosity.

The heat flux at the sub-grid scale is expressed as

$$\overline{q_j}^t = \bar{\rho}\left(\tilde{u_j E} - \tilde{u}_j\tilde{E}\right) \ , \tag{1.26}$$

where E is the sensible energy, which is modeled as follows:

$$\overline{q_j}^t = -\lambda_t \frac{\partial \tilde{T}}{\partial x_j} + \sum_{k=1}^{N} \overline{J_{j,k}}^t \tilde{H_{s,k}} \tag{1.27}$$

$$\text{with } \lambda_t = \frac{\mu_t C_p}{P_r^t} \tag{1.28}$$

for a constant number of Prandtl.

1.4 LES equation closure

The role of the turbulent subgrid model is to correctly account for the interaction between the resolved and the unresolved scales. The subgrid scales are assumed to have a universal behavior. Their contribution is generally represented as purely dissipative, which is a valid hypothesis in the frame of the Kolmogorov [1941] cascade theory. In complex turbulent flow, energy transfer from small residual scales to the largest scale is also possible through backscatter (Leslie and Quarini 1979). However, in the following models, the energy is transferred only from the filtered motions to the residual motions, with no backscatter. The main subgrid models available in AVBP and used in the simulations are described below:

1.4.1 Smagorinsky's model

The turbulent viscosity is expressed as follows:

$$\nu_T = (C_s\Delta)^2\sqrt{2\tilde{S}_{ij}\tilde{S}_{ij}}\ , \tag{1.29}$$

with Δ the characteristic size of the LES filter corresponding to the cubic root of the volume of the mesh and C_s the constant of the model estimated from Kolmogorov spectrum and fixed at 0.17. This model is able to correctly predict the decay of turbulence in homogeneous isotropic turbulence (Lilly 1967). However, the turbulent viscosity ν_T of Eq. (1.29) is non-vanishing in pure shear flows and is therefore generally not suitable for wall-bounded flows (Sagaut 2002) where it is generally too dissipative (Germano et al. 1991). In practice, the Smagorinsky [1963] model must be combined with wall laws for closed flows. This allows to compensate for the impossibility of using a fine mesh close to walls because of an expensive computation time. For all combustion simulations, adiabatic wall law will be used in this thesis.

1.4.2 Sigma's model

The SIGMA model was proposed by Nicoud et al. [2011]. The singular values $\sigma_1 \geq \sigma_2 \geq \sigma_3$ of the velocity gradient tensor $\dfrac{\partial u_i}{\partial x_j}$ are use to build the turbulent viscosity

$$\nu_t = (C_\sigma\Delta)^2\frac{\sigma_3(\sigma_1-\sigma_2)(\sigma_2-\sigma_3)}{\sigma_1^2}, \tag{1.30}$$

with the constant $C_\sigma = 1.35$. The SIGMA model has the correct asymptotic behavior at the wall and has an improved behavior for rotating flows. In this work, the SIGMA model is preferred in jet simulations: it has a correct asymptotic behavior for wall-bounded flows. The correct treatment of axisymmetric expansion might also be important when considering jet flow expansion.

1.5 Chemical kinetics

The reaction rate is modeled by an Arrhenius law written for N reactive and M reactions. $\dot{\omega}_k$ is the sum of reaction rates of species k on reactions j, j varying from 1 to M:

$$\dot{\omega}_k = \sum_{j=1}^{M}\dot{\omega}_{kj} = W_k\sum_{j=1}^{M}\nu_{kj}Q_j\ . \tag{1.31}$$

The coefficients ν_{kj} are the total stoichiometric coefficients of the reaction calculated from the stoichiometric coefficients of the reagents ν'_{kj} and the products ν_{kj} for each reaction j (j varying from 1 to M). Q_j is the progress variable of the reaction j:

$$Q_j = K_{f,j} \prod_{k=1}^{N} \left(\frac{\rho Y_k}{W_k}\right)^{\nu'_{kj}} - K_{r,j} \prod_{k=1}^{N} \left(\frac{\rho Y_k}{W_k}\right)^{\nu''_{kj}} . \tag{1.32}$$

$K_{f,j}$ and $K_{r,j}$ are the constants of the reaction j for the direct and the indirect sense respectively:

$$K_{f,j} = A_{f,j} exp\left(-\frac{E_{a,j}}{RT}\right) , \tag{1.33}$$

$$K_{r,j} = \frac{K_{f,j}}{K_{eq}} , \tag{1.34}$$

where $A_{f,j}$ is the pre-exponential factor of the reaction j, $E_{a,j}$ is the activation energy and K_{eq} is the equilibrium constant of the reaction J.

$$K_{eq} = \left(\frac{p_0}{RT}\right)^{\sum_{k=1}^{N} \nu_{kj}} exp\left(\frac{\Delta S_j^0}{R} - \frac{\Delta H_j^0}{RT}\right) . \tag{1.35}$$

p_0 is the reference pressure equal to 1 bar, ΔH_j^0 is the enthalpy variation (sensitive and chemical) and ΔS_j^0 is the entropy variation for reaction j.

$$\Delta H_j^0 = h_j(T) - h_j(0) = \sum_{k=1}^{N} \nu_{kj} W_k (h_{s,k}(T) + \Delta h_{f,k}^0) , \tag{1.36}$$

$$\Delta S_j^0 = \sum_{k=1}^{N} \nu_{kj} W_k s_k(T) , \tag{1.37}$$

where $\Delta h_{f,k}^0$ is the enthalpy of formation of species k at temperature $T_0 = 0$ K. $S_k(T)$ and $h_{s,k}(T)$ are respectively the entropy and enthalpy of each species as a function of temperature. These variables are computed with JANAF tables (Stull and Prophet 1971) and interpolated between 0 K and 5000 K.

The rate of heat release $\dot{\omega}_T$ is defined as

$$\dot{\omega}_T = -\sum_{k=1}^{N} \dot{\omega}_k \Delta h_{f,k}^0 . \tag{1.38}$$

The heat loss due to radiation is denoted by $\bar{Q}_r$. In the case of the simulations presented in Chapter 6, radiation will not be considered.

1.6 Combustion models

A major difficulty in reacting LES is to know how to deal with the thickness of the flame front which is generally much smaller than the LES filter size Δ. As the interaction between the flame and turbulent structure are known to be primordial to solve flame dynamics, combustion models have been built to take into account these effects and overcome this issue. Different approaches have been developed in the literature (Poinsot and Veynante [2011]):

- Algebraic models based on an infinite thin flame Fureby and Løfstrøm [1994].
- Geometrical approaches where the flame front is assumed to be thin compared to integral length scales Pitsch [2006]. The flame is then described as a propagating interface between fuel and oxidizer (non-premixed) or between fresh and burned gases (premixed). These approaches use flame front tracking techniques using a particular field variable which can be physical or not. It can be cited for example the G-equation where an arbitrary G variable is defined, generally related to the distance to the flame front (Kerstein et al. 1988). Another approach is the flame surface density assumption where the physical progress variable balance equation is filtered (Boger et al. 1998).
- Statistical analysis where scalar fields may be collected and analyzed for any location within the flow. Filtered values and correlations are afterwards extracted via knowledge of Filtered Probability Density Functions (FPDF) to be determined either by a presumed assumption or by solving a FPDF-transport equation (presumed Probability Density Function (PDF), Conditional Moment Closure (CMC)) Meneveau and Poinsot [1991]; Cook and Riley [1994]; Pierce and Moin [1998]. The fundamental idea is that the fluctuations lost by the filtering procedure can be described by introducing a probability density function which describes the chemical state of the system.
- Artificially thickening the flame front. In this approach a flame thicker than the real one is considered, but that has the same laminar flame speed Butler and O'Rourke [1977]; Angelberger et al. [1998]; Colin et al. [2000].

The last model is used in the numerical simulations of combustion presented in this work. The main idea of the thickened flame model is the resolution of the flame front on a mesh in which the mesh size is larger than the reacting zone always encountered in LES. Thickening alters the interaction between the vortices and the flame front: eddies smaller than the thickened reaction zone do not interact with the flame. As the flame surface is reduced, the reaction rate is underestimated. In order to correct this effect, an efficiency function ϵ has been developed from DNS

results and implemented into AVBP (Colin and Rudgyard [2000]). The Thickened Flame model is well suited to simulate perfectly premixed flames. For partially premixed cases, a dynamic approach is developed (Légier et al. [2000]).

Chapter 2

Generation and propagation of direct and indirect noise in turbine stages

Abstract While direct noise is generated inside the combustion chamber and propagates downstream through the components of the chamber, another potential source of noise need to be considered: turbulent mixing, unsteady combustion, and dilution holes induce non-acoustic perturbations such as velocity, temperature and mixture composition inhomogeneities. These non-acoustic perturbations exit the combustion chamber and interact with mean-flow gradients in downstream turbine stages. These interactions generate acoustic pressure fluctuations, known as indirect noise. Indirect noise can be separated into two contributions: the vortex noise coming from vorticity fluctuations and the entropy noise coming from temperature fluctuations as hot or cold spots. All these mechanisms of generation and propagation in the turbine have to be properly described. The contribution of the mixture inhomogeneities to indirect noise is not treated in this work: combustion is supposed to be complete when hot gases reach the nozzle.

2.1 Actuator disk theory

Using high-fidelity Computational Fluid Dynamics (CFD) methods for all the core noise flow path (combustion chamber, turbine, jet) remains impossible today. Even if LES is a powerful and precise method to predict the unsteady activity in a combustion chamber, it remains very difficult to use it to predict all the indirect mechanisms of noise generation and propagation in the turbine stages. An hybrid approach is required, and analytical methods seem to be a good alternative to describe quickly and simply the turbine geometry and the flow characteristics in which the combustion noise propagates. Due to the low-frequency nature of

combustion noise, the problem to study is simplified. Several methods to mimic the acoustic behavior in nozzles and turbines exist. It begins with the compact nozzle theory of Tsien [1952] and Marble and Candel [1977] for one-dimensional cases. An extension for two-dimensional cases is proposed by Cumpsty and Marble [1977] and Dowling [1995]). Later, the nozzle length has been considered in the work of Goh and Morgans [2011]). Other linear (Moase, Brear, and Manzie 2007; Giauque, Huet, and Clero 2012) and non-linear nozzle analysis (Giauque et al. 2013) have been developed. Finally, the expansion methods proposed by Duran and Moreau [2013]; Duran and Morgans [2015], allow to consider nozzle geometry effects on transmission and reflection of waves at non-compact frequencies. In a real turbofan-engine turbine, the blade axial chord is small (generally of about 3 cm) compared to the acoustic wavelengths of combustion noise (30 cm at 1000 K, considering the extreme frequency limit of combustion noise, i.e. 2000 Hz, and more than 6 m at 100 Hz). Consequently each blade row can be seen as a thin interface and the two-dimensional compact theory of Cumpsty and Marble [1977] can be used. This theory is valid for small Helmholtz numbers, $He = L_x^{blade}\omega/c$ (with L_x^{blade} the blade axial chord, c the speed of sound and ω the angular frequency). It has been shown by Leyko et al. [2010] and Mishra and Bodony [2013] with two-dimensional numerical simulations of turbine stage that the theory gives good prediction with an Helmholtz number smaller than 0.6. Only planar and azimuthal modes are considered since the cut-on frequency of radial mode is higher than the compact frequency limit. To take into account the azimuthal modes, an additional criterion must be considered. As mentioned before, a compact theory assumes the blade pitch-chord ratio to be low. However Mishra and Bodony [2013] found that there are local entropy disturbances smaller than the blade pitch L_y so that noise related to these convected perturbations is not well captured. Therefore azimuthal modes are safely predicted for $L_y/\lambda_y = \dfrac{m}{N_b - 1} < 0.1$ where λ_y is the azimuthal wavelength of the mode m for a turbine row of N_b blades. Two modes were enough according to Turboshaft Engine Exhaust Noise Identication (TEENI) investigation (Livebardon et al. 2015)

The actuator disk theory is written at the mid-span plane of the blade row for a two-dimensional unwrapped annular duct as shown in Fig. 2.1.

The linearized Euler equations describing the uniform flow between the compact blade rows and its small acoustic, entropy and vorticity perturbations, are first introduced in section 2.1.1. The small perturbations will be written at the inlet of turbine blade row as related to acoustic or convective (entropy and vorticity) waves, section 2.1.2. Then transfer functions across the blade row are derived to mimic the generation of acoustics (the so called indirect noise due to the acceleration of entropy and vorticity waves) and the propagation of four waves (upstream-propagating and downstream-propagating acoustic waves, entropy and

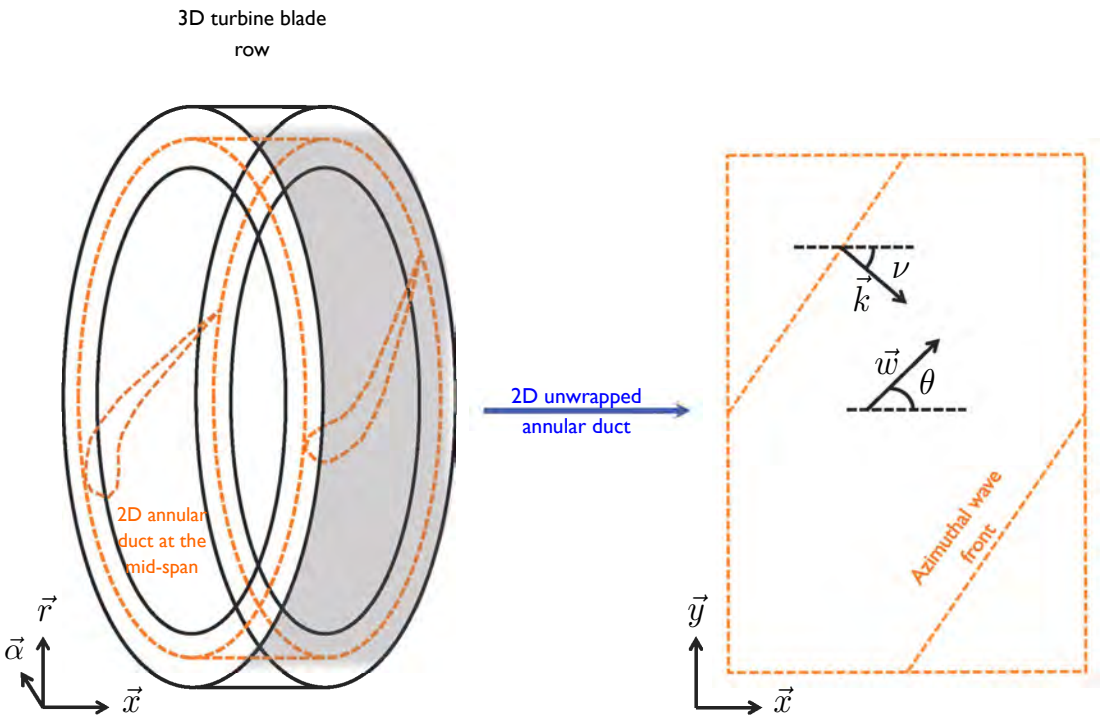

Figure 2.1: Sketch of the 2D unwrapped annular duct considered in CHORUS at the mid-span of a blade row

vorticity waves), giving the waves at the outlet of the row, section 2.1.3.

2.1.1 The linearized Euler equations

In order to describe the mean flow of a turbine stage, the flow is assumed two-dimensional, homogeneous, inviscid and isentropic. This flow is characterized by the mean velocity vector $\vec{w}$ (defined by its modulus w and its deviation angle θ with respect to the axial direction), the mean Mach number M, the mean pressure p and the mean density ρ. Perturbations are supposed to be sufficiently small not to disturb the mean flow so that linearized Euler equations can be applied. These equations are written in function of four dimensionless primitive variables as done by Cumpsty and Marble [1977]:

- Pressure fluctuations $\dfrac{p'}{\gamma p}$

- Entropy fluctuations $\frac{s'}{c_p}$, where c_p is the specific heat capacity at constant pressure
- Velocity modulus fluctuations $\frac{w'}{c}$
- Velocity deviation angle fluctuations θ'

For a mean steady homogeneous flow, where the mean velocity is composed of axial and circumferential velocities, respectively $u = w\cos(\theta)$ and $v = w\sin(\theta)$, they read:

$$\frac{D}{Dt}\left(\frac{\rho'}{\rho}\right) + \frac{\partial u'}{\partial x} + \frac{\partial v'}{\partial y} = 0, \tag{2.1}$$

$$\frac{D}{Dt}\left(u'\right) = -\frac{1}{\rho}\frac{\partial p'}{\partial x}, \tag{2.2}$$

$$\frac{D}{Dt}\left(v'\right) = -\frac{1}{\rho}\frac{\partial p'}{\partial y}, \tag{2.3}$$

$$\frac{D}{Dt}\left(\frac{s'}{c_p}\right) = 0. \tag{2.4}$$

The material derivative is defined as a time-derivative plus a convective part:

$$\begin{aligned} \frac{D}{Dt} &= \frac{\partial}{\partial t} + \vec{w}.\nabla \\ &= \frac{\partial}{\partial t} + u\frac{\partial}{\partial x} + v\frac{\partial}{\partial y}. \end{aligned} \tag{2.5}$$

Knowing that entropy can be written as $s = c_v \ln \frac{p}{\rho^\gamma}$, with c_v the specific heat capacity at constant volume, the fluctuations of entropy are obtained by logarithmic differentiation:

$$\frac{s'}{c_p} = \frac{p'}{\gamma p} - \frac{\rho'}{\rho}. \tag{2.6}$$

All pressure variations are only associated with acoustic waves, thus the pressure fluctuations in Eq. (2.6) correspond to the density fluctuations linked to the acoustic pressure variations of the entropy field.
The vorticity fluctuations are stated as:

$$\xi' = \frac{\partial v'}{\partial x} - \frac{\partial u'}{\partial y}. \tag{2.7}$$

Taking the derivative of the axial and circumferential linearized momentum equations (Eqs. 2.2,2.3) over y and x respectively:

$$\frac{\partial}{\partial y}\left(\frac{D}{Dt}(u')\right) = -\frac{1}{\rho}\frac{\partial^2 p'}{\partial y \partial x}, \tag{2.8}$$

$$\frac{\partial}{\partial x}\left(\frac{D}{Dt}(v')\right) = -\frac{1}{\rho}\frac{\partial^2 p'}{\partial x \partial y}, \tag{2.9}$$

and subtracting Eq. (2.8) from Eq. (2.9), the propagation equation of vorticity is obtained. Using Schwartz's theorem, the pressure terms are removed, then:

$$\frac{D}{Dt}(\xi') = 0. \tag{2.10}$$

To obtain the propagation equation of the pressure fluctuations by eliminating density and velocity fluctuations, Eqs. (2.1 to 2.4) are combined. First, Eq. (2.4) is used to replace the density term of Eq. (2.1) by pressure fluctuations. Considering the total derivative of the resulting equation gives:

$$\frac{D}{Dt}\left(\frac{D}{Dt}\left(\frac{p'}{\gamma p}\right) + \frac{\partial u'}{\partial x} + \frac{\partial v'}{\partial y}\right) = 0. \tag{2.11}$$

Combining the derivative over x of the axial linearized momentum (Eq. 2.2) and the derivative over y of the circumferential linearized momentum (Eq. 2.3) with Eq. (2.11), and knowing that $c^2 = \gamma p/\rho$, the propagation equation of the pressure fluctuations is finally written as:

$$\left(\frac{D}{Dt}\right)^2\left(\frac{p'}{\gamma p}\right) - c^2\left(\frac{\partial^2}{\partial x^2} + \frac{\partial^2}{\partial y^2}\right)\left(\frac{p'}{\gamma p}\right) = 0. \tag{2.12}$$

2.1.2 Wave decomposition

The mean flow has been described and propagation equations for each fluctuation have been stated in Sec. 2.1.1. These fluctuations can now be related to an acoustic or a convective wave. Four waves w^ϕ (upstream-propagating and downstream-propagating acoustic waves, entropy and vorticity waves) are written in their harmonic form:

$$\begin{aligned} w^\phi &= \hat{w}^\phi \exp\left(i(\omega t - \vec{k}^\phi.\vec{x})\right) \\ &= \hat{w}^\phi \exp\left(i(\omega t - k_x^\phi.x - k_y^\phi.y)\right) \\ &= \hat{w}^\phi \exp\left(i(\omega t - k^\phi.(x\cos(\nu^\phi) + y\sin(\nu^\phi)))\right),\ \forall \phi = +, -, s, v \end{aligned} \tag{2.13}$$

where (x, y) are the coordinate systems of the turbine-blade cascades (x being the engine axis), ω the angular frequency, $\vec{k}^\phi$ the wave vector composed of its

modulus k^ϕ and its wave front angle ν^ϕ with respect to the axial direction. It can be split into axial and azimuthal components, respectively $k_x^\phi = k^\phi \cos(\nu^\phi)$ and $k_y^\phi = k^\phi \sin(\nu^\phi)$.

To simplify, the wave vector $\vec{k}^\phi$ is scaled with the mean speed of sound c and the angular frequency ω, giving the dimensionless wave number magnitude $K^\phi = k^\phi c/\omega$. In addition, a mode-matching is assumed based on Marble and Candel [1977], meaning that there is continuity of pressure and velocity fields between two connected ducts of different diameters. Because of circumferential symmetry there is no scattering into other m modes. Therefore a wave conserves its frequency and the circumferential component of its wave vector k_y^ϕ through each blade row. This component is defined here as $K_y^\phi = k_y^\phi c/\omega = mc/R\omega$ with m the azimuthal mode number and R the mean radius at the mid-span of the blade. Knowing this azimuthal component K_y^ϕ, a dispersion equation is formulated to obtain the axial component of the dimensionless wave number K_x^ϕ.

2.1.2.1 Entropy wave

The entropy wave can be written as:

$$w^s = \frac{s'}{c_p} = \hat{w}^s \exp\left(i(\omega t - k^s.(x\cos(\nu^s) + y\sin(\nu^s)))\right). \tag{2.14}$$

Using this equation (2.14) and the entropy conservation, Eq. (2.4), a dispersion relation is obtained:

$$K^s M \cos(\nu^s - \theta) = 1, \text{ with } M \text{ the Mach number and } K^s = k^s c/\omega. \tag{2.15}$$

This wave does not generate velocity or pressure fluctuations since there is no acceleration. Thus dimensionless primitive variables linked to this wave are expressed as:

$$\begin{vmatrix} s'/c_p \\ w'/c \\ p'/\gamma p \\ \theta' \end{vmatrix}_s = |M_s| w^s, \quad \text{with the transition vector } |M_s| = \begin{vmatrix} 1 \\ 0 \\ 0 \\ 0 \end{vmatrix}. \tag{2.16}$$

2.1.2.2 Vorticity wave

In the same way as for the entropy wave, the vorticity wave is written in its harmonic form:

$$w^v = \xi' = \hat{w}^v \exp\left(i(\omega t - k^v.(x\cos(\nu^v) + y\sin(\nu^v)))\right). \tag{2.17}$$

Introducing this equation (2.17) in the propagation equation for the vorticity, Eq. (2.10), the dispersion relation is:

$$K^v M \cos(\nu^v - \theta) = 1. \tag{2.18}$$

The isentropic vorticity fluctuations are purely hydrodynamic and do not produce pressure or entropy fluctuations. Associating Eqs. (2.4 and 2.1), the continuity equation is rewritten as:

$$\frac{\partial u'}{\partial x} + \frac{\partial v'}{\partial y} = 0. \tag{2.19}$$

Velocity fluctuations u'/c and v'/c are related to the vorticity wave:

$$\frac{u'}{c} = -i\xi' \frac{\sin \nu^v}{\omega K^v} \quad \text{and} \quad \frac{v'}{c} = i\xi' \frac{\cos \nu^v}{\omega K^v}. \tag{2.20}$$

By using simple trigonometric relations, it can be written:

$$\frac{u'}{u} = \frac{w'}{w} - \theta' \tan(\theta), \tag{2.21}$$

$$\frac{v'}{v} = \frac{w'}{w} + \theta' / \tan(\theta). \tag{2.22}$$

Axial and azimuthal velocity fluctuations in terms of velocity magnitude fluctuations w'/c and deviation angle fluctuations θ' gives:

$$\frac{w'}{c} = -i\xi' \frac{\sin(\nu^v - \theta)}{\omega K^v} \quad \text{and} \quad \theta' = i\xi' \frac{\cos(\nu^v - \theta)}{\omega M K^v}. \tag{2.23}$$

Therefore the relation between the vorticity wave and the four primitive variables used in Cumpsty and Marble [1977] is:

$$\begin{vmatrix} s'/c_p \\ w'/c \\ p'/\gamma p \\ \theta' \end{vmatrix}_v = |M_v| w^v, \quad \text{with the transition vector } |M_v| = \begin{vmatrix} 0 \\ -i\dfrac{\sin(\nu^v - \theta)}{K^v} \\ 0 \\ i\dfrac{\cos(\nu^v - \theta)}{M K^v} \end{vmatrix}. \tag{2.24}$$

2.1.2.3 Acoustic waves

In Cumpsty and Marble [1977], pressure fluctuations considered are only due to acoustics, so that:

$$\frac{p'}{\gamma p} = w^+ + w^-, \tag{2.25}$$

w^+ and w^- being respectively the downstream and the upstream propagating acoustic waves. Dissociating the acoustic waves amplitudes from the pressure fluctuations implies to express the wave vector corresponding to each wave and the associated velocity components. First, the harmonic pressure fluctuations are:

$$\frac{p'}{\gamma p} = \left(\frac{\hat{p'}}{\gamma p}\right) \exp\left(i(\omega t - k.(x\cos(\nu) + y\sin(\nu)))\right). \tag{2.26}$$

Then, to satisfy the equation (2.12), the dispersion equation reads:

$$(1 - KM\cos(\nu - \theta))^2 - K^2 = 0, \tag{2.27}$$

and has two solutions. Involving the axial $K_x = K\cos(\nu)$ and azimuthal $K_y = K\sin(\nu)$ components of the dimensionless wave vector, the dispersion equation (2.27) becomes:

$$(1 - K_x M\cos(\theta) - K_y M\cos(\theta))^2 - (Kx^2 + K_y^2) = 0. \tag{2.28}$$

Solving Eq. (2.28) gives either complex or real roots related to upstream and downstream acoustic waves, respectively w^+ and w^-. The two real solutions correspond to acoustic waves that propagate without attenuation through the mean steady flow while complex roots are evanescent azimuthal waves that cannot propagate in the considered flow below a critical value of the azimuthal wave number K^y.

	Upstream-propagating $\mathbf{w^-}$	**Downstream-propagating $\mathbf{w^+}$**
Real	$K_x^- = A + B$	$K_x^+ = A - B$
Complex (evanescent azimuthal modes)	$K_x^- = A - iB$	$K_x^+ = A + iB$

Table 2.1: Axial wave number K_x for real or complex roots

The axial wave numbers obtained by solving Eq. (2.28) are expressed in Table (2.1), with:

$$A = \frac{M\cos\theta(1 - MK_y\sin\theta)}{(M\cos\theta)^2 - 1}, \tag{2.29}$$

$$B = \frac{\sqrt{1 - 2K_y M\sin\theta + K_y^2(M^2 - 1)}}{(M\cos\theta)^2 - 1}. \tag{2.30}$$

If $1-2K_yMsin\theta+K_y^2(M^2-1)>0$, the solutions of Eq. (2.28) lead to axial wave numbers for propagating acoustic waves. Otherwise if $1-2K_yMsin\theta+K_y^2(M^2-1)<0$, they give axial wave numbers which have an imaginary part and correspond to evanescent azimuthal modes.

Once the wave vectors K^- and K^+ of upstream and downstream acoustic waves are known and K_x is rewritten in complex form as $K_x^{\pm}=K_x^{(1)\pm}+iK_x^{(2)\pm}$, velocity components w'/c and θ' associated to the acoustic pressure fluctuations $p'/\gamma p$ can be determined as in Table (2.2).

	Upstream-propagating $\mathbf{w^-}$	**Downstream-propagating $\mathbf{w^+}$**
$\frac{\mathbf{w'}}{\mathbf{c}}$	$\frac{p'}{\gamma p}\frac{K^-\cos(\theta-\nu^-)-iK_x^{(2)-}\cos\theta}{1-K^-M\cos(\nu^--\theta)+iK_x^{(2)-}M\cos\theta}$	$\frac{p'}{\gamma p}\frac{K^+\cos(\theta-\nu^+)+iK_x^{(2)+}\cos\theta}{1-K^+M\cos(\nu^+-\theta)-iK_x^{(2)+}M\cos\theta}$
θ'	$\frac{p'}{\gamma p}\frac{1}{M}\frac{K^-\sin(\nu^--\theta)-iK_x^{(2)-}\sin\theta}{1-K^-M\cos(\nu^--\theta)+iK_x^{(2)-}M\cos\theta}$	$\frac{p'}{\gamma p}\frac{1}{M}\frac{K^+\sin(\nu^+-\theta)+iK_x^{(2)+}\sin\theta}{1-K^+M\cos(\nu^+-\theta)-iK_x^{(2)+}M\cos\theta}$

Table 2.2: Velocity components w'/c and θ' associated to upstream and downstream acoustic waves, w^- and w^+

Finally the relation between the acoustic waves and the four primitive variables is:

$$\begin{vmatrix} s'/c_p \\ w'/c \\ p'/\gamma p \\ \theta' \end{vmatrix}_{\pm} = |M_{\pm}| w^{\pm}, \tag{2.31}$$

with the transition vectors

$$|M_-| = \begin{vmatrix} 0 \\ \dfrac{K^- \cos(\theta - \nu^-) - iK_x^{(2)-} \cos\theta}{1 - K^- M \cos(\nu^- - \theta) + iK_x^{(2)-} M \cos\theta} \\ 1 \\ \dfrac{1}{M} \dfrac{K^- \sin(\nu^- - \theta) - iK_x^{(2)-} \sin\theta}{1 - K^- M \cos(\nu^- - \theta) + iK_x^{(2)-} M \cos\theta} \end{vmatrix}, \tag{2.32}$$

and

$$|M_+| = \begin{vmatrix} 0 \\ \dfrac{K^+ \cos(\theta - \nu^+) + iK_x^{(2)+} \cos\theta}{1 - K^+ M \cos(\nu^+ - \theta) - iK_x^{(2)+} M \cos\theta} \\ 1 \\ \dfrac{1}{M} \dfrac{K^+ \sin(\nu^+ - \theta) + iK_x^{(2)+} \sin\theta}{1 - K^+ M \cos(\nu^+ - \theta) - iK_x^{(2)+} M \cos\theta} \end{vmatrix}. \tag{2.33}$$

2.1.2.4 Relating acoustic and convective waves to primitive variables: matrix formulation

A formulation describing the fluctuations of the primitive variables generated by each wave has been obtained in the previous sections. Transition vectors relating primitive variables to the waves have been written. Each wave can now be expressed as a function of these fluctuations. These expressions can be reformulated through a matrix system by combining all the transition vectors:

$$\left[P\right] = \left[M\right]\left[W\right] \tag{2.34}$$

$$\left[P\right] = \left[|M_s| \quad |M_v| \quad |M_+| \quad |M_-|\right]\left[W\right] \tag{2.35}$$

where $[P]$ is the primitive vector:

$$\left[P\right] = \begin{bmatrix} s'/c_p \\ w'/c \\ p'/\gamma p \\ \theta' \end{bmatrix}, \tag{2.36}$$

$[W]$ is the wave vector:

$$\left[W\right] = \begin{bmatrix} w^s \\ w^v \\ w^+ \\ w^- \end{bmatrix}, \tag{2.37}$$

and M reads:

$$\begin{bmatrix} 1 & 0 & 0 & 0 \\ 0 & -i\dfrac{\sin(\nu^v-\theta)}{K^v} & \dfrac{K^+\cos(\theta-\nu^+)+iK_x^{(2)+}\cos\theta}{1-K^+M\cos(\nu^+-\theta)-iK_x^{(2)+}M\cos\theta} & \dfrac{K^-\cos(\theta-\nu^-)-iK_x^{(2)-}\cos\theta}{1-K^-M\cos(\nu^--\theta)+iK_x^{(2)-}M\cos\theta} \\ 0 & 0 & 1 & 1 \\ 0 & i\dfrac{\cos(\nu^v-\theta)}{MK^v} & \dfrac{1}{M}\dfrac{K^+\sin(\nu^+-\theta)+iK_x^{(2)+}\sin\theta}{1-K^+M\cos(\nu^+-\theta)-iK_x^{(2)+}M\cos\theta} & \dfrac{1}{M}\dfrac{K^-\sin(\nu^--\theta)-iK_x^{(2)-}\sin\theta}{1-K^-M\cos(\nu^--\theta)+iK_x^{(2)-}M\cos\theta} \end{bmatrix}.$$

2.1.3 Matching conditions trough a blade row

Acoustic and convective waves are known at the interface between the homogeneous flow and the turbine blade row inlet. To get the transfer functions of a blade row in terms of primitive variables, matching relations are needed. These relations will provide the downstream conditions (d) of a blade row from upstream conditions (u) (cf Fig. 2.2). Using the dimensionless wave vector magnitude K, ν and θ at each one of these states, $[M^u]$ and $[M^d]$ are obtained to convert primitive variables into waves.

With the approach of Marble and Candel [1977], conservation relations are written between the inlet and the outlet of the row, considering it as a thin interface. These relations are linearized in order to link the fluctuating primitive variables at upstream and downstream states. To solve the two-dimensional problem, four

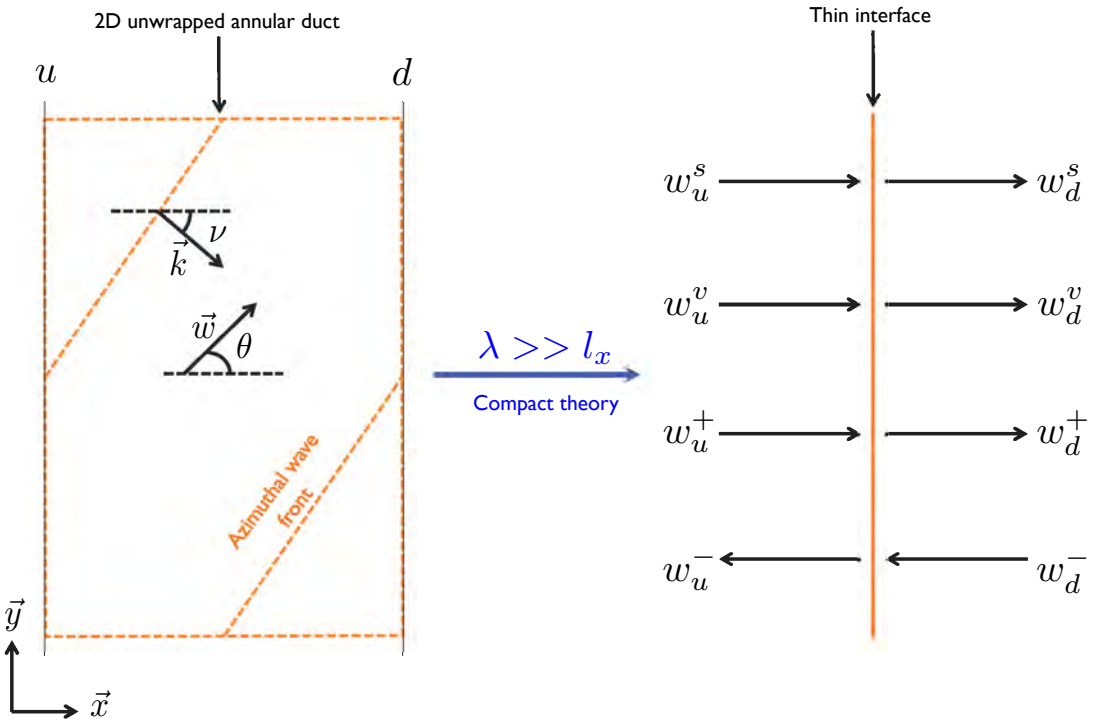

Figure 2.2: Sketch of the compact theory

matching relations are required and will depend on the blade row type (stator or rotor) and on the sonic state at the trailing edge of the blade as summarized in Table (2.3).

Through a stator blade, the flow expansion is isentropic so that enthalpy is conserved (Peng 2008). On the contrary, through a rotor blade, the rotational mean flow provides mechanical work to the row and rothalpy conservation law is used instead. Contrarily to what is assumed by Cumpsty and Marble [1977], Leyko et al. [2010], Duran and Moreau [2011] and Leyko et al. [2014] have shown using fully unsteady simulations that entropy wave is not conserved through a row: turbulent mixing, combined with the acceleration and deviation induced by the turbine blades, leads to a planar wave distortion and a damping of entropy waves through each passage. Becerril [2017] showed that there is conservation of the entropy fluctuation but conversion of plane wave into azimuthal modes (dispersion). Energy is redistributed into other azimuthal modes and far less indirect noise is generated in the last stages. To consider the scattering of the entropy wave, an

Stator case	Rotor case
Mass conservation	Mass conservation
Enthalpy conservation	Rothalpy conservation
Entropy conservation	Entropy conservation
Subsonic flow: Kutta condition	Subsonic flow: Kutta condition
Supersonic flow: 1D mass flow rate in an isentropic choked nozzle	Supersonic flow: 1D mass flow rate in an isentropic choked nozzle

Table 2.3: Relations used to build linearized matching relations through a blade row

attenuation function of the longitudinal entropy wave has been implemented and verified by Livebardon et al. [2015] on the two-dimensional simulations of Leyko et al. [2010] and Duran and Moreau [2011]. Bauerheim et al. [2016] has shown the importance of the velocity profile and the boundary layer on the entropy wave distortion. A last relationship depends on the mean flow state at the trailing edge of the blade. For a subsonic flow, a Kutta condition is used and replaced for choked flow by the conservation of the mass flow rate through a one-dimensional isentropic choked nozzle. These conditions are linearized in the following sections.

2.1.3.1 Mass conservation

Using mass conservation principle, the mass flow rate for a stator or rotor vane reads:

$$\begin{aligned} \dot{m} &= \rho u \\ &= \rho w \cos\theta, \end{aligned} \tag{2.38}$$

conservation of the fluctuating mass flow rate is obtained by logarithmic differentiation:

$$\begin{aligned} \frac{\dot{m}'}{\dot{m}} &= \frac{\rho'}{\rho} + \frac{w'}{w} - \frac{\theta' \sin\theta}{\cos\theta} \\ \frac{\dot{m}'}{\dot{m}} &= \frac{\rho'}{\rho} + \frac{1}{M}\frac{w'}{c} - \theta' \tan\theta. \end{aligned} \tag{2.39}$$

Substituting the density term by pressure one using Eq. (2.6) gives:

$$\frac{\dot{m}'}{\dot{m}} = \frac{p'}{\gamma p} - \frac{s'}{c_p} + \frac{1}{M}\frac{w'}{c} - \theta' \tan\theta. \tag{2.40}$$

2.1.3.2 Energy conservation: enthalpy for a stator or rothalpy for a rotor

According to the first law of thermodynamics, the total enthalpy $H_t = c_p T + w^2/2$ is conserved and its conservation is equivalent to the conservation of the total temperature T_t (Bauerheim et al. 2016). From the isentropic relation, the total temperature is:

$$T_t = T\left(1 + \frac{\gamma - 1}{2} M^2\right). \tag{2.41}$$

Then using logarithmic differentiation and the state law, Eq. (2.41) becomes:

$$\frac{T_t'}{T_t} = \frac{(\gamma - 1)\dfrac{p'}{\gamma p} + \dfrac{s'}{c_p} + (\gamma - 1) M \dfrac{w'}{c}}{\mu}, \tag{2.42}$$

where

$$\mu = 1 + \frac{\gamma - 1}{2} M^2 \tag{2.43}$$

For a rotor, the conservation of the total enthalpy in the moving frame is considered and defined as rothalpy I, with:

$$\begin{aligned} I &= H_t - U w \sin\theta \\ &= H_t - U v. \end{aligned} \tag{2.44}$$

In practice, rothalpy is the total enthalpy from which the work provided to the rotor is deduced, U being the rotational velocity of the rotor. The linearization of Eq. (2.45) yields:

$$\frac{I'}{I} = \frac{H_t' - U v'}{H_t - U v} = \frac{\dfrac{H_t'}{H_t} - \dfrac{U v'}{H_t v}}{1 - \dfrac{U v}{H_t}}. \tag{2.45}$$

Defining $\chi = \dfrac{U v}{H_t}$ and combining Eqs. (2.42, 2.22 and 2.45) the linearized rothalpy equation becomes:

$$\frac{I'}{I} = \frac{1}{1 - \chi}\left(\frac{T_t'}{T_t} - \chi\left(\frac{1}{M}\frac{w'}{c} + \frac{\theta'}{\tan\theta}\right)\right) \tag{2.46}$$

If the rotational velocity of the rotor is null so that $\chi = 0$, the linearized equation for rothalpy Eq. (2.46) is equivalent to the linearized total temperature equation Eq. (2.42).

2.1.3.3 Entropy conservation

It is assumed by Cumpsty and Marble [1977] that entropy fluctuations are conserved through a blade row. Actually the entropy is not necessarily conserved mode-by-mode. Leyko et al. [2010], Duran and Moreau [2011] and Bauerheim et al. [2016] show with two-dimensional LES of a stator and a stator-rotor configurations that the entropy wave convected by the mean flow is scattered to higher-order azimuthal modes since the convective velocity is not uniform. Considering the streamlines distortion due to this non-uniformity, a time-delay of the convected entropy particles compared with the entropy wave front has to be included as done by Livebardon et al. [2015]. A simple assumption is to define the axial velocity profile as parabolic. To build a model in order to scatter the entropy, few parameters have to established first. Choosing a dimensionless perimeter r restricted between 0 and 1, it can be written a dimensionless pitch length y also limited between 0 and 1:

$$y(r) = N_{vane}.r - i_{vane}, \tag{2.47}$$

for the i^{th} considered blade vane i_{vane} of N_{vane} blade vanes. For a complete blade row, the dimensionless axial velocity profile is:

$$\frac{U_x^{axial}(r)}{U_{max}^{axial}} = 4y(r)(1 - y(r)). \tag{2.48}$$

Given the mass conservation over the row, the integration over the perimeter r of the axial velocity profile in Eq. (2.48) gives the maximum velocity U_{max}^{axial} in function of the mean velocity U_{mean}^{axial}.

$$U_{max}^{axial} = \frac{U_{mean}^{axial}}{\int_0^1 U_x^{axial}(r)dr}. \tag{2.49}$$

Naming $\tau(r)$ the convective time through a blade row of axial chord L_x, the axial velocity is written as:

$$U_x^{axial}(r) = \frac{L_x}{\tau(r)}. \tag{2.50}$$

By log-differentiation of Eq. 2.50 it comes:

$$\frac{dU_x^{axial}(r)}{U_{mean}^{axial}} = -\frac{\tau_d}{\tau_{mean}}, \tag{2.51}$$

where $\tau_{mean} = L_x/U_{mean}^{axial}$ and the time-delay τ_d is written as:

$$\tau_d(r) = -\frac{L_x(U_x^{axial}(r) - U_{mean}^{axial})}{U_{mean}^{axial}} \tag{2.52}$$

Finally an entropy transfer function $H_s(f)$ of the azimuthal mode m across a blade row is written in function of the frequency f as:

$$H_s(f) = \frac{w_d^s}{w_u^s} = \int_0^1 \exp(i2\pi(f\tau_d(r) + mr))dr. \tag{2.53}$$

This expression represents the phase-shift between the entropy particles and the entropy wave front, due to streamlines distortion, as verified by Livebardon et al. [2015] using the numerical results of Leyko et al. [2010], Duran and Moreau [2011] and Leyko et al. [2014]. Bauerheim et al. [2016] has developed a generic axi-symmetric power-low to describe the mean axial velocity in a blade vane. This allow to consider more realistic geometries. It has been demonstrated that the entropy signal power is scattered to higher azimuthal modes of index m, multiples of the number of blade vanes. These azimuthal modes are evanescent below a cut-on frequency higher than the compactness limit. Therefore these modes are not fed by the scattering of the entropy mode. In the tool CHORUS, no entropy transfer is taken into account from planar to azimuthal mode. Only an attenuation of the entropy planar mode ($m = 0$) is considered with the entropy transfer function. These results have been corroborated by Sattelmayer [2003] and Morgans et al. [2013] with analytical approaches and a DNS.

2.1.3.4 Kutta condition for subsonic flow

Kutta condition imposes the deviation of the flow at the trailing edge of a blade, Fig. 2.3. No fluctuation of the velocity angle is allowed at the trailing edge, thus:

$$\theta_1' = \beta\theta_2', \tag{2.54}$$

with β a numerical parameter set to an infinitesimal quantity.

Kutta condition requires to be extended to the rotor case. Consequently Eq. (2.54) is written in the moving frame of the rotor. Considering the angle flow tangent:

$$\tan\theta_r = \frac{v - U}{u}, \tag{2.55}$$

and doing a log-differentiation, this leads to:

$$\frac{(\tan\theta_r)'}{\tan\theta_r} = \frac{v'}{v - U} - \frac{u'}{u}. \tag{2.56}$$

Finally an equation for the fluctuating flow angle θ_r' in the relative frame is written using Eqs. (2.21,2.22):

$$\theta_r' = f_w \left(\frac{U}{w\cos\theta} \frac{1}{M} \frac{w'}{c} + \theta' \left(1 + (\tan\theta)^2 - \frac{U}{w\cos\theta}\tan\theta \right) \right), \tag{2.57}$$

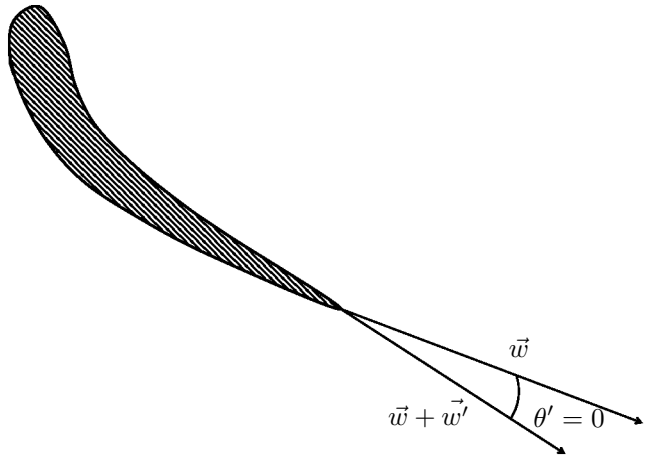

Figure 2.3: Fluctuating angle imposed by Kutta condition at the trailing edge

with

$$f_w = \frac{(w\cos\theta)^2}{w^2 - 2wU\sin\theta + U^2} \tag{2.58}$$

Assuming $U = 0$, Eq. (2.57) gives $\theta'_r = \theta'$ in the case of a stator blade.

2.1.3.5 Mass flow rate conservation for choked flow

As it is often the case for industrial configuration, the first stator of high pressurized turbines can be supersonic. Hence Kutta's condition which fixes the circulation around the airfoil to locate the stagnation point at the trailing edge is no longer verified. The expression of the mass flow rate for choked nozzle is used instead. The mass flow rate can be written as:

$$\dot{m} = \frac{p}{\sqrt{T}}\left(1 + \frac{\gamma - 1}{2}M^2\right)^{\frac{\gamma+1}{2(\gamma-1)}}, \tag{2.59}$$

and linearized to obtain:

$$\frac{\gamma - 1}{2}\frac{p'}{\gamma p} + \frac{1}{2}\frac{s'}{c_p} - \frac{1}{M}\frac{w'}{c} + \tan\theta\frac{1 + \frac{\gamma-1}{2}M^2}{1 - M^2}\theta' = 0. \tag{2.60}$$

In the relative frame of the rotor, Eq. (2.60) becomes:

$$\begin{aligned}
&\frac{\gamma-1}{2}\frac{p'}{\gamma p}+\frac{1}{2}\frac{s'}{c_p} \\
&+\quad \frac{w'}{c}\left(\frac{\gamma+1}{2}\frac{M_r^2}{1-M_r^2}\frac{1}{M}\eta\left(1-\frac{U}{w}\sin\theta\right)-\frac{\mu}{M(1-M_r^2)}\right) \\
&+\quad \theta'\left(\tan\theta-\left(\eta\frac{U}{w}\cos\theta\right)\left(\frac{\gamma+1}{2}\frac{M_r^2}{\mu}\right)\right)\frac{\mu}{1-M_r^2}=0,
\end{aligned} \tag{2.61}$$

with

$$\eta=\frac{1}{1+\left(\frac{U}{w}\right)^2-2\frac{U}{w}\sin\theta}, \tag{2.62}$$

and

$$M_r=\frac{\sqrt{(w\sin\theta-U)^2+(w\cos\theta)^2}}{c}. \tag{2.63}$$

Finally a linearized equation for the relative Mach number is obtained from Eq. (2.61):

$$\frac{M_r'}{M_r}=-\frac{\gamma-1}{2}\frac{p'}{\gamma p}-\frac{1}{2}\frac{s'}{c_p}+\eta\frac{1}{M}\left(1-\frac{U}{w}\sin\theta\right)\frac{w'}{c}-\eta\cos\theta\frac{U}{w}\theta'. \tag{2.64}$$

If the rotor velocity U is equal to zero, Eq. (2.61) is equivalent to Eq. (2.60) for a stator.

2.1.3.6 Tranfer functions across a blade row: matrix formulation

To combine the relations of the fluctuating primitive variables between the upstream u and the downstream d of a blade row, a matrix system is written:

$$\left[T^u\right]\left[P^u\right]=\left[T^d\right]\left[P^d\right] \tag{2.65}$$

It has been verified previously that the relations for a stator match with the rotor ones when the rotor velocity U is zero, leading to $\chi=0$. Hence the matrix $[T]$ is defined for a subsonic or a supersonic rotating blade row. In the case of a subsonic stage, the matrices at the upstream and downstream of a row read:

$$\left[T^u\right]=\begin{bmatrix}
H_s(f) & 0 & 0 & 0 \\
-1 & \frac{1}{M} & 1 & -\tan\theta \\
\frac{1}{1-\chi}\frac{1}{\mu} & \frac{1}{1-\chi}\left(\frac{(\gamma-1)M}{\mu}-\frac{\chi}{M}\right) & \frac{1}{1-\chi}\frac{\gamma-1}{\mu} & -\frac{1}{1-\chi}\frac{\chi}{\tan\theta} \\
0 & f_w\frac{U}{Mw\cos\theta} & 0 & f_w\left(1+(\tan\theta)^2-\frac{U\tan\theta}{w\cos\theta}\right)
\end{bmatrix}, \tag{2.66}$$

and

$$\left[T^d\right]=\begin{bmatrix} H_s(f) & 0 & 0 & 0 \\ -1 & \frac{1}{M} & 1 & -\tan\theta \\ \frac{1}{1-\chi}\frac{1}{\mu} & \frac{1}{1-\chi}\left(\frac{(\gamma-1)M}{\mu}-\frac{\chi}{M}\right) & \frac{1}{1-\chi}\frac{\gamma-1}{\mu} & -\frac{1}{1-\chi}\frac{\chi}{\tan\theta} \\ 0 & f_w\frac{U}{Mw\cos\theta}\beta & 0 & f_w\left(1+(\tan\theta)^2-\frac{U\tan\theta}{w\cos\theta}\right)\beta \end{bmatrix}. \quad (2.67)$$

Otherwise for a supersonic stage, Kutta's condition is replaced by the linearized relation of the mass flow rate for one-dimensional choked nozzle, so that the matrices become:

$$\left[T^u\right]=\begin{bmatrix} H_s(f) & 0 & 0 & 0 \\ -1 & \frac{1}{M} & 1 & -\tan\theta \\ \frac{1}{1-\chi}\frac{1}{\mu} & \frac{1}{1-\chi}\left(\frac{(\gamma-1)M}{\mu}-\frac{\chi}{M}\right) & \frac{1}{1-\chi}\frac{\gamma-1}{\mu} & -\frac{1}{1-\chi}\frac{\chi}{\tan\theta} \\ \frac{1}{2} & H_w & \frac{\gamma-1}{2} & H_\theta \end{bmatrix}, \quad (2.68)$$

and

$$\left[T^d\right]=\begin{bmatrix} H_s(f) & 0 & 0 & 0 \\ -1 & \frac{1}{M} & 1 & -\tan\theta \\ \frac{1}{1-\chi}\frac{1}{\mu} & \frac{1}{1-\chi}\left(\frac{(\gamma-1)M}{\mu}-\frac{\chi}{M}\right) & \frac{1}{1-\chi}\frac{\gamma-1}{\mu} & -\frac{1}{1-\chi}\frac{\chi}{\tan\theta} \\ \beta & \beta & \beta & \beta \end{bmatrix}, \quad (2.69)$$

where

$$H_w=\frac{\gamma+1}{2}\frac{M_r^2}{1-M_r^2}\frac{1}{M}\eta\left(1-\frac{U}{w}\sin\theta\right)-\frac{\mu}{M(1-M_r^2)}, \quad (2.70)$$

and

$$H_\theta=\frac{\mu}{1-M_r^2}\left(\tan\theta-\left(\eta\frac{U}{w}\cos\theta\right)\left(\frac{\gamma+1}{2}\frac{M_r^2}{\mu}\right)\right). \quad (2.71)$$

2.1.4 Acoustic description of a complete turbine stage

In the previous section, transfer functions have been written across a blade row to obtain fluctuating primitive variables at both sides of the interface. Combining Eq. (2.65) with Eq. (2.34), acoustic, entropy and vorticity waves are obtained at the outlet of the turbine stage:

$$\left[T^u\right]\left[M^u\right]\left[W^u\right] = \left[T^d\right]\left[M^d\right]\left[W^d\right], \tag{2.72}$$

with $[T]$ the transfer function matrix defined in section (2.1.3.6), $[M]$ the matrix detailed in section (2.1.2.4) to convert primitives variables into waves and W the wave vector. This matrix system is used to solve the problem with boundary conditions correctly imposed. First, waves coming from the combustion chamber have to be decomposed in modes related to K_y and frequencies ω. Then $[M]$ and $[T]$ are computed at both sides of the blade row for each pair of (K_y, w). The product of $[T]$ by $[M]$ is noted $[A]$ to simplify the system. To account for the propagation in the inter-blade regions of a complete turbine, a phase shift based on the wave travel times between rows is applied. Although stators and rotors are assumed compact, these travel times make the formulation frequency dependent. Validations of this model have been performed for a stator and a stator-rotor configurations by Duran and Moreau [2012]. The phase shift is expressed in function of the axial wave number K_x, the axial spacing L_x between two successive rows i^{th} and $(i+1)^{th}$ and the axial chord L_x^{blade} of the considered i^{th} row. A diagonal matrix $[L]$ is written to consider the phase shift, so that the diagonal components are:

$$L_{ii} = \exp(-iK_x(L_x + L_x^{blade})). \tag{2.73}$$

Finally the wave vector at the leading edge of the $(i+1)^{th}$ row is written as:

$$\left[W_{i+1}^u\right] = \left[L\right]\left[W_i^d\right]. \tag{2.74}$$

For a complete turbine composed of N rows (cf Fig. 2.4), implementing the phase-shift Eq. (2.74) in Eq. (2.72), the system becomes:

$$\left[\prod_{i=1}^{N-1}\left(\left[A_{i+1}^u\right]\left[L_i\right]\left[A_i^d\right]^{-1}\right)\right]\left[A_1^u\right]\left[W_1^u\right] = \left[A_N^d\right]\left[W_N^d\right]. \tag{2.75}$$

This system has four unknowns, the three downstream-propagating waves at the turbine exit and the reflected acoustic wave in the combustion chamber, see Fig. 2.5. The boundary conditions are the three downstream-propagating waves at the inlet

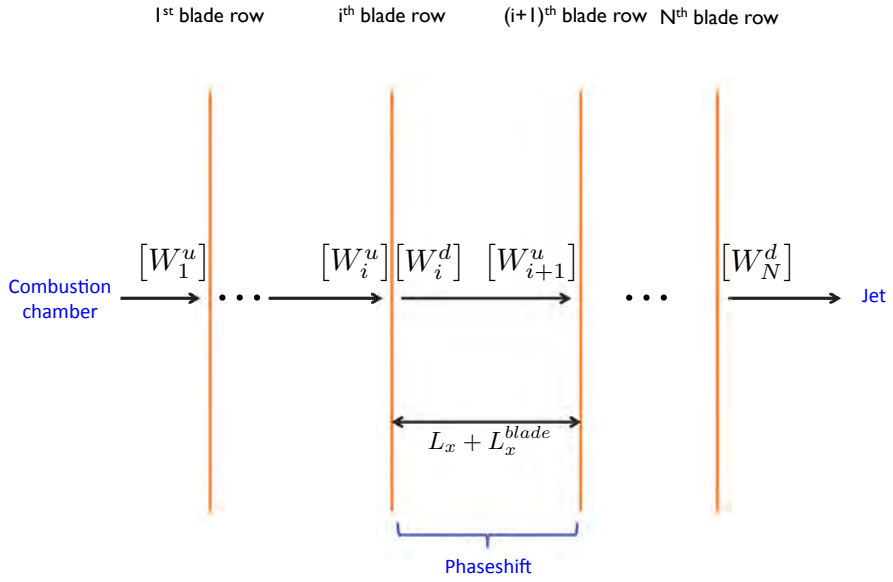

Figure 2.4: Sketch of a turbine of N blade rows

of the turbine provided by the LES, and the non-reflecting boundary condition imposed at the exit of the turbine, $w^- = 0$. To solve the system, the unknown waves at the inlet and outlet of the turbine have to be first provided. Then Eq. (2.75) is used to consider the intermediate blade rows in the complete system and finally to obtain the correct downstream-propagating waves at the outlet of the turbine. It is important to notice that the problem is only solved for a subsonic wave propagation even if supersonic flow can be considered at the exit of a blade row. Therefore the mean Mach number has to be limited to $1/\cos\theta$. This limitation is always verified in real engines.

Finally, the acoustic power of the i^{th} blade row is obtained using the formulation of Bretherton and Garrett [1968] to take into account the convective terms. This computation is made for each mode related to K_y and each noise mechanism: direct, indirect due to entropy and indirect due to vorticity. The acoustic intensity of the i^{th} blade row is:

$$I^{(i)} = [[(M\cos\theta + \cos\nu^+)(1 + M\cos(\theta - \nu^+))]^{(i)}(w_i^+)^2 + [(M\cos\theta + \cos\nu^-)(1 + M\cos(\theta - \nu^-))]^{(i)}(w_i^-)^2](\gamma pc)^{(i)}. \tag{2.76}$$

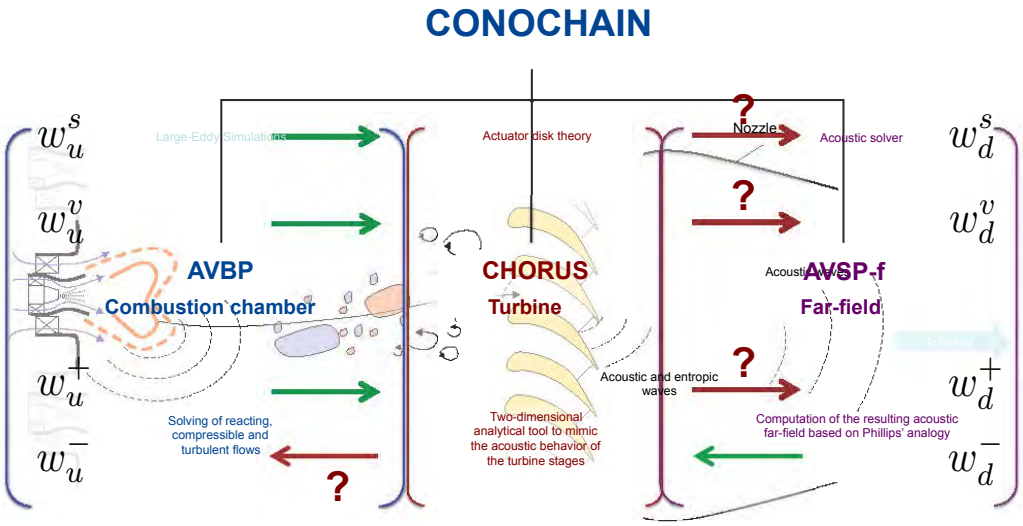

Figure 2.5: Boundary conditions of the problem to solve

2.2 Post-processing waves provided by a combustion chamber LES

As seen in section (2.1.4), boundary conditions are required to compute the acoustic generation and propagation through turbine stages in the frequency domain of longitudinal and azimuthal modes. The three downstream-propagating waves at the inlet of the turbine are given by the LES after a specific post-processing. A large set of instantaneous field at the exit of the combustion chamber is interpolated on successive structured cartesian planes. The time step between each instantaneous solutions has to be sufficiently small to avoid aliasing giving a maximal possible frequency of $F_{max} = 1/\Delta t$. The numerical simulation time gives the minimal frequency computed $F_{min} = 1/t_{LES}$.

The planes are normal to the engine axis and placed approximatively one chord before the high pressurized turbine stator (HPTS), Fig. 2.6. The pressure p, the entropy s, the velocity magnitude w and the angle θ are extracted on each plane to build the wave vector $[W]$.

2.2.1 Construction of the primitive vector [P]

The actuator disk theory of Cumpsty and Marble [1977] requires fluctuations of four dimensionless primitive variables: pressure fluctuations $p'/\gamma p$, entropy fluctuations s'/c_p, velocity fluctuations w'/c and deviation angle fluctuations θ'. First,

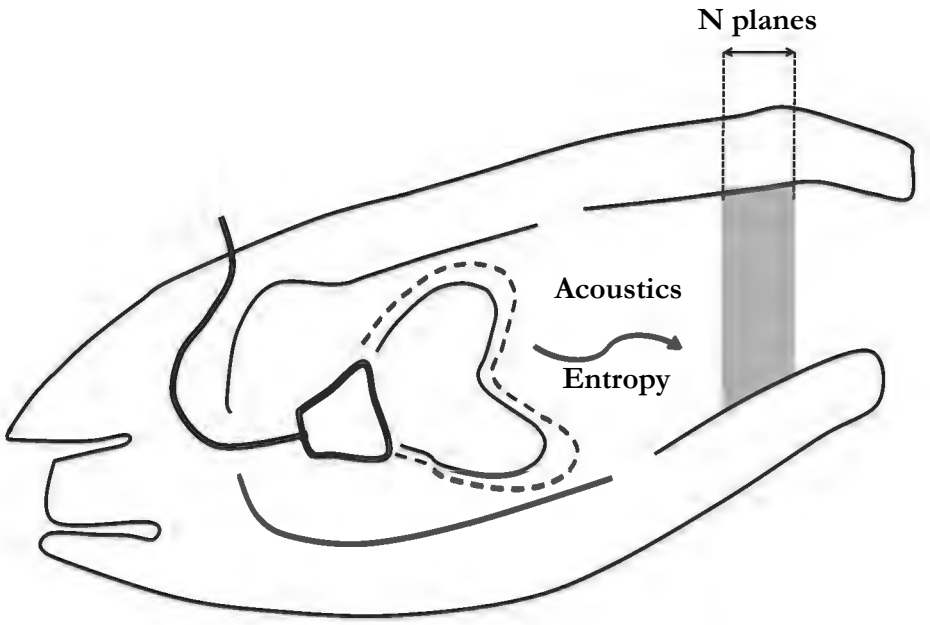

Figure 2.6: Location of N planes in a combustion chamber, one chord before the high pressurized turbine

a radial averaging of the primitive variables over the different planes is performed to comply with the theory, which is developed for a two-dimensional unwrapped annular duct, Fig. 2.7.

Then each fluctuation of the primitive variables is obtained by subtraction of temporal and spatial averaging of the set of instantaneous interpolated fields. This gives the primitive vector $[P(x, \alpha, t)]$ at x and α positions and at time t:

$$\Big[P(x,\alpha,t)\Big] = \begin{bmatrix} s'/c_p \\ w'/c \\ p'/\gamma p \\ \theta' \end{bmatrix}. \tag{2.77}$$

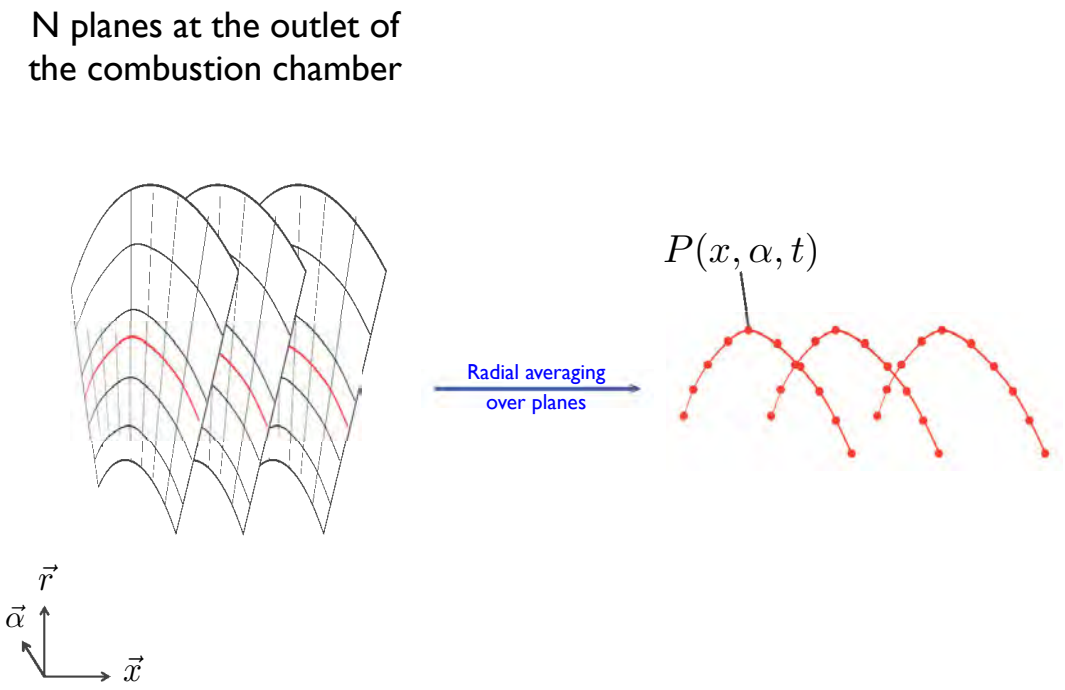

Figure 2.7: 2D structured planes at the outlet of a combustion chamber

2.2.2 From primitives variables to the wave vector [W]

Once the primitive vector $[P]$ is obtained, it must be decomposed into modes and frequencies for CHORUS (Fig. 2.5). Using temporal Fourier transform, the primitive vector $[P]$ is expressed in the frequency domain. By applying a Welch windowing, the time signal is split into N segments with an overlap in order to average and to smooth the power spectral densities. Then a spatial Fourier transform is applied to obtain the azimuthal modes of the primitive vector $[P]$. Finally the primitive vector in terms of frequencies ω and modes m is expressed as:

$$\Big[P(x, m, \omega)\Big] = \frac{1}{\alpha_{max} - \alpha_{min}} \int_{\alpha_{min}}^{\alpha_{max}} \Big[P(x, \alpha, \omega)\Big] \exp^{im\alpha} d\alpha. \tag{2.78}$$

Applying the wave decomposition of Eq. (2.34) on the primitive vector of Eq. (2.78) leads to a wave vector $[W(x, m, \omega)]$ which depends on frequencies and modes for

each Cartesian plane:

$$\Big[P(x,m,\omega)\Big] = \Big[M\Big]\Big[W(x,m,\omega)\Big] \tag{2.79}$$

In the theory presented here, there is no dissociation between hydrodynamic pressure and acoustic pressure. At low frequencies, acoustic is mainly two-dimensional. Although the radial averaging over the planes removes a large quantity of hydrodynamic pressure, it is necessary to introduce an hydrodynamic filtering to keep only acoustic pressure. As explained by Polifke et al. [2003] (plane wave masking) acoustic and convective waves can be identified considering the wave velocity and the axial spacing between planes. To do that, N_{planes} axial planes are used so that a filtered wave w^{ϕ} is written:

$$\hat{w}^{\phi}(m,\omega) = \frac{1}{N_{planes}} \sum_{j=1}^{N_{planes}} w^{\phi}(x_j,m,\omega)\exp(-iK_x^{\phi}x_j), \tag{2.80}$$

where K_x^{ϕ} is the projection of the dimensionless wavenumber on the engine axis and x_j are the axial position of the extraction planes. These filtered waves are used to compute the generation and propagation of acoustics in a turbine.

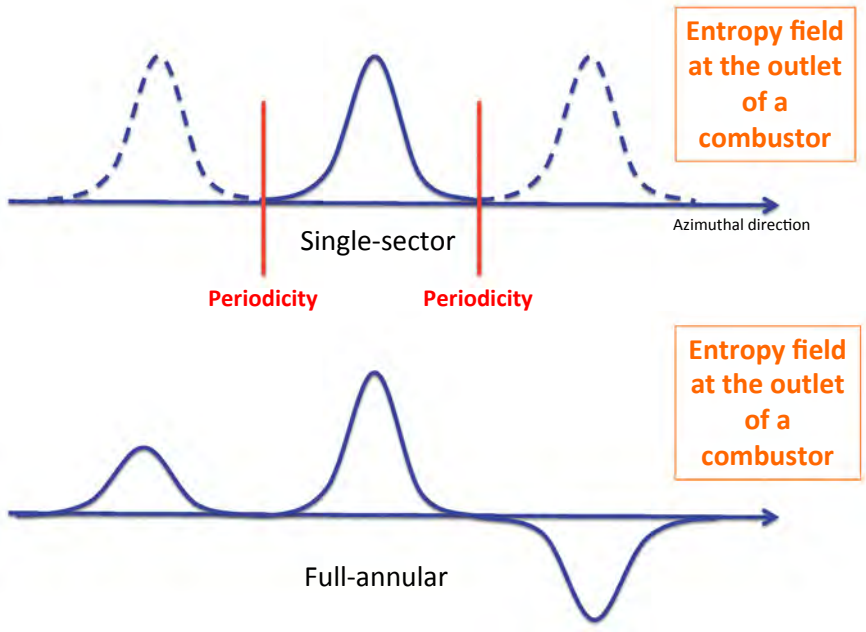

Figure 2.8: Entropy field at the outlet of a combustion chamber

To reduce the computational cost of LES, only one sector of a combustion chamber is generally simulated using periodicity assumption. This periodicity implies an entropy signal in phase sector-by-sector. However Livebardon et al. [2015] showed performing a full 360° annular combustor LES that the entropy fluctuations generated by a full combustor are not the same as the fluctuations produced by a single sector: entropy fluctuations produced by the N sectors are not in phase (Fig. 2.8) leading to interference effects. As a result, the overall signal level of the entropy planar mode decreases. Therefore a random phase-shift is implemented to mimic the entropy planar mode of a full annular combustion chamber. The entropy mode of the N_s sectors can be related to the full annular entropy mode:

$$w_s = \frac{1}{N_s} \sum_{j=1}^{N_s} w_s^j \exp(i\phi_j). \tag{2.81}$$

More generally the entropy planar mode of a full annular combustor computing only k sectors is defined as:

$$w_s = \frac{k}{N_s} \sum_{j=1}^{[\frac{k}{N_s}]+1} \kappa_j w_s^j \exp(i\phi_j). \tag{2.82}$$

with

$$\kappa_j = 1 \tag{2.83}$$

$$\text{or} \tag{2.84}$$

$$\kappa_j = \frac{k}{N_s} \text{ for } j = [\frac{k}{N_s}] + 1.$$

The entropy modes of each sector w_s^j are assumed to be identical (but not their phases ϕ_j) so that a correction F_k can be written as:

$$F_k = \frac{k}{N_s} \left| \sum_{j=1}^{[\frac{k}{N_s}]+1} \kappa_j \exp(i\phi_j) \right|. \tag{2.85}$$

To get an accurate filter F_k, Eq. (2.85) has to be averaged on a sufficient number

of realizations, here 100 000:

$$\hat{F}_k = \frac{1}{10^5}\left(\sum_{1}^{10^5}\frac{k}{N_s}\left|\sum_{j=1}^{[\frac{k}{N_s}]+1}\kappa_j \exp(i\phi_j)\right|\right). \tag{2.86}$$

If the number of k simulated sectors is closed to the full annular combustor, the filter $\hat{F}_k$ tends to 1. Otherwise for a computation of only one sector in a machine having N_s sectors ($N_s \approx 15$), this filter tends to 0.23, a surprisingly simple result to avoid having a full 360° LES and relying only on one single sector computation. The implementation of the filter has been verified by Livebardon et al. [2016] on the simulations of the TEENI European project. This filter function is used for all presented cases if not mentioned otherwise.

The theory used in the tool CHORUS has been introduced. This analytical method based on the theory proposed by Cumpsty and Marble [1977] allows a wave decomposition of quantities extracted from a combustion chamber simulation. The waves obtained at the outlet of the combustion chamber are propagated through a turbine. Finally the power spectral densities are obtained at the turbine exit and split into direct and indirect noise. At this point, we have not discussed how these perturbations are propagated to the far-field (Fig. 2.5). This is the topic addressed in the next chapter.

Chapter 3

Numerical investigation of far-field aircraft engine combustion noise using a zero Mach number frequency propagation tool

Abstract Direct and indirect mechanisms of combustion noise have been investigated through the turbine rotor/stator stages. Acoustic waves obtained at the turbine exit must be introduced in the nozzle and propagate to the far-field. This last step is performed using a zero-Mach number Helmholtz solver for the acoustic propagation. The jet flow effects on the propagation can not be considered, however, temperature inhomogeneities are taken into account. This chapter is composed of two sections. The first one presents the acoustic analogy used for the acoustic propagation and its assumptions. The last one describes models for the heterogeneous mean temperature fields of simple and dual-stream jets. The impact of an inhomogeneous temperature field on the noise directivity is evaluated.

3.1 Far-field propagation using a Helmholtz solver

In most cases, experimental data on engine noise is only available in the far-field. Therefore waves obtained by CHORUS need to be propagated through a nozzle to the atmosphere in order to be compared with experimental data at large distances (45 m). This requires a computation of the acoustic propagation through a jet of hot gases by means of a numerical simulation in a domain big enough to extend from the engine until the noise measurement locations. The engine operating points in which combustion noise is identifiable are the idle and aircraft taxiing conditions. In these phases the jet has a low Mach number, usually smaller than 0.3, so that refraction effects due to the shear layers are negligible. Because of the thermal layers naturally present in hot jets, a temperature gradient exists

and impacts the acoustic propagation. Therefore we chose to use a propagation tool which does not account for convection (Mach number = 0) but accounts for sound speed changes due to temperature variations: AVSP-f, based on the Phillips' analogy.

3.1.1 Phillips' analogy

Phillips' acoustic analogy (Phillips 1960) allows to take into account the speed of sound variations and thus to account for the inhomogeneous temperature and density fields induced by the hot jet. The speed of sound variations can be considered by combining the first and second laws of thermodynamics to obtain:

$$\frac{dp}{p} - \gamma \frac{d\rho}{\rho} = \frac{1}{c_v} ds. \tag{3.1}$$

From the mass conservation equation, it follows that:

$$\frac{\partial u_j}{\partial x_j} = -\frac{1}{\rho}\frac{d\rho}{dt} = -\frac{1}{\gamma p}\frac{dp}{dt} + \frac{1}{c_p}\frac{ds}{dt}. \tag{3.2}$$

A new variable π based on the logarithm of the pressure is introduced by Phillips

$$\pi = \frac{1}{\gamma} ln\left(\frac{p}{p_\infty}\right) \tag{3.3}$$

which allows to reformulate equation (3.2) and the momentum conservation as

$$\frac{d\pi}{dt} + \frac{\partial u_j}{\partial x_j} - \frac{1}{c_p}\frac{ds}{dt} = 0 \tag{3.4}$$

$$\frac{du_i}{dt} + c^2 \frac{\partial \pi}{\partial x_i} - \frac{1}{\rho}\frac{\partial \tau_{ij}}{\partial x_j} = 0 \tag{3.5}$$

A wave equation can be obtained by taking the time derivative of Eq. (3.4) from which the divergence of Eq. (3.5) is subtracted, which yields:

$$\frac{d}{dt}\left[\frac{d\pi}{dt} + \frac{\partial u_j}{\partial x_j} - \frac{1}{c_p}\frac{ds}{dt}\right] - \frac{\partial}{\partial x_i}\left[\frac{du_i}{dt} + c^2\frac{\partial \pi}{\partial x_i} - \frac{1}{\rho}\frac{\partial \tau_{ij}}{\partial x_j}\right] = 0 \tag{3.6}$$

Noting that the partial derivative ∂x_i does not commute with the material derivative d/dt, it follows that:

$$\frac{\partial}{\partial x_i}\frac{d}{dt} = \frac{d}{dt}\frac{\partial}{\partial x_i} + \frac{\partial u_j}{\partial x_i}\frac{\partial}{\partial x_j}. \tag{3.7}$$

The convective wave equation of Phillips is finally obtained:

$$\frac{d^2\pi}{dt^2} - \frac{\partial}{\partial x_i}\left(c^2\frac{\partial \pi}{\partial x_i}\right) = \frac{\partial u_i}{\partial x_j}\frac{\partial u_j}{\partial x_i} + \frac{d}{dt}\left(\frac{1}{c_p}\frac{ds}{dt}\right) - \frac{\partial}{\partial x_i}\left(\frac{1}{\rho}\frac{\partial \tau_{ij}}{\partial x_j}\right) \tag{3.8}$$

If a low Mach number flow is assumed, the convective part of the material derivative can be neglected, so that the material derivative can be approximated with the time derivative. Therefore the wave equation (3.8) introduced by Chiu and Summerfield [1974] and Kotake [1975] becomes:

$$\frac{\partial^2\pi}{\partial t^2} - \frac{\partial}{\partial x_i}\left(c^2\frac{\partial \pi}{\partial x_i}\right) = \frac{\partial u_i}{\partial x_j}\frac{\partial u_j}{\partial x_i} + \frac{\partial}{\partial t}\left(\frac{1}{c_p}\frac{\partial s}{\partial t}\right) - \frac{\partial}{\partial x_i}\left(\frac{1}{\rho}\frac{\partial \tau_{ij}}{\partial x_j}\right) \tag{3.9}$$

The variable π can be decomposed into a mean value and a perturbation part:

$$\pi = \pi_0 + \pi' = \pi_0 + \frac{1}{\gamma}\frac{p'}{p_\infty}\frac{p_\infty}{p} = \pi_0 + \frac{p'}{\gamma p}. \tag{3.10}$$

With the low Mach number hypothesis, also the convective terms of Eq. (3.9) can be neglected. Assuming that entropy is locally conserved along streamlines allows to neglect the second source term of the right hand side of Eq. (3.9). Finally, considering that the pressure variations will be small compared to the mean pressure, the wave equation can be rewritten as:

$$\frac{1}{\gamma\bar{p}}\frac{\partial^2 p'}{\partial t^2} - \frac{\partial}{\partial x_i}\left(\frac{c^2}{\gamma\bar{p}}\frac{\partial p'}{\partial x_i}\right) = 0 \tag{3.11}$$

A time Fourier transform of the resulting wave equation yields the following Helmholtz equation:

$$\frac{\partial}{\partial x_i}\left(c^2\frac{\partial \hat{p}}{\partial x_i}\right) + \omega^2\hat{p} = 0. \tag{3.12}$$

Note that Eq. (3.12) is limited to low Mach number flows (average jet Mach number at the nozzle exit $M_j < 0.3$). This is the case of the industrial application presented in chapter 5.

Other acoustic analogies has been proposed in the literature, allowing to consider simultaneously temperature and velocity flow inhomogeneities. As an example one can refer to the Möhring analogy (Möhring et al. 1983; Mohring 2010, see annex B). Accounting for both an arbitrary flow field and for temperature inhomogeneities remains a difficult issue.

3.1.2 Numerical description of the AVSP-f solver

Equation (3.12) must be solved numerically as there is no known analytical solution. This equation becomes the following eigenvalue problem (Silva 2010):

$$\underbrace{A}_{\nabla.c^2\nabla+\omega^2 I} \underbrace{x}_{\hat{p}} = 0, \tag{3.13}$$

with c the speed of sound, $\hat{p}$ the harmonic acoustic pressure fluctuation and ω the angular frequency. This linear system is solved using the Generalized Minimum REsidual Generalized Minimum REsidual method (GMRES) method that can deal with large, sparse and non Hermitian linear systems and belongs to the class of Krylov based iterative methods (Salas 2013). It allows using only Matrix-vector products. To consider three-dimensional geometries, unstructured meshes are used. Equation (3.12) is discretized using finite volume method. The numerical scheme is of second order and combined with a cell-vertex method.

The waves obtained at the outlet of the turbine are injected into AVSP-f as a boundary condition imposed at the inlet patch of the solver (Fig. 6). Forcing is performed through a boundary patch, where the incoming acoustic wave $A^+ = p' + \rho c u'$ is injected through an acoustically non-reflecting inlet.

3.2 Description of the mean field of a double-stream jet

In a real turbofan-engine configuration, the nozzle exhaust is often double-stream with a primary hot flow and a secondary cold flow, so that temperature inhomogeneities exist. The temperature gradients have a major impact on acoustic waves propagation (Ihme et al. 2006) and have to be considered in the description of the mean field. They impose the field of c in Eq. (3.13). Livebardon et al. [2015] show how to analytically describe a simple low Mach number hot jet using the correlations of Zaman [1998] and Pope [2000].

In order to illustrate the impact of the temperature gradient on the propagation of waves, simulations have been performed for a simple jet configuration. An arbitrary nozzle geometry has been chosen. The same amplitude of 100 Pa is imposed at the inlet of the nozzle for a frequency range from 0 to 1000 Hz, and for two different initializations of the mean field. In the first case, an isothermal field (T = 300 K) is imposed, while in the second one, the mean field is obtained from correlations for a simple hot jet flow, see Fig. (3.1). Pressure module is extracted from 90° to 180° as illustrated in Fig. 3.2.

As shown in Fig. 3.3 the temperature field has a major impact on the directivity of the acoustic field. For the isothermal field the maximum directivity is in the jet

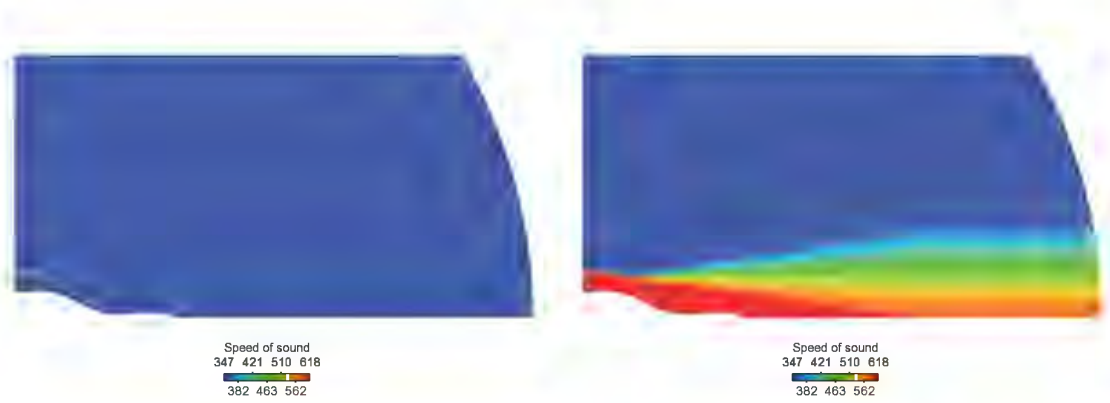

(a) Isothermal temperature field (b) Temperature field of a hot jet

Figure 3.1: Speed of sound fields for a) an isothermal temperature field, b) a temperature field of a hot jet

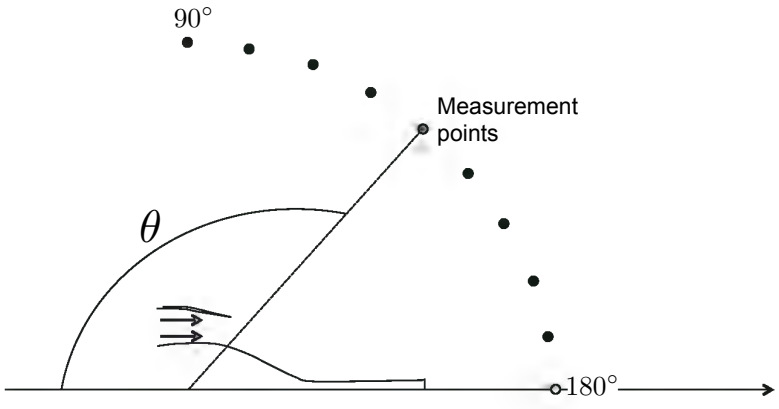

Figure 3.2: Measurement points location

direction (180°), whereas the maximum directivity is at an angle of 130° for the stratified temperature field. The refraction of sound is frequency dependent. At high frequencies, waves are more sensitive to temperature inhomogeneities. On the contrary, at low frequencies (below 500 Hz), the heterogeneous temperature region due to the shear layers of the jet is compact compared to the acoustic wavelengths and the heterogeneities weakly impact the sound propagation. Livebardon et al. [2015] used these correlations to validate the far-field propagation in the TEENI case and found a good agreement between experimental data and numerical results.

Assuming geometrical approximation to consider acoustic waves as acoustic rays, the refraction of the planar waves across the jet can actually be computed by means of Fermat's principle (Rienstra and Hirschberg 2003), which implies the conservation of tangential wavenumbers (cf Fig. 3.4 and annex C).

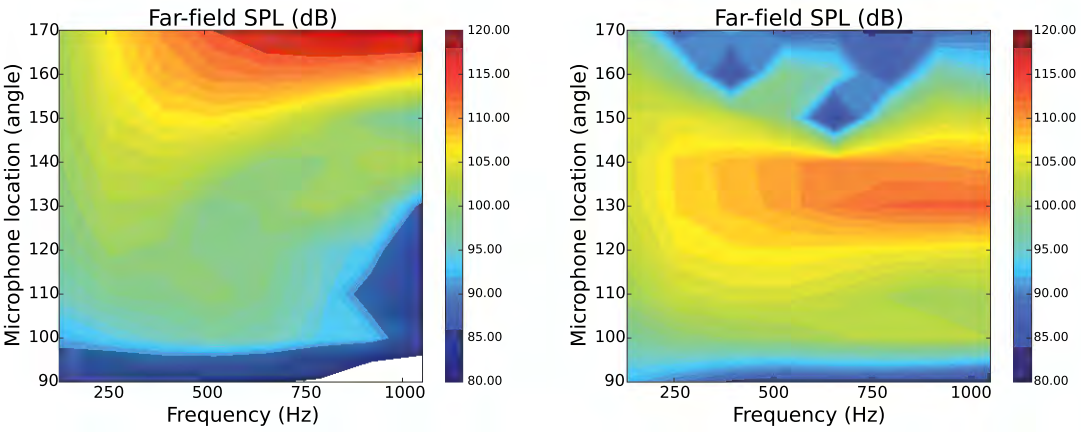

(a) Isothermal temperature field (b) Temperature field of a hot jet

Figure 3.3: Noise radiation maps: a) isothermal temperature field, b) temperature field of a hot jet

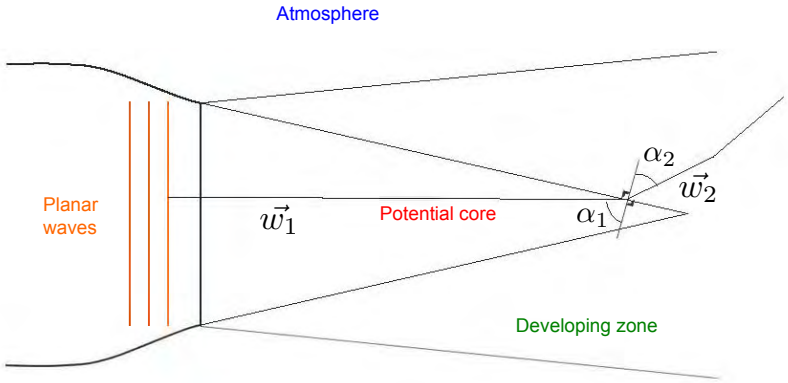

$$k_1 . \sin(\alpha_1) = k_2 . \sin(\alpha_2)$$

Figure 3.4: Refraction of waves across a simple hot jet

The introduction of dual stream jets is a technological breakthrough for reducing jet noise, which is nowadays widely used in civil aviation. Indeed, the secondary cold flow allows to increase the thrust by increasing the total mass flow. Hence, at fixed thrust, the exhaust velocity of the primary hot jet can be reduced, inducing a strong reduction of jet noise. Moreover it allows a reduction of the fuel consumption.

The dynamic of these dual stream jets is more complex, since two mixing layers interact. According to Ko and Kwan [1976]; Kwan and Ko [1977], a double stream

jet can be decomposed into three regions, Fig. 3.5. Similarity of the mean-velocity and turbulent-intensity profiles within the two mixing regions inside the initial merging zone, and within the mixing region inside the fully merged zone, has been observed. However, in the transition zone where the two mixing layers interact, no similarity is found.

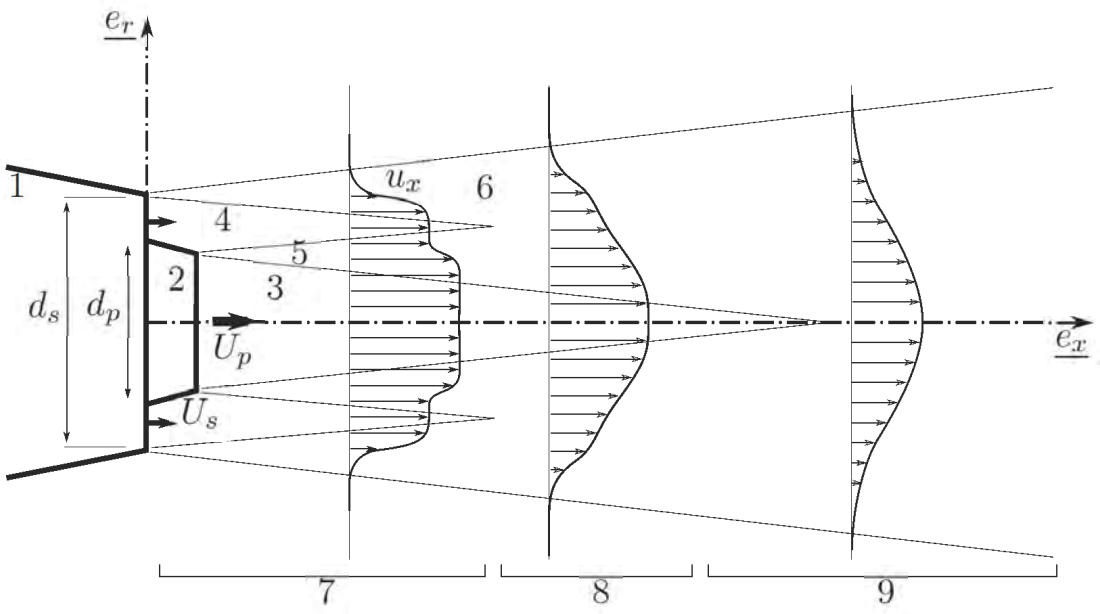

Figure 3.5: Scheme of a double stream jet of a coplanar nozzle exhaust: the external nozzle (1), the internal nozzle (2), the primary potential core (3), the secondary potential core (4), the internal mixing layer (5), the external mixing layer (6), the initial merging zone (7), the intermediate zone of transition (8) and the fully merged region (9)

For more complex configurations as double-stream jet, AVSP-f computations cannot be initialized by means of a subsonic jet flow model. Therefore AVSP-f computations are fed using mean flow fields provided by prior RANS simulations performed using ANSYS-Fluent in an axi-symmetric mode.

Phillips' analogy is intended to be used in low Mach number configurations (below 0.3), neglecting the convection and refraction effects of the shear layer on the sound propagation (Pridmore-Brown 1958; Doak 1972; Lilley 1974). Indeed, all flow-acoustic interactions are not included on the left hand side of Eq. (3.9), and the shear-refraction term is still contained in the linear part of the first source

term $\frac{\partial u_i}{\partial x_j}\frac{\partial u_j}{\partial x_i}$. These flow-acoustic interactions will be considered in the methodology presented in chapter 4. Nevertheless, Phillips' analogy has the advantage to take into account temperature heterogeneities in the wave operator contrary to Lighthill's analogy.

Chapter 4

Large Eddy Simulations of jet noise pulsed with combustion noise using a time LES code for propagation to the far-field

Abstract The methodology combining CFD methods and analytical models for the combustion noise prediction has been described in the previous chapters (Fig. 6). The acoustic sources of combustion noise were first captured using LES of single sector of combustion chamber (AVBP). These sources were then propagated across a turbine using analytical methods in the frequency domain. Finally, a far-field propagation were computed with a zero-Mach number Helmholtz solver (AVSP-f). The temperature impact on the directivity has been highlighted and is taken into account with Phillips' analogy. However, the impact of the velocity field itself could not be considered because of a zero-Mach number strong assumption used for the far-field simulation in AVSP-f. Indeed, the mean flow deformation and perturbations exiting the engine core induce noise mechanisms through the modifications of the jet noise sources. Moreover, it has been shown that disturbances, boundary layers and operating conditions impact the development of the shear layer, the potential core and the turbulent flow structure of the exhaust jet and consequently the acoustic field. Therefore, it is important to consider these effects in the combustion noise propagation. Another method consisting in a LES of the jet flow coupled with combustion noise forcing is presented in this chapter.

4.1 Generation of a temporal signal for combustion noise coming from the outlet of a turbine

To have a more complete understanding of the far-field combustion noise propagation, the jet flow has to be considered to take into account the refraction of sound due to the shear layers. A full unsteady resolution of a three-dimensional double-stream jet forced by acoustic waves due to combustion was performed with AVBP. This is an alternative solution to AVSP-f (Chapter 3): more precise but also more expensive. The acoustic sources due to the combustion process and computed with CHORUS are introduced at the inlet of the primary hot jet. These sources have been computed previously in chapter 2 at the outlet of a turbine. The acoustic waves obtained by CHORUS are written in Fourier space as a function of modes and frequencies. Therefore, it is necessary to build a temporal signal to introduce the incoming acoustic wave in a temporal jet flow simulation. As the waves are in their harmonic form:

$$\begin{aligned} w^+ &= \hat{w}^+ \exp(i(\omega t + \phi)) \\ &= \hat{w}^+ (\cos(\omega t + \phi) + i \sin(\omega t + \phi)), \end{aligned} \tag{4.1}$$

the amplitude $\hat{w}^+$ is equivalent to

$$\hat{w}^+ = |w^+| = \sqrt{w^+ \bar{w}^+}\,, \tag{4.2}$$

where $\bar{f}$ is the complex conjugate of f. The phase ϕ can be written as

$$\phi = \arg(w^+) = \arccos\left(\frac{(w^+ + \bar{w}^+)/2}{\sqrt{w^+ \bar{w}^+}}\right). \tag{4.3}$$

A temporal signal of the incident acoustic planar wave w_d^+ (Fig. 2.5) is built using the amplitudes and the phases computed for each CHORUS frequency ω_i. This signal is expressed as

$$p'^f(t) = \sum_{i=1}^{N} \gamma p \hat{w_i}^+ \sin(\omega_i t + \phi_i), \tag{4.4}$$

where p'^f is the forced acoustic pressure fluctuation induced by the incident acoustic planar wave. Only the incident acoustic planar wave, occurring from direct and indirect mechanisms, is considered since there is no generation of entropy in the turbine, most of the indirect noise is generated in the first stage, as shown by MT1 simulations (Papadogiannis et al. 2016; Becerril 2017), and the entropy fluctuations are low at the outlet of the first turbine stages.

4.2 Injection of combustion noise through Navier-Stokes Characteristic Boundary Condition

A temporal signal $p'^f(t)$ of an acoustic wave has been generated in the previous section from the outputs of CHORUS. The wave has to be injected now in the LES simulation through an inlet boundary-condition to force the flow without creating spurious noise. AVBP being an unsteady compressible solver, acoustics can be propagated in the flow and dealt properly at the boundary conditions to avoid numerical errors. Navier-Stokes Characteristic Boundary Conditions (NSCBC) are used at the inlets and outlets of simulations to control acoustic reflections (Poinsot and Lele 1992; Selle et al. 2004b) and evaluate the amplitude of the incoming waves. The NSCBC method consists in reformulating the governing equations through a characteristic analysis in order to link the primitive Navier-Stokes variables (p, u_1, u_2, u_3 and ρ) to the waves amplitudes L_i.

At a subsonic inflow boundary where velocity and temperature conditions are set, four waves have to be imposed, L_1 the downstream-propagating acoustic wave, L_3 and L_4 the two vorticity waves and L_5 the entropy wave (Fig. 4.1). A relaxation formulation of the characteristic waves variations leads to (Poinsot et al. 1992):

$$\delta L_1 = 2K_{u_n}(u_n^t - u_n)\Delta t, \tag{4.5}$$

$$\delta L_3 = K_{u_{t_1}}(u_{t_1}^t - u_{t_1})\Delta t, \tag{4.6}$$

$$\delta L_4 = K_{u_{t_2}}(u_{t_2}^t - u_{t_2})\Delta t, \tag{4.7}$$

$$\delta L_5 = \frac{\rho(\gamma-1)}{c}(K_{u_n}(u_n^t - u_n)\Delta t) - \frac{\rho}{T}K_T(T^t - T)\Delta t, \tag{4.8}$$

where u_n is the normal velocity, u_{t_1}, u_{t_2} the tangential parts of the velocity vector. The superscript t refers to target values, K is the relaxation coefficient associated with the different variables imposed at the boundary condition and Δt is the iterative time step. Two forcing methods are available (Kaufmann et al. 2002):

- Inlet Velocity Modulation (IVM): The most intuitive method in which the velocity directly imposed at the inlet is pulsated. However, this technique can lead to resonance phenomena. Therefore, this method will be rejected.

- Inlet Wave Modulation (IWM): The proper forcing technique which modulates the entering acoustic wave amplitude L_1 while letting the other waves (L_2) leaving the domain without reflection.

The second method (IWM) is chosen to perform the introduction of combustion noise. At the inlet boundary, i.e. x_0, in the limit of linear acoustics, the unsteady

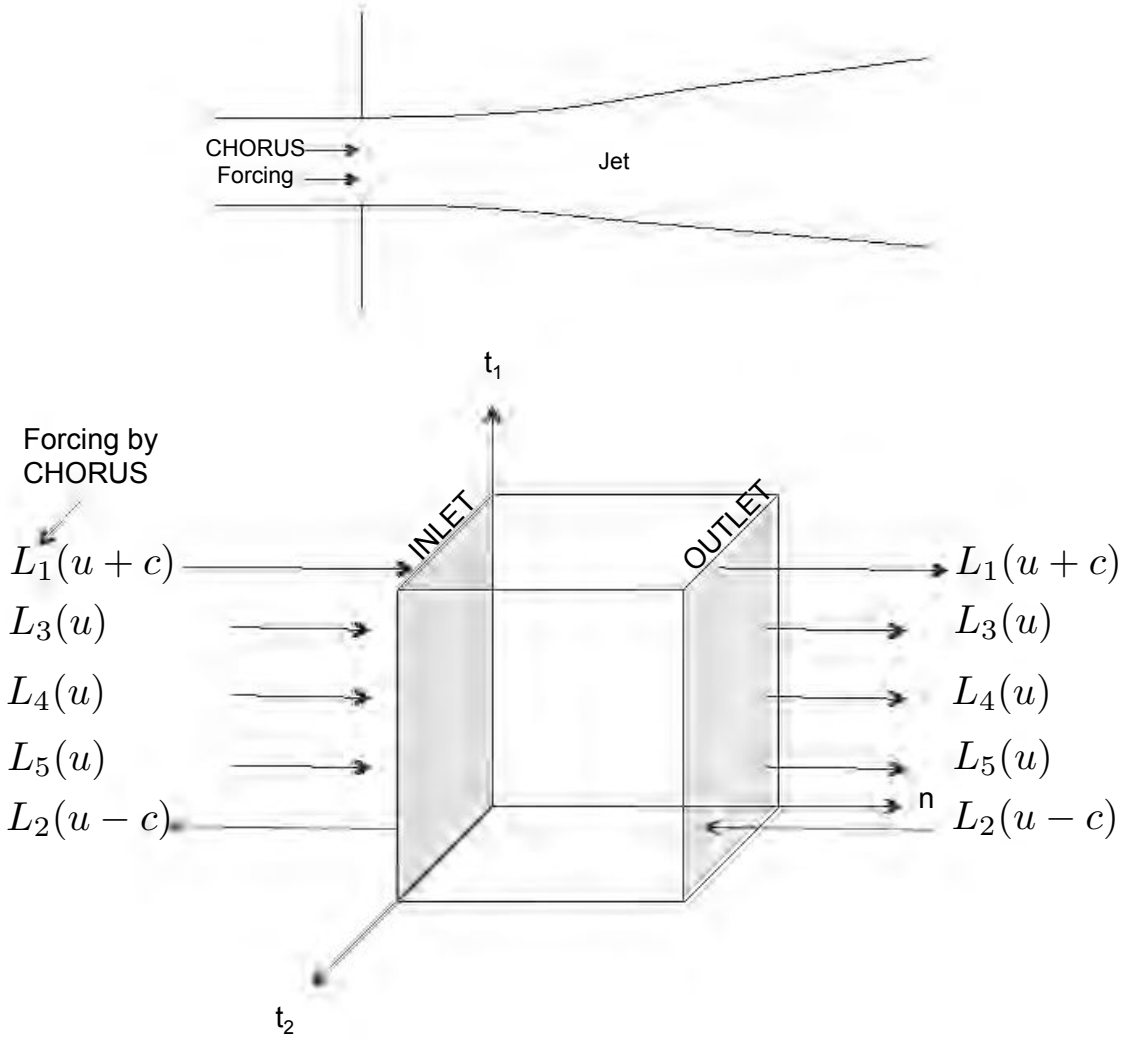

Figure 4.1: Boundary conditions at subsonic inflow and outflow where $\vec{u} = (u_1, u_2, u_3)$ and c is the speed of sound. The incoming acoustic wave L_1 will carry the acoustic forcing computed with CHORUS.

velocity and pressure are:

$$\begin{aligned} u'(x_0,t) &= \frac{1}{\rho_0 c_0}\left(L_1 e^{ikx_0-i\omega t} - L_2 e^{-ikx_0-i\omega t}\right) \qquad (4.9)\\ &= \frac{1}{\rho_0 c_0}\left(L_1 - L_2\right) e^{-i\omega t} \\ p'(x_0,t) &= \left(L_1 e^{ikx_0-i\omega t} + L_2 e^{-ikx_0-i\omega t}\right) \qquad (4.10)\\ &= \left(L_1 + L_2\right) e^{-i\omega t}. \end{aligned}$$

In order to introduce the acoustic perturbations coming from the combustion process and propagated to the outlet of a turbine, a forcing term has to be implemented in the NSCBC formalism. The expression of the downstream-propagating acoustic wave δL_1 is modified in order to contain the acoustic forcing contribution. This forcing term generates also an entropy contribution as the entropy wave δL_5 depends on the acoustic wave δL_1, Eq. (4.8). Finally, an acoustic forcing at an inflow boundary yields:

$$
\begin{aligned}
\delta L_1 &= 2K_{u_n}(u_n^t - u_n)\Delta t + \underbrace{2\left(K_{u_n}\frac{p'^f(t)}{\rho c} + \frac{1}{\rho c}\frac{dp'^f(t)}{dt}\right)\Delta t}_{\textbf{Acoustic forcing contribution}}, \\
\delta L_3 &= K_{u_{t_1}}(u_{t_1}^t - u_{t_1})\Delta t, \\
\delta L_4 &= K_{u_{t_2}}(u_{t_2}^t - u_{t_2})\Delta t, \\
\delta L_5 &= \frac{\rho(\gamma-1)}{c}\left(K_{u_n}(u_n^t - u_n)\Delta t\right) - \frac{\rho}{T}K_T(T^t - T)\Delta t - \\
&\qquad \underbrace{\frac{\rho}{T}K_T\frac{p'^f(t)}{\rho c}\Delta t}_{\textbf{Temperature fluctuations induced by the acoustic forcing}}.
\end{aligned}
\tag{4.11}
$$

The acoustic forcing contribution corresponds to the acoustic wave related to combustion noise $\frac{1}{\rho c}\frac{dp'^f(t)}{dt}$, where $p'^f(t)$ is the temporal signal obtained in Eq. (4.4), and the velocity fluctuations induced by the relaxation coefficient $K_{u_n}\frac{p'^f(t)}{\rho c}$. Only the term $\frac{1}{\rho c}\frac{dp'^f(t)}{dt}$ is coming from the exact NSCBC theory. The terms $K_{u_n}\frac{p'^f(t)}{\rho c}$ and $K_T\frac{p'^f(t)}{\rho c}$ are added to the wave expression to avoid a suppression of the velocity and temperature fluctuations induced by the acoustic forcing since the NSCBC formulation will try to stay at the target values of the imposed variables. This procedure is equivalent to set the target velocity in the relaxation term to $u_n^t + \frac{p'^f(t)}{\rho c}$ which is indeed the value reached at the inlet when the acoustic wave $p'^f(t)$ is imposed if there is no reflected wave.

4.3 Validation of the acoustic forcing with tests cases

Validation tests are performed first in order to assess the solver ability to introduce the combustion noise signal. A one-dimensional stationary flow is computed with

a quasi one-dimensional rectangular mesh of 1 m composed of 200 cells (Fig. 4.2). The initial state before any perturbation is set to 300 K at 101325 Pa with a bulk velocity of 0 m.s^{-1}. The flow is excited acoustically by imposing at the inlet the temporal signal of an incoming wave A^+. Two forcing cases are tested: an acoustic pulse and an harmonic acoustic wave (sum of sinus) generated as in section 4.1.

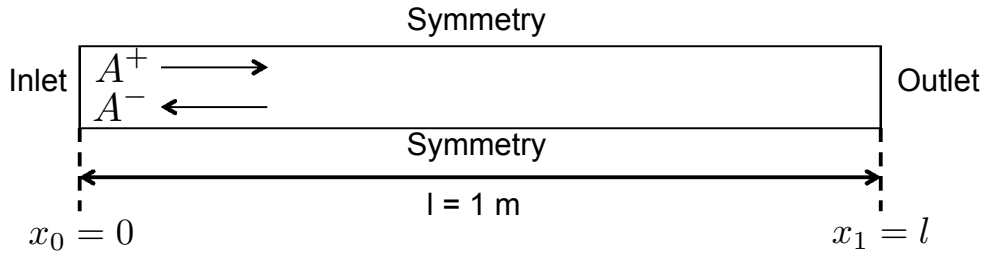

Figure 4.2: 2D configuration of the validation test domain with anechoic outlet

For 1D problems, NSCBC often works without the relaxation terms of Eqs. (4.5) to (4.8) (by setting $K_{u_n} = K_{u_{t_1}} = K_{u_{t_2}} = K_T = 0$). For the test case of Fig. 4.2, choosing a non-reflecting inlet boundary condition by setting a zero relaxation coefficient on velocity, the general form of the incoming acoustic wave for an acoustic pulse is written as:

$$A^+ = \rho_0 c_0 (\alpha \sin(2\pi f(t)))\Delta t, \tag{4.12}$$

where α is the amplitude of the oscillating velocity. In the same way, the incoming acoustic wave coming from CHORUS:

$$A^+ = \rho_0 c_0 (\frac{1}{\rho c} \frac{dp'^f(t)}{dt})\Delta t, \tag{4.13}$$

can be written as a sum of sinuses, reading as

$$A^+ = \sum_{i=1}^{N} \rho_0 c_0 (\alpha_i \sin(2\pi f_i t + 2\pi\phi_i))\Delta t. \tag{4.14}$$

For this test, the outlet boundary condition is set to non-reflecting by imposing a zero relaxation coefficient on pressure, so that $A^- = 0$. Therefore it can be written:

$$A^- = \frac{1}{2}\left(p' - \rho_0 c_0 u'\right) = 0, \tag{4.15}$$

$$A^+ = \frac{1}{2}\left(p' + \rho_0 c_0 u'\right), \tag{4.16}$$

and

$$u' = \frac{A^+}{\rho_0 c_0}. \tag{4.17}$$

In order to validate the boundary condition that allows to introduce a polychromatic signal, a first verification is performed by injecting the signal of the incoming wave defined in Eq. (4.14) but at the unique frequency of 1000 Hz with an amplitude of $\alpha = 1$ m.s^{-1}. Forcing begins at t =1 ms. The unsteady pressure measured at the inlet is compared with the analytical signal of an acoustic pulse of the same amplitude and same frequency, Eq. (4.12). The time variation of u' and p' are verified in Fig. 4.3. The forcing signal is correctly introduced since both velocity and pressure fluctuations are superimposed on the analytical solution.

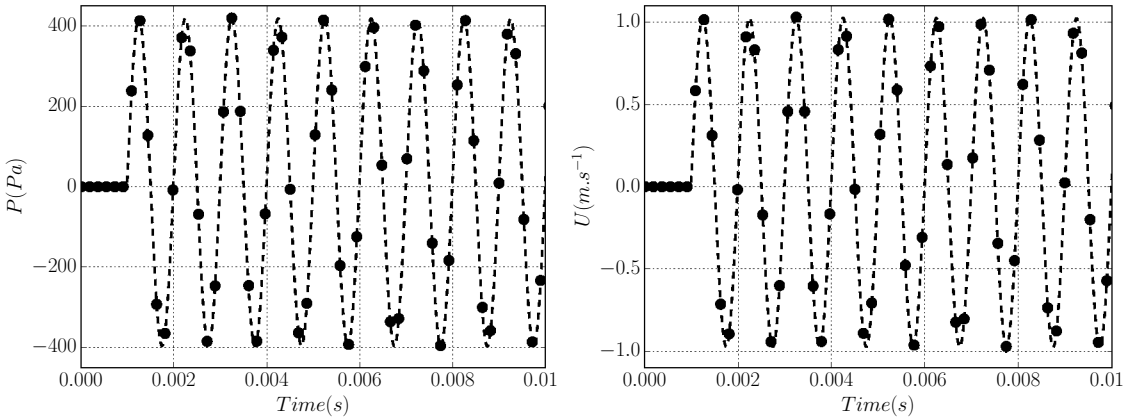

(a) Pressure

(b) Velocity

Figure 4.3: (a) Pressure and (b) velocity fluctuations at the inlet of the domain for a simple sinus forcing (●) compared with the analytical acoustic pulse (- -).

It has been verified that the inlet boundary-condition (Eq. (4.11)) correctly introduces a simple sinus acoustic wave. The combustion noise acoustic wave (Eq. (4.13)) obtained with CHORUS at the outlet of a turbine is presently injected in Fig. 4.4 for a signal $p'^f(t)$ obtained from a typical CHORUS simulation. It can be seen that the inlet and outlet signals match perfectly with the initial injected signal, both in terms of pressure and velocity fluctuations. The outlet signal can be fitted with the initial signal by considering the phase-shift in time $\tau = l/c$ (where l is the length of the computational box and c the speed of sound of the medium, τ = 2.9 ms) induced by the distance between the inlet and the outlet as shown in Fig. 4.4(b). No amplitude loss is observed between the inlet and the outlet signals, meaning that acoustic waves are well propagated at all frequencies.

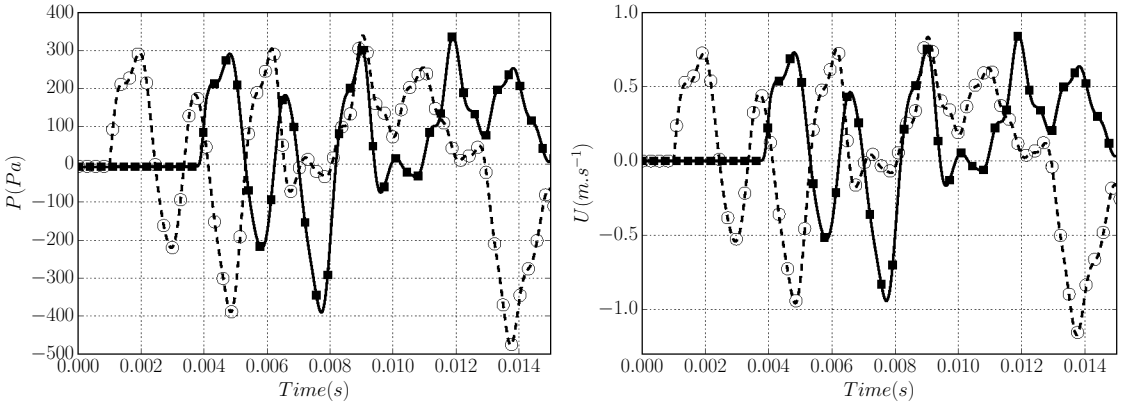

(a) Pressure (b) Velocity

Figure 4.4: (a) Pressure and (b) velocity fluctuations at the inlet (○) and outlet (–■–) of the domain compared with the initial signal (- -) of the incoming wave originated from combustion process

This test case has also been performed for a three-dimensional domain with walls, non-reflecting inlet and outlet, a quiescent flow (U=0 m.s^{-1}) and gives exactly the same results as the one-dimensional case.

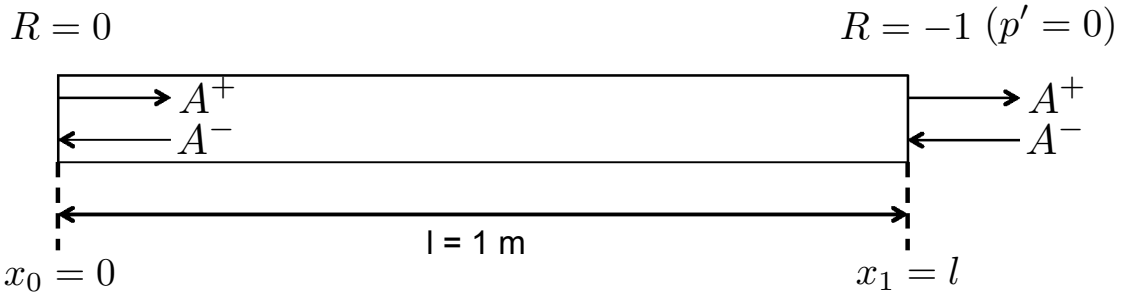

Figure 4.5: Quasi-1D configuration of the validation test domain with constant pressure at the outlet

The forcing boundary condition has been tested and validated in ideal conditions where there is no reflexion. In all other cases, A^- is non zero and the reflected waves will interact with the forcing imposed at the inlet. If we now consider that the tube ends in a large domain, then to first order, pressure is constant at the outlet, yielding $p'(x_1, t) = 0$. Therefore, to validate this case and verify that the downstream-propagating wave A^+ cross the reflected wave A^- at the inlet without interaction, pressure is imposed at the outlet with a fully reflective boundary

condition (Fig. 4.5). Knowing that the pressure and velocity fluctuations can read

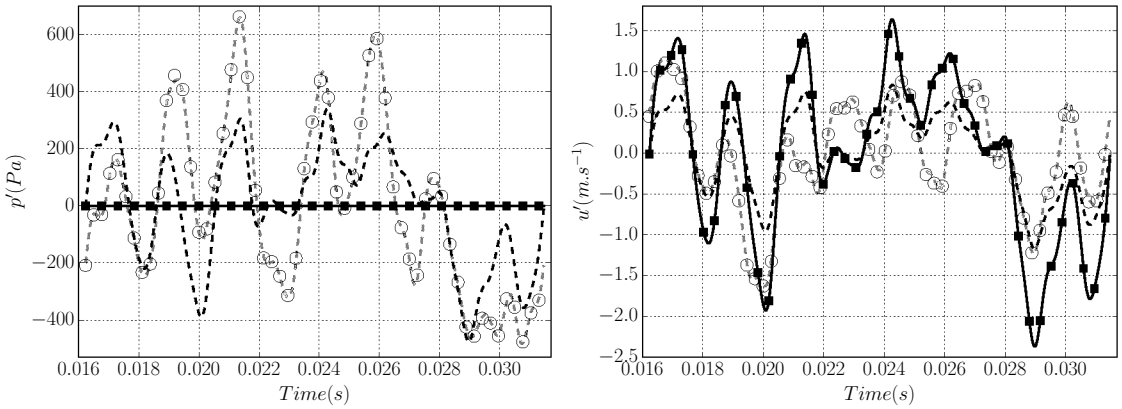

(a) Pressure (b) Velocity

Figure 4.6: (a) Pressure and (b) velocity fluctuations at the inlet (○) and outlet (■) of the domain compared with the analytical signal at x_0 (- -) and at x_1 (–) considering the incoming forced wave originated from combustion process (- -)

(by assuming linear acoustics):

$$p'(x,t) = A^+ \exp(ikx - i\omega t) + A^- \exp(-ikx - i\omega t), \tag{4.18}$$

$$u'(x,t) = \frac{1}{\rho c}\left(A^+ \exp(ikx - i\omega t) - A^- \exp(-ikx - i\omega t)\right), \tag{4.19}$$

the reflected wave A^- can be determined at the outlet ($p'(x_1 = l) = 0$) as

$$A^- = -A^+ \exp(i2kl), \tag{4.20}$$

where A^+ is the ingoing acoustic wave imposed as in Eq. (4.13). Therefore, the pressure and velocity fluctuations at the inlet ($x_0 = 0$) can be written as

$$p'(x_0,t) = A^+ \exp(-i\omega t)\left(1 - \exp(i2kl)\right), \tag{4.21}$$

$$u'(x_0,t) = \frac{1}{\rho c} A^+ \exp(-i\omega t)\left(1 + \exp(i2kl)\right). \tag{4.22}$$

At the outlet of the tube ($x_1 = l$), the pressure and velocity fluctuations will be:

$$p'(x_1,t) = 0, \tag{4.23}$$

$$u'(x_1,t) = \frac{2}{\rho c} A^+ \exp\left(ikl - i\omega t\right). \tag{4.24}$$

Fig. 4.6 shows that the simulation predicts the correct acoustic behavior by imposing $p' = 0$ at the outlet. Both pressure and velocity fluctuations at inlet and outlet of the domain match with the analytical solution. At the inlet, the extracted fluctuations come from the imposed ingoing acoustic wave A^+ and the reflected acoustic wave A^-. At the outlet, the acoustic wave A^+ is completely reflected with an opposite phase inducing a zero pressure fluctuation while the velocity fluctuation will be at its maximum.

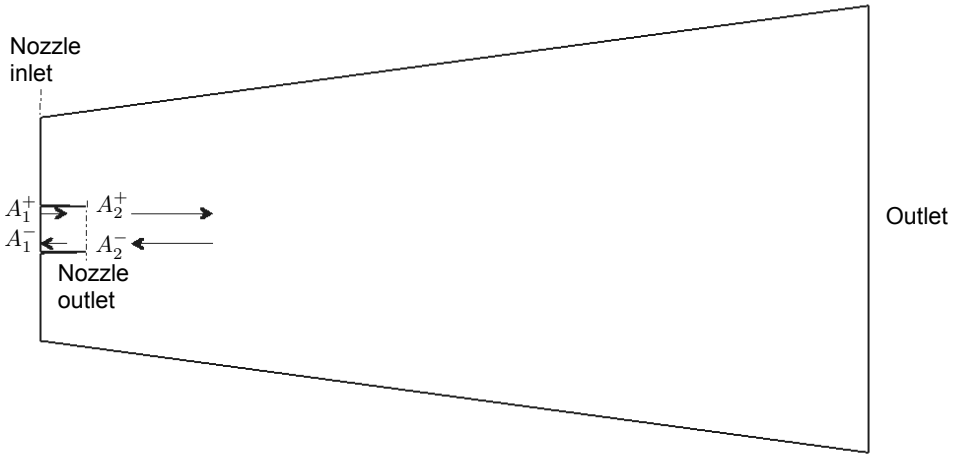

Figure 4.7: 3D configuration of a nozzle ending in a large domain

In order to be more representative of a jet flow simulation, a three-dimensional case has also been tested with a nozzle ending in a large domain (atmosphere), Fig. 4.7. The nozzle inlet is non-reflecting so that the desired A^+ is conserved everywhere and should correspond to the forced wave defined in Eq. (4.13). Slip walls are used for the nozzle and non-reflecting boundary conditions imposing the pressure are used at the boundaries of the large domain. The initial state before any perturbation is set to 300 K at 101325 Pa with a bulk velocity of 0 m.s^{-1}.

An instantaneous field of pressure fluctuations (Fig. 4.8) reveals that pressure fluctuations are propagated towards the far-field and that the contributions of all frequencies of the forcing signal are present in this field. There is no jet noise in this test since the exit mean speed is zero. Saturation can be observed at the outlet of the nozzle, as well as a dark spot more upstream of the exit, meaning that there is reflexion at the nozzle outlet. By computing $A^- = \frac{1}{2}(p' - \rho c u')$ at

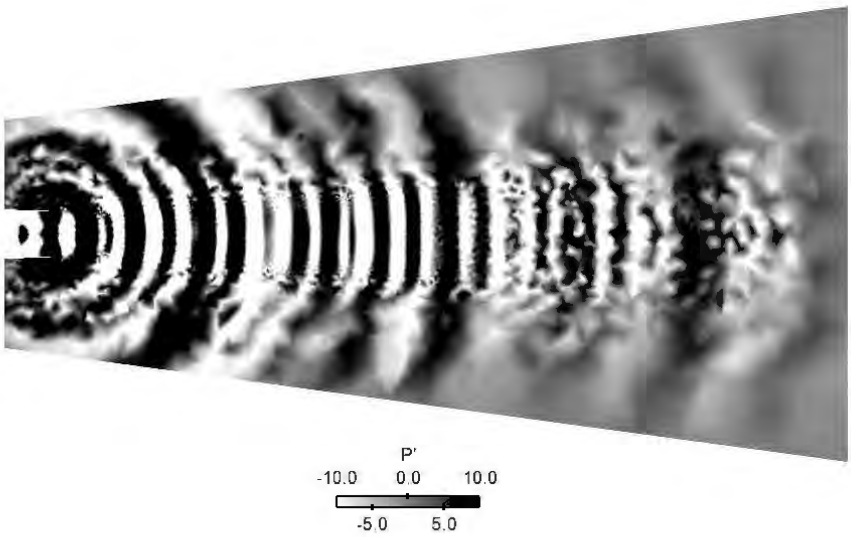

Figure 4.8: Far-field propagation of pressure fluctuations induced by the forcing inlet boundary condition

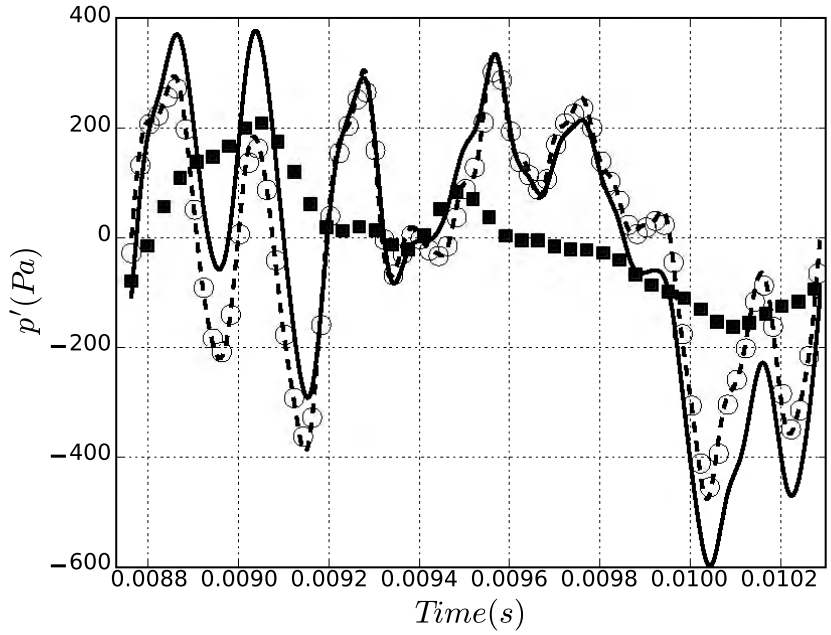

Figure 4.9: Pressure fluctuations (–), A^+ (○) and A^- (■) at the outlet compared with the incoming forced wave originated from combustion process (- -)

the outlet of the nozzle and knowing that:

$$p' = A^+ + A^-, \tag{4.25}$$

it can be verified that A^+ at the exit of the nozzle corresponds to the forced wave injected at the inlet (Eq. (4.13)) as shown in Fig. 4.9. It can also be concluded that in this case $A^- \neq -A^+$ so that $p' \neq 0$ and $R > -1$.

To conclude, this section has shown that an incoming acoustic wave provided by CHORUS can be correctly introduced through a non-reflecting inlet boundary-condition into an LES compressible code for different test cases and outlet boundary-conditions.

Part III

Application to a complex configuration: a turbofan-engine case

Table of Contents

Chapter 5

Configuration and operating points

Abstract The CONOCHAIN tools proposed for the combustion noise prediction of aeronautical engines have been presented in the previous chapters. They explain the generation and the propagation of the combustion acoustic sources from the combustion chamber to the turbine and nozzle exhaust up to the far-field. An alternative to the Helmholtz propagation tool AVSP-f which also considers the jet flow field has been introduced for the far-field propagation by forcing a LES of jet with combustion noise sources. The first two steps of CONOCHAIN in Fig. (6) have been tested in the case of the TEENI European project and show promising results for the prediction of the pressure levels at the turbine exit (Livebardon et al. 2015). A more complex realistic configuration is proposed to stress the robustness of the method and validate the far-field propagation prediction. For this case, only far-field data is available experimentally.

5.1 A realistic turbofan-engine configuration

The chosen configuration is an industrial turbofan engine for which only far-field measurements of acoustic pressure levels exist. These measurements are static bench data where the engine is fixed on a pylon at 5 meters high (Fig 5.1). Microphones are disposed along an arc on the ground with the center at the engine core and a radius of 45 meters, from 90° to 180° with respect to the jet axis. This is the convention chosen for far field angles (Fig 5.2). Aft noise measurements are performed with an acoustic barrier shielding noise from the inlet of the engine, so that jet noise and combustion noise are isolated from the upstream sources. The data is corrected to account for the ground reflections.

The configuration is a turbofan-engine with double body and double flow. It includes, from upstream to downstream in the flow direction, a fan, a low pressure compressor, a high pressure compressor, a combustion chamber, a high pressure turbine, a low pressure turbine and a nozzle. The gases entering the turbofan-

Figure 5.1: Acoustic test bench of a turbofan engine, CFM property

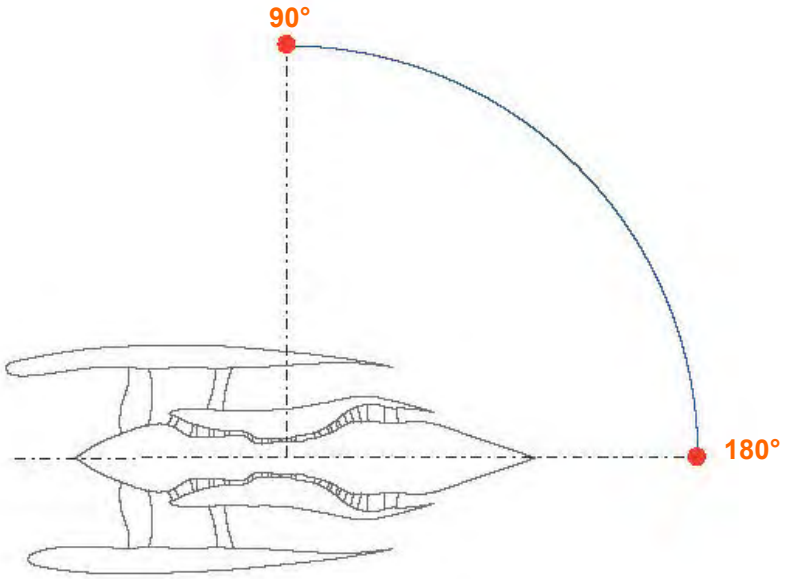

Figure 5.2: Sketch of the microphone convention in far field

engine are split into a primary and secondary flow after the fan blades.

The core noise is essentially related to the primary flow path throw the gas generator (the compressors, the combustion chamber and the turbines), combustion noise being the main contributor at low frequency. As the combustion noise is the subject of the study, only some parts of the turbofan-engine will be treated: the combustion chamber, the two turbines and the double stream nozzle.

5.2 The combustion chamber

The configuration is an optimised Rich-Quench-Lean (RQL) single annular combustor of a modern turbofan engine. Kerosene is injected by 18 identical injectors distributed circumferentially around the chamber. The computational domain used for the first part of CONOCHAIN is a 20° single sector of the chamber with only one injector (Fig. 5.3), followed by the High Pressurized Turbine Stator (HPTS).

Each sector is divided into three parts :

- An injector with two contrarotative swirlers
- A by-pass duct
- The flame tube

5.2.1 The flame tube

The Rich-Burn, Quick-Mix, Lean-Burn (RQL) combustor concept was introduced in 1980 as a strategy to both reduce nitrogen oxides and enhance the stability of the combustion by means of rich burn condition in the primary zone (equivalence ratio close to 1.8, Mosier and Pierce 1980). However, this leads to an higher concentration of partially oxidized and partially pyrolized hydrocarbon species, hydrogen, and carbon monoxide in the primary rich zone. Therefore, a lean burn condition zone is created prior to the exit plane of the combustor, by the addition of air taken from the by-pass duct and injected through the so called primary holes to oxidize the carbon monoxide, hydrogen, and hydrocarbon intermediates. A second range of dilution holes allows to cool the hot gases as well as to homogenize and smooth the turbine input temperature profiles.

The thermal energy produced by combustion induces thermal stresses in the chamber elements and in the high pressure turbine blades. Moreover, it is during combustion that pollutants such as carbon monoxide or nitrogen oxides (NOx) are formed. The main challenges in the design of combustion chambers are therefore to have a more homogeneous combustion regime to increase the life of the mechanical parts and to respect environmental standards in terms of pollution.

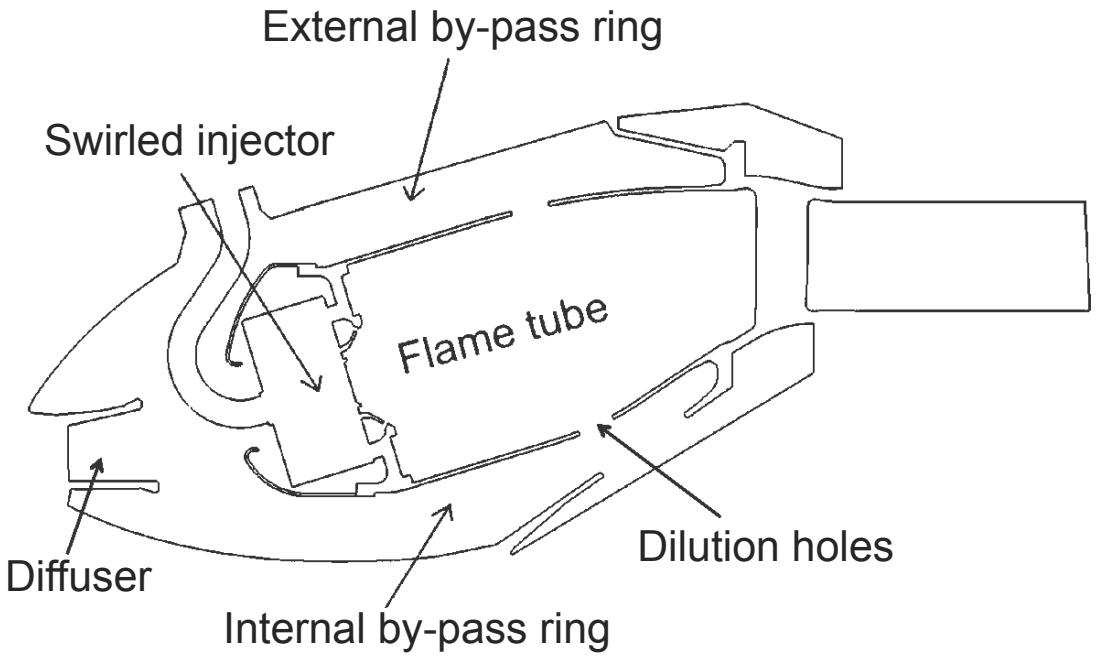

(a)

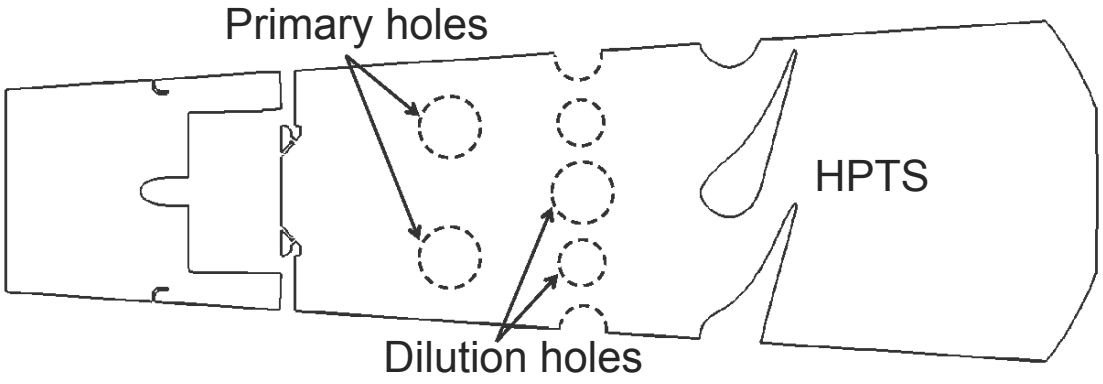

(b)

Figure 5.3: Computational domain of the combustion chamber for LES

5.2.2 The swirled injector

The injectors of aeronautical chambers are mainly swirled injectors. The principle of the swirler is to impart a rotational motion to the air and the fuel flows. Moreover, as the swirler induces recirculation zones, the flame remains compact and attached and so more stable. This allows to reduce the volume of the chambers. In certain conditions, Precessing Vortex Cores (PVC) which are unstable modes

of swirling flows can also be a result of the swirl conditions (Candel et al. 2014).

5.2.3 Operating conditions

In order to study combustion noise, three operating points have been investigated. The first one corresponds to a low power (Table 5.1), used for taxiing. At these operating conditions the jet velocity is very low and jet noise is negligible. The second operating point is the high power case, corresponding to take off conditions. The last operating point is an intermediate one between the first and the second operating conditions, where combustion noise is still noticeable.

	Low	Intermediate	High
Diffuser inlet pressure ratio	11%	85%	100%
Diffuser inlet temperature ratio	54%	97%	100%
Air mass flow rate ratio	13%	79%	100%
Fuel mass flow rate ratio	9%	86%	100%
Fuel/Air ratio	1.25×10^{-3}	1.85×10^{-3}	1.92×10^{-3}

Table 5.1: Main characteristics of the operating points used for the LES presented in section 6.1

5.3 The turbines

The turbojet engine chamber is followed by two turbines (Fig. 5.4). The first one is a high pressure turbine (HPT) composed of one stator and one rotor, *i.e.* one single stage. The last one is a low pressure turbine (LPT) composed of three stages. The only purpose of the high pressure turbine is to extract enough energy from the hot gases to drive the high pressure compressor. Together, these components make up the high spool. Then, the hot flow passes through the large low pressure turbine. This turbine has two purposes. First, it extracts enough energy from the hot gases to drive the low pressure compressor upstream of the engine core. These low pressure turbine and low pressure compressor are connected by a second shaft, which actually passes through the center of the high spool. However, the second and more important job of the low pressure turbine is to drive the large fan blades upstream of the engine core. The fan is connected to the same shaft as the low

pressure compressor and low pressure turbine. Together, these three components make up the low spool.

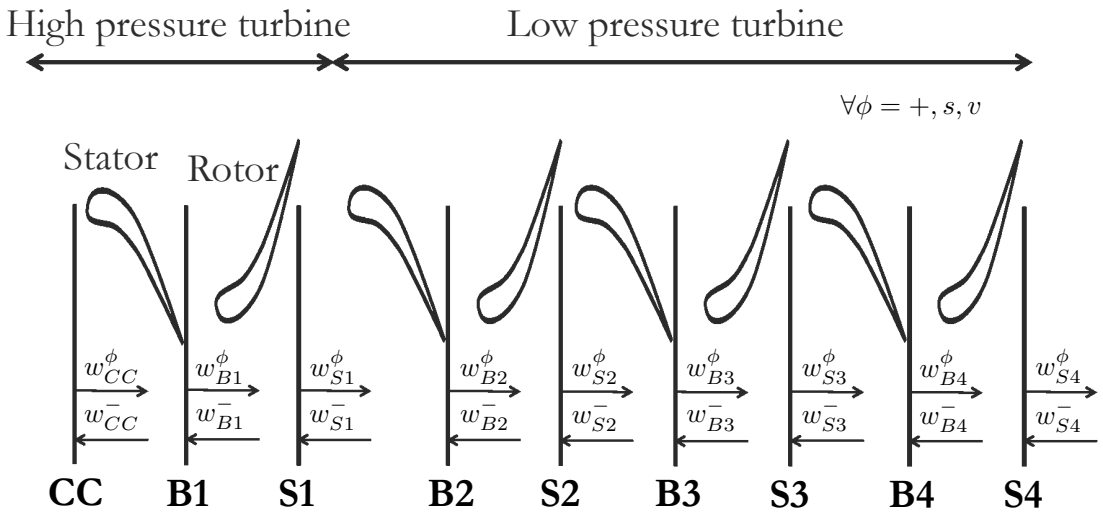

Figure 5.4: Sketch of the high and low presurized turbines

For each operating point the turbines have particular characteristics, which are summarized in Table 5.2. The rotational speeds are normalized by the high power case speed, while pressure and temperature are divided by the inlet conditions of the high pressure turbine.

		Low	Intermediate	High
HPT	Dimensionless rotational speed	62%	85%	100%
	Inlet pressure ratio	100%	100%	100%
	Inlet temperature ratio	100%	100%	100%
	Outlet pressure ratio	59%	29%	31%
	Outlet temperature ratio	79%	70%	70%
LPT	Dimensionless rotational speed	22%	49%	100%
	Inlet pressure ratio	53%	30%	26%
	Inlet temperature ratio	75%	70%	68%
	Outlet pressure ratio	48%	19%	7%
	Outlet temperature ratio	73%	67%	53%

Table 5.2: Characteristics of each turbine operating points computed in section 6.2

5.4 The nozzle exhaust

The nozzles of a turbofan-engine are designed to accelerate a flow and provide an efficient thrust. The thrust developed is proportional to the variation of the momentum between the turbofan-engine inlet and outlet:

$$\vec{F} = \dot{m}_2 \boldsymbol{v}_2 - \dot{m}_1 \boldsymbol{v}_1 \ , \tag{5.1}$$

where $\dot{m}_1$, $\dot{m}_2$, $\boldsymbol{v}_1$ and $\boldsymbol{v}_2$ are respectively the mass flow rates and velocities of gas at the turbofan-engine inlet and exit. Thus, to provide a thrust, two strategies are possible:

- Ejecting a small gas flow rate at very high speed. This is the principle used in most military engines.
- Ejecting a large gas flow rate at low speed. The evolution of civil engines tends towards high dilution rates, ie high ratio between secondary mass flow rate and primary mass flow rate. This allows to slowly accelerate a large volume of gas. This concept permits a significant reduction in engine consumption. In addition, the low gas exhaust velocities reduce jet noise. This trend explains the increase in the diameters of the current engines.

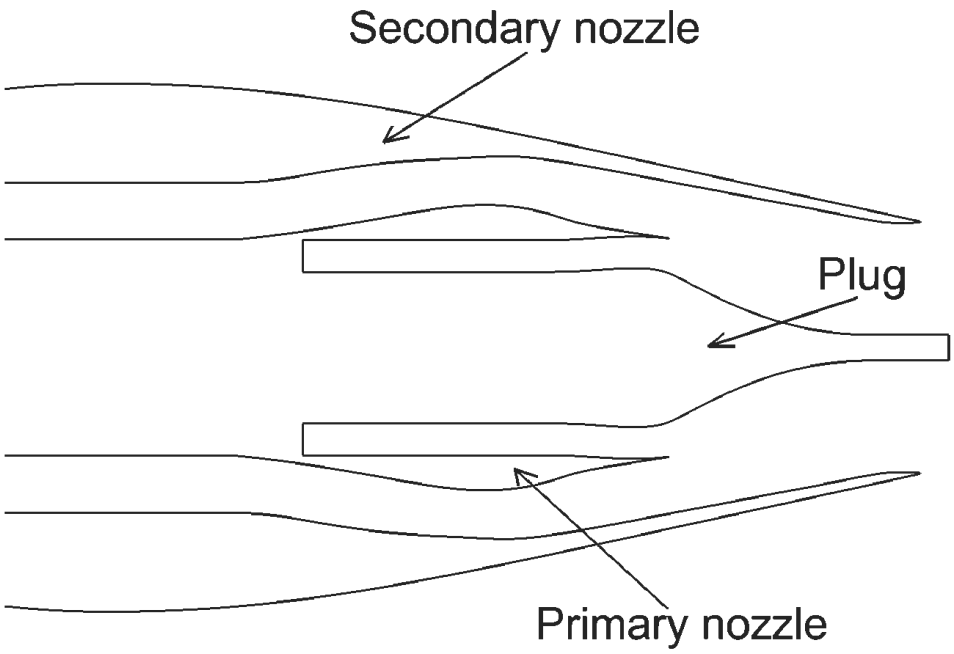

Figure 5.5: View of the double stream nozzle

The exhaust of the chosen turbofan-engine is double stream, with a lobe mixer in order to homogenize the primary and secondary flows and attenuate the noise. However, due to confidential issues, the mixer is replaced by a primary nozzle with similar flow conditions at the inlet (Fig. 5.5). Both nozzles have a divergent-convergent shape.

The turbofan-engine nozzle includes also a plug which has an aerodynamic shape to guide the primary gas exhaust. Moreover, the plug allows the degassing of fluids such as oil vapor and cooling gases from the engine core. The degassing is done by suction, the pressure in the plug being lower than the pressure in the turbofan engine.

In order to reduce the noise in the nozzle, which is composed of low frequency combustion noise and high frequency turbine noise, acoustic coatings such as honeycombs can be used in the primary nozzle. However, combustion noise cannot be reduced with acoustic treatments in the primary nozzle as the available volume is not enough to handle low frequencies. Therefore, the plug can be modified to contain honeycombs and resonance cavities forming Helmholtz resonators to deal with combustion noise lowest frequencies (Bouty et al. 2007).

Operating conditions used for the RANS computations of the double stream jet are presented in Table 5.3.

		Low	Intermediate	High
Primary nozzle	Inlet pressure ratio	66%	70%	100%
	Inlet temperature ratio	92%	72%	100%
	Mach at the exit	0.08	0.21	0.49
Secondary nozzle	Inlet pressure ratio	63%	69%	100%
	Inlet temperature ratio	86%	87%	100%
	Mach at the exit	0.15	0.29	0.8

Table 5.3: Main characteristics of the operating points used for the RANS computations of the double stream jet, section 6.3, and LES, Chapter 8

The robustness of the combustion noise prediction method is tested by comparing results with data obtained in the far field from the engine test bench. Aft noise measurements are performed with an acoustic barrier shielding noise from the inlet and available at 45.72 m.

Chapter 6

Using a zero Mach number frequency far-field propagation

Abstract This chapter presents the Large-Eddy simulations of a realistic turbofan-engine annular combustion chamber to provide unsteady fields at the exit of the combustor and apply the CONOCHAIN methodology described in chapters 1, 2 and 3. To do so, numerical simulations correspond to the operating points of the acoustic test bench of the turbofan engine presented in chapter 5. This chapter is composed of three main sections:

- the first section describes the numerical setup of the LES of the combustion chamber and the mean features of the simulations at three operating points, low power, middle power, and full power,
- the second one presents the computation of direct and indirect combustion noise levels from the high pressure turbine to the turbine exit,
- the last section concerns far-field noise propagation from the turbine outlet since the far-field noise is actually the only relevant quantity for acoustic certification.

6.1 Large Eddy Simulations of an industrial combustion chamber

6.1.1 Numerical parameters

The numerical simulations presented in this section are performed with the parallel unstructured LES solver AVBP. It solves the compressible Navier-Stokes equations, presented in chapter 1, in three dimensional complex geometries (Poinsot and Veynante 2011) with a finite volume method based on a cell-vertex formulation, and a

Two-step Taylor-Galerkin numerical Scheme (TTGC) that is third order accurate in space and time (Colin and Rudgyard 2000). The compressible feature of the solver allows to deal with acoustic propagation, and the numerical scheme permits to limit dispersion and dissipation. Colin's sensor is used to remove numerical instabillity in zones with strong gradients, such as in the swirler as well as in the high pressure distributor (Colin et al. 2000), and the Smagorinsky [1963] model is used for sub-grid scale stresses.

6.1.1.1 Boundary conditions

Fuel is injected in the LES in gaseous phase close to the lips of the swirler to mimic the fast evaporation of the kerosene spray. A cold flow is injected in the by-pass duct and around the walls by inlet films and multiperforated plates, to cool the chamber walls. Multiperforated plates are modeled by a homogeneous plate with a specific effusion condition (Mendez and Eldredge 2009), contrary to primary and dilution holes which are resolved. For all simulations (low, medium and high power), the high pressure distributor is choked, and no additional boundary condition is needed at the chamber outlet (Fig. 6.1). A Navier Stokes Characteristic Boundary Condition (NSCBC) is used at the inlet of the combustor to limit acoustic reflections (Poinsot and Lele 1992; Selle et al. 2004b). All walls of the chamber are defined as adiabatic with a turbulent wall-law model to evaluate and impose the wall shear stress and the heat flux. The computation includes the HPTS and stops in a choked region downstream of it.

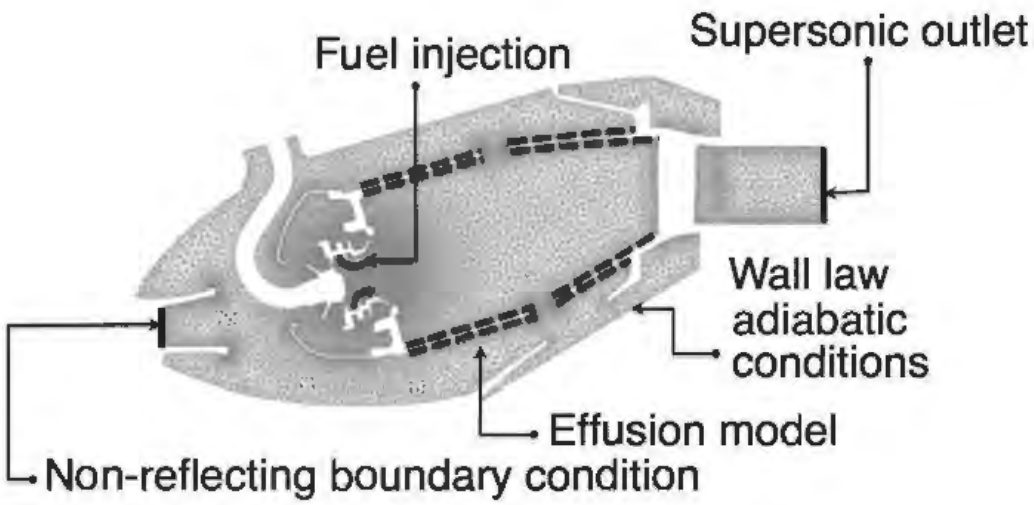

Figure 6.1: Boundary conditions used in the LES simulations

6.1.1.2 Chemistry and combustion model

Kerosene/air chemistry is modeled using a synthetic fuel surrogate equivalent to $C_{10}H_{20}$ and described by a reduced mechanism involving 6 species and 2 reactions (Franzelli et al. 2010) called BFER:

$$Fuel + 10O_2 \implies 10CO + 10H_2O \tag{6.1}$$

$$CO + \frac{1}{2}O_2 \iff CO_2 \tag{6.2}$$

This scheme provides correct values for the laminar flame properties (flame speeds, flame thicknesses). Reaction rates are modeled by Arrhenius laws (Poinsot and Veynante 2011) presented in chapter 1, where the pre-exponential constants are fitted in rich regimes to recover proper laminar flame speeds and realistic adiabatic temperatures.

This is coupled with the Dynamic Thickened Flame (DTF) approach (Colin et al. 2000; Selle et al. 2004a; Poinsot and Veynante 2011) to describe flame-turbulence interactions. The flame front is locally thickened while conserving the mixture in the fresh or burnt gases and consequently obtaining a good resolution of the entropic waves at the outlet of the chamber. Moreover, this method reduces the mesh cost and allows the modeling of the energy structures in the flame thickness. The DFT LES model is based on the laminar flame characteristics, so that laminar flame computations have to be performed to set the flame properties required in the DTF LES model at the stoichiometry. The laminar flame characteristics corresponding to the chosen operating conditions are summarized in Table 6.1.

Operating points	Low power	Intermediate power	High power
Flame speed (m.s^{-1})	0.33	0.75	0.84
Flame thickness (m)	5.077×10^{-4}	9.78×10^{-5}	4.13×10^{-5}

Table 6.1: Laminar flame properties for the DFTLES model

6.1.2 Mesh

The geometry is fully discretized with tetrahedral elements (Table 6.2). In order to accurately capture small geometrical details and physics, a fine discretization is required around the injection and the flame zone ($\Delta_x = 0.4$ mm), the primary and dilution holes, as well as the primary zone where combustion occurs ($\Delta_x = 0.8$ mm). In the lean combustion regime zone, the mesh refinement must be

sufficient to properly describe the entropy convection through the flame tube (Δ_x = 1.4 mm). Indeed, it is known that entropy is responsible for the indirect noise generation, so that it is important not to neglect its resolution. This is a new constraint compared to usual flame LES where there is no need to correctly convect entropy waves downstream of the flame zone.

Number of cells	33 134 438
Number of nodes	6 199 870
Smallest volume	$2.3.10^{-14}$ m^3
Time step	3.10^{-8} s

Table 6.2: Mesh parameters

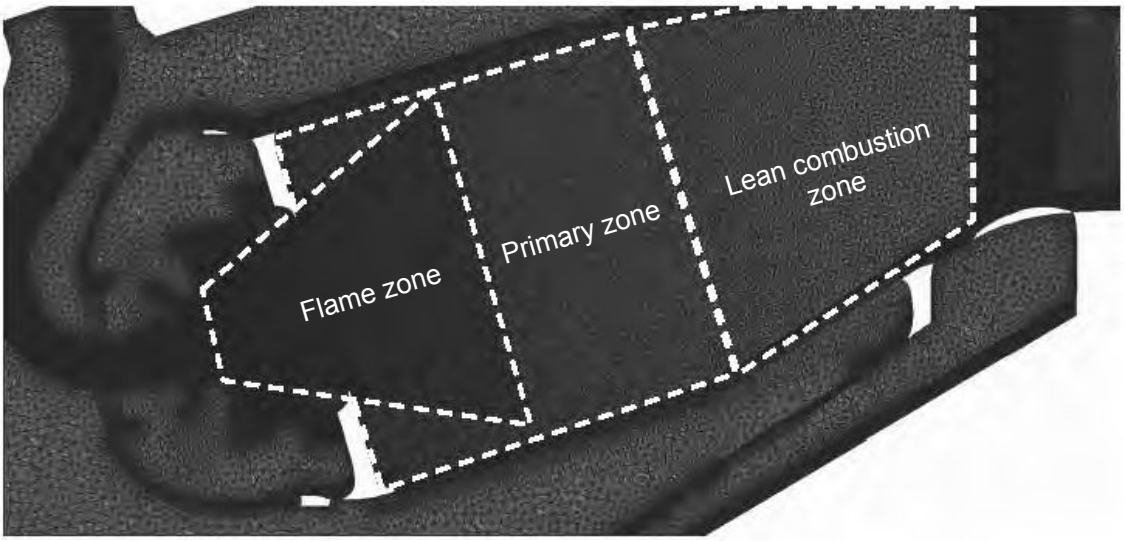

Figure 6.2: Tetrahedral mesh of the computational domain

6.1.3 Simulation setup

The first simulation for the high power case (Table 5.1) has been initialized at SAFRAN Aircraft Engines (SAE) with a Lax-Wendroff (LW) numerical scheme. The simulation has then been converged on 4 convective times with TTGC, $\tau_c = \rho V/\dot{m} = 18$ ms (V volume of the combustion chamber, $\dot{m}$ imposed inlet mass flow rate, ρ mean density in the combustor). Simulations for low and intermediate power cases have been initialized from the high power case. Inlet flow speed and outlet pressure imposed have progressively been reduced to reach the desired operating point. Simulations have then been converged on 4 convective times. Converged LES of a single sector are run for 48 ms of physical time with a time-step of 3 10^{-8}s respecting a maximum CFL number of 0.7 and being controlled by the speed of sound (Lamarque 2007):

$$\Delta t = \min \left[\frac{CFL.\Delta x}{u + c} \right] \tag{6.3}$$

6.1.4 Mean flow description

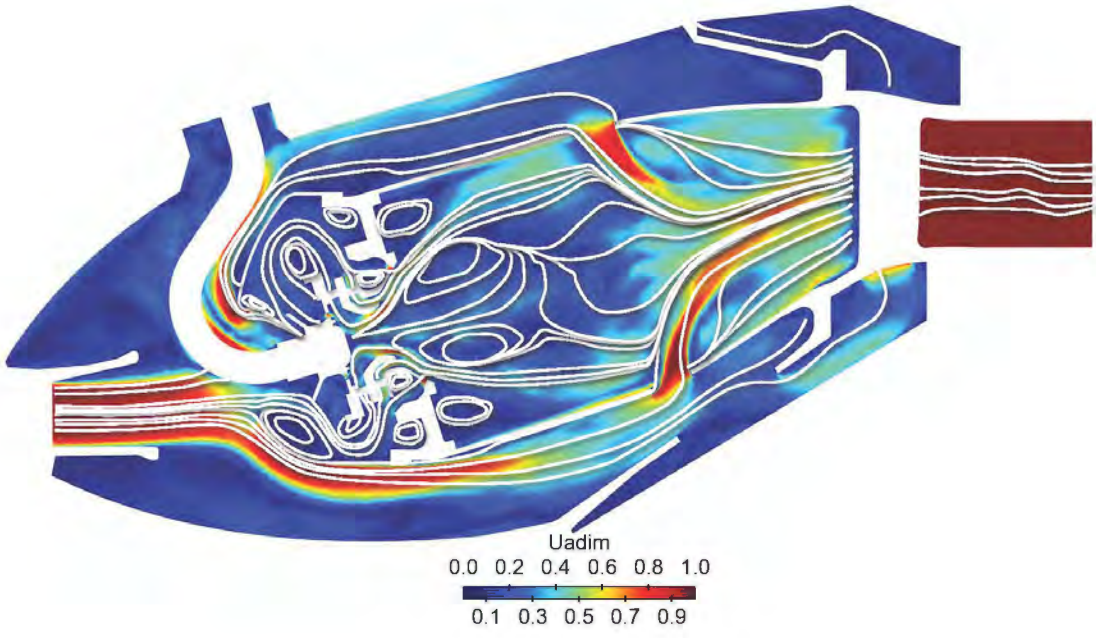

Figure 6.3: Mean dimensionless velocity magnitude $\frac{U}{U_{inlet}}$ with white mean streamlines at low power

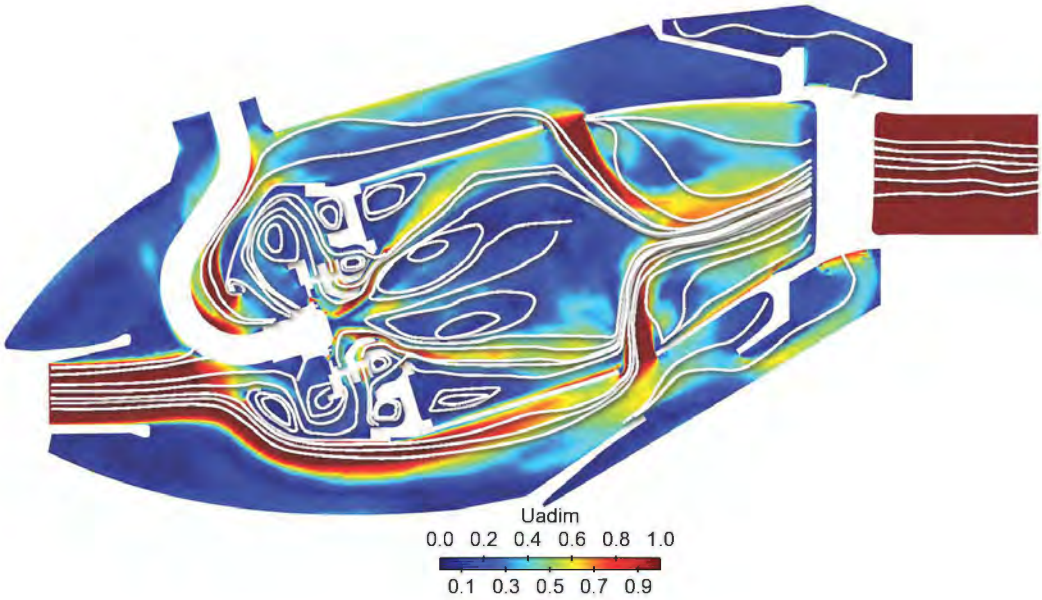

Figure 6.4: Mean dimensionless velocity magnitude $\frac{U}{U_{inlet}}$ with white mean streamlines at intermediate power

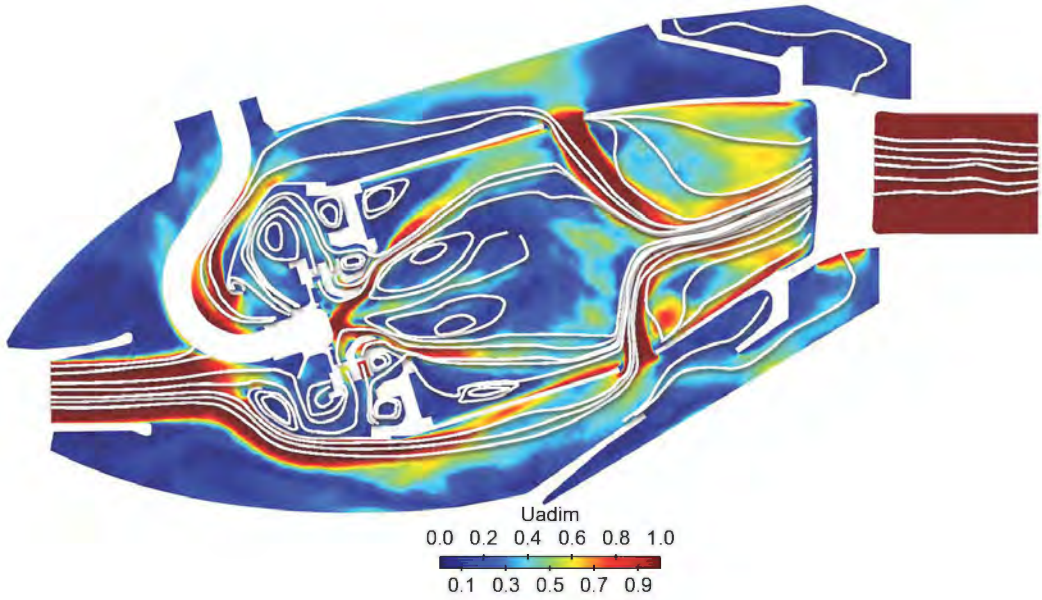

Figure 6.5: Mean dimensionless velocity magnitude $\frac{U}{U_{inlet}}$ with white mean streamlines at high power

Mean velocity fields are presented in Figs. 6.3 to 6.5 and scaled by the inlet mean velocity U_{inlet} of the high power case. High pressurized cold flow is injected through the diffuser, and is split in three different directions: the internal and external by-pass ring, the flame tube. The part of the flow which enters in the flame tube, is injected through the swirler where it is mixed with fuel gas and then reacts at high temperature. Because of the strong swirling motion, the high-velocity jet expands rapidly after the swirler, leading to the formation of a large Inner Recirculation Zone (IRZ) in the central part of the combustor. This recirculation zone ends with the injection of cold flow through the dilution holes. Outer Recirculation Zones (ORZ) are also formed in the combustion chamber corners under the effect of the outer shear layer of the swirling jet. These recirculation zones stabilize the flame. The hot swirling flow is accelerated at the exit of the combustion chamber. The cold flow going through the by-pass ring is injected through multi-perforated plates, primary and dilution holes and is also used to cool the HPTS. The same description for all the operating points can be done with an increasing velocity magnitude with the power-engine rise. This repartition of the velocity field and particularly the cross flow jets at the exit of the combustion chamber induce temperature stratification.

The dimensionless mean temperature fields are represented in Figs. 6.6 to 6.8 and correspond to $\frac{T - T_{inlet}}{T_{max} - T_{inlet}}$, where T_{inlet} is the mean inlet temperature and T_{max} is the mean maximum temperature of the burnt gases. The mean temperature fields are characterized by a primary zone in which combustion takes place to reach the adiabatic temperature. In this primary zone, a flame, more or less extended, may be observed. The flame is longer in the low power case (Fig. 6.6(a)) and shorter in the high power case (Fig. 6.8(a)). A strong temperature stratification of the burnt gases is observed in particular in the plane parallel to the swirler axis (Figs. 6.6(b) and 6.7(b)). Indeed, successive decreasing temperature levels are obtained with the introduction of cold air flow through the primary holes. This helps to create a lean burn condition zone. On the contrary, the high power case seems less stratified, with a large zone of high temperature (Fig. 6.8(b)). To reduce the mean temperature before the high pressure turbine, cold air flow is injected from the dilution holes. It can be observed that the bigger dilution hole on the center of the ferrule has a strong impact at the junction of the two dilution jets (external/internal bypass) yielding the entropy spots through the turbine. Burnt gases exit through the HPTS where they are accelerated and relaxed. The mean flame location is highlighted by the iso-lines of the mean heat-release. The most reactive zones are confined close to the swirler but there is also a reacting zone near the dilution holes for the three operating points. Close to the swirler, a "broken" flame is observed, particularly at low power case in Fig 6.6(a). Indeed, around the ORZ, combustion pockets are observed.

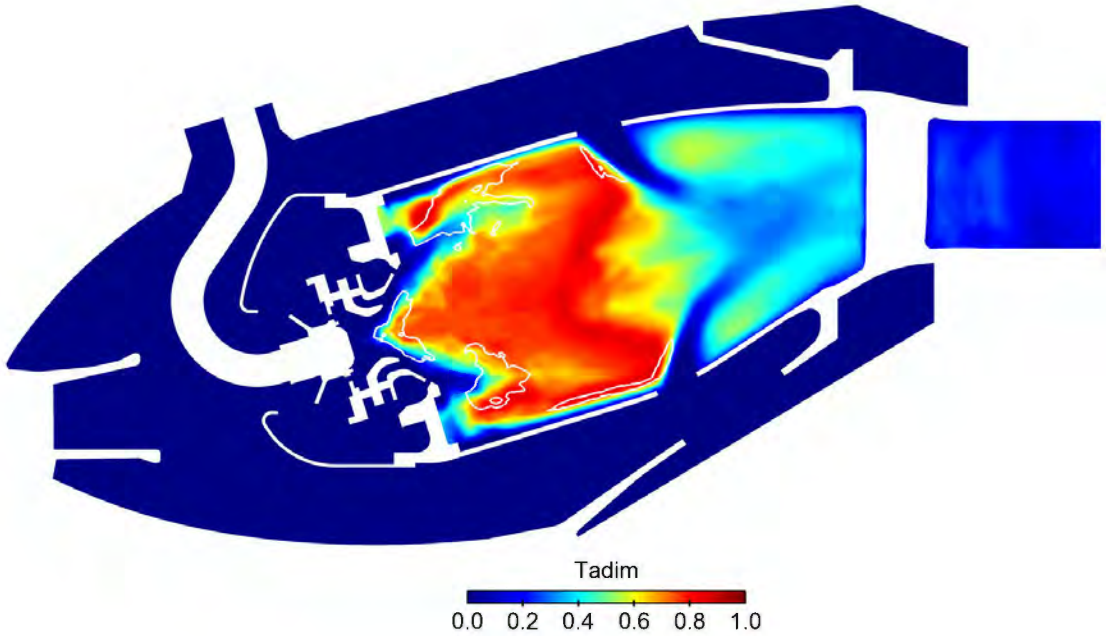

(a)

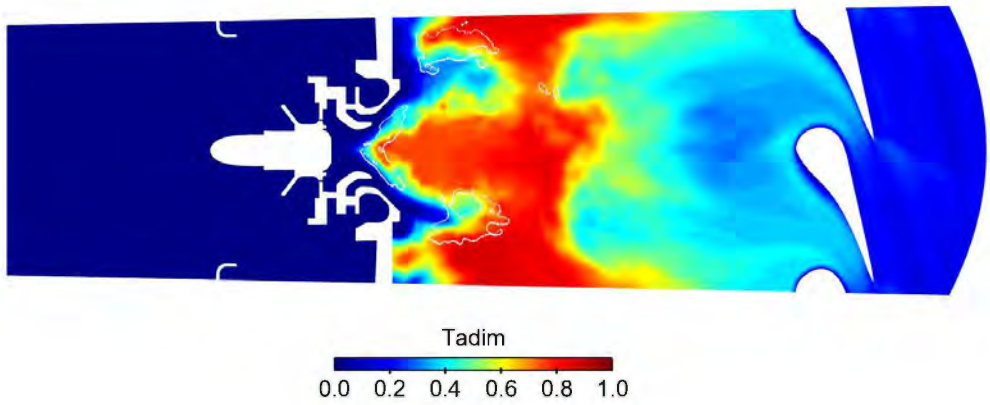

(b)

Figure 6.6: Mean dimensionless temperature field $\frac{T - T_{inlet}}{T_{max} - T_{inlet}}$ with white isolines of mean heat release rate (W/m^3), at low power. a) Longitudinal plane at $\vec{z} = 0$, b) longitudinal plane parallel to the swirler axis.

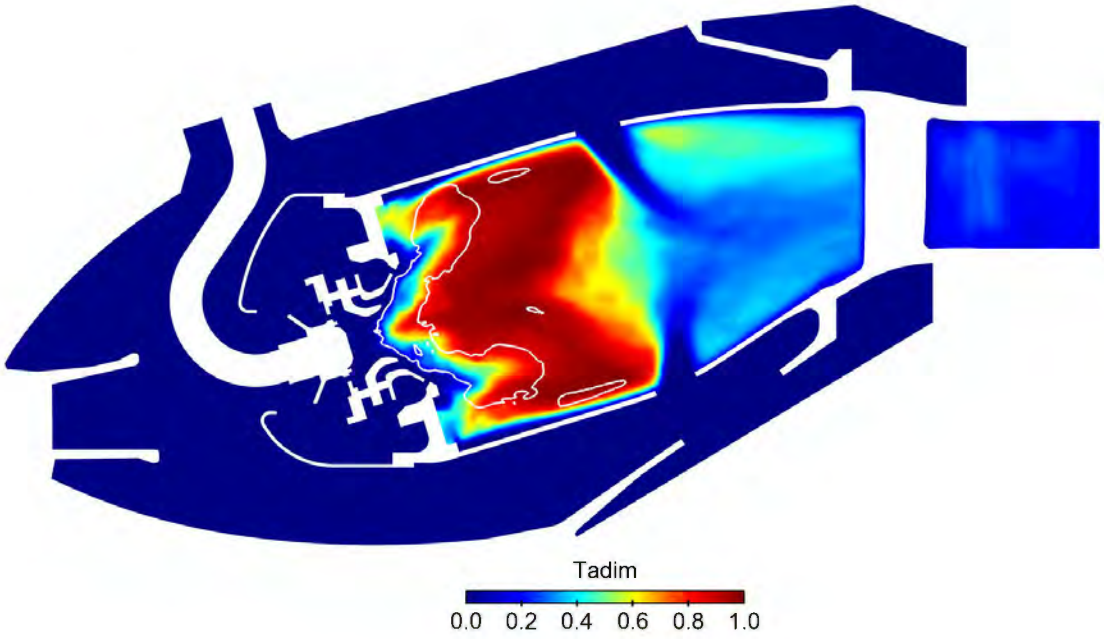

(a)

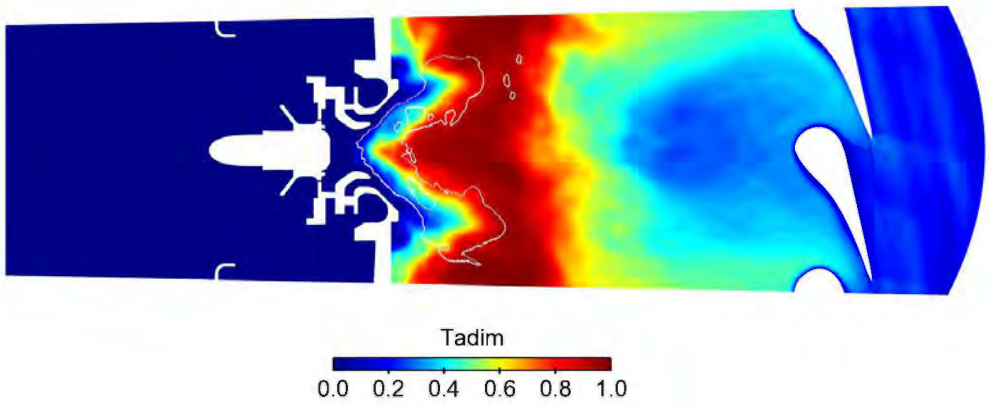

(b)

Figure 6.7: Mean dimensionless temperature field $\frac{T - T_{inlet}}{T_{max} - T_{inlet}}$ with white isolines of mean heat release rate (W/m^3) at intermediate power. a) Longitudinal plane at $\vec{z} = 0$, b) longitudinal plane parallel to the swirler axis.

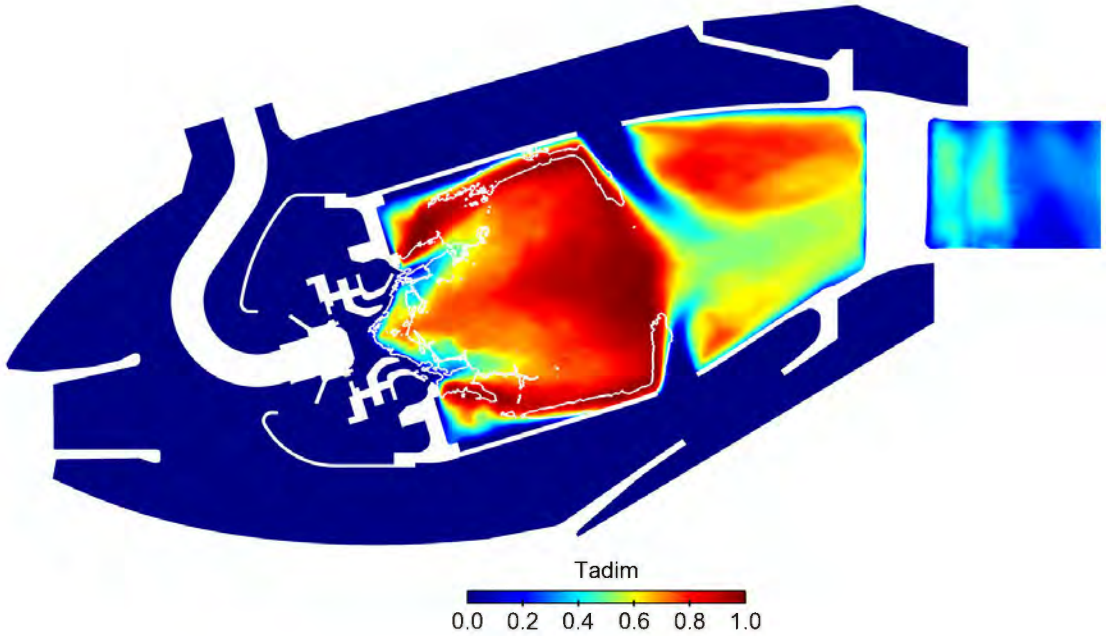

(a)

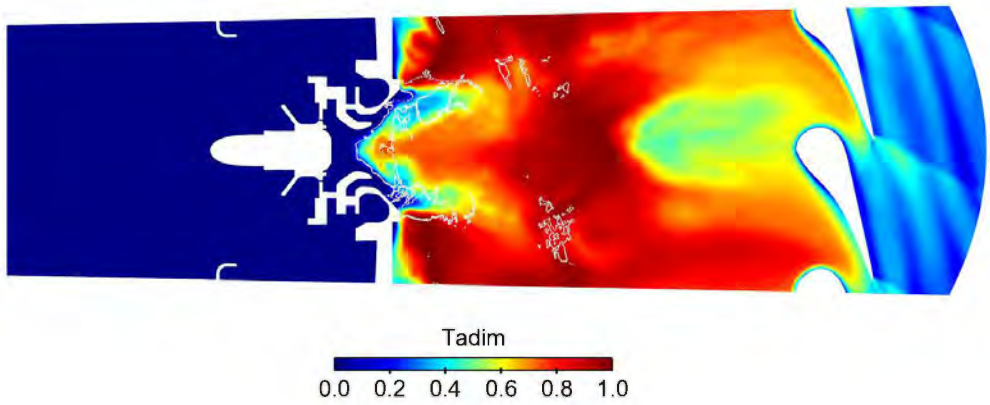

(b)

Figure 6.8: Mean dimensionless temperature field $\frac{T - T_{inlet}}{T_{max} - T_{inlet}}$ with white isolines of mean heat release rate (W/m^3) at high power. a) Longitudinal plane at $\vec{z} = 0$, b) longitudinal plane parallel to the swirler axis.

Due to the rich combustion regime, fuel is not completely burnt at the outlet of the swirler. Burnt gases with small residual amounts of fuel are convected and react with the fresh air which is introduced at the corner of the flame tube. Therefore, combustion of burnt gases occurs at successive steps.

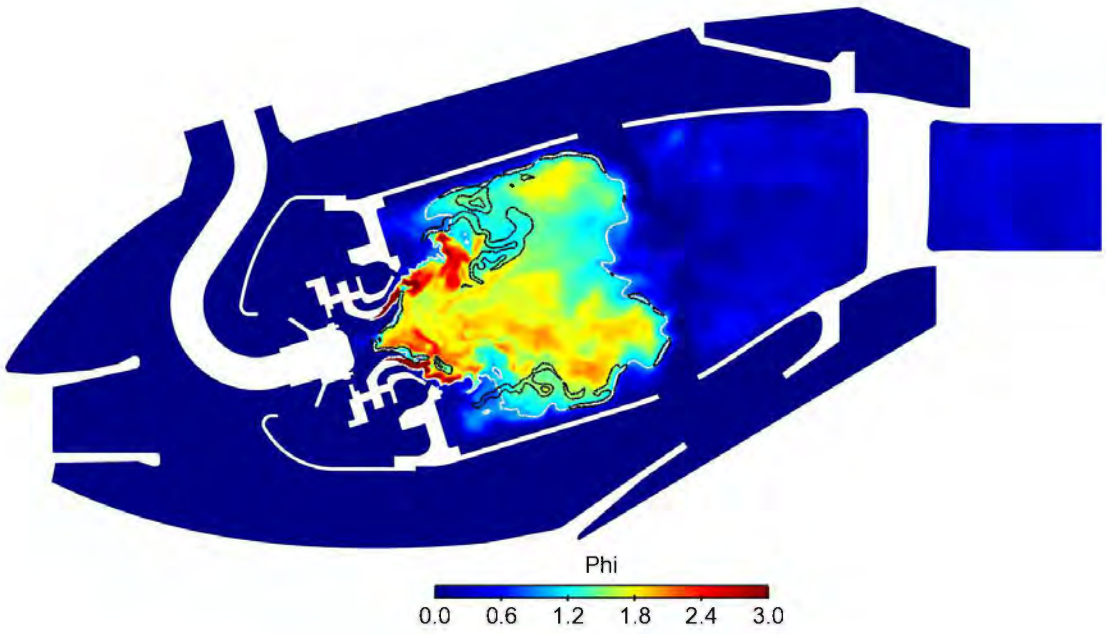

(a)

Figure 6.9: Instantaneous equivalence ratio ϕ field with white isolines of $\phi = 1$ and dark isolines of instantaneous heat release rate at low power.

The combustion regime can be observed on the instantaneous equivalence ratio fields in Figs. 6.9 to 6.11. In the primary zone, the composition of gases is very rich, particularly at low and high power conditions. Combustion process takes place first close to the swirler at very rich condition ($\phi > 2.5$). The burnt gases are convected through the flame tube where cold air is injected through the primary holes. Therefore a second step of combustion occurs at still rich condition ($\phi \approx 1.5$). Near the dilution holes and the multi-perforated walls, two flame fronts can be observed at rich ($\phi \approx 1.2$) and lean ($\phi \approx 0.8$) conditions. At high power condition, the combustion pockets at lean condition gather (Fig. 6.11). While the low and high power cases have a similar equivalence ratio repartition with a rich flame front longitudinally expanded in the flame tube, the intermediate power case exhibits a different behavior. Indeed, the rich flame front is more concentrated around the swirler jet and the equivalence ratio of the burnt gases in the primary zone is leaner ($\phi = 1.2$) as observed in Fig. 6.10.

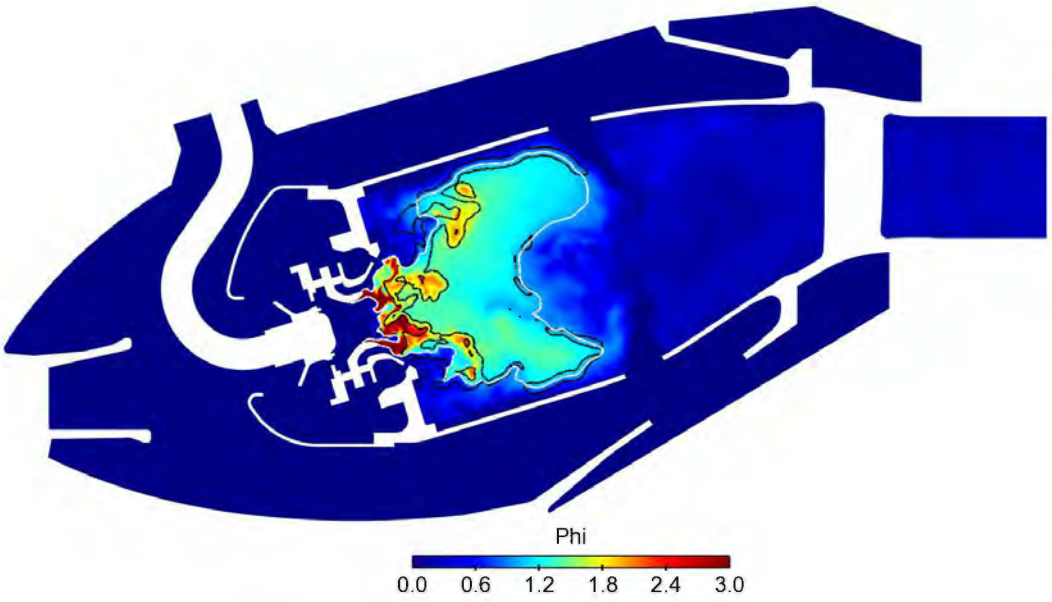

(a)

Figure 6.10: Instantaneous equivalence ratio ϕ field with white isolines of $\phi = 1$ and dark isolines of instantaneous heat release rate at intermediate power.

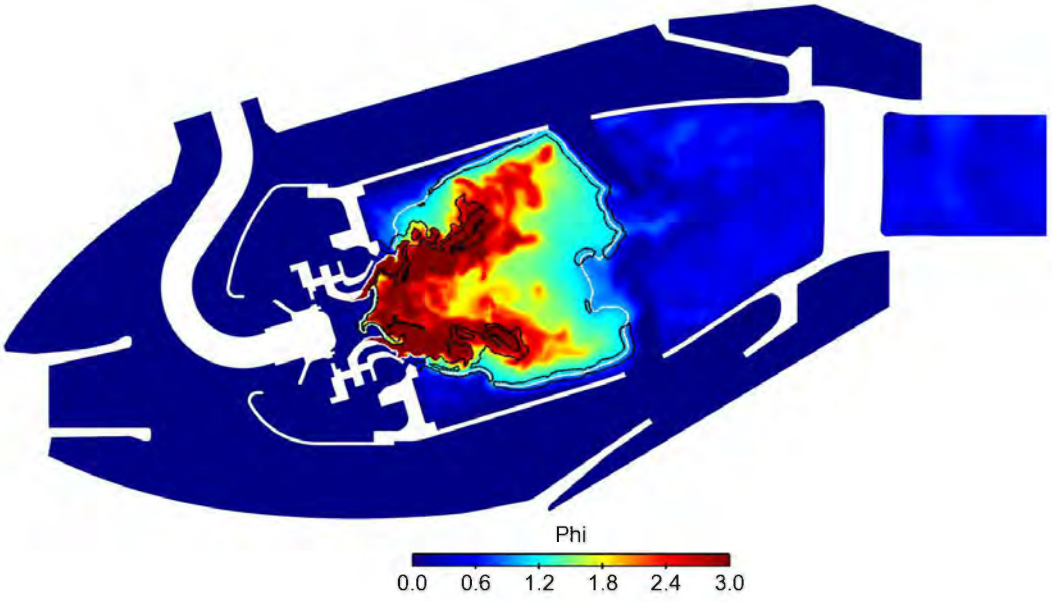

(a)

Figure 6.11: Instantaneous equivalence ratio ϕ field with white isolines of $\phi = 1$ and dark isolines of instantaneous heat release rate at high power.

The Root-Mean-Squared (RMS) pressure fields are shown in Figs. 6.12 to 6.14. In each case, the high pressure fluctuation amplitudes are mainly located close to the swirler and the dilution jet interaction zones. These pressure fluctuations are either acoustic or hydrodynamic. Due to the highly swirling flow, high hydrodynamic pressure levels are generated in the flame zone. Therefore, it is complicated to visually dissociate acoustics from hydrodynamics without filtering. In terms of fluctuating pressure levels, the amplitudes increase with the increasing power condition (increase of the mean pressure conditions in the combustion chamber). The high operating point has levels of fluctuation at least ten times higher than the low power case.

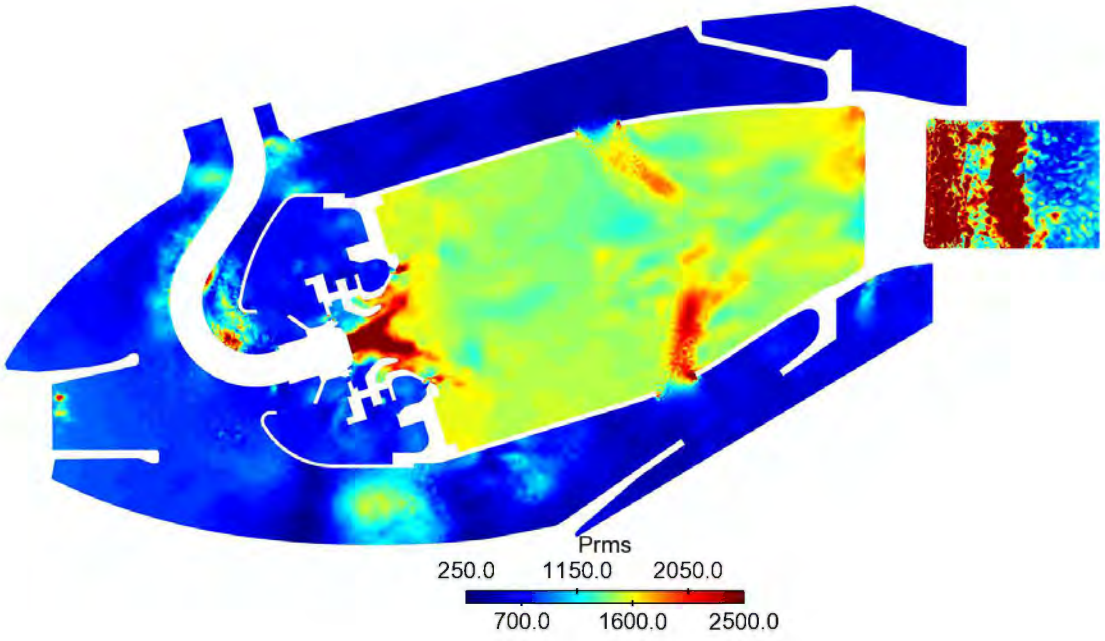

Figure 6.12: Root-mean-squared pressure (Pa) at low power

The RMS temperature fields (Figs. 6.15 to 6.17) reveal two main zones of fluctuating temperature. First, in the primary zone, temperature fluctuations correspond to the reactive zones (the turbulent flame close to the swirler and the combustion pockets near the multi-perforated walls) represented by the isoline of mean heat release rate. Turbulent structures interact with the flame front which convects fresh gases across the reacting zone. Therefore, hot and cold spots are generated in the flame region. Secondly, the interaction of the cold dilution jet flows with the hot burnt gases at the end of the primary zone generates the strongest temperature fluctuations, particularly at low and high power cases as shown in Figs. 6.15 and 6.17.

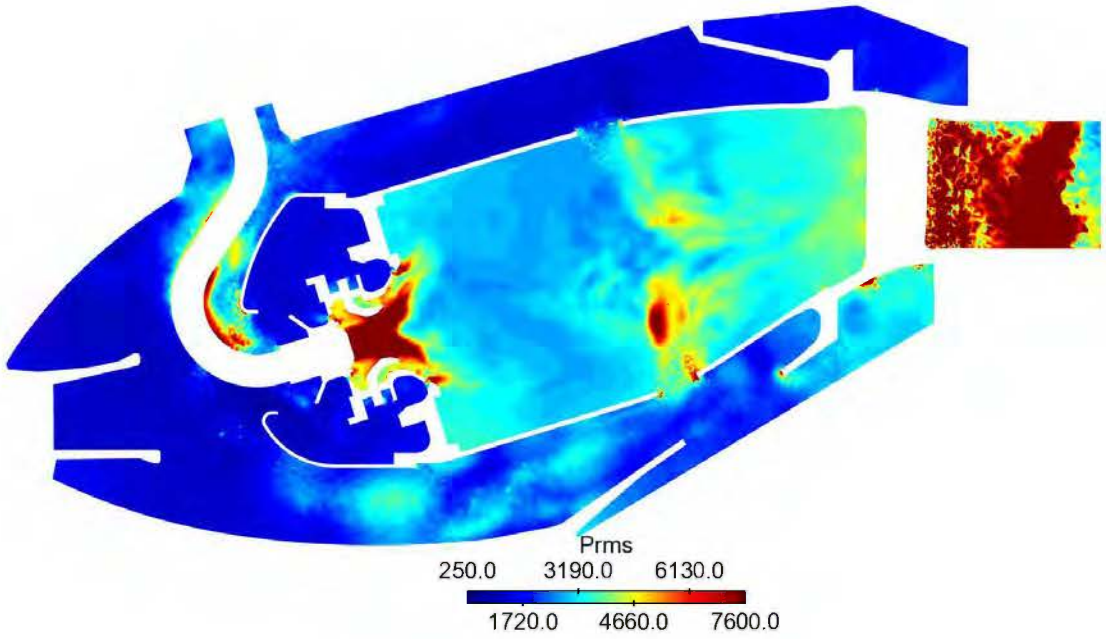

Figure 6.13: Root-mean-squared pressure (Pa) at intermediate power

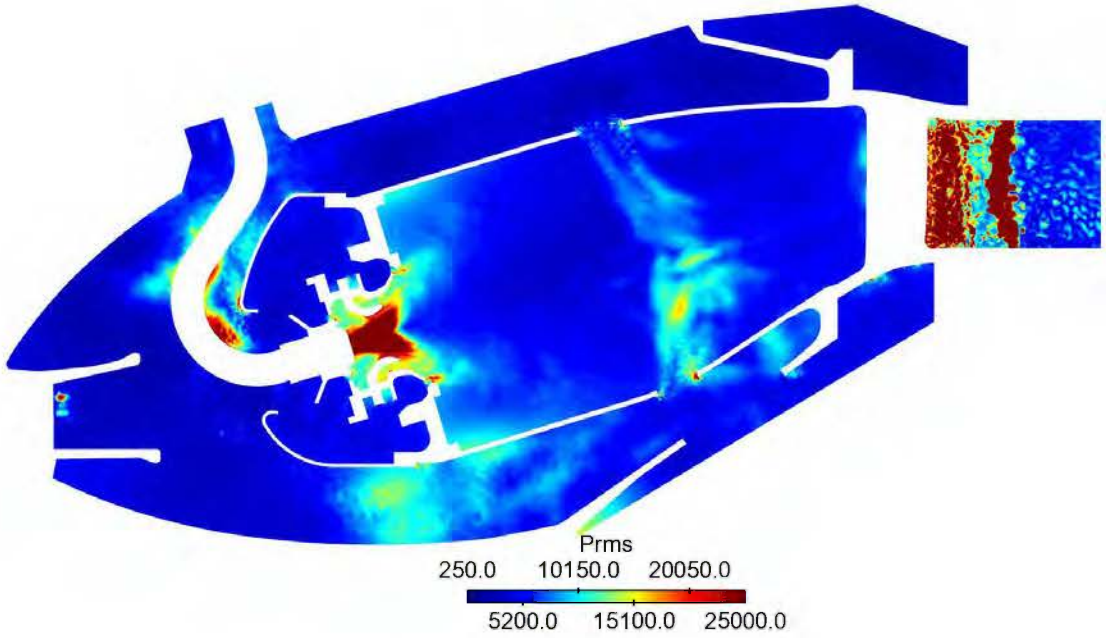

Figure 6.14: Root-mean-squared pressure (Pa) at high power

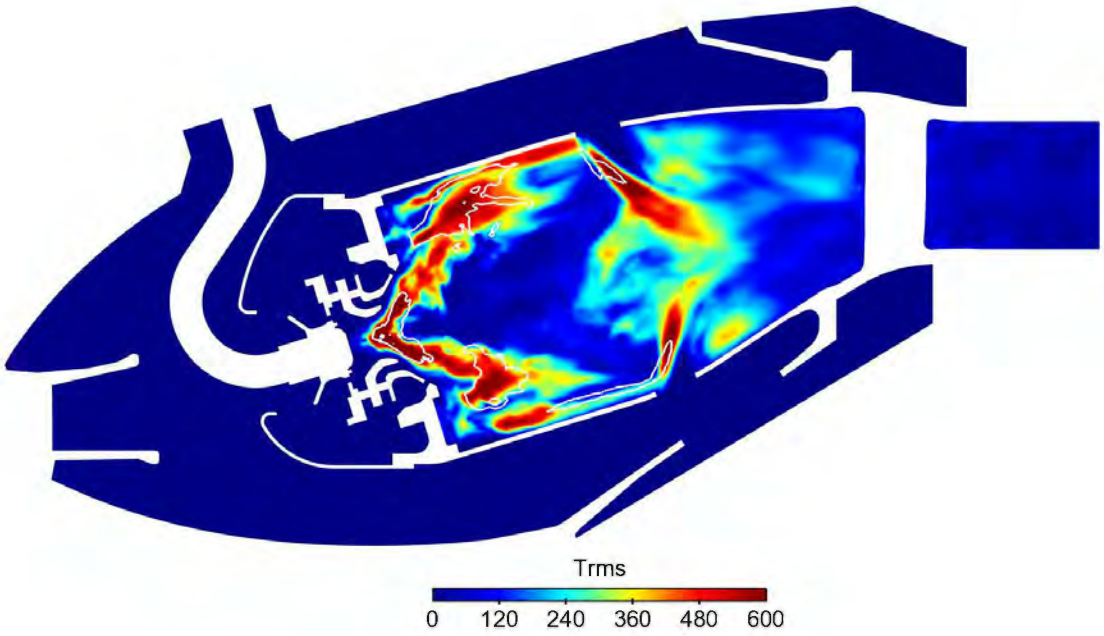

Figure 6.15: Root-mean-squared temperature (K) with white isoline of mean heat release rate (W/m^3) at low power

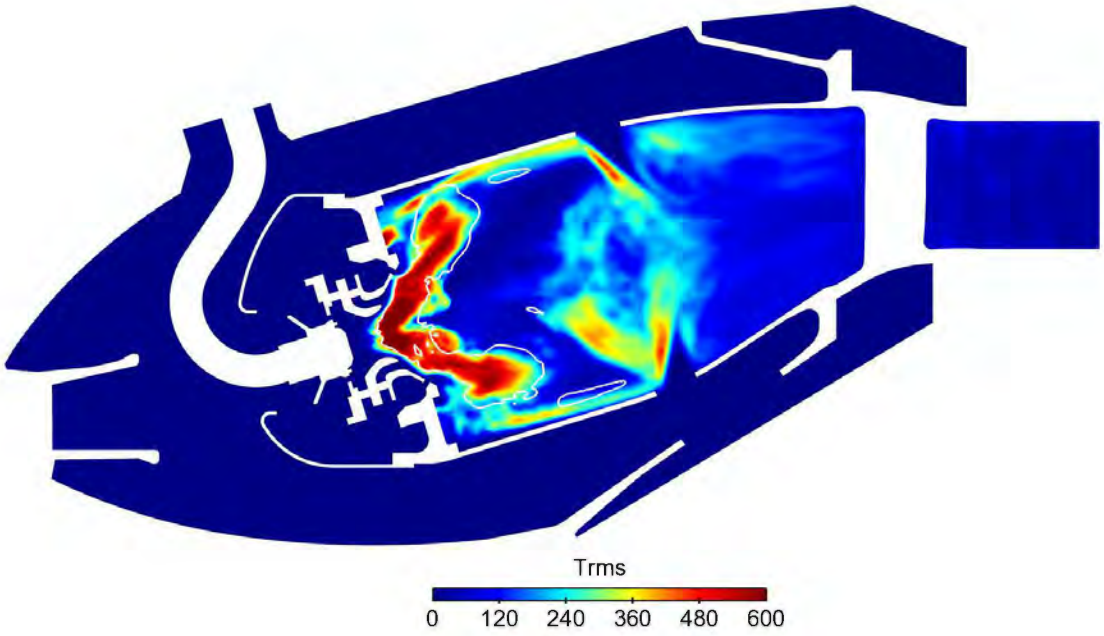

Figure 6.16: Root-mean-squared temperature (K) with white isoline of mean heat release rate (W/m^3) at intermediate power

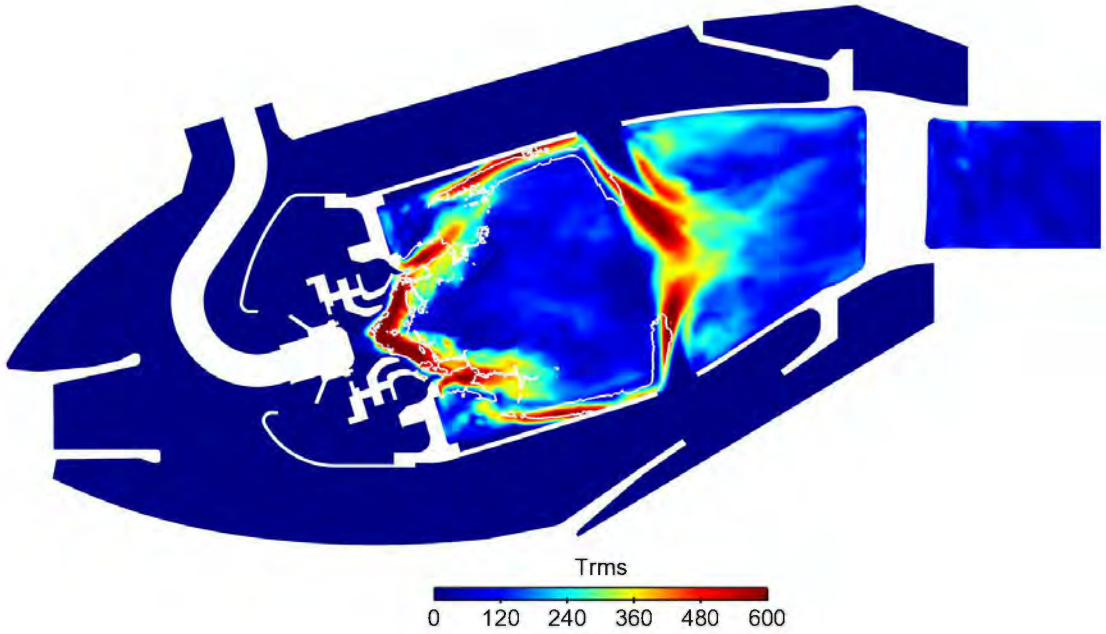

Figure 6.17: Root-mean-squared temperature (K) with white isoline of mean heat release rate (W/m^3) at high power

The turbulent structures colored by the heat release rate can be visualized in Figs. 6.18 to 6.20. More turbulent structures can be observed with the increase of the power-engine regime. The combustion is concentrated in the highly swirled jet where the flame is more anchored to the injector at low and high power cases than at intermediate power. High heat release rate can also been observed between the primary and dilution holes. Helical structures wrap around the primary and dilution jets where combustion occurs again particularly at high power conditions (Fig. 6.20). Again, far less heat release rate is observed around the dilution jets for the intermediate power case (Fig. 6.19) as noticed before in Fig. 6.10(a).

The hot and cold spots which will be the source of the indirect noise are captured by LES and highlighted in Figs. 6.21 to 6.23. The dimensionless fluctuating temperature shows that the largest hot and cold spots are generated in the second half of the flame tube with the injection of cold air through the dilution holes. The flame also generates smaller temperature spots which are almost dissipated in the IRZ, particularly in the intermediate power case (Fig. 6.22). Qualitatively, this confirms that the primary source of indirect noise is the interaction of the burnt gases created by the primary zone with the dilution jets. Controlling indirect noise can be achieved by manipulating dilution jets.

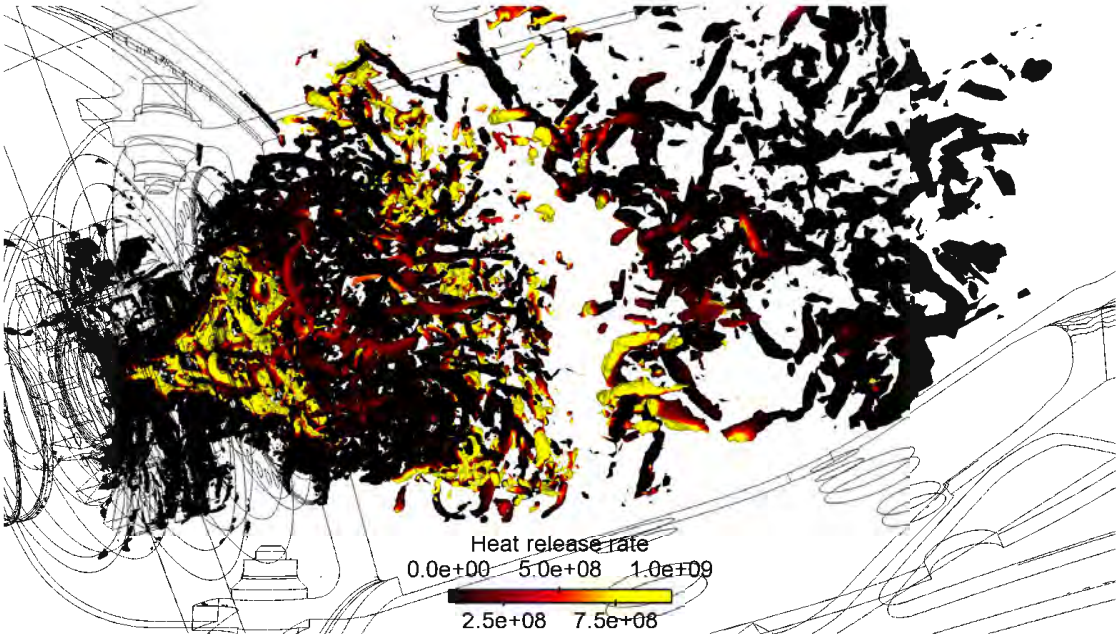

Figure 6.18: Iso-criterion Q ($Q = 10^9$) colored by the heat release rate (W/m^3) at low power

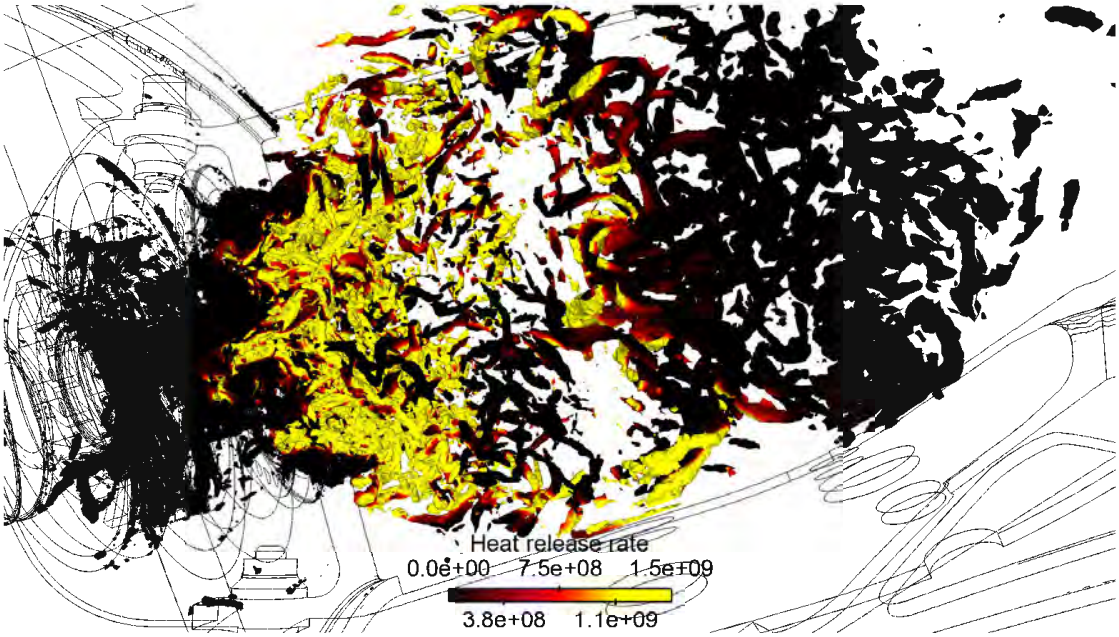

Figure 6.19: Iso-criterion Q ($Q = 10^9$) colored by the heat release rate (W/m^3) at intermediate power

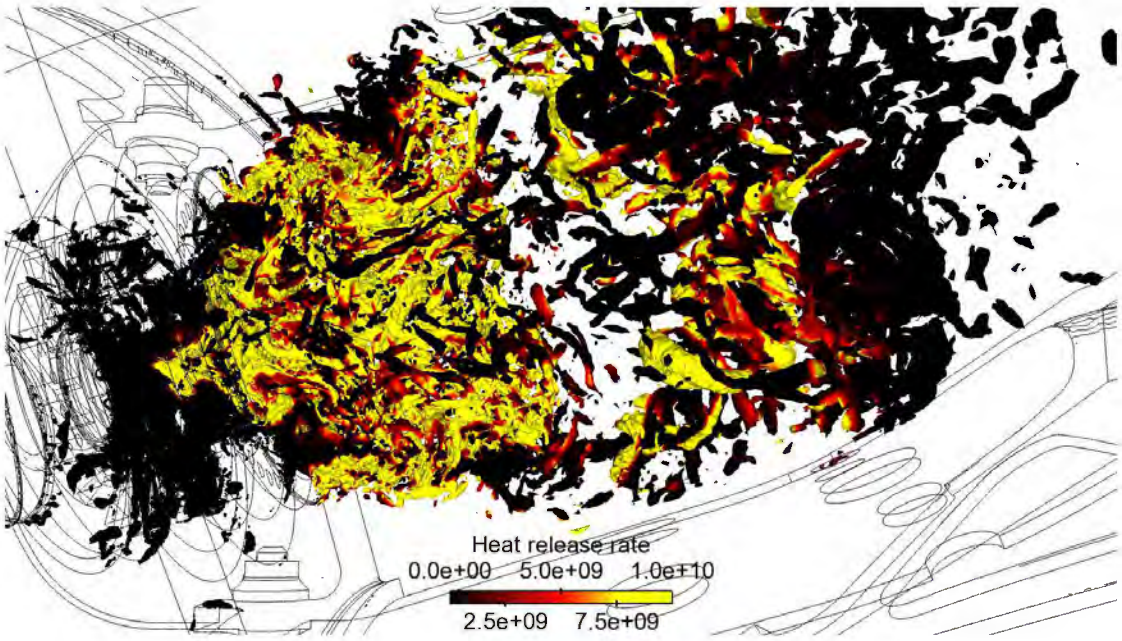

Figure 6.20: Iso-criterion Q ($Q = 10^9$) colored by the heat release rate (W/m^3) at high power

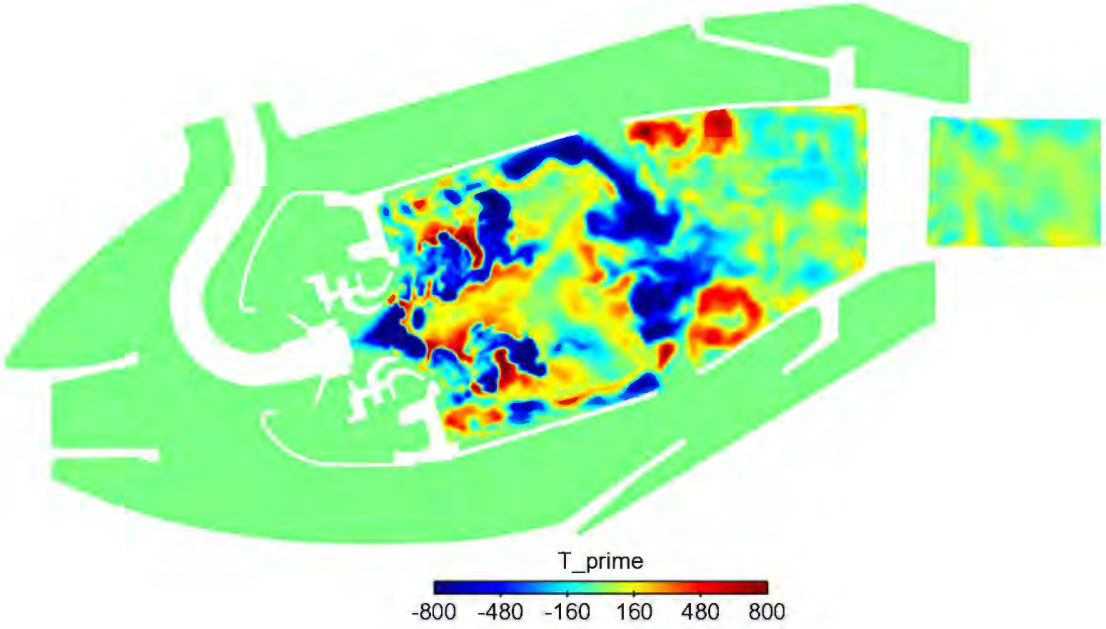

Figure 6.21: Example of instantaneous fluctuating temperature (K) at low power

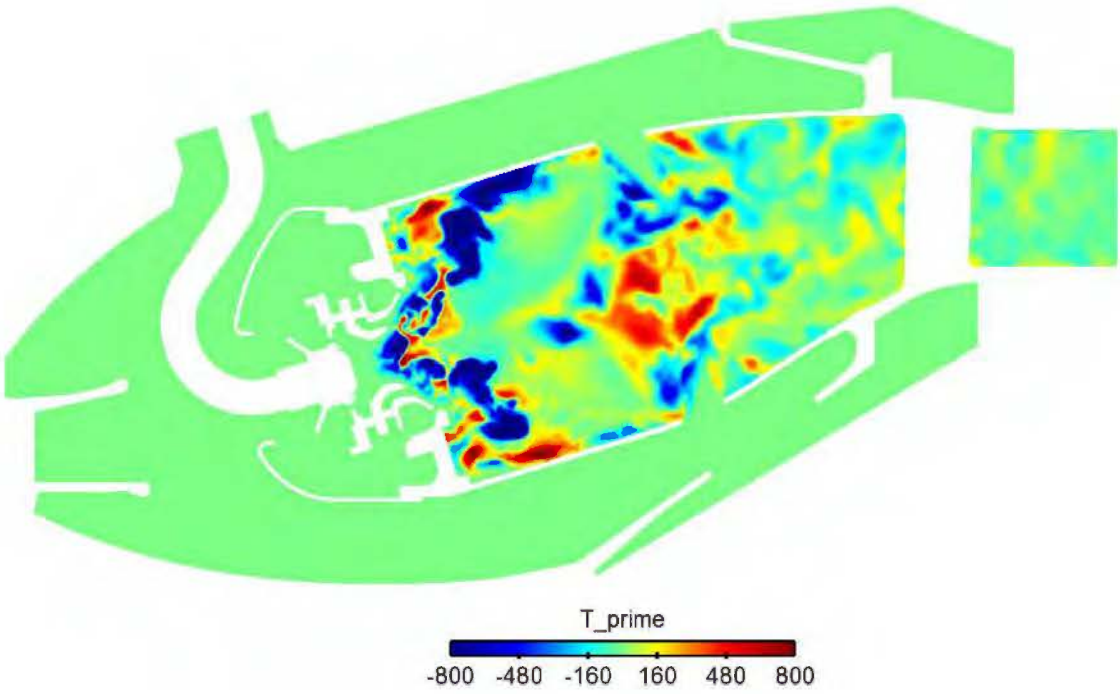

Figure 6.22: Example of instantaneous fluctuating temperature (K) at intermediate power

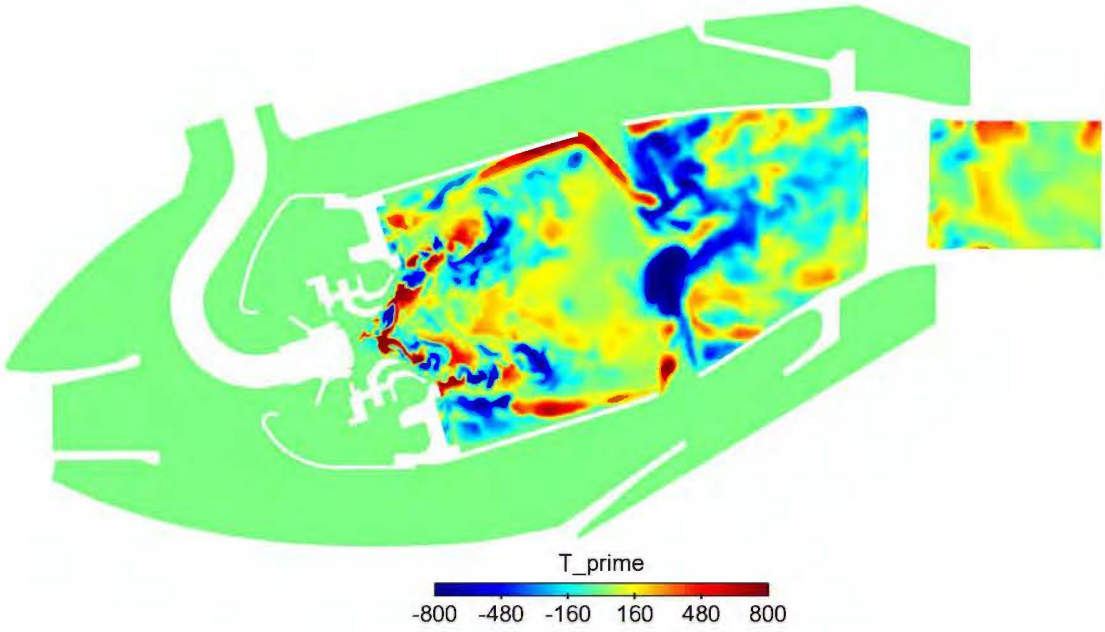

Figure 6.23: Example of instantaneous fluctuating temperature (K) at high power

6.2 Propagation of combustion noise through turbine stages

6.2.1 Extraction of waves from the LES at the combustor exit

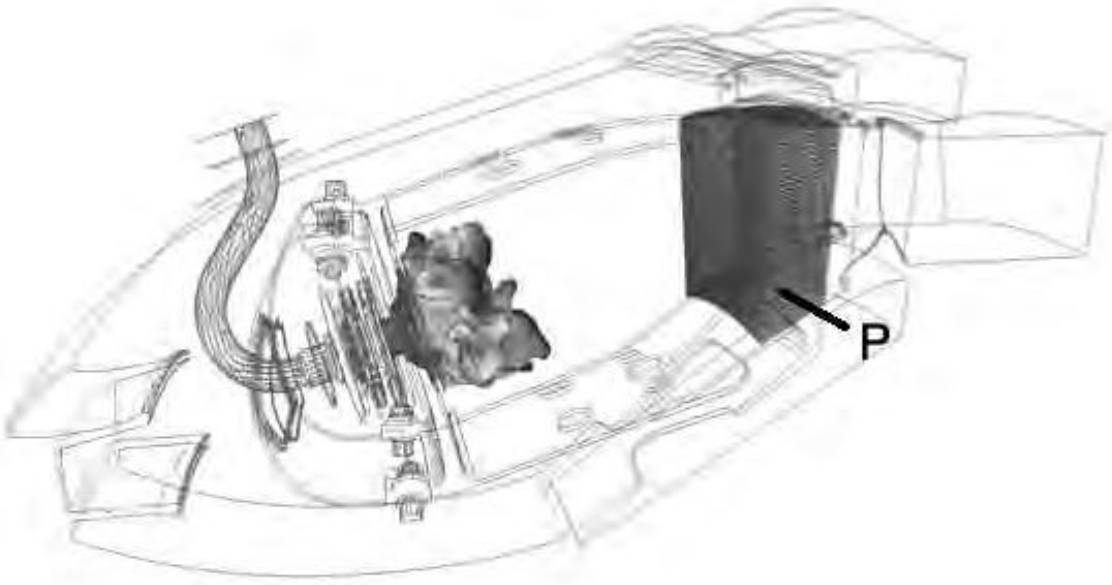

Figure 6.24: Planes used to extract acoustic and entropy waves from LES snapshots

In order to propagate the combustion noise sources in the turbine, fluctuations of pressure and entropy are first extracted in region **P** located one chord before the HPTS as shown in Fig. 6.24. Fluctuations of pressure obtained in the last plane of region **P** and normalized by the mean pressure condition at the outlet of the combustor are plotted for the three operating points in Fig. 6.25(a). The low power case exhibits the higher percentage of pressure fluctuations proportionally to its mean pressure condition (2%), against 1% for the intermediate case and 0.5% for the high power case. However, it must be reminded that the mean pressure condition in the combustion chamber increases with the rise in power-engine regime (10 times higher at high power than at low power), so that pressure fluctuations at high power condition are not lower than at low power condition. Low power and high power cases show similar levels of entropy fluctuation (10% of c_p) while the intermediate case exhibits less amplitude levels (5%). This corroborates the observations made for the temperature fluctuations (Figs. 6.16 and 6.22) where less

temperature spots are generated and a lower amplitude of fluctuation is observed close to the dilution holes.

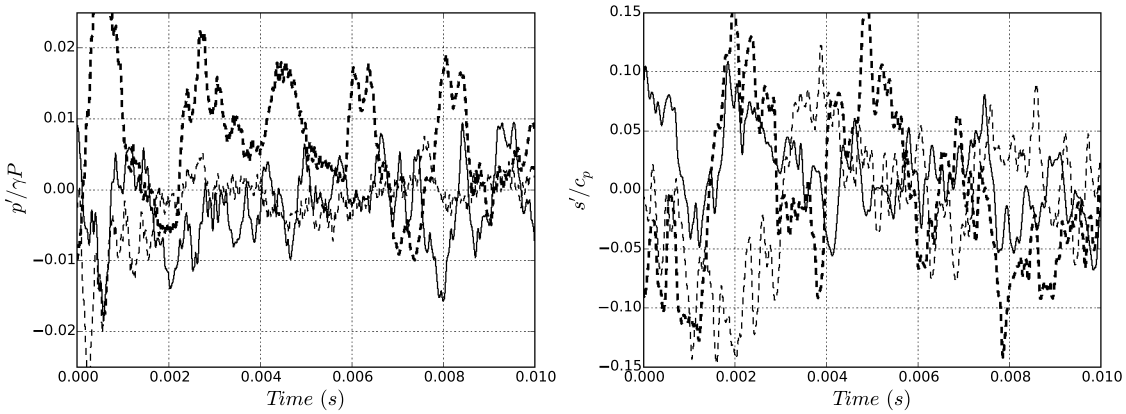

(a) $p'/\gamma p$ (b) s'/c_p

Figure 6.25: a) Dimensionless pressure fluctuations and b) dimensionless entropy fluctuations within the flame tube (last plane of the region **P** in Fig. 6.24) for low power (**- -**), intermediate power (–) and high power conditions (- -).

Using temporal Fourier transform, with Welch windowing and overlapping, the fluctuations extracted in the region **P** are expressed in the frequency domain. In terms of pseudo sound, pressure fluctuation levels in dB, the spectral shape at low and high power conditions is similar (Fig. 6.26). As expected, the broadband noise level increases with an increasing power rating. The peak frequency increases with the increasing engine regime (450 Hz at low power, 550 Hz at high power). At high frequency ($f > 1000$ Hz), a straight attenuation of the noise levels is observed: there is far less combustion noise as expected from the literature. On the contrary, at intermediate power, it seems that the behavior differs from the other operating points. An attenuation of noise at high frequency is observed but the noise levels at high frequency are closer to the noise levels of the high power operating point. At low frequency, the noise levels are closer to the low power case. A bump is also noticeable at 625 Hz. Either this is due to a lack of time convergence or this indicates different sources of noise with the power rise. All simulations have been converged on a simulated physical time of same order, so that this simulation should be sufficiently converged. Moreover, if it was due to a lack of time convergence, the noise levels should be overestimated at low frequency, and that is not consistent with the observations. This is more in agreement with different combustion processes (combustion regime, flame shape) as highlighted in the previous section 6.1.4. The narrow-band bumps could be explained by a strong

thermoacoustic activity at a discrete tone related to the acoustic resonances of the combustor, particularly at low and intermediate power. The discrete tone at which the thermoacoustic coupling occurs can be shifted slightly by the flame response (Dowling and Mahmoudi 2015). Due to the time convergence of the simulations, the frequency resolution achieved is not able to give a precise discrete tone.

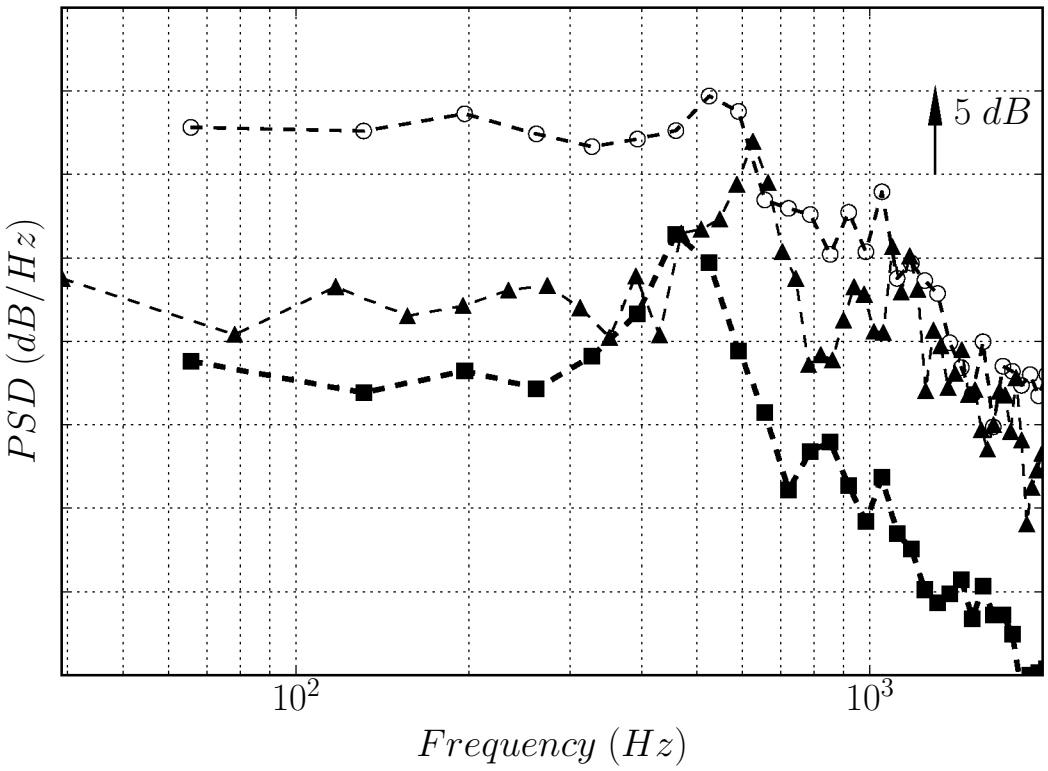

Figure 6.26: Power spectral density of the sound pressure levels within the flame tube (last plane of the region **P** in Fig. 6.24) for low power (■), intermediate power (▲) and high power conditions (○).

A spatial Fourier transform is then applied to decompose the frequency primitive fluctuations into modes for CHORUS as expressed in Eq. 2.78. The new primitive variables $P(m, \omega)$ in terms of frequencies ω and modes m in the last plane of region **P** are presented in the following section.

6.2.1.1 Modal decomposition of the pressure field

In a confined geometry, multiple acoustic modes exist (planar and azimuthal modes) as studied by Karchmer [1983] and Royalty and Schuster [2008]. A planar mode ($m = 0$) is a mode which propagates only axially and is homogeneous in the other directions. The planar acoustic mode can always propagate, while the other acoustic modes ($m > 0$) can only propagate if the frequency is higher than their cut-on frequency, $f_c = mc/(2\pi R)$. If the frequency is lower than this cut-on

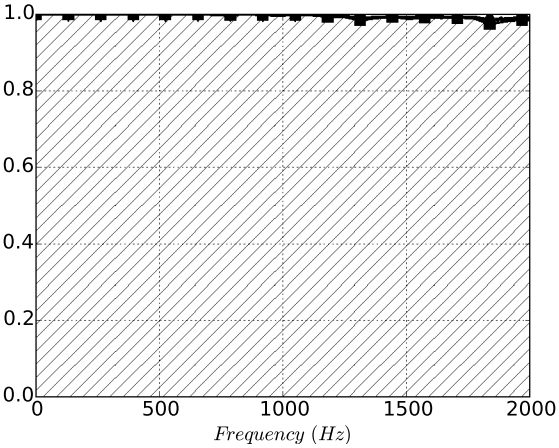

(a) Low power

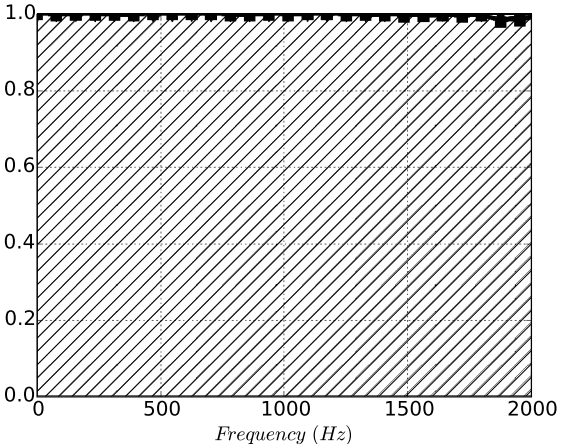

(b) Intermediate power

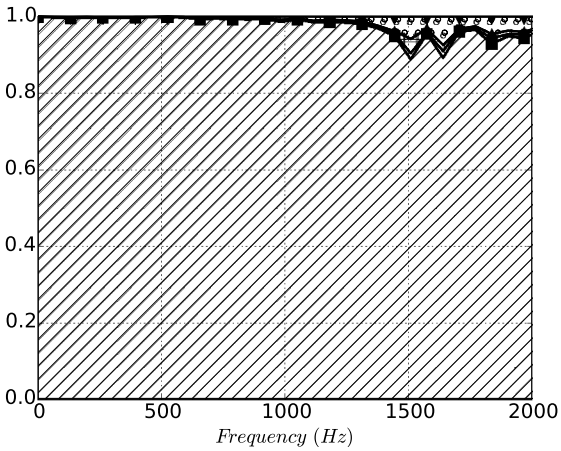

(c) High power

Figure 6.27: Normalized modal PSD of the pressure field at the combustor exit, mode = 0 (■), mode = - $N_{sectors}$ (●), mode = $N_{sectors}$ (▲) and higher modes (▼).

frequency, the mode is evanescent. Therefore the planar mode ($m = 0$) is dominant for frequencies up to the cut-on frequency of the first azimuthal mode pair ($m = \pm 1$). For higher frequencies, the most recent cut-on mode pair dominates the unsteady pressure field. That is to say that successively higher azimuthal modes dominate with increasing frequency.

From the extraction of the pressure field at the outlet of the combustion chamber with CONOCHAIN, a modal decomposition can be obtained to evaluate the normalized power repartition between the different spatial acoustic modes. The modal PSD of the pressure field is plotted in Fig. 6.27 by adding the successive normalized modal contributions $[p'/\gamma P](m, \omega)$ to the precedent one. The first computed CHORUS mode will be $m = 0$ for planar acoustic wave while the first higher modes computed will be $m = -N_{sectors}$ and $m = N_{sectors}$, $N_{sectors}$ being the number of sectors of the complete combustion chamber module. As only one single sector of the combustion chamber has been computed, the acoustic field provided by the LES can only exhibit planar characteristics at low frequency, as shown by Livebardon [2015]. Indeed, the first higher mode which is computed corresponds to the number of sectors of the complete combustion chamber module ($N_{sectors} = 18$). Therefore its cut-on frequency is too high and this mode can not propagate. This is confirmed for the three operating points where the pressure field is mainly carried by the planar mode up to 2000 Hz (the mode $m = 0$ is enough to reach $\sum modes = 1$, without adding other modal contributions).

6.2.1.2 Modal decomposition of the entropy field

As for the pressure field, a modal decomposition of the entropy field at the outlet of the combustor is performed to evaluate the spatial repartition of the power. In Fig. 6.28, unlike the pressure field, the entropy field has a more complex structure. Indeed, the planar mode is not enough to describe precisely the entropy field and azimuthal components are required. An equivalent repartition of power (about 20%) is found between the planar mode and the first azimuthal components $N_{sectors}$ computed and corresponding to the number of sectors. Low power and high power operating points clearly highlight that more power is carried by the planar mode at low frequency, specially around 500 Hz. No dominant peak frequency is observed at intermediate power case, although the power is more distributed on the low frequencies.

Now that the primitive variables have been decomposed into modes and frequencies for CHORUS, the wave decomposition of Eq. 2.34 can be applied to obtain four waves for each plane of region **P**: upstream and downstream propagating acoustic waves and two convective waves (entropy and vorticity). These waves depend also on frequencies and modes. An hydrodynamic filtering (Polifke et al. 2003) considering the wave velocity and the axial spacing between **P** planes

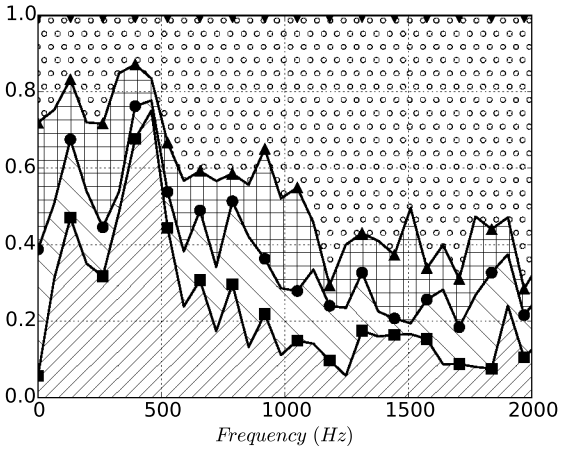

(a) Low power

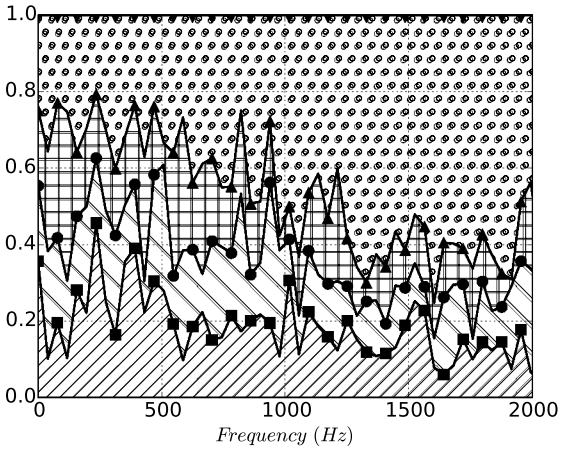

(b) Intermediate power

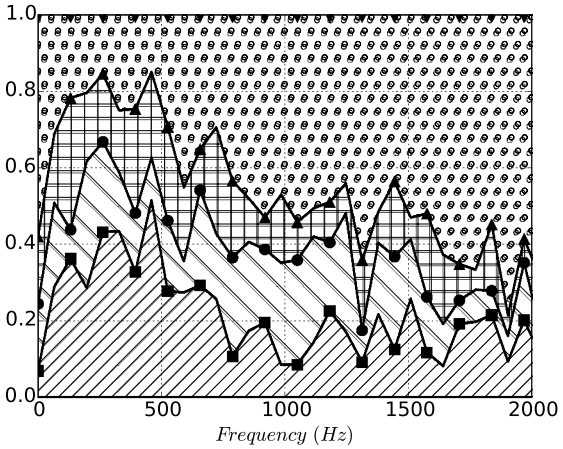

(c) High power

Figure 6.28: Normalized modal PSD of the entropy field at the combustor exit, mode = 0 (■), mode = - $N_{sectors}$ (●), mode = $N_{sectors}$ (▲) and higher modes (▼).

is performed to keep only acoustic pressure. These filtered waves can be now used to compute the generation and propagation of acoustics in the turbine with CHORUS.

6.2.2 Transfer functions through the turbine stages (CHORUS)

CONOCHAIN allows the propagation of higher modes ($m \neq 0$). However, it has been seen that the higher modes are well predicted for $He = m/(N_b - 1) < 0.1$, while $He = 0.5$ for the first higher computed modes $N_{sectors}$. Therefore, only the filtered planar waves (using all **P** planes as explained in section 2.2.2) and the transfer functions of planar modes ($m = 0$) will be investigated in this section. For the planar modes, at 2000 Hz (extreme frequency limit of combustion noise), the most constraining blade row has a Helmholtz number equal to 0.1. Therefore, it is well below the limit of compactness for planar modes ($He < 0.6$) and the planar modes should be well predicted.

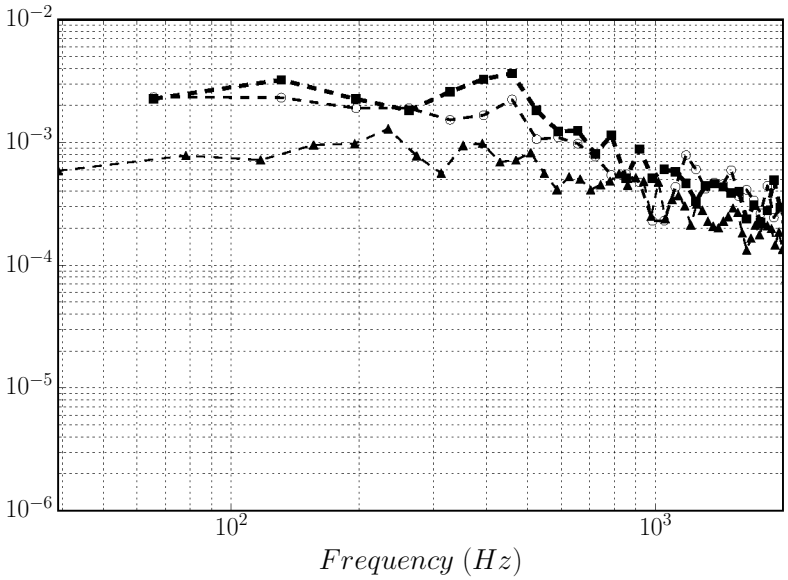

Figure 6.29: Power spectral density of entropy wave amplitude w^s within the flame tube (position **P** in Fig. 6.24) for low power (■), intermediate power (▲) and high power conditions (○).

Filtered planar waves at the inlet boundary condition of the high pressurized turbine are presented in Figs. 6.29, 6.30 and 6.31 for the entropy, vorticity and acoustic planar modes respectively. The acoustic wave should be related to the flame activity whereas, the entropy wave should be related to the temperature fluctuations and the vorticity wave to the turbulent activity in the combustion chamber.

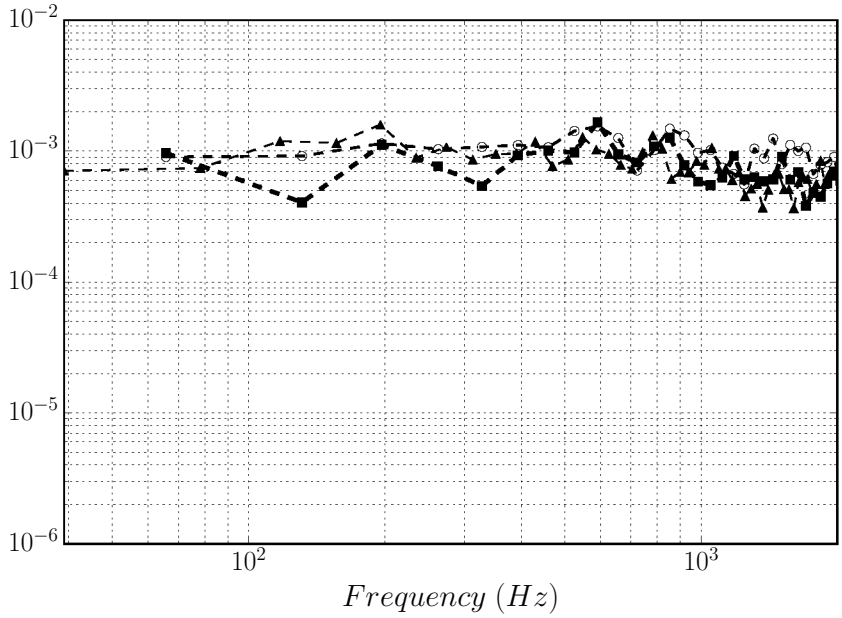

Figure 6.30: Power spectral density of vorticity wave amplitude w^v within the flame tube (position **P** in Fig. 6.24) for low power (■), intermediate power (▲) and high power conditions (○).

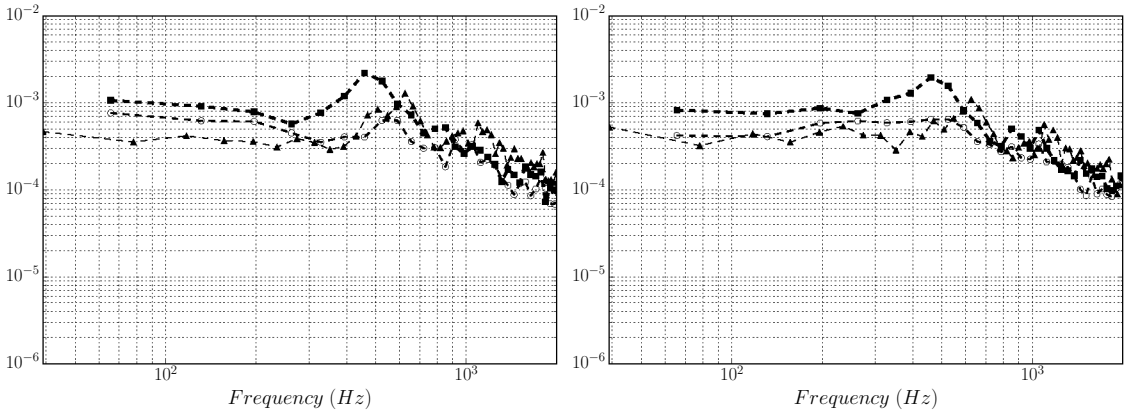

(a) Downstream-propagating acoustic wave w^+ (b) Upstream-propagating acoustic wave w^-

Figure 6.31: Power spectral density of acoustic wave amplitudes $w^{\pm}$ within the flame tube (position **P** in Fig. 6.24) for low power (■), intermediate power (▲) and high power conditions (○).

Using the filtered waves (Polifke et al. 2003) where the hydrodynamic contribution has been retrieved, it is more noticeable that intermediate power case generates less acoustic and entropy proportionally to its mean condition than the other cases (Figs. 6.29 and 6.31). The low power case exhibits a strong acoustic activity around 450 Hz (Fig. 6.31), that is probably linked to a thermoacoustic instability. Same characteristics can be observed for the entropy wave with a broadband peak at the same frequency (Fig. 6.29). Dimensionless vorticity level is of similar magnitude for all operating points in Fig. 6.30 meaning that all operating points have similar turbulent activity.

Now that we know the wave amplitudes at point **P**, upstream of the turbine, we can use CHORUS and predict how these waves will be transmitted through the turbine. To do this, we will use the successive transfer functions which characterize the transmission and reflection coefficients of the turbine blade rows. From these transfer functions, the waves at the outlet of the turbine are obtained in function of the waves extracted at the outlet of the combustion chamber. The transfer functions presented below are obtained with the matrix system detailed in Eq. (2.75) for low, intermediate and high power conditions where unitary waves are considered.

6.2.2.1 Acoustic-to-acoustic transfer functions from CHORUS

The acoustic-to-acoustic transfer function w^+/w^+_{cc} represents the amplitude of the downstream-propagating acoustic wave w^+ normalized by the downstream-propagating acoustic wave w^+_{cc} (combustion chamber exit) at successive rotor blades exit (Fig. 5.4), from $S1$ to $S4$ in Figs. 6.32(a) to 6.35(a). These transfer functions were obtained from Eq. (2.72) to (2.75) using the geometry of each of the turbine stage. The input parameters needed for this are (for each stage):

- the axial chord L_x^{blade},
- the axial spacing between two successive rows L_x,
- the external (R_{ext}) and internal (R_{int}) radii of the row,
- the Mach numbers upstream (M_1) and downstream (M_2) of the row,
- the speeds of sound upstream (c_1) and downstream (c_2) of the row,
- the flow angles upstream (θ_1) and downstream (θ_2) of the row,
- the heat capacity ratios upstream (γ_1) and downstream (γ_2) of the row,
- the rotational speed of the row U,
- and the relaxation rate $\pi = P_{t2}/P_{t1}$ where P_t is the stagnation pressure.

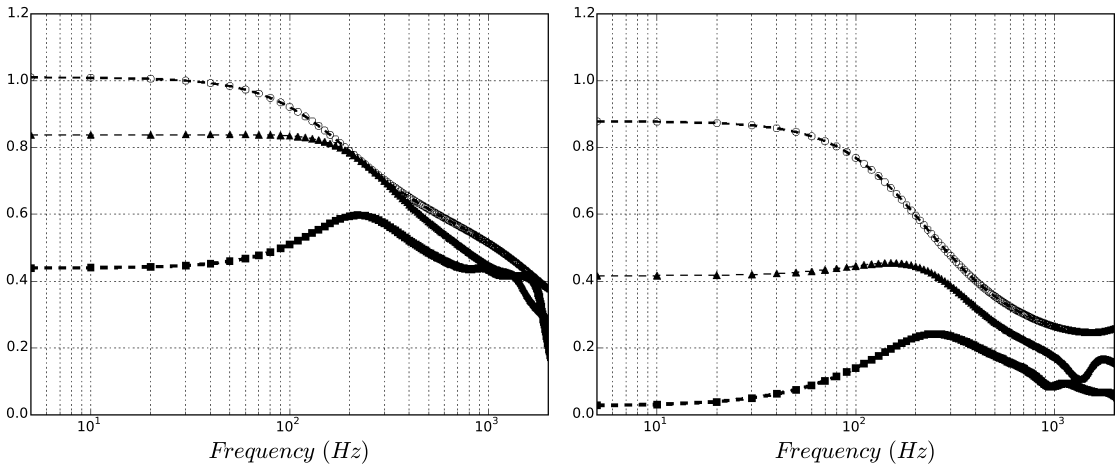

(a) w^+_{S1}/w^+_{cc} (b) w^-_{S1}/w^+_{cc}

Figure 6.32: Analytical acoustic-to-acoustic transfer functions (Eq. 2.75) at position **S1** in Fig. 5.4, for low power (■), intermediate power (▲) and high power conditions (○).

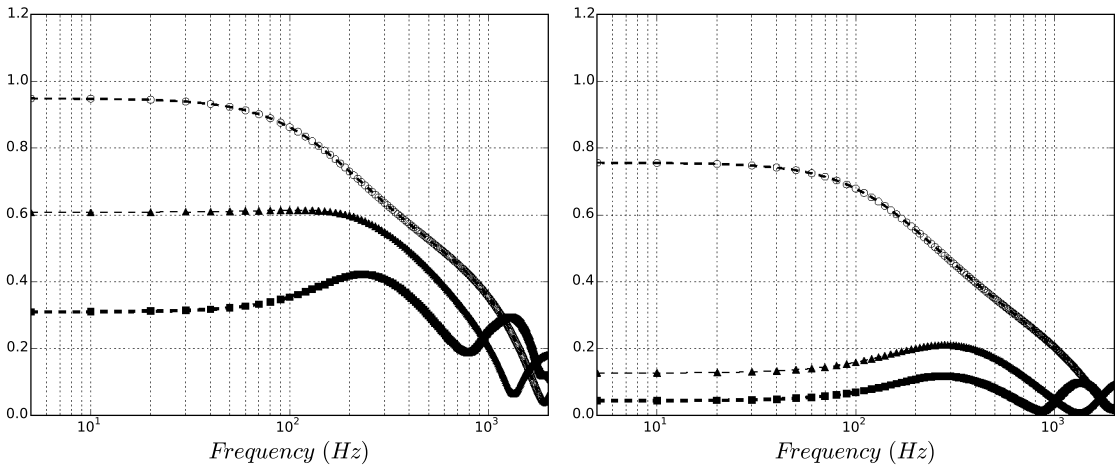

(a) w^+_{S2}/w^+_{cc} (b) w^-_{S2}/w^+_{cc}

Figure 6.33: Analytical acoustic-to-acoustic transfer functions (Eq. 2.75) at position **S2** in Fig. 5.4, for low power (■), intermediate power (▲) and high power conditions (○).

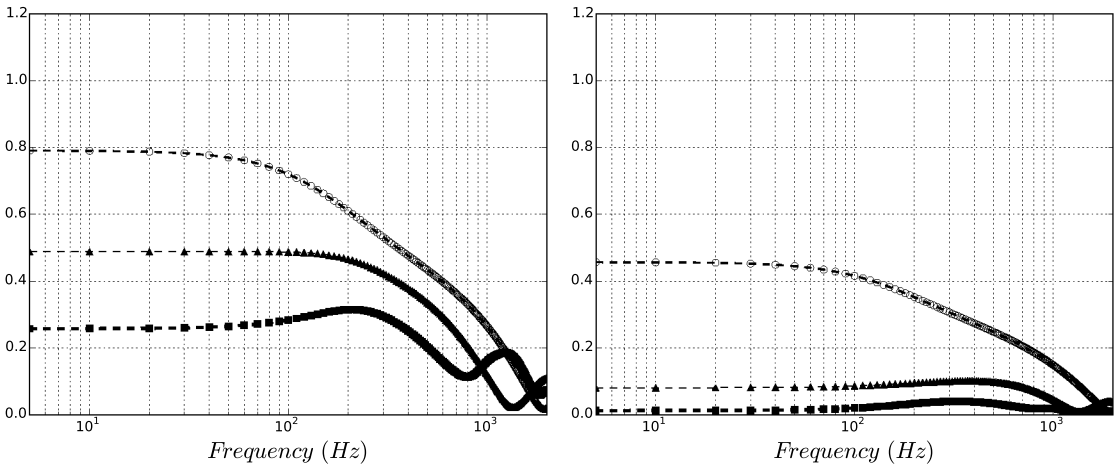

(a) w^+_{S3}/w^+_{cc} (b) w^-_{S3}/w^+_{cc}

Figure 6.34: Analytical acoustic-to-acoustic transfer functions (Eq. 2.75) at position **S3** in Fig. 5.4, for low power (■), intermediate power (▲) and high power conditions (○).

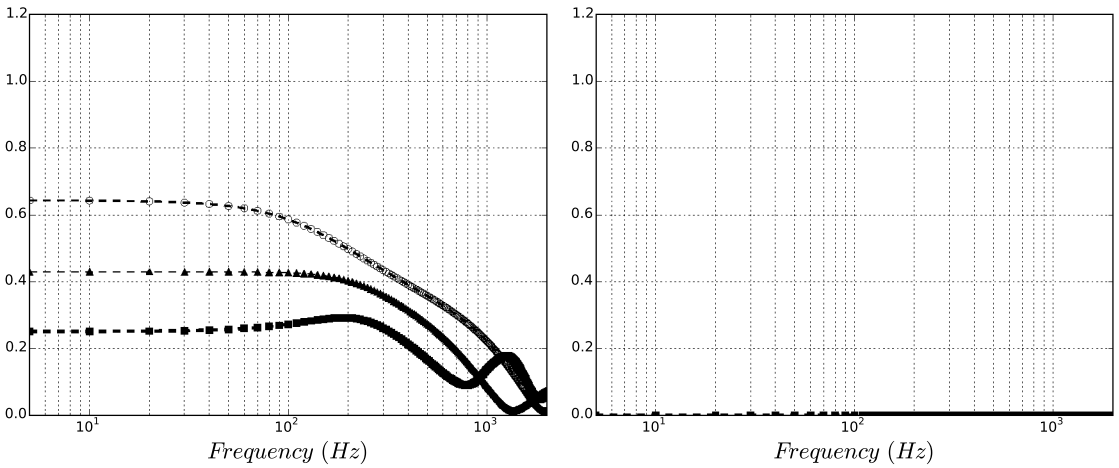

(a) w^+_{S4}/w^+_{cc} (b) w^-_{S4}/w^+_{cc}

Figure 6.35: Analytical acoustic-to-acoustic transfer functions (Eq. 2.75) at position **S4** in Fig. 5.4, for low power (■), intermediate power (▲) and high power conditions (○).

It can be seen that the transmission of acoustic wave is very dependent on the operating point. Moreover the transfer functions are frequency dependent since the resonance between the blade rows is considered. To give an example of the turbine acoustic behavior, the propagation of a non-dimensional acoustic wave of amplitude 1 is looked at 250 Hz. At low power, 60 % of the direct noise generated in the combustion chamber has been transmitted at the exit of the first high pressure turbine stage (stator/rotor) S_1 (Fig. 6.32(a)). At the exit of the next stage S_2, it remains 40 % of direct noise (Fig. 6.33(a)). Going further in the turbine (S_3), the acoustics at the third stage exit represents 30 % of w^+_{cc} (Fig. 6.34(a)). Eventually, less than 25% of the amplitude of the downstream-propagating wave w^+_{cc} has reached the turbine exit (S_4) at 250 Hz (Fig. 6.35(a)). Same analysis can be done at intermediate and high power cases. At the turbine exit, it remains 38% of w^+_{cc} at intermediate power against 45% at high power (Fig. 6.35(a)). Therefore, it can be said that the acoustic turbine attenuation which reduces noise from the high pressure turbine to the low pressure turbine exit is more efficient at low power conditions. In other words, the direct noise transmission capacity increases with an increase of the engine-power.

To explain how this acoustic behavior is dependent on the operating point and on the flow angle upstream (θ_1) and downstream (θ_2) of the blade row, acoustic transfer functions have been plotted in Figs. 6.36 to 6.39 by isolating each blade row of the turbine (positions **B1** to **S4** in Fig. 5.4). As each blade row is isolated, there is no acoustic resonance and so the transfer functions are not dependent on the frequency. At the same Mach number condition, if the deviation angle θ_2 increases then less acoustics is transmitted through the blade row. Meaning that a small change in the deviation angle is enough to modify the acoustic transfer function. If there is no deviation ($\theta_2 = 0$), then there is no reflexion for a stator. These observations are in agreement with the observations made by Leyko et al. [2014]. Moreover, it can be noticed that a rotor has an acoustic transfer function less efficient than a stator and that the upstream flow angle θ_1 will have more impact as the transfer functions are scattered over a wider area (Figs. 6.36(a) and 6.36(b)). For a same blade row, it can be seen that different Mach conditions will induce slightly different deviation angles (red markers), this explains why a same turbine blade row can give different acoustic transfer functions depending on the operating point. Indeed, the deviation angle and the Mach number will differ in function of it. Coupling each turbine acoustic characteristics with the acoustic phase-shift between each row give the transfer functions in Figs. 6.32(a) to 6.35(a).

In the same way, the transfer functions of the upstream-propagating acoustic wave can be obtained in Figs. 6.32(b) to 6.35(b). The transfer functions obtained at the exit of a blade row consider the whole turbine stages. Therefore, w^- is

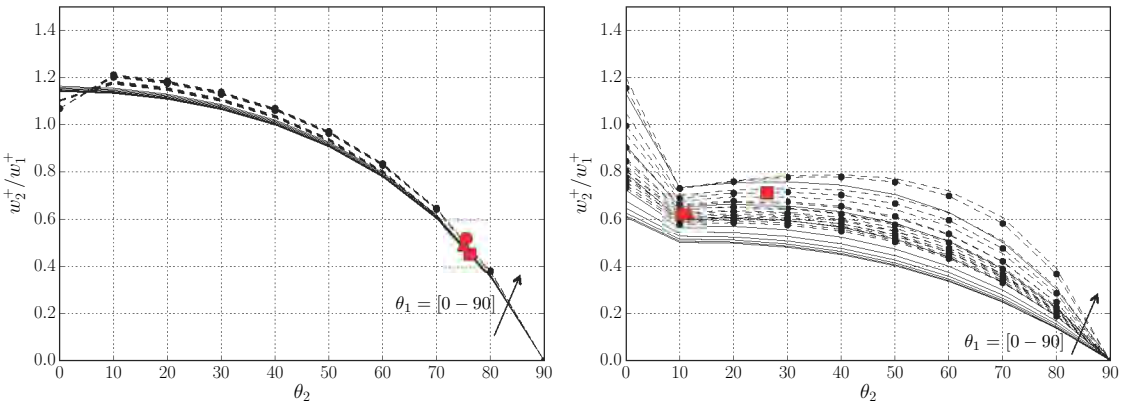

(a) **B1** (b) **S1**

Figure 6.36: Analytical acoustic-to-acoustic transfer functions of each isolated blade row of the first turbine stage (positions **B1** and **S1** in Fig. 5.4) related to the flow angle, for Mach conditions of low power (–), intermediate power (- -) and high power (- ● -), real flow angle conditions of low power (■), intermediate power (▲) and high power (●)

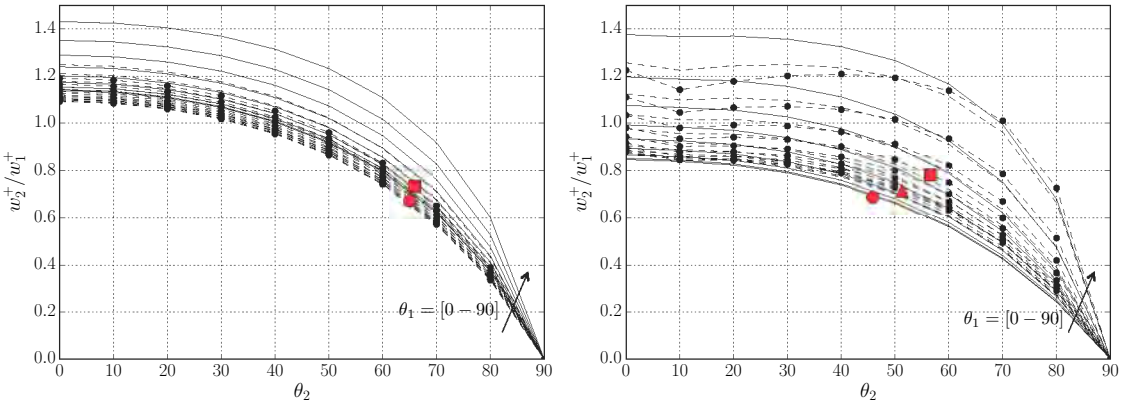

(a) **B2** (b) **S2**

Figure 6.37: Analytical acoustic-to-acoustic transfer functions of each isolated blade row of the second turbine stage (positions **B2** and **S2** in Fig. 5.4) related to the flow angle, for Mach conditions of low power (–), intermediate power (- -) and high power (- ● -), real flow angle conditions of low power (■), intermediate power (▲) and high power (●)

not solely the reflective part of a downstream incident wave at a blade row exit but the contribution of this reflective part and the upstream-propagating wave

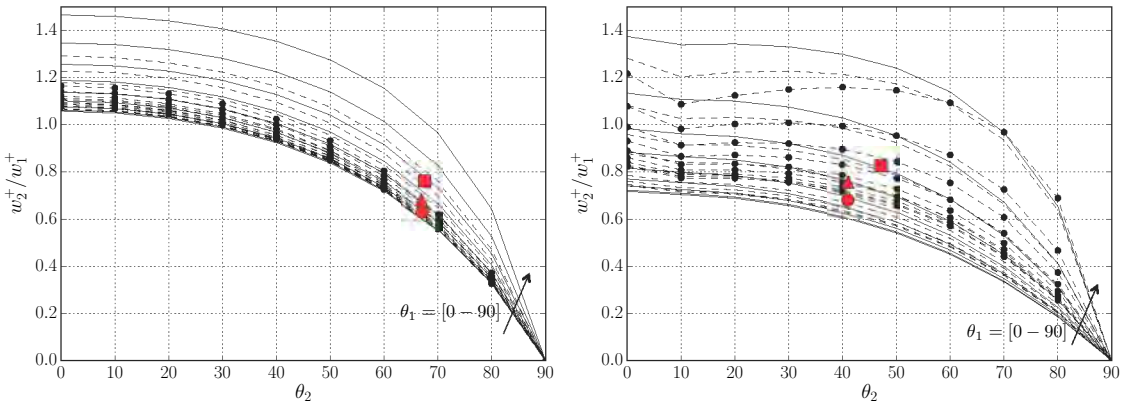

(a) **B3** (b) **S3**

Figure 6.38: Analytical acoustic-to-acoustic transfer functions of each isolated blade row of the third turbine stage (positions **B3** and **S3** in Fig. 5.4) related to the flow angle, for Mach conditions of low power (–), intermediate power (- -) and high power (- ● -), real flow angle conditions of low power (■), intermediate power (▲) and high power (●)

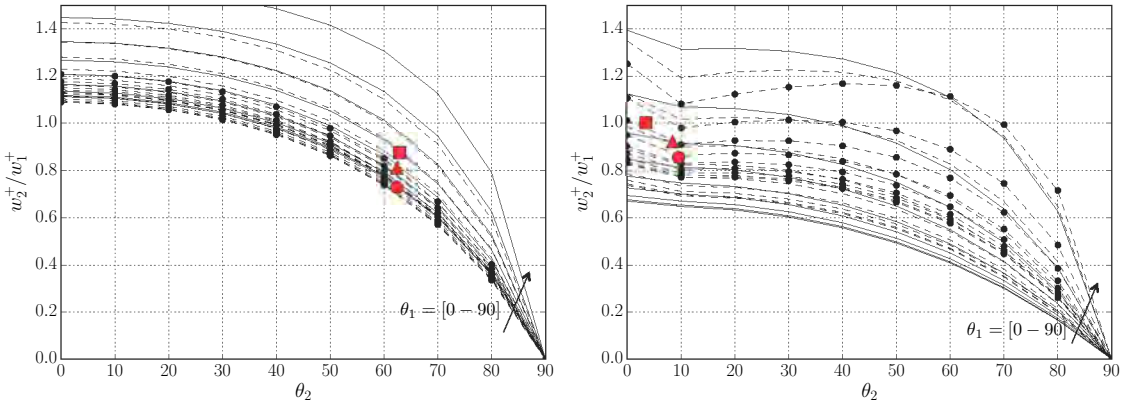

(a) **B4** (b) **S4**

Figure 6.39: Analytical acoustic-to-acoustic transfer functions of each isolated blade row of the last turbine stage (positions **B4** and **S4** in Fig. 5.4) related to the flow angle, for Mach conditions of low power (–), intermediate power (- -) and high power (- ● -), real flow angle conditions of low power (■), intermediate power (▲) and high power (●)

coming from the next blade row. At the end of the low pressure turbine (S_4), it can be noted that no reflected acoustic wave is computed because of the non-

reflecting boundary condition imposed, see section 2.1.4. The reflective capacity of the turbine also increases with the rise of the operating point although the transmission capacity is enhanced.

6.2.2.2 Entropy-to-acoustic transfer functions

The entropy-to-acoustic transfer functions w^+/w^s_{cc} represents the amplitude of the downstream-propagating acoustic wave w^+ normalized by the entropy wave w^s_{cc} (combustion chamber exit) at successive rotor blades exit (Fig. 5.4), from $S1$ to $S4$ in Figs. 6.40 to 6.43. Again, the difference between each operating point can be noticed. Considering non-dimensional waves, the generation of acoustics from entropy waves can be evaluated. To explain the acoustic behavior of the turbine, the propagation of an entropy wave of unitary amplitude is observed at 250 Hz for the low power case. At the outlet of the first turbine stage S_1 (stator/rotor), the entropy wave w^s_{cc} generates an acoustic wave w^-_{S1} of about 9 % of its amplitude (Fig. 6.40(a)). This acoustic wave w^-_{S1} continues to propagate towards the outlet of the second turbine stage S_2 (Fig. 6.41(a)). However, an acoustic wave of lower amplitude is observed (7.5 % of w^s_{cc}). This means that either the acoustics has been attenuated or has been reflected. By looking at the exit of this turbine stage (Fig. 6.40(b)), the existence of an upstream acoustic wave w^-_{S2} is highlighted. This upstream acoustic wave is composed of two contributions. The first contribution is a part of the upstream acoustic wave w^-_{S3} coming from the third turbine stage S_3 (Fig. 6.42(b)). To this contribution is added the reflected part of the downstream acoustic wave arriving at the exit of the second stage S_2. The upstream acoustic wave w^-_{S2} continues to propagate towards the turbine inlet and its contribution is added to the reflective wave at the outlet of the first stage S_1 (Fig. 6.40(b)). The upstream-propagating acoustic wave w^-_{S1} is composed of all the contributions of the reflective waves at the successive blade rows and represents 4 % of w^s_{cc}. Going further towards the turbine exit S_4, the amplitude of the acoustic wave generated by the entropy wave continues to be attenuated and finally reaches an amplitude of 5 % of w^s_{cc} (Fig. 6.43(a)). Same observations can be done for the intermediate power case but with higher coefficients of transmission and reflection. For instance at 250 Hz, the entropy wave generates an acoustic wave of about 18 % its amplitude at the first turbine stage exit S_1 (Fig. 6.40(a)). This acoustic wave propagates towards the turbine exit with an amplitude of about 13 % of w^s_{cc}, while a reflective wave with an amplitude of 8 % w^s_{cc} reaches the first stage exit. The high power case exhibits a different behavior. Indeed, indirect noise is mainly generated at the first turbine stage and then attenuated across the last turbine stages for the low and intermediate power cases.

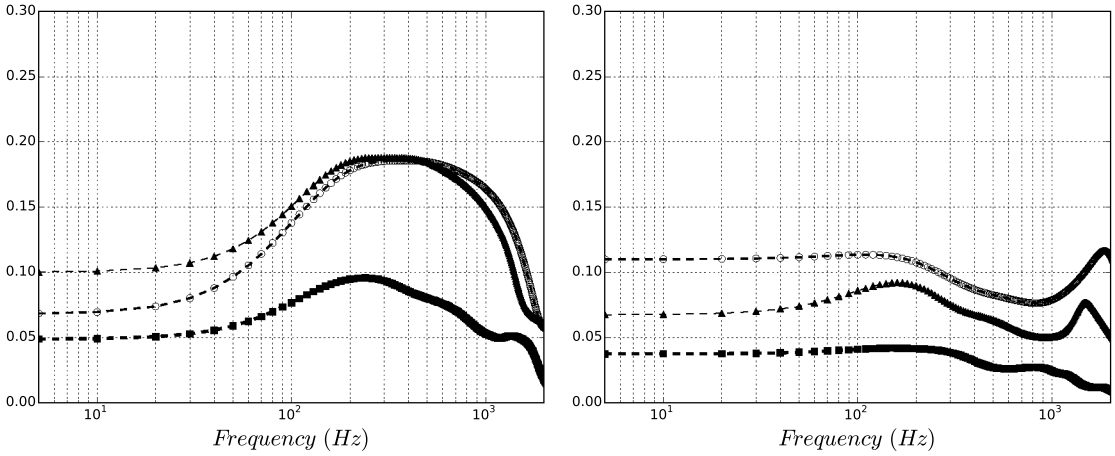

(a) w^{+}_{S1}/w^{s}_{cc} (b) w^{-}_{S1}/w^{s}_{cc}

Figure 6.40: Analytical entropy-to-acoustic transfer functions (Eq. 2.75) at position **S1** in Fig. 5.4, for low power (■), intermediate power (▲) and high power conditions (○).

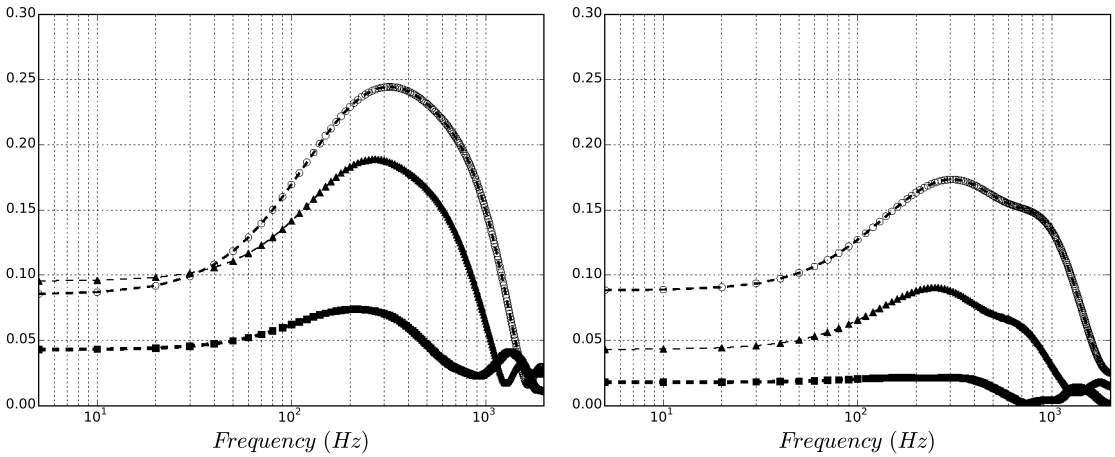

(a) w^{+}_{S2}/w^{s}_{cc} (b) w^{-}_{S2}/w^{s}_{cc}

Figure 6.41: Analytical entropy-to-acoustic transfer functions (Eq. 2.75) at position **S2** in Fig. 5.4, for low power (■), intermediate power (▲) and high power conditions (○).

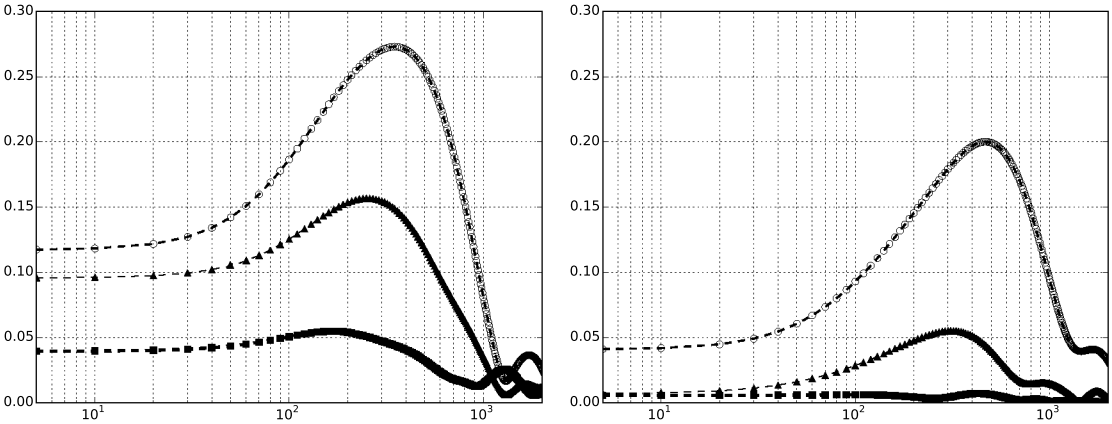

(a) w^+_{S3}/w^s_{cc} (b) w^-_{S3}/w^s_{cc}

Figure 6.42: Analytical entropy-to-acoustic transfer functions (Eq. 2.75) at position **S3** in Fig. 5.4, for low power (■), intermediate power (▲) and high power conditions (○).

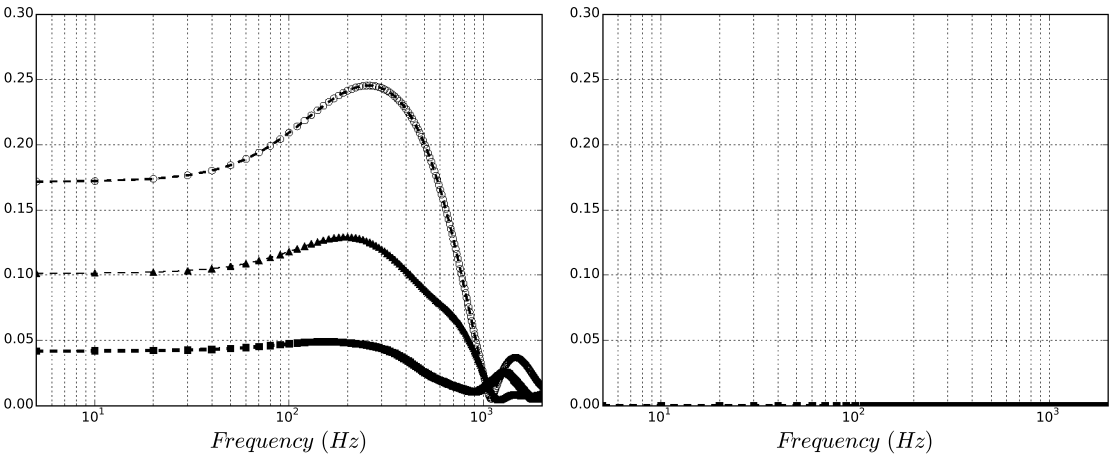

(a) w^+_{S4}/w^s_{cc} (b) w^-_{S4}/w^s_{cc}

Figure 6.43: Analytical entropy-to-acoustic transfer functions (Eq. 2.75) at position **S4** in Fig. 5.4, for low power (■), intermediate power (▲) and high power conditions (○).

On the contrary, in the high power case, indirect noise is still generated in the next turbine stages. For an entropy wave of same unitary amplitude, higher amplitude levels of indirect noise are obtained. For instance at 250 Hz, a unitary entropy wave generates an acoustic wave of 18 % its amplitude at the exit of the first turbine stage S_1. This acoustic wave propagates towards the second turbine stage exit S_2 where strong acoustic reflections occur (17 % of w^s_{cc}) as shown in Fig. 6.41(b). However, the contribution of acoustics generated at the second stage is added, so that the downstream-propagating acoustic wave w^+_{S2} has an amplitude level of 24 % of w^s_{cc}. The acoustic wave amplitude increases (27 % of w^s_{cc}) at the exit of the third turbine stage S_3 (Fig. 6.42(a)) to finally be attenuated at the last turbine stage exit S_4. Still, entropy wave at the outlet of the combustor generates an acoustic wave with an amplitude of about 25 % of w^s_{cc} at the turbine exit.

Once again, acoustic characteristics of the turbine can be obtained as function of the flow angles θ_1 and θ_2 in Figs. 6.44 to 6.47 by isolating each blade row of the turbine (positions **B1** to **S4** in Fig. 5.4). Only the null frequency has been investigated for simplicity. For a stator, at same Mach number condition, if the deviation angle θ_2 increases then less indirect noise is generated through the blade row. In the same way, by decreasing the Mach number, the capacity of a blade row to generate indirect noise is lower. Therefore, the high power case generates much more indirect noise than the low power case (Fig. 6.44(a)). For a rotor, a particular behavior can be observed. Overall, a rotor generates less indirect noise than a stator (Figs. 6.44(a) and 6.44(b)). As for a stator, the increase of the Mach number induces more acoustics generated through the blade row. However, the capacity of a rotor to generate indirect noise will increase for downstream flow angles up to $40° - 50°$ whereas, less indirect noise will be generated for bigger flow angles. Coupling each turbine acoustic characteristics with the acoustic phase-shift between each row give the transfer functions in Figs. 6.32(a) to 6.35(a).

To summarize, for an entropy wave of same amplitude extracted at the outlet of the combustion chamber, the turbine will exhibit different acoustic characteristics depending on the operating point. With an increase of the engine power, higher velocity magnitude are obtained in the turbine stages. Therefore, more indirect noise is generated and propagates towards the turbine exit, even if noise reflection is also more important.

The transfer functions are obtained considering the attenuation of the entropy planar wave amplitudes. From Fig. 6.48, it can be seen that the attenuation of the entropy wave w^s_{cc} increases with the successive blade rows and the increase in frequency. It can also be noticed that this attenuation is stronger at lower power. Indeed, at 500 Hz, it remains less than 70% of the initial entropy wave w^s_{cc} (Fig. 6.48(a)) at the outlet of the low pressure turbine, against 90% for intermediate power (Fig. 6.48(b)) and 98% for high power (Fig. 6.48(c)). The attenuation of

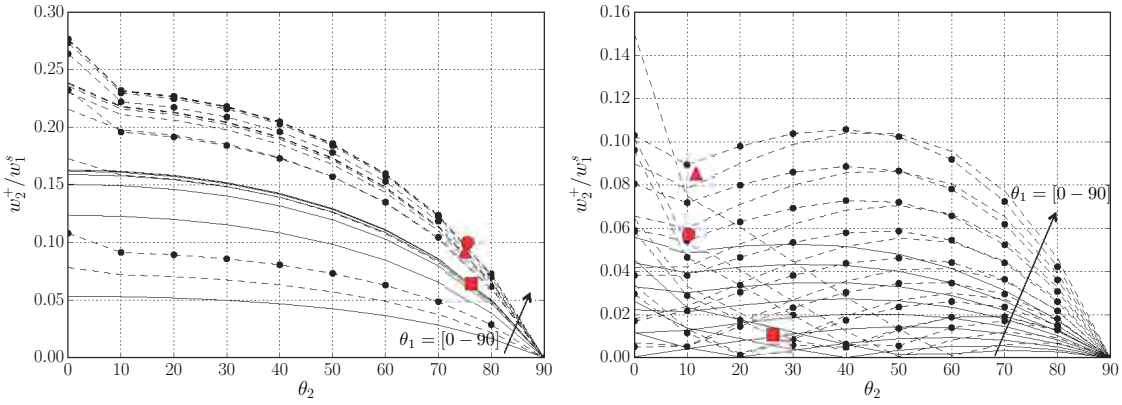

(a) **B1** (b) **S1**

Figure 6.44: Analytical entropy-to-acoustic transfer functions of each isolated blade row of the first turbine stage (positions **B1** and **S1** in Fig. 5.4) related to the flow angle, for Mach conditions of low power (–), intermediate power (- -) and high power (- ● -), real flow angle conditions of low power (■), intermediate power (▲) and high power (●)

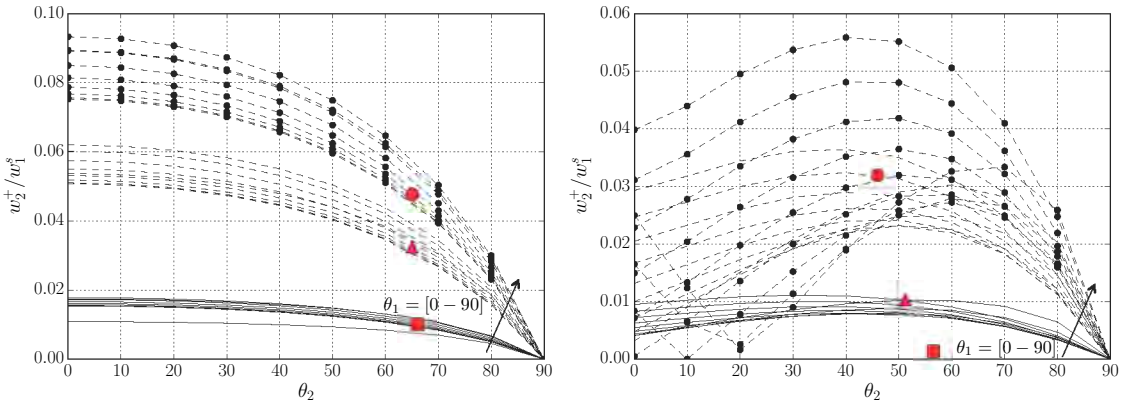

(a) **B2** (b) **S2**

Figure 6.45: Analytical entropy-to-acoustic transfer functions of each isolated blade row of the second turbine stage (positions **B2** and **S2** in Fig. 5.4) related to the flow angle, for Mach conditions of low power (–), intermediate power (- -) and high power (- ● -), real flow angle conditions of low power (■), intermediate power (▲) and high power (●)

the entropy planar wave amplitudes is described by Eq. (2.53). In this equation, the time delay of the entropy particles is dependent on the axial velocity profile

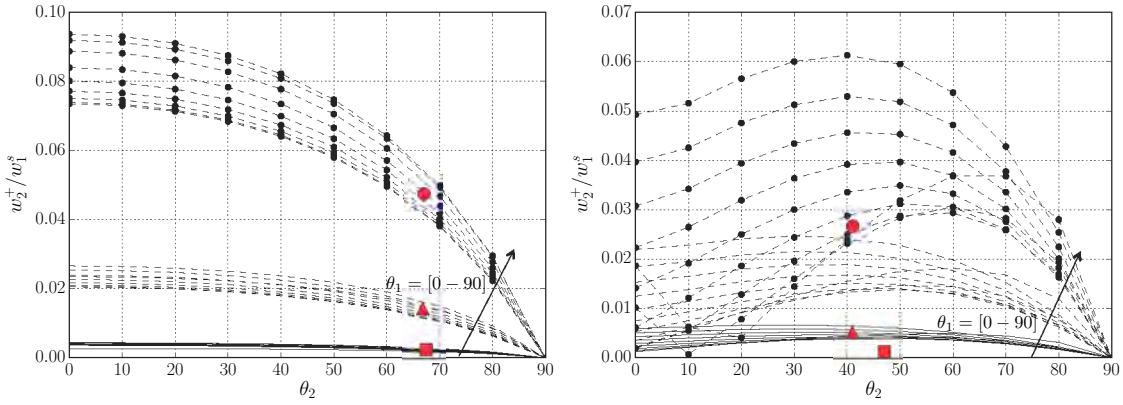

(a) **B3** (b) **S3**

Figure 6.46: Analytical entropy-to-acoustic transfer functions of each isolated blade row of the third turbine stage (positions **B3** and **S3** in Fig. 5.4) related to the flow angle, for Mach conditions of low power (–), intermediate power (- -) and high power (- ● -), real flow angle conditions of low power (■), intermediate power (▲) and high power (●)

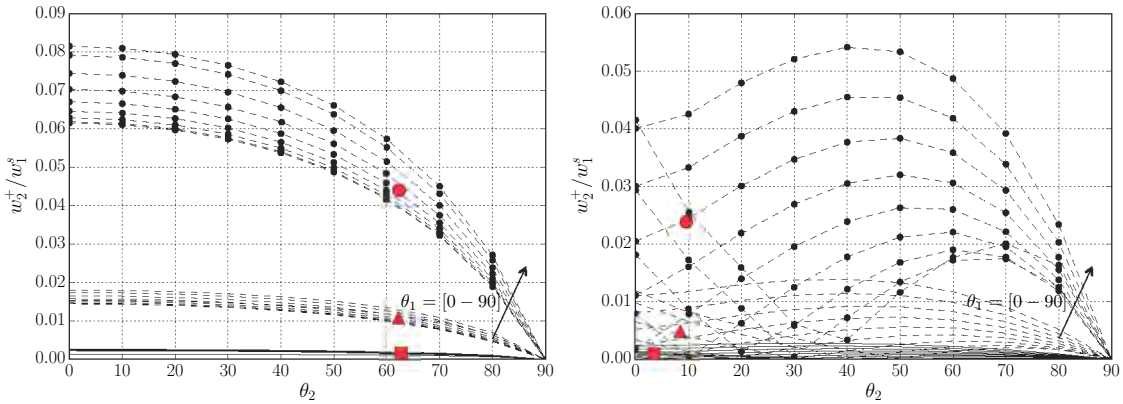

(a) **B4** (b) **S4**

Figure 6.47: Analytical entropy-to-acoustic transfer functions of each isolated blade row of the last turbine stage (positions **B4** and **S4** in Fig. 5.4) related to the flow angle, for Mach conditions of low power (–), intermediate power (- -) and high power (- ● -), real flow angle conditions of low power (■), intermediate power (▲) and high power (●)

in the blade vane. By looking at the evolution of the Mach number through the turbine (Fig. 6.49), it can be noticed that attenuation of entropy wave is most

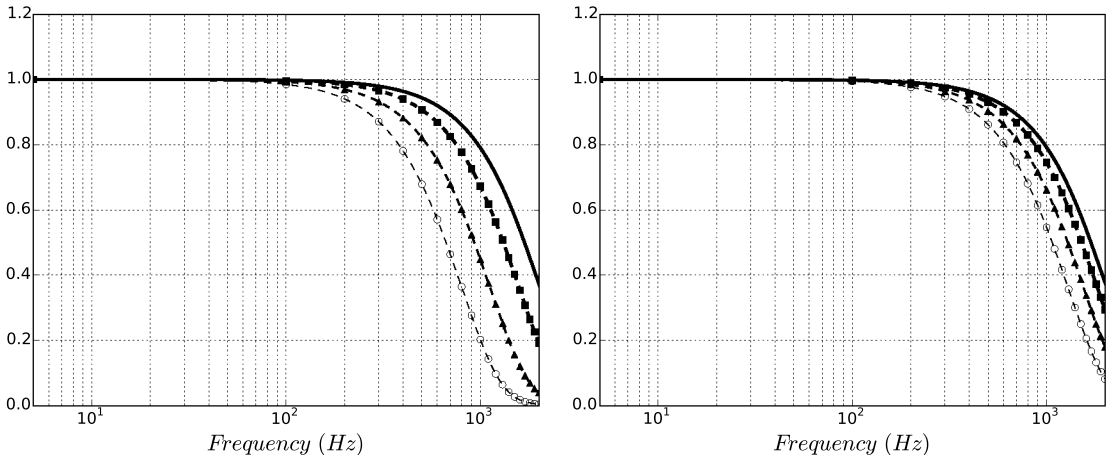

(a) Low power

(b) Intermediate power

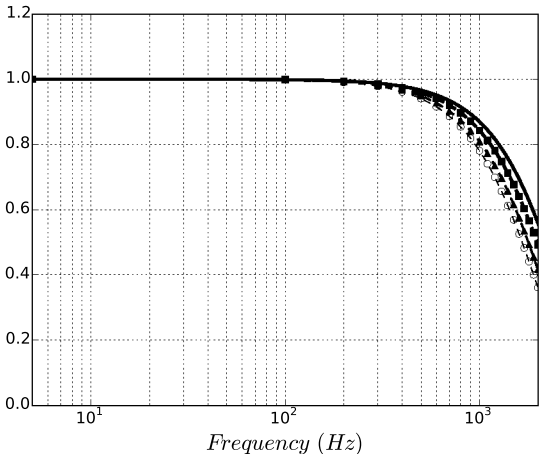

(c) High power

Figure 6.48: Analytical entropy-to-entropy transfer functions w^s/w^s_{cc} at positions **S1** (–), **S2** (■), **S3** (▲) and **S4** (○) in Fig. 5.4.

important for phase of flow acceleration in the stator whereas entropy amplitudes are much less attenuated when the flow is decelerated through the rotor. The model for the entropy attenuation could be improved with stator/rotor simulation where streamlines are extracted to obtain the good attenuation of the entropy wave (Becerril 2017).

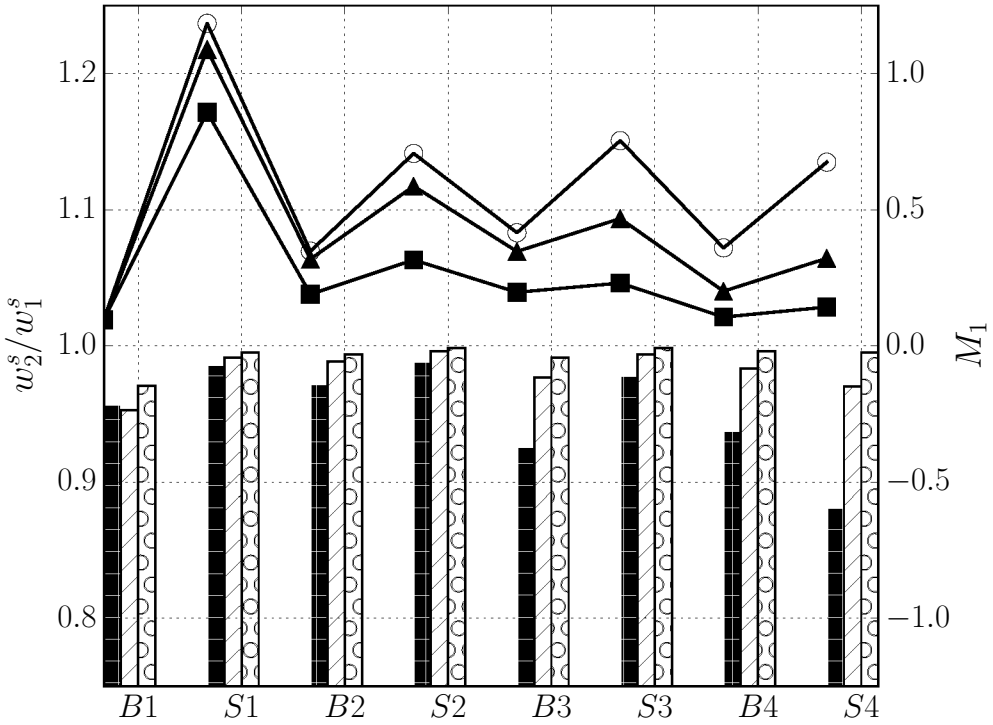

Figure 6.49: Transfer function of the entropy wave (w_2^s/w_1^s) across each turbine blade row (Fig. 5.4) at 500 Hz, for low power (■), intermediate power (//) and high power conditions (○) . Evolution of the Mach number across the turbine, for low power (■), intermediate power (▲) and high power conditions (○).

6.2.2.3 Vorticity-to-acoustic transfer functions

The vorticity-to-acoustic transfer functions w^+/w_{cc}^v represents the amplitude of the downstream-propagating acoustic wave w^+ normalized by the vorticity wave w_{cc}^v (combustion chamber exit) at successive rotor blades exit (Fig. 5.4), from $S1$ to $S4$ in Figs. 6.50 to 6.53. Their magnitudes are less than 10^{-7}, meaning that the vorticity waves are strongly damped in the turbine stages as it was shown by Livebardon [2015]. Nevertheless, some vortex noise generations are not considered in these transfer functions. The noise generation induced by the blade-vortex interaction which is known to be out of the frequency range of interest is not taken into account. Moreover, additional vorticity can be created by the acceleration and deviation of entropy and acoustic waves (Palies et al. 2011; Duran and Morgans 2015).

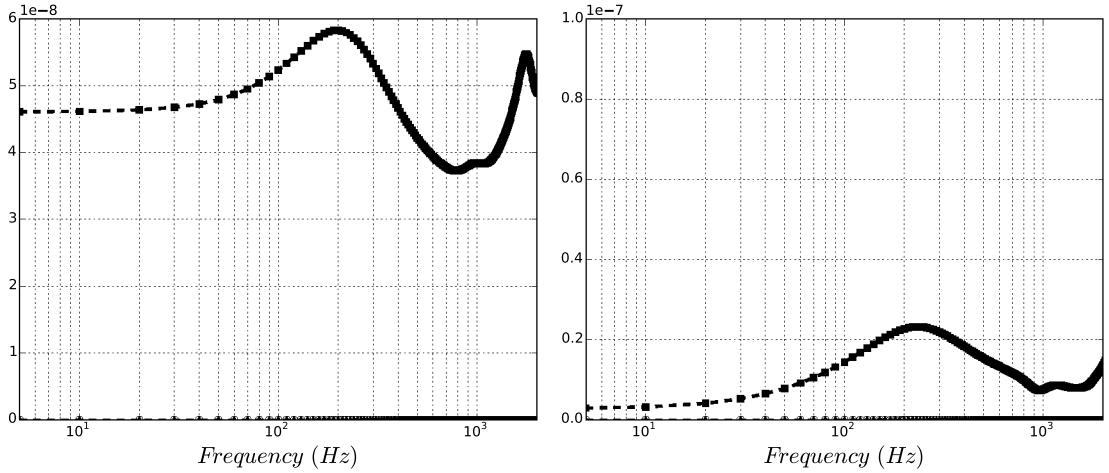

(a) w^{+}_{S1}/w^{v}_{cc} (b) w^{-}_{S1}/w^{v}_{cc}

Figure 6.50: Analytical vorticity-to-acoustic transfer functions (Eq. 2.75) at position **S1** in Fig. 5.4, for low power (■), intermediate power (▲) and high power conditions (○).

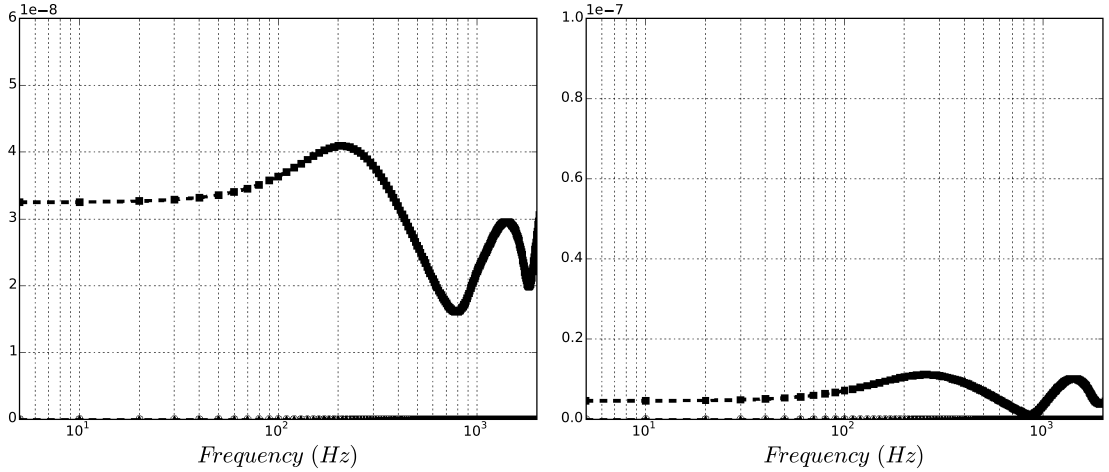

(a) w^{+}_{S2}/w^{v}_{cc} (b) w^{-}_{S2}/w^{v}_{cc}

Figure 6.51: Analytical vorticity-to-acoustic transfer functions (Eq. 2.75) at position **S2** in Fig. 5.4, for low power (■), intermediate power (▲) and high power conditions (○).

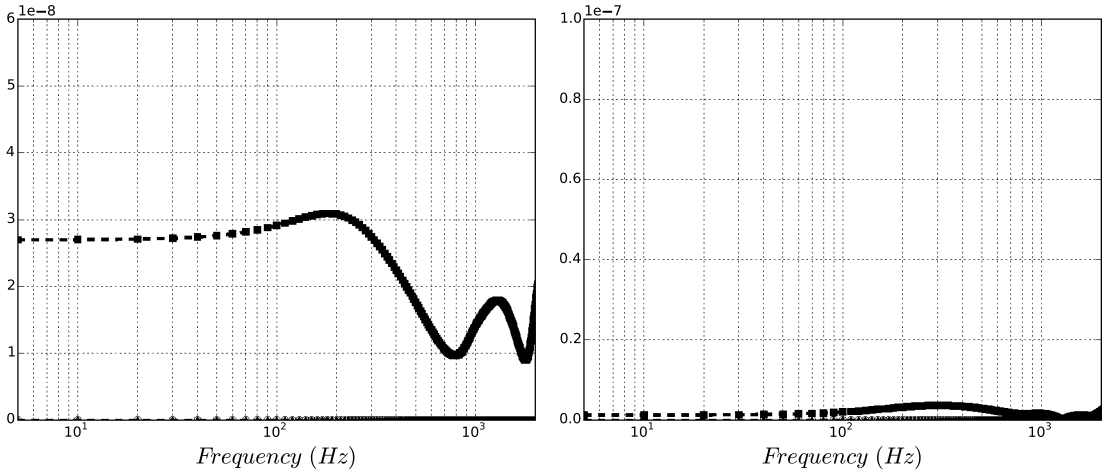

(a) w^{+}_{S3}/w^{v}_{cc} (b) w^{-}_{S3}/w^{v}_{cc}

Figure 6.52: Analytical vorticity-to-acoustic transfer functions (Eq. 2.75) at position **S3** in Fig. 5.4, for low power (■), intermediate power (▲) and high power conditions (○).

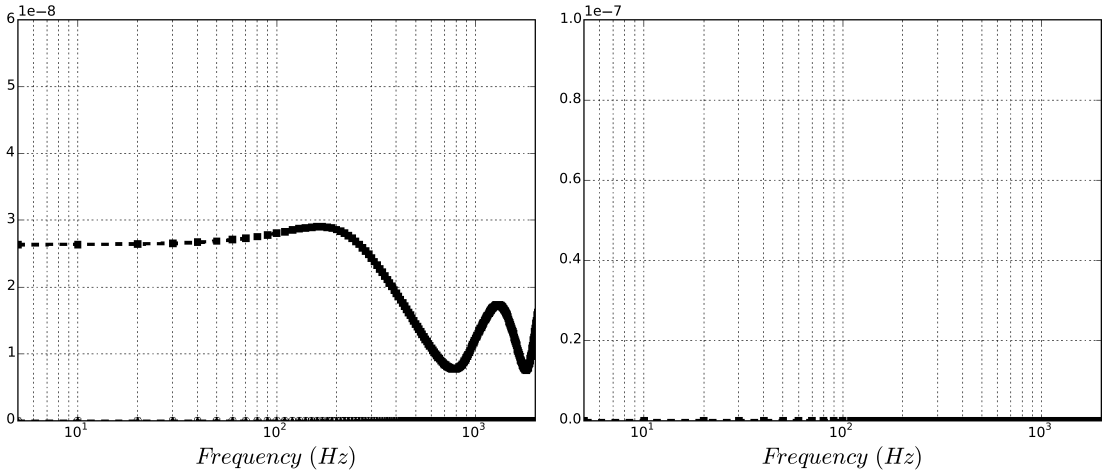

(a) w^{+}_{S4}/w^{v}_{cc} (b) w^{-}_{S4}/w^{v}_{cc}

Figure 6.53: Analytical vorticity-to-acoustic transfer functions (Eq. 2.75) at position **S4** in Fig. 5.4, for low power (■), intermediate power (▲) and high power conditions (○).

The acoustic characteristics of the two turbines have been described with transfer functions which give the reflection and transmission coefficients of each blade row. The ability of the turbine to produce indirect noise and to propagate both direct and indirect noise has been highlighted. For waves of same amplitude at the inlet of the turbine, it has been seen that the acoustic behavior of the turbine is frequency dependent and different according to the operating conditions.

Combining the transfer functions with the acoustic, entropy and vorticity waves presented in the beginning of the section, the propagation of direct and indirect noise through a complete turbine can be evaluated quantitatively for each operating point. However, as the vorticity noise generation is not important for the planar mode according to the computed transfer functions, it is not considered thereafter.

6.2.3 Acoustic power in turbine stages

6.2.3.1 Indirect and direct noise across the turbines

Acoustic and entropy waves extracted at the exit of the combustor, w^+_{cc} and w^s_{cc}, are propagated through the turbine stages by means of the CHORUS transfer functions presented in section 6.2.2. The distribution of direct and indirect noise is obtained at the outlet of each i^{th} row of the turbine for low power case in Fig. 6.54:

$$w^+_{i\_direct} = \frac{w^+_i}{w^+_{cc}} \times w^+_{cc} \tag{6.4}$$

$$w^+_{i\_indirect} = \frac{w^+_i}{w^s_{cc}} \times w^s_{cc} \tag{6.5}$$

Power losses occur through the turbine stages due to acoustic turbine attenuation as observed in Fig. 6.54 for the low power case. This acoustic attenuation is more important in the first stages where the pressure and velocity gradients are strong as the flow is accelerated. Since the velocity gradient is more important in the first stage, most of the indirect noise is generated there. Moreover, due to the distortion of the entropy wave, the entropy planar mode is scattered into higher azimuthal modes. Therefore, the planar entropy fluctuation amplitude is attenuated when crossing the successive blade rows. Less indirect noise is generated and its propagation is attenuated across the turbines.

For all CHORUS computations, it is assumed that the entropy planar modes are not in phase sector-by-sector. A random phase-shift is considered as done by Livebardon et al. [2016]. Indeed, for a 360° full-annular combustor, Livebardon et al. [2016] shows that the overall signal level of indirect noise is lower compared

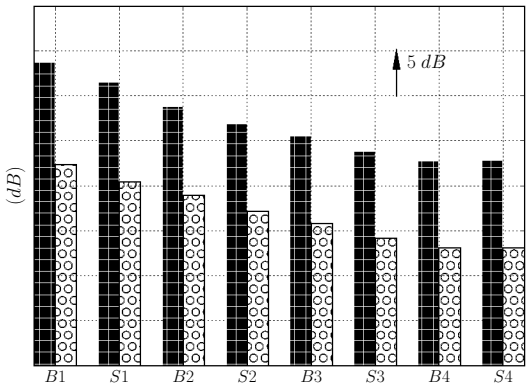

(a) Low power

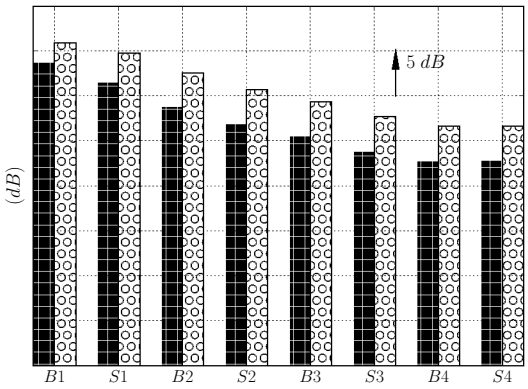

(b) Low power with entropy planar modes in phase

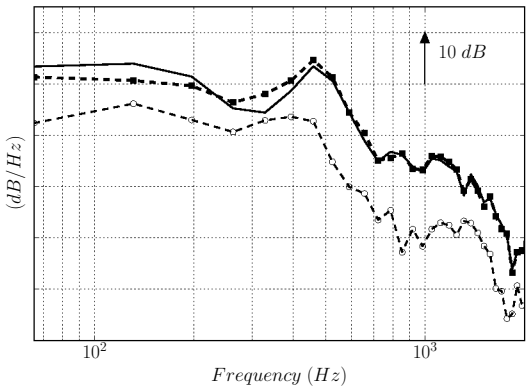

(c) Low power

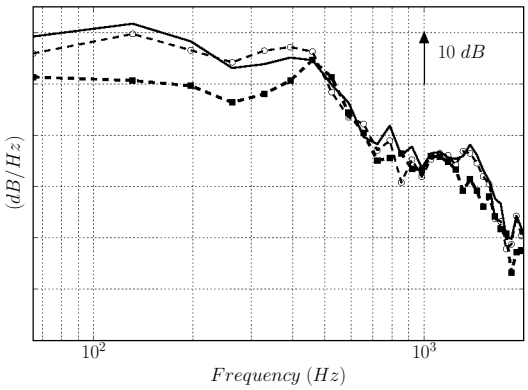

(d) Low power with entropy planar modes in phase

Figure 6.54: Acoustic power through the turbine stages (**B1** - **S4** in Fig. 5.4) at a) low power and b) low power with entropy planar modes in phase. PSD of combustion noise at the turbine exit **S4** at c) low power and d) low power with entropy planar modes in phase. Direct noise (■), indirect noise (○), total noise (–)

with the entropy planar mode of a single sector. Due to the periodicity assumption used to perform LES of single sector, it was also assumed that each burner was in phase. However, there are no correlations between the entropy planar mode of each sector, so that destructive contributions lead to lower amplitude of the 360° planar entropy mode (Fig. 6.55). Therefore, the decrease of the entropy planar mode amplitude allows the direct noise to become the dominant mechanism in the low power case (Fig. 6.54(a)). However, if a thermoacoustic instability exists,

the heat release rate and the pressure fluctuations being coherent, the entropy signal should also be in phase sector-by-sector. Hence, the validity of the model used to mimic the entropy planar mode of a full annular combustion chamber is questionable in the occurrence of a thermoacoustic instability. If no random phase-shift is taken into account for the entropy planar mode, then the indirect mechanism becomes dominant at each blade row of the turbine, because of noise levels higher than the direct noise levels (Fig. 6.54(b)). This implies an increase of the total noise levels at low frequency (< 500 Hz) since indirect noise becomes noisier than direct noise in this range of frequency (Fig. 6.54(d)). Nevertheless, the only way to verify the validity of the random phase-shift model, in the case of a combustion regime with a strong thermoacoustic activity, should be to perform a LES of a 360° full annular combustor.

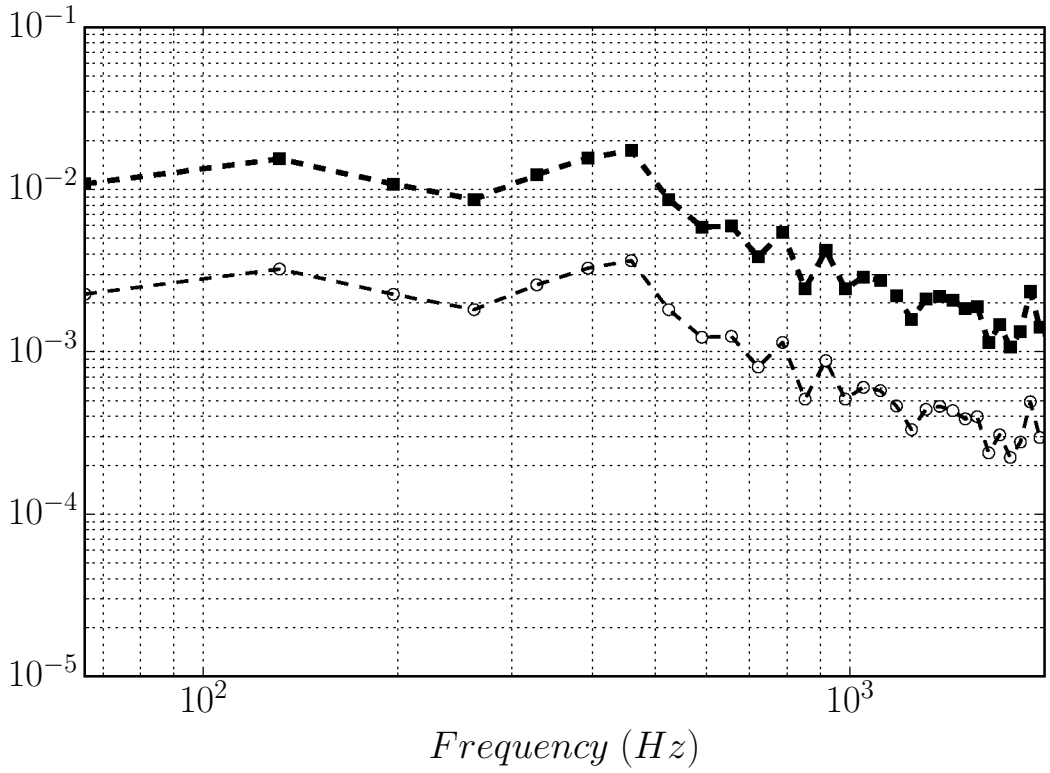

Figure 6.55: Entropy planar wave amplitudes: in phase sector-by-sector (■), no correlations between sectors (○)

At intermediate power conditions in Fig. 6.56(a), the direct mechanism is still dominant. A strong attenuation of direct noise occurs between the first two blade

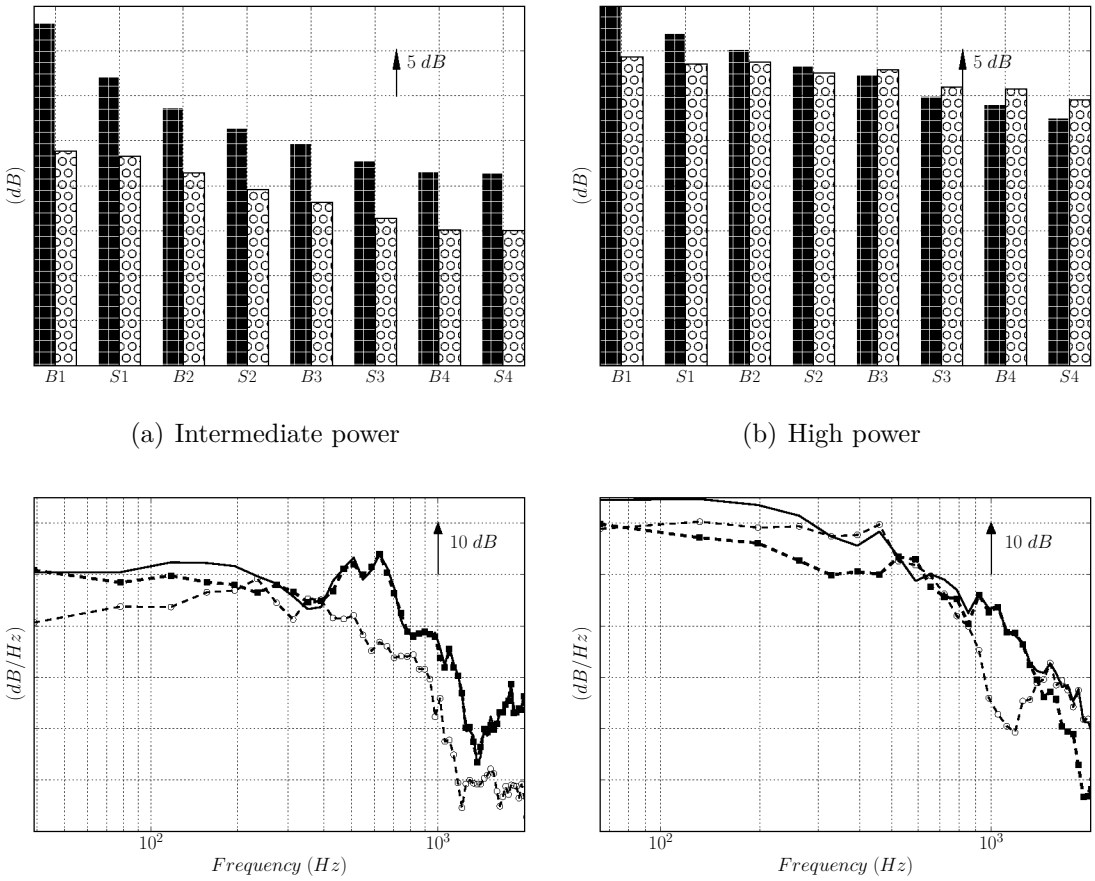

(a) Intermediate power

(b) High power

(c) Intermediate power

(d) High power

Figure 6.56: Acoustic power through the turbine stages (**B1** - **S4** in Fig. 5.4) at a) intermediate power and b) high power. PSD of combustion noise at the turbine exit **S4** at c) intermediate power and d) high power. Direct noise (■), indirect noise (○), total noise (–)

rows **B1** and **S1**, then the masking effect is attenuated. The PSD of direct and indirect noise at the turbine exit (Fig. 6.56(c)) are broadband and low frequency. Above 1000 Hz, the noise levels are strongly damped. A bump is still noticeable at 625 Hz as for the PSD of pressure fluctuations at the outlet of the combustion chamber (Fig. 6.26). This bump is only marked for direct noise, meaning that the acoustic activity in the chamber is more important around the resonant frequency of the combustion chamber and conserves this characteristic across the turbine. This can also be noted for the low power case with a bump at 500 Hz, even if the indirect noise presents also a bump less marked (Fig. 6.54(c)). This bump in the

PSD of indirect noise could be due to a thermoacoustic instability for which all the signals are coherent and at a discrete tone.

At high power conditions, the dominant mechanism between indirect and direct noise cannot be clearly identified (Fig 6.56(b)). For the first stages, direct noise is dominant, then the balance changes and indirect noise becomes dominant for the last stages. The power losses through the turbine stages are less important than before. Indirect noise is much more present for this operating point than at low or intermediate power, as it was shown from the analysis of the turbine characteristics. Entropy wave is less attenuated than at other power cases (Fig. 6.48(c)) and more noise is generated with high velocity gradients across the complete turbine. Miles [2009] shows that indirect noise was low frequency ($f < 200\ Hz$), while direct noise was related to higher frequencies ($< 200f <$ 400 Hz). By observing the spectra at the turbine exit S_4 (Figs. 6.54(c), 6.54(d), 6.56(c) and 6.56(d)), the broadband peak frequency of the indirect noise spectra is more around 400 Hz, while the broadband peak frequency of direct noise is always at higher frequency ($>$ 500 Hz) than the one of the indirect noise. However, the mechanism that shows more activity around a certain frequency is not necessarily the dominant mechanism at this frequency.

6.2.3.2 Acoustic turbine attenuation

The turbine acoustic attenuation or the so-called acoustic masking describes the acoustic loss of combustion noise propagating across the turbine. It has been highlighted only from engine noise correlations with bench data of engine manufacturers. This term includes a lot of physical interactions in the turbine: acoustic reflection, dissipation due to vorticity, scattering to other modes, acoustic loss due to heat transfer, viscosity and a lot of interactions that are not known. From correlations, it is often assumed that a stage has an acoustic loss of 2 dB.

By considering the total noise (contribution of direct and indirect noise) emitted by the investigated turbofan-engine case, no trend can be clearly stated at this point for the acoustic loss (Fig. 6.57). Large acoustic losses are observed between the combustion chamber exit and the first stage exit (**S1**). The acoustic masking (turbine attenuation) of the successive blade rows is dependent on the operating point and very sensitive to the aerodynamics in the turbine. More or less reflection will be generated according to the deviation angle and the Mach number (Fig. 6.58) as highlighted by Leyko et al. [2014] and shown for each isolated blade row of the turbine (positions **B1** to **S4** in Fig. 5.4) in sections 6.2.2.1 and 6.2.2.2. Globally, the intermediate blade rows (from S_1 to S_3) lose 2 dB, and the acoustic masking effect is attenuated on the last stages.

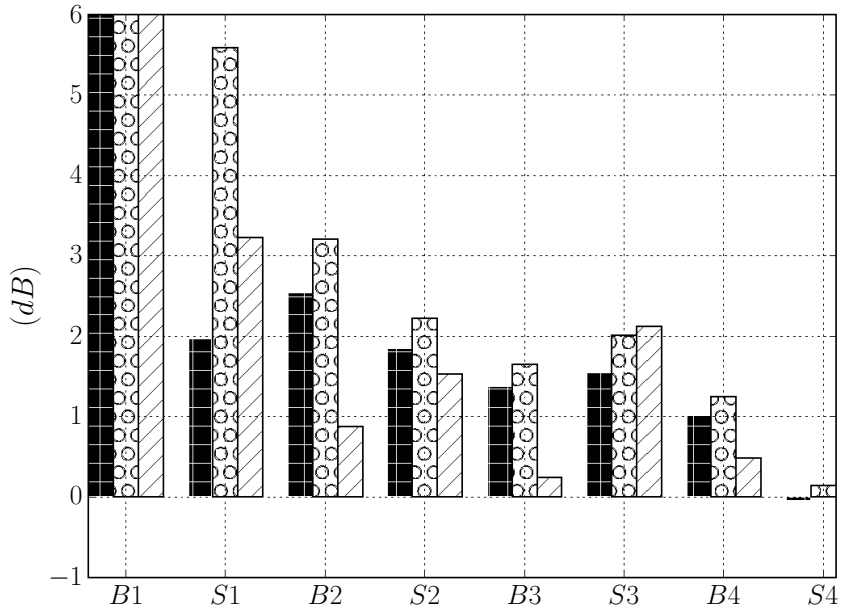

Figure 6.57: Acoustic power losses across the turbines, for low power (■), intermediate power (○) and high power conditions (//).

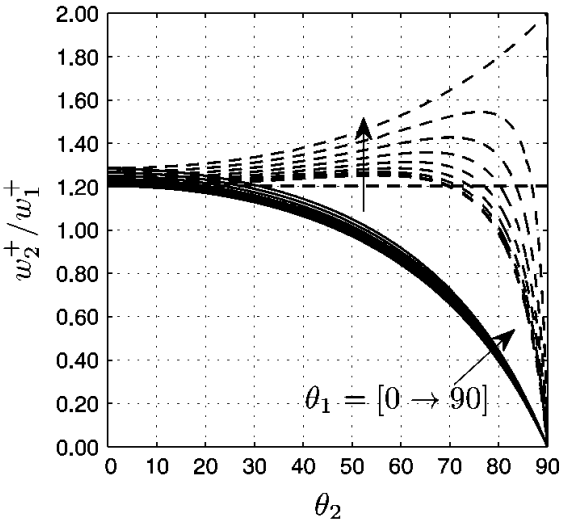

Figure 6.58: Acoustic response of the blade row at the outlet to an acoustic perturbation at the inlet for different flow directions (Leyko et al. 2014), θ_1 at the inlet and θ_2 at the outlet. Cumpsty and Marble 2D model (–), Marble and Candel 1D model (- -).

6.3 Computation of acoustic far-field propagation with an Helmholtz solver

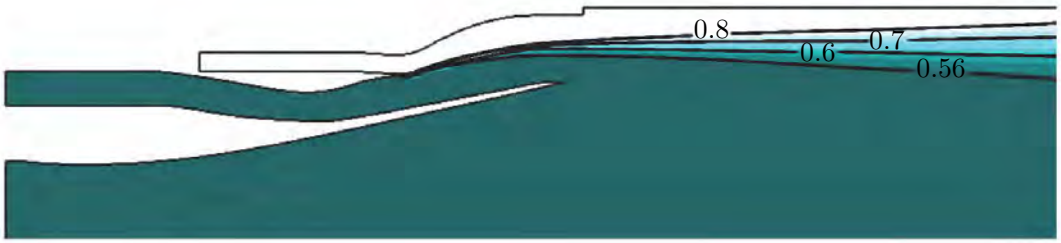

(a) Low power

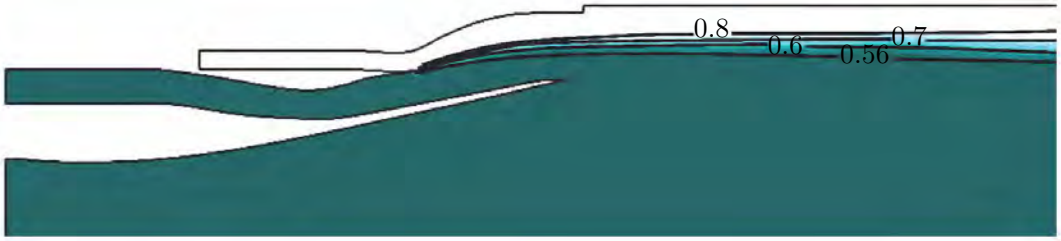

(b) Intermediate power

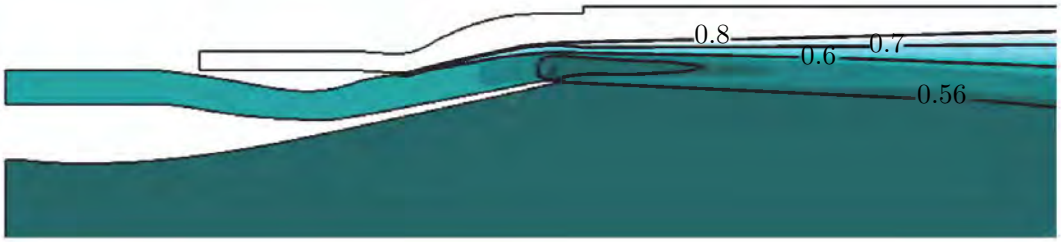

(c) High power

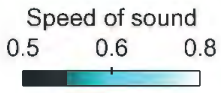

Figure 6.59: Sound speed fields

The real configuration has a double stream jet with a lobe mixer to reduce jet noise by improving the mixing between the primary hot flow and the secondary cold flow. However mixing is not perfect and temperature inhomogeneities still exist. In order to simplify the geometry and due to confidential issues, the mixer is replaced by a primary nozzle with the same inlet flow conditions. However, as there is no mixing, the jet flow will subsequently be different.

Due to the double stream, a subsonic jet flow model cannot be used to initialize the AVSP-f computations. Therefore AVSP-f computations are initialized using mean flow fields provided by prior RANS simulations performed using ANSYS-Fluent in an axi-symmetric mode, as shown in Fig. 6.59. The RANS simulations have been performed on a hybrid grid resolving the boundary layers in the nozzle. A standard k - ϵ model for turbulence has been used with first order upwind scheme for the turbulent variables only. Otherwise second order high resolution is used for all conservative variables and has shown to be accurate in single stream (ARN, SMC, Fosso-Pouangué et al. June 4-6 2012, JEAN) and dual-stream jet (EXEJET, Sanjose et al. 2014).

Similar normalized speed of sound fields are obtained for the three operating points. Higher sound speed levels are located in the hot primary jet. Successive decreasing sound speed level layers are then observed when the hot jet interacts with the colder secondary jet. At high power condition, the radial expansion of the jet is wider (Fig. 6.59(c)). It can be noticed that the speed of sound of the secondary stream is higher than the speed of sound of the atmosphere due to higher temperature. Therefore, the interface between the atmospheric conditions and the secondary stream conditions is more noticeable than for the other cases.

The acoustic computational domain is represented in Fig. 6.60. Since a single sector of combustor has been computed, only plane waves are meaningful. By considering low frequency ($<$ 2000 Hz) plane modes, the computational domain can be reduced to a slice of the atmosphere. To have a good resolution up to 2000 Hz ($\lambda_{2000Hz} = 17.2cm$), ten nodes per wavelength are used. AVSP-f is used to obtain the modulus and phase of the acoustic pressure up to 7.5 m from 90° to 180°. To obtain pressure levels in the far-field, the acoustic pressure module obtained at 7.5 m has been propagated up to 45.72 m (available experimental data). A monopolar radiation and a spherical wave propagation are assumed leading to:

$$|p_2| = |p_1|\frac{r_1}{r_2}, \tag{6.6}$$

where $|p_2|$ is the acoustic pressure module at a distance r_2 from the acoustic source and $|p_1|$ is the acoustic pressure module at a distance r_1 from the source.

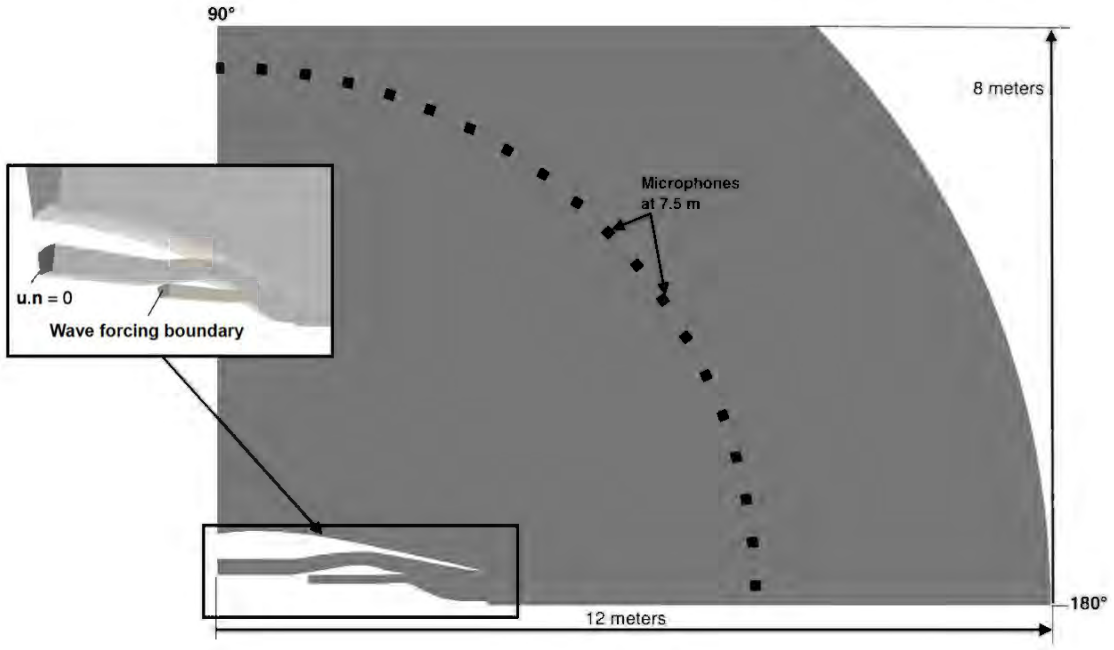

Figure 6.60: Acoustic domain and boundary conditions

During the acoustic certification of the engine, the engine is placed on a pylon at a height of $h = 5$ m as shown in Fig. 6.61. The height being not considered in the simulations, the position of the probes (θ_{AVSP-f}) has to be computed to correspond to the experimental microphones location (θ_{micro}). Indeed, the reference plane of the experimental microphones is on the ground with the microphone at 180° located in the direction parallel to the jet axis. However, for the acoustic simulations, the reference plane is at the center of the engine, so that there is a shift of angle between the two planes. Assuming a spherical noise radiation, there is a conservation of the pressure fluctuation at an equidistant direction. Therefore, the experimental microphones position has to be projected in the engine reference plane. The location of the AVSP-f probes corresponds to the intersection of the reference engine plane with the acoustic pressure iso-contour in a given direction. The experimental data have been corrected considering the reflection on the ground.

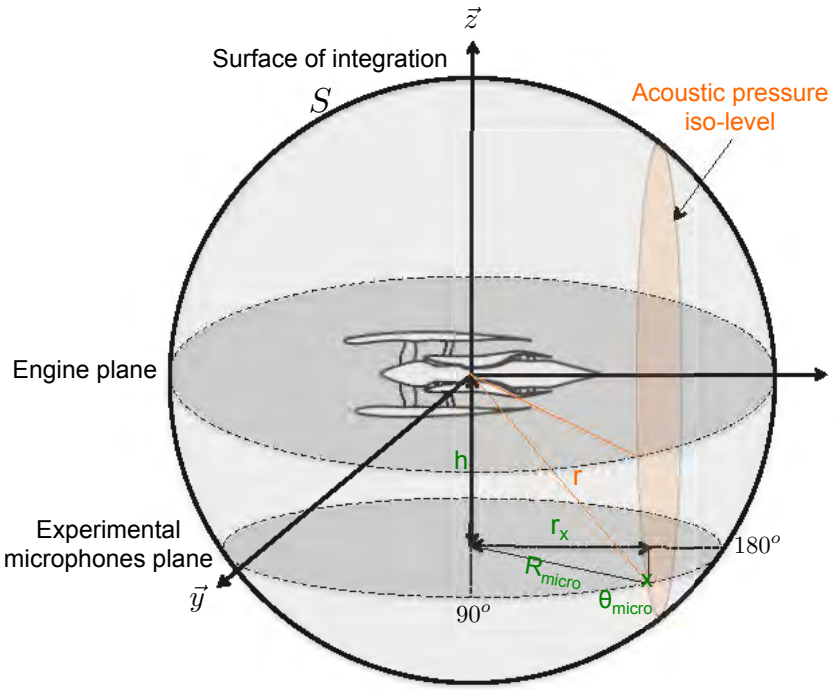

(a) Overall view of noise radiation

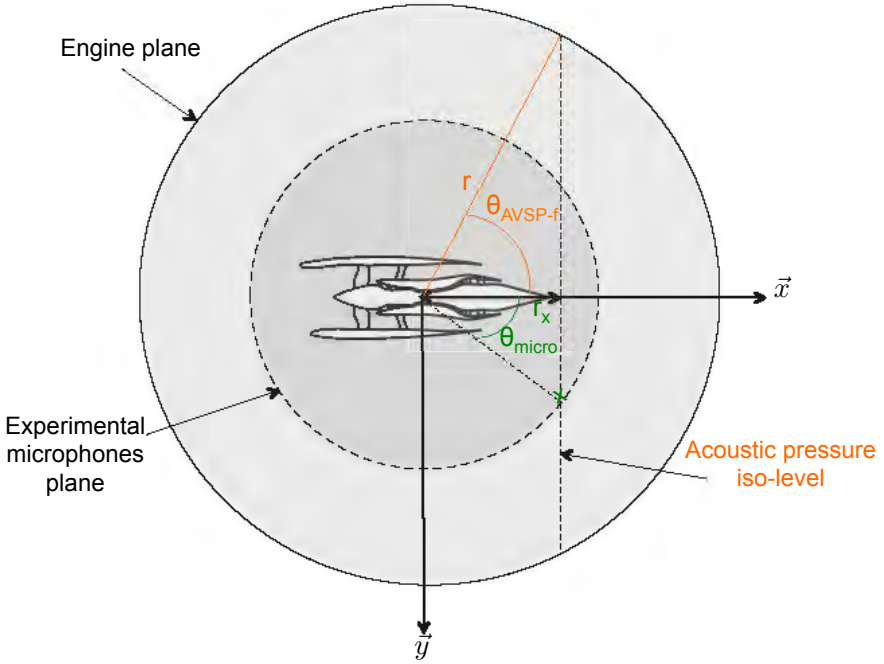

(b) Top view of noise radiation

Figure 6.61: Overall view of the noise radiation

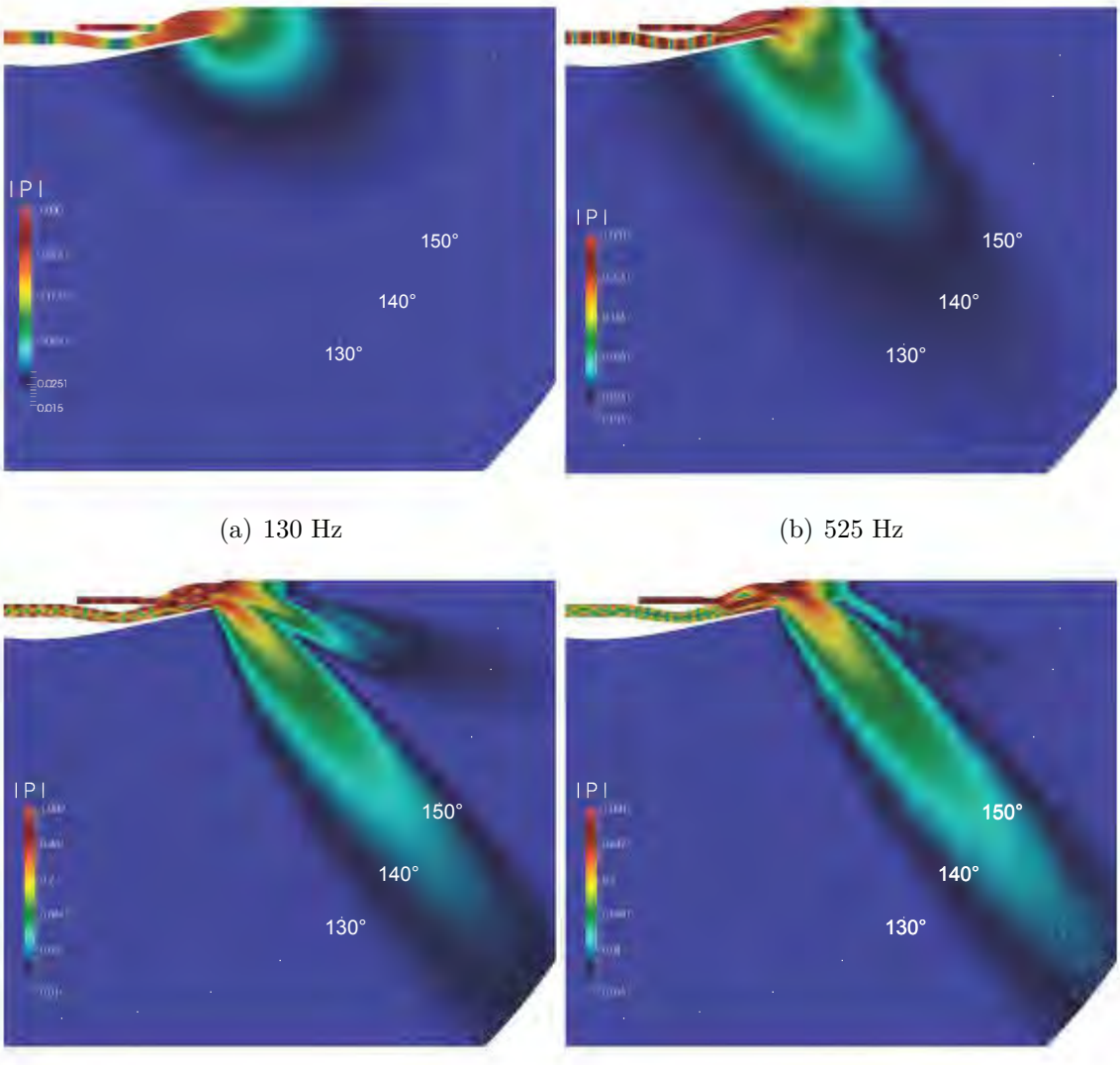

(a) 130 Hz (b) 525 Hz

(c) 1050 Hz (d) 1300 Hz

Figure 6.62: Fields of the acoustic pressure module at different frequencies in the low power case induced by an unitary acoustic forcing through the primary nozzle inlet

The fields of the acoustic pressure module are shown in Figs. 6.62 to 6.64 for the low power, intermediate power and high power cases at different frequencies. It can be noticed that the directivity is dependent on the frequency and on the operating point. This corroborates the influence of the mean speed of sound field on the acoustic propagation. At low frequency (100 Hz), the directivity is quasi-monopolar whereas, at higher frequency the directivity is most between 140° and

150°. Diffraction is observed at 160°-170°. The intermediate case exhibits also diffraction at 120°. Silent zones can be seen at 90° and 180°.

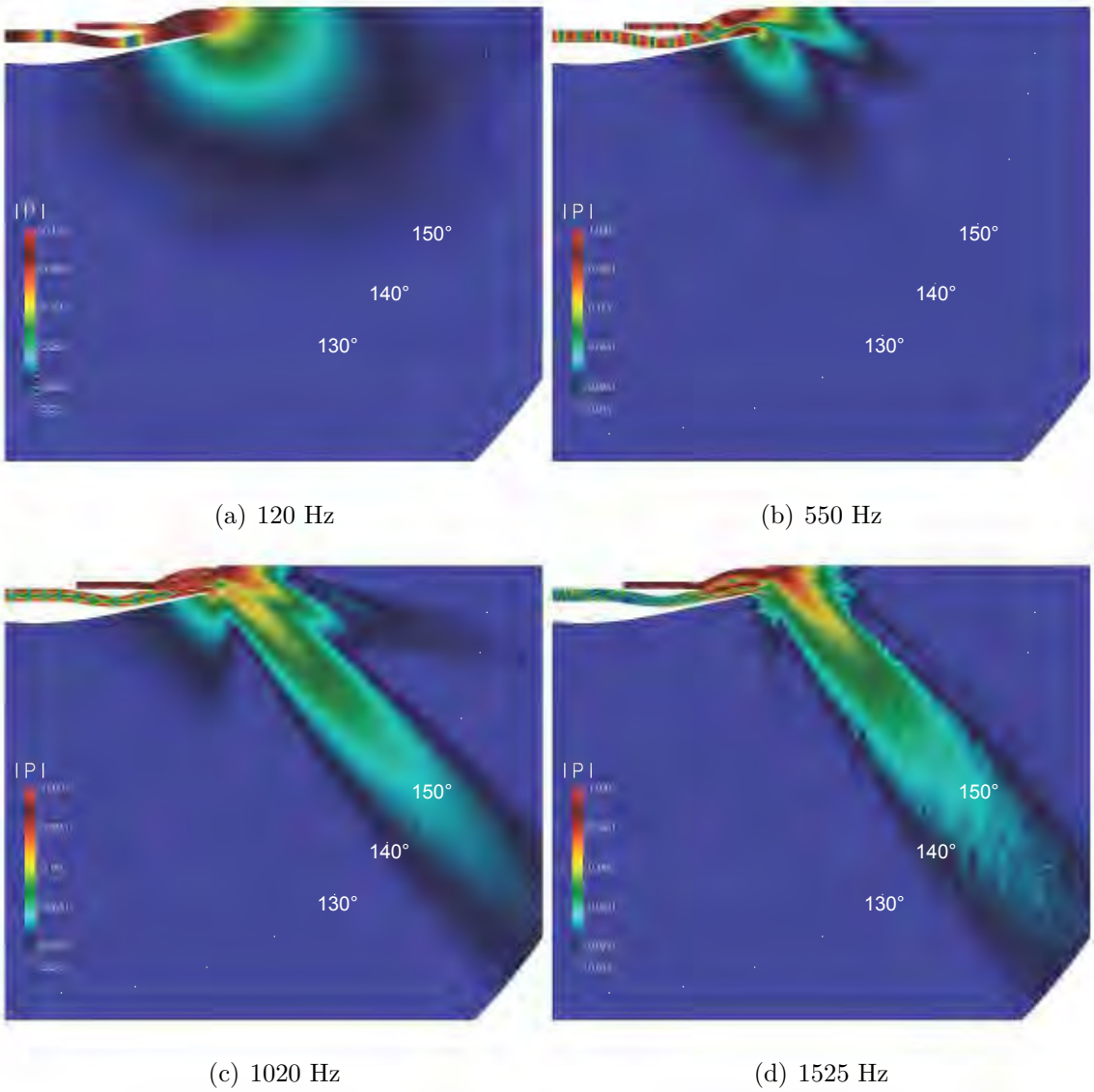

(a) 120 Hz

(b) 550 Hz

(c) 1020 Hz

(d) 1525 Hz

Figure 6.63: Fields of the acoustic pressure module at different frequencies in the intermediate power case induced by an unitary acoustic forcing through the primary nozzle inlet

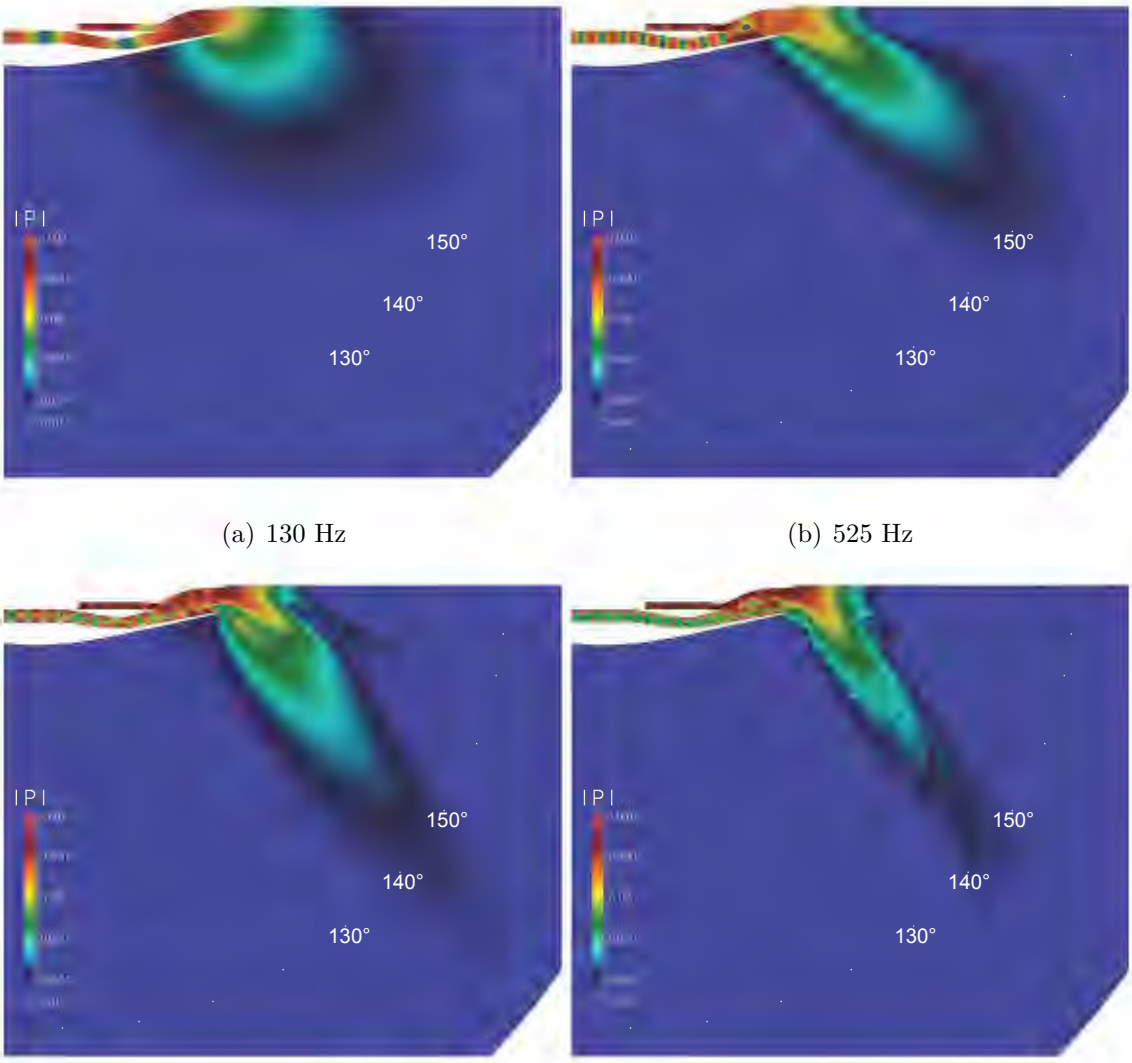

(a) 130 Hz

(b) 525 Hz

(c) 1050 Hz

(d) 1500 Hz

Figure 6.64: Fields of the acoustic pressure module at different frequencies in the high power case induced by an unitary acoustic forcing through the primary nozzle inlet

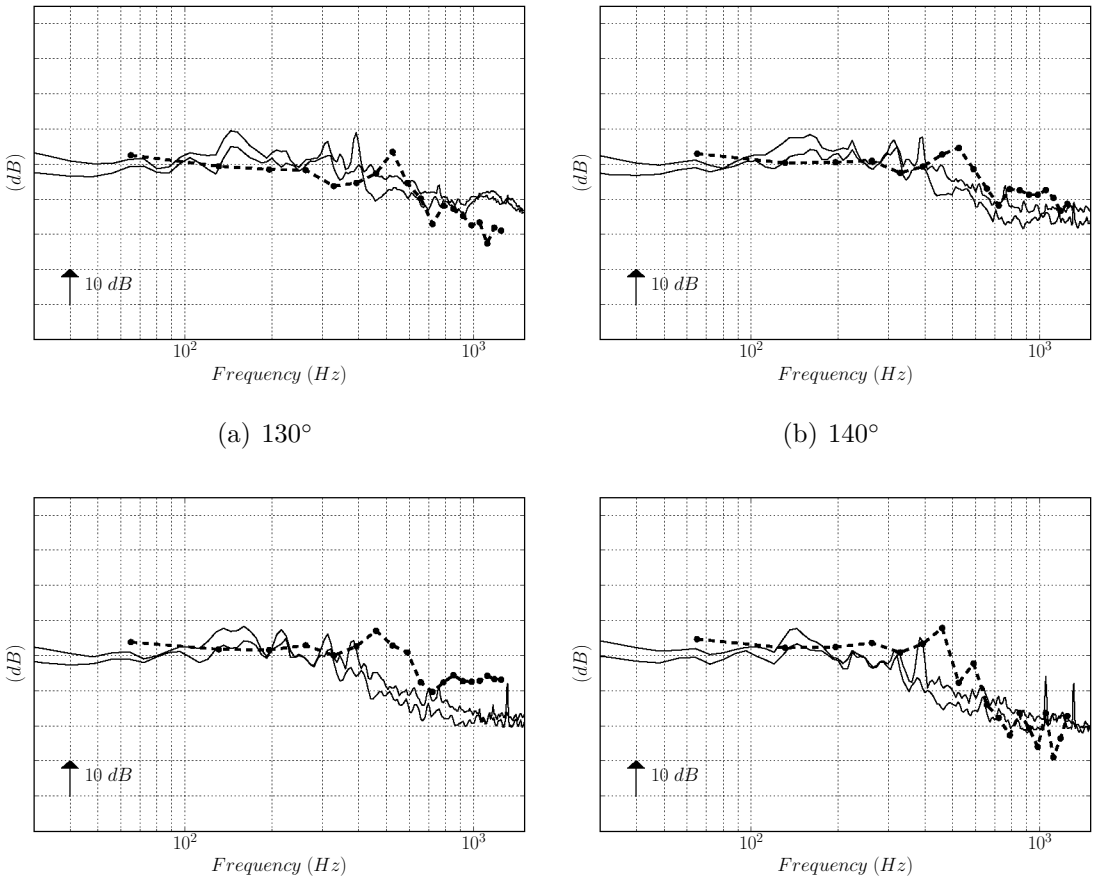

(a) 130°

(b) 140°

(c) 150°

(d) 160°

Figure 6.65: Computed combustion noise in far field (45.72 m) at low power. Total predicted combustion noise (●) and experimental SPL of downstream engine noise (gray area)

In Figs. 6.65 to 6.67 results are compared with sound pressure levels of the turbofan-engine tests at 45.72 m, at power regime close to the computed one. At low power (Fig. 6.65), jet velocity is low, thus jet noise is negligible. Consequently combustion noise is the main source of acoustic emissions at low frequency: the spectral content is correctly predicted and the order of magnitude is captured. This confirms the results of Livebardon et al. [2016] but for a more complex dual-stream case with axial high pressurized and low pressurized turbines. Spectra are broadband with one tone around 500 Hz, as observed before in the combustion chamber (Fig. 6.26) and in the turbine (Fig. 6.54(c)). However a slight shift of the bump frequency can be observed between the simulation and the experimental data. More frequency resolution could be achieved in order to correctly identify the

peak frequency of the narrow-band spectra. Moreover, acoustics is very sensitive to boundary conditions. More recently, Kraus et al. [2017] shows how thermal transfers can control thermoacoustic instability. The implementation of a thermal coupling in the simulations to have the good temperature imposed at the walls allows a shift of the frequency to obtain the good tone.

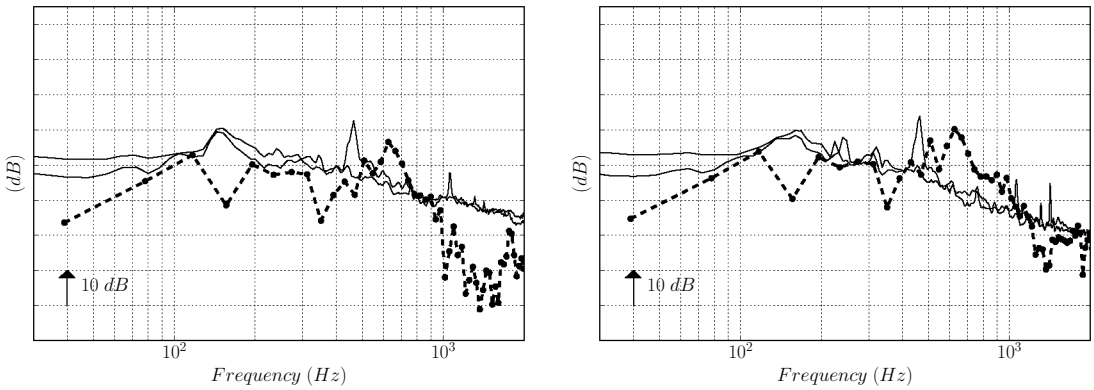

(a) 130°

(b) 140°

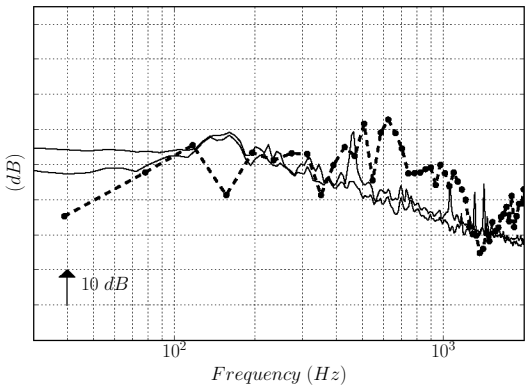

(c) 150°

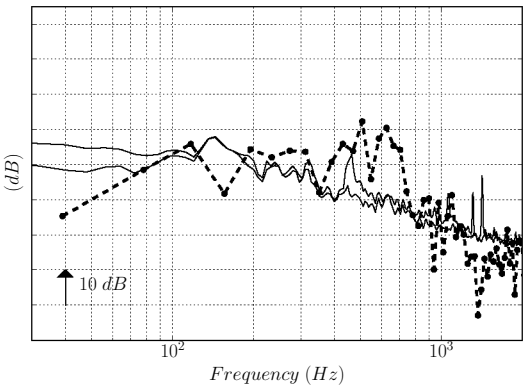

(d) 160°

Figure 6.66: Computed combustion noise in far field (45.72 m) at intermediate power. Total predicted combustion noise (●) and experimental SPL of downstream engine noise (gray area)

At intermediate power (Fig. 6.66), jet velocity is no more negligible. Still, combustion noise seems to reach the levels of the experimental SPL of the downstream engine noise, meaning that its contribution is still important at this power regime. At some frequencies, acoustic level destructions appear which could correspond to cut modes linked to the geometry at this operating point. Bumps at 510 Hz and

625 Hz are still present as also noted at the turbine exit (Fig. 6.56(c)).

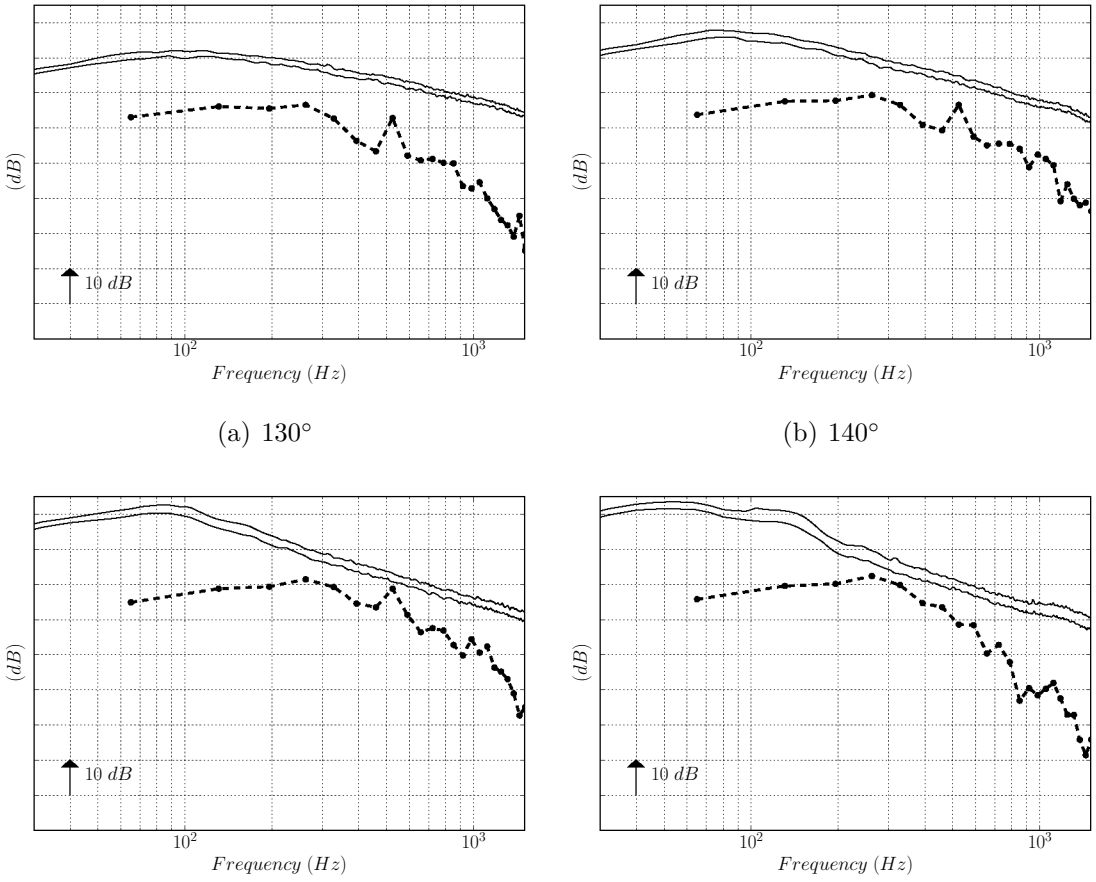

(a) 130°

(b) 140°

(c) 150°

(d) 160°

Figure 6.67: Computed combustion noise in far field (45.72 m) at high power. Total predicted combustion noise (●) and experimental SPL of downstream engine noise (gray area)

At high power (Fig. 6.67), the noise spectrum is still broadband but with a maximum of radiation at 250 Hz. A strong decrease is observed between 500 and 2000 Hz, while a smaller decline is noted for the total engine noise spectra. At high power, jet noise is present, therefore combustion noise is not the main source anymore and sound pressure levels are higher for the experimental data. It is necessary to obtain the other sources of noise to compare results with turbofan-engine bench data in the far-field.

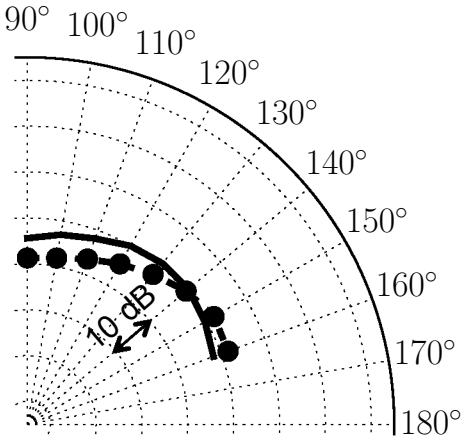

(a) Low power

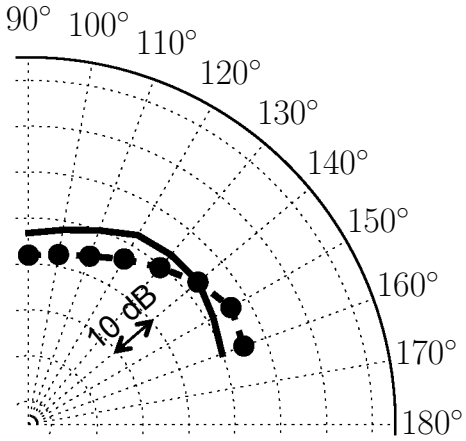

(b) Intermediate power

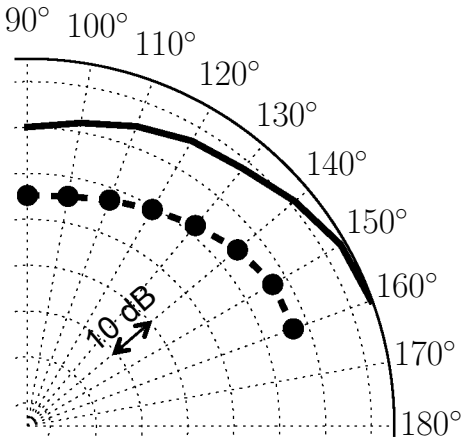

(c) High power

Figure 6.68: Over All Sound Pressure Level (OASPL) of combustion noise in far field (45.72 m). Total predicted combustion noise (●) and experimental OASPL of downstream engine noise (–).

The overall sound can be analyzed in function of the angle of directivity θ. By integrating the acoustic pressure levels on the frequency range at each angle, the Over All Sound Pressure Level (OASPL) of the three computed operating points are presented in Fig. 6.68:

$$OASPL(\theta) = \int_f (P_{rms}/P_{ref})^2 df. \tag{6.7}$$

All the computed cases exhibit a maximum directivity at 150°, meaning that it is the preferred propagation direction of combustion noise. However, experimental data rather show a directivity between $130° - 140°$ for low and intermediate power. It must be kept in mind, that the mean velocity flow is neglected so that shear layer refraction is not considered. This could change the directivity of the combustion noise. According to Amiet [1978], refraction of sound occurs when reaching the shear layers of a jet. This results in an angle and amplitude change in the far-field. The relation between θ and θ_{SL} (the propagation angles before and after shear layer refraction) can be computed as:

$$\tan\theta = \eta/(\beta^2 \cos\theta_{SL} + M_e), \tag{6.8}$$

where

$$\eta^2 \equiv (1 - M_e \cos\theta_{SL})^2 - \cos^2\theta_{SL}, \qquad \beta^2 \equiv 1 - M_e^2. \tag{6.9}$$

As the configuration is a dual-stream nozzle with hot primary and cold secondary flows, an equivalent Mach number M_e can be defined using Fisher's model for simple coaxial jets with heated primary flow (Fisher et al. 1998). M_e is written as

$$M_e = \frac{1 + L^2 B\Delta}{\sqrt{(1 + LB\Delta)(1 + LB)}} M_p, \tag{6.10}$$

with

$$L = U_s/U_p, \qquad B = A_s/A_p \qquad \text{and } \Delta = T_p/T_s. \tag{6.11}$$

The subscripts s and p stand respectively for the secondary flow and the primary flow. U denotes the exhaust velocity of the regarding nozzle, A the outlet surface, T the static temperature and M the Mach number.
Using these assumptions, the hypothetic propagation angle (θ_{SL}) after shear layer refraction can be found as shown in Fig. 6.69. Refraction becomes more important as the exhaust Mach number increases. Considering a maximum directivity of 150° for all the computed cases, this would lead to a maximum directivity of 138° for the low power case, 132° for the intermediate case and 115° for the high power case. This is more in agreement with the experimental data.

Moreover, it must be reminded that the geometry of the nozzle has been modified to replace the lobe mixer by a divergent-convergent primary nozzle, so that the hydrodynamics is also modified. (Pouangué et al. 2014) has shown that double stream jet configuration with a lobe mixer generates more noise at very high frequency but reduces noise at low frequency. This could also modify the directivity.

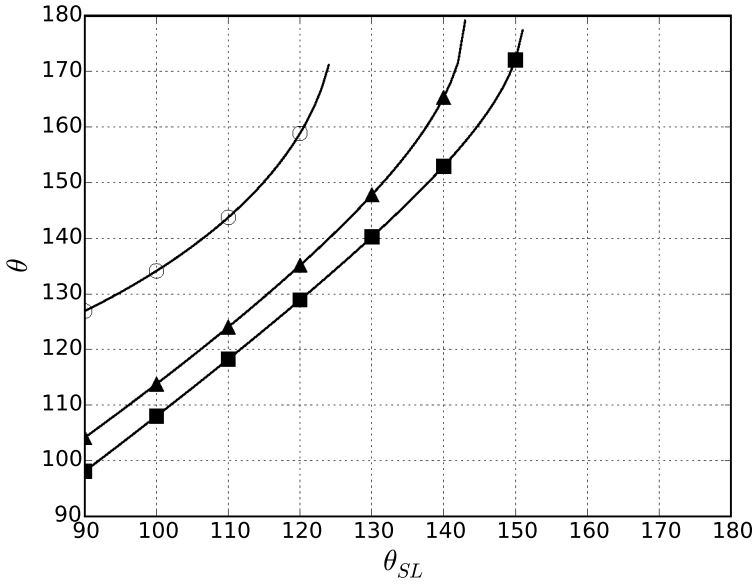

Figure 6.69: Propagation angles before (θ) and after (θ_{SL}) shear layer refraction for low power (■), intermediate power (▲) and high power conditions (○)

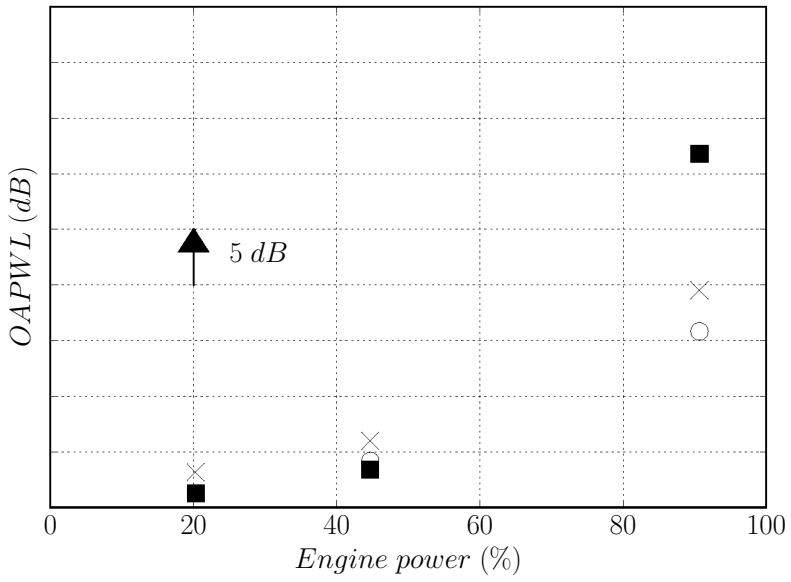

Figure 6.70: Over All Power Level (OAPWL) in the far field (45.72 m), total predicted combustion noise (○) and experimental OAPWL of downstream engine noise (■). OAPWL of predicted combustion noise at the turbine exit **S4**, (×)

Indeed there is an underestimation of the OASPL between 100° and 130°, while the OASPL is overestimated between 150° and 160°. At high power (Fig. 6.68(c)), OASPL of combustion noise are under the levels of the downstream engine noise. Combustion noise could indeed propagates at 115° as assumed with the Amiet's assumptions (Fig. 6.69). However at this operating condition jet noise is present and is the dominant source, that explains the directivity at 160° observed in Fig. 6.68(c).

Another quantity which can be evaluated is the Over All Power Level (OAPWL) which represents the acoustic power integrated over all frequencies and angles of directivity (Fig. 6.70):

$$OAPWL = \int_S \int_f (P_{rms}/P_{ref})^2 df\, dS. \tag{6.12}$$

At low and intermediate power, combustion noise is seen to be the major contributor of engine noise since the OAPWL match the measurements. On the contrary, as seen before, this source of noise is not the most important at high power, since the OAPWL of combustion noise is 15 dB below the engine noise OAPWL. Still, it can be said that the power of combustion noise increase with an increase of the engine-power. The prediction of far-field combustion noise is quite good at low and intermediate powers. Moreover, these computed far-field results have power levels close to the OAPWL computed at the end of the turbine (power conservation), meaning that the prediction of noise propagation in the turbine is also correct. It can be concluded that the planar mode is dominant and enough to predict the far-field combustion noise.

Numerical simulations have been performed with the CONOCHAIN methodology to investigate the combustion noise generation and propagation of a real turbofan-engine. Three operating points have been computed: low power (20 % of engine power), intermediate power (44 %) and high power (90 %). The CONOCHAIN method consists first in the accurate acquisition of noise sources thanks to LES of combustion chamber. The acoustic behavior of the turbine is then described with transfer functions obtained from Cumpsty and Marble [1977] and the acoustic sources have been propagated through the turbine stages. Finally, the acoustic waves at the outlet of the the turbine are injected in the AVSP-f Helmholtz solver which allows to consider some effects of the flow, notably the temperature heterogeneous field. From LES observations, it can be noticed that low power and high power conditions exhibit similar behavior (mean velocity field, equivalence ratio, temperature fluctuation). However, it seems that at intermediate power condition, the combustion occurs at a leaner regime. This can be responsible for the differences observed in the direct noise spectra extracted at the combustion chamber exit. Moreover, less temperature fluctuations were observed, yielding less

entropy fluctuation. The acoustic behavior of the two turbines (High Pressurized Turbine (HPT) and Low Pressurized Turbine (LPT)) has been analyzed. It has been found that an increase in the engine power leads to a higher transmission of noise through the turbines. A generation of indirect noise in the turbines stages has been demonstrated, as the effect of the acceleration of hot and cold spots. Once again an increase in engine power leads to a higher generation of indirect noise. This has been found to be due to higher velocity gradients. Contrarily on what generally found in literature, where almost all the indirect noise has been seen to be generated in the first turbine stage, it has been noticed how, for high engine powers, the indirect noise is generated also in the subsequent turbine stages. The propagation in the far field by means of AVSP-f of the waves obtained by CHORUS shows a noise directivity at nearly 150°. Experimental data shows a directivity at 140°; this difference is probably linked to the differences between the experimental (mixed dual core jet) and numerical setups (non-mixed dual core jet) but also to the fact that shear layer refraction is not considered. Using Amiet's assumption allows to correct the combustion noise directivity. It appears that refraction is not negligible even at low Mach number. An analysis of the noise levels (OAPWL) show how at low and intermediate power the noise predicted by the numerical simulations chain reach the overall noise of the experimental bench data. This confirms how combustion noise is the dominant noise source at these engine regimes. Finally it has been found how the overall combustion noise increases with an increase in engine power.

Chapter 7

Comparison with empirical methodology

Abstract Combustion noise is a very complex problem where many processes and variables are involved. Due to this complexity, it is not easy to develop a theory to understand or predict combustion noise. The mechanisms responsible for combustion noise generation have been identified for direct noise and indirect noise. However, the origin of the direct noise is not fully defined. Details at different scales (kinetic, turbulence) could be involved in the process but are not well known. In the same way, acoustic analogies have been developed for the propagation of combustion noise. However, too many descriptions of the combustion noise source term exist so that it is not easy to choose which one to use. Empirical methods are another possible approach which can be a good first step to overcome the complexity of physical problems.

Engine manufacturers have been using empirical approach to predict noise at the preliminary design stages of aircraft modules. Empirical methods have been anchored in their community since the 1970's. The empirical approach is presented in the first section. CONOCHAIN results are compared with prediction results of an empirical law in the last section.

7.1 Empirical methodologies to predict combustion noise

Since the introduction of jet engines in civil aviation, acoustics has been widely studied. Therefore, a large database for engine noise and a lot of experimental measurements on open flames are available. These data constitute the basis of the empirical and semi-empirical methods which can be classified between methods for fundamental cases and methods for applied cases.

In the first case, models to characterize open-flame noise are obtained from

correlations of experimental data with variations in physical parameters. Three quantities are of interest for the far-field noise: the intensity, the directivity and the spectra. For open-flames, it is known that the source of noise acts as a monopole, so that the acoustic propagation is isotropic. Kotake and Takamoto [1987, 1990] highlighted that the spectral shape of combustion noise is not related to the burner size, the equivalence ratio, the flow conditions or the turbulence. All spectra exhibit a dominant broad peak so that a generic spectrum can be obtained. Tam [2015] proposed a universal spectrum for flames similarly to its model for jets spectra. However, the intensity is dependent on a multitude of parameters. Therefore, an empirical law has to be built by choosing the most influent parameters to predict the combustion noise intensity. For instance, by assuming the acoustic pressure fluctuations related to the heat release rate, a proportionality law can be derived for the intensity:

$$I \propto \dot{m}_f / r^2, \tag{7.1}$$

where $\dot{m}_f$ is the fuel consumption rate, r the distance to the observer. The proportionality constant depends on the burner design.

Same approach can be used to relate real engine noise levels to operating parameters. However, in the literature, only few engine data is reported. Most engine manufacturers (General Electric Company (GE), Pratt & Whitney (PW), SAFRAN) treat their own noise data and develop their own in-house noise prediction codes. Either the prediction method is purely empirical using only correlations of the database or it is semi-empirical using analytical models coupled to correlations. These acoustic prediction codes provide generally good results with data closed to the database used to create the model but not necessarily with data from other manufacturers (Mahan and Karchmer 1991). Consequently, the method is dependent on the database, that is to say the burner design.

The prediction methods generally consist in the prediction of the OAPWL. The OAPWL can be obtained from analytical models using the physical variables $\mathcal{P}$ related to combustion noise and correlated coefficients $\mathcal{C}$ obtained from the database:

$$OAPWL = 10 \log_{10}(\Pi(\mathcal{P}, \mathcal{C}) / \Pi_{ref}), \tag{7.2}$$

where $\Pi_{ref} = 1 \times 10^{-12}$ W. This formulation can also take into account a model for the prediction of the peak frequency and a function for the turbine attenuation of the broadband combustion noise. According to engine noise investigations, the peak frequency model is often related to the burner geometry.

Third octave band empirical Power Level spectrum (PWL) and directivity OASPL patterns are then obtained by adjusting the levels with the computed

OAPWL:

$$OASPL(\theta) = 10\log_{10}(\rho_\infty c_\infty \Pi(\mathcal{P},\mathcal{C})D(\theta)/4\pi r^2 p_{ref}^2), \tag{7.3}$$

$$PWL(f_b) = 10\log_{10}(\Pi(\mathcal{P},\mathcal{C})/\Pi_{ref} S(f_b)), \tag{7.4}$$

where $p_{ref} = 2\times10^{-5}$ Pa is the acoustic pressure of reference and r is the distance from the source. $D(\theta)$ is an empirical directivity function that gives the OASPL generic shape in function of the angle θ. $S(f_b)$ is a spectrum function which gives the generic shape of the PWL in function of the 1/3 octave band center frequency f_b.

Finally, Sound Pressure Level (SPL) can be obtained considering the OAPWL, the OASPL and the PWL:

$$SPL(f_b,\theta) = 10\log_{10}(\rho_\infty c_\infty \Pi(\mathcal{P},\mathcal{C})D(\theta)S(f_b)/4\pi r^2 p_{ref}^2) \tag{7.5}$$

The flowchart of the empirical or semi-empirical models can be summarized as in Fig. 7.1

7.2 Discussion of the CONOCHAIN results compared with an SAE empirical law

An empirical method developed by SAE is tested. The purpose of this method is to use a large amount of engine bench data to establish the global acoustic behavior of the studied turbofan engine in function of its cycle values only. The empirical law is built using an experimental dataset of physical quantities identified as the main drivers for combustion noise. These quantities are determined by correlated observations of the database in order to get the best set of variables:

- $W36$: air mass-flow rate at the diffuser outlet,
- $T3$ and $T4$: stagnation temperatures at the combustor inlet and outlet,
- $P3$ and $P4$: stagnation pressures at the combustor inlet and outlet,
- $T4D8N$: temperature loss between the combustor outlet and the nozzle throat.

The correlated coefficients (α, β, γ, θ, η, χ and ξ) are obtained with a least square minimization process on the known engine OAPWLs of the database. The OAPWL of the conceptual engine combustion noise reads:

$$\begin{aligned} OAPWL &= \alpha\log_{10}(W36) + \beta\log_{10}(T4-T3) + \gamma\log_{10}(P3) \\ &+ \theta\log_{10}(T3) + \eta\log_{10}(T4D8N) - \chi N_{stage} + \xi. \end{aligned} \tag{7.6}$$

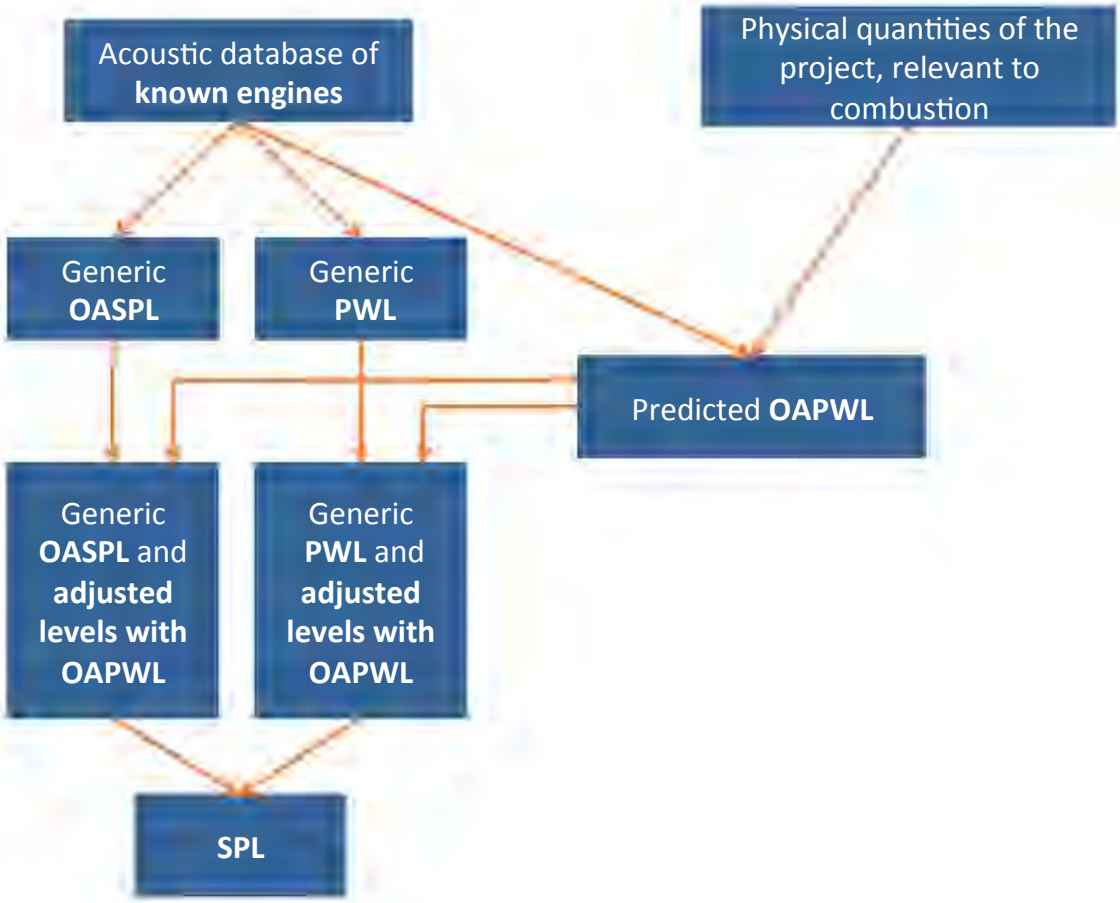

Figure 7.1: Flowchart of an empirical or semi-empirical prediction method

This model also takes into account the turbine attenuation of the combustion noise considering the number of stages N_{stage}. The last constant ξ considers the type of the nozzle exhaust (mixed or not mixed double flow).

The predicted OAPWL obtained with this method is compared with the experimental data and the CONOCHAIN results (Fig. 7.2). The evolution of the OAPWL is plotted in function of the inlet fan rotational speed $XN12R$. At low fan rotational speeds (between low and intermediate power conditions), the experimental downstream engine noise (jet and combustion) and CONOCHAIN predicted combustion noise levels are in agreement. This means that at these power-engine conditions, the combustion noise is dominant (jet noise negligible) and high enough to reach the downstream noise levels. CONOCHAIN provides a good estimation of the combustion noise evolution. The empirical method estimates levels lower than the experimental downstream engine noise. This method is calibrated with

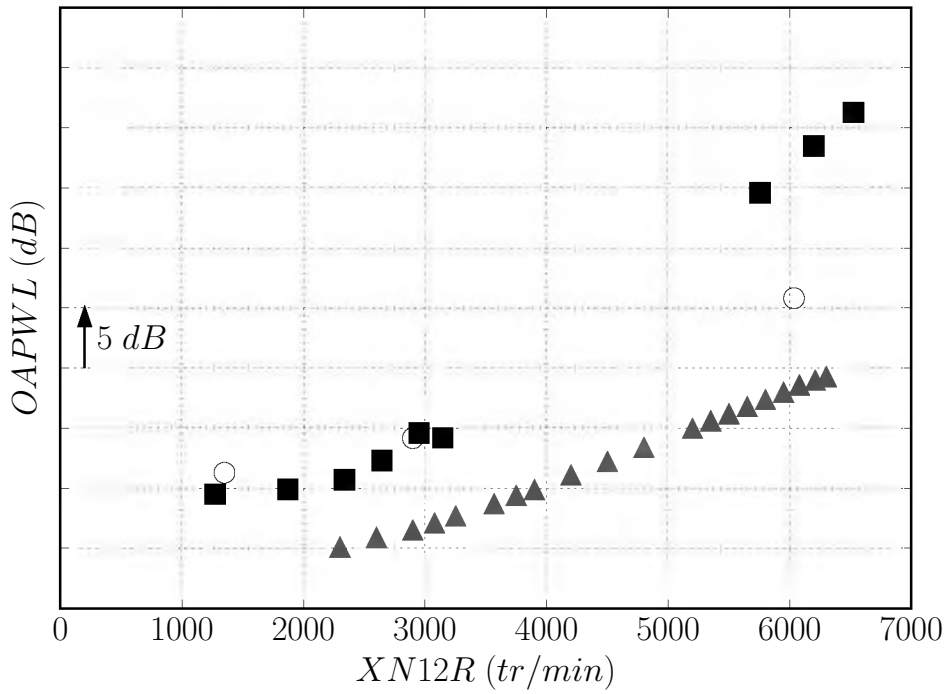

Figure 7.2: Over All Power Level (OAPWL) in the far field (45.72 m), total predicted combustion noise (○) and experimental OAPWL of downstream engine noise (■). OAPWL of predicted combustion noise with an empirical method (▲)

data which are supposed to be only combustion noise after noise sources decomposition and thus is dependent on the decomposition. After the intermediate power condition, different slopes can be observed. The experimental curve related to the downstream engine noise shows the strongest increase of noise levels. This is in agreement with the increase of jet noise in function of the increasing exhaust velocity at the secondary nozzle exit as shown in Fig. 7.3. According to Lighthill [1952, 1954], the velocity exponent of the velocity-scaling law for jet noise is eight. The predicted evolution of combustion noise with both CONOCHAIN and the empirical method also exhibits an increase in combustion noise when increasing the power-engine conditions. The rise is however smoother than for jet noise ($\propto U_j^{2.1}$). However, the empirical law underestimates combustion noise levels compared with CONOCHAIN. At higher operating conditions, the combustion noise is masked by the jet noise. Therefore, it is difficult to extract the combustion noise from the engine noise and thus it is difficult to built an empirical law for its prediction.

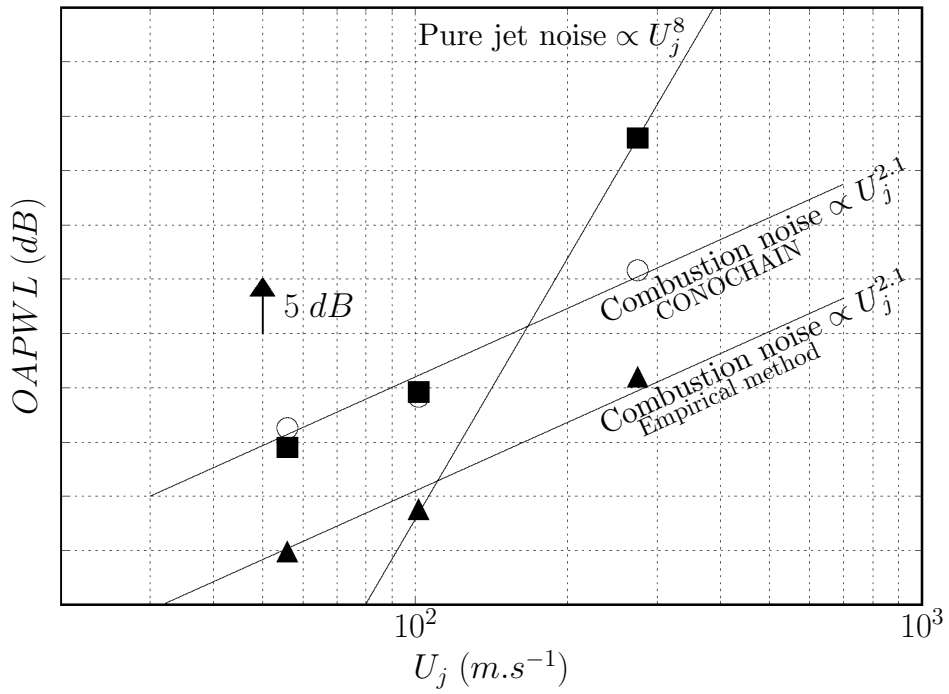

Figure 7.3: Over All Power Level (OAPWL) in the far field (45.72 m) related to the exhaust velocity U_j at the secondary nozzle exit. Total predicted combustion noise (○) and experimental OAPWL of downstream engine noise (■). OAPWL of predicted combustion noise with an empirical method (▲)

Considering the velocity-scaling law of Lighthill [1954], it could be suggested that jet noise becomes dominant for exhaust velocity greater than 180 m.s^{-1} and that below this value combustion noise is not negligible.

More investigations are required to find the limits of the empirical methods and understand why both prediction methods (CONOCHAIN and the empirical law) give different estimations of combustion noise. However, it must be reminded that the empirical law used correlations with only some of the physical variables involved in the combustion process and that this method is also dependent on the noise decomposition which assumes no interaction between each noise source. Moreover, the increase of direct noise due to thermoacoustic instability as well as the increase of indirect noise due to different acceleration through different number of turbine stages are not considered. This method is also constrained by the lack of available engine data. On the contrary, CONOCHAIN allows to

solve the combustion problem considering more physical interactions (chemistry, turbulence, acoustics with real combustor design). This prediction method tends to say that the combustion noise is not negligible and that the noise levels are more important than the one estimated with the empirical law or obtained from the noise decomposition.

Chapter 8

Using LES for combustion noise propagation to the far-field

Abstract In order to consider the combustion noise propagation in a jet flow (i.e. shear layer refraction, a phenomenon which was not taken into account in Chapter 6), the jet flow has to be resolved using LES. LES has the advantage to solve multi-physical and multi-scale problems. Therefore, the interaction between acoustics and turbulence can be taken into account. To do so, LES of jet flow are performed at the low and high power conditions of a typical dual-stream turbo-engine presented in chapter 5. This chapter is divided into three sections:

- the first section is dedicated to the presentation of the numerical setup and to the description of the mean aerodynamic features of the jet flow at both operating points,
- the second section deals with the injection of combustion noise in the LES of jet flow and investigates the impact of perturbations coming from combustion on the mean features of the flow,
- the last one discusses the combustion noise influence on the far-field acoustic propagation.

One aspect discussed here is the fact that most noise strategies assume that combustion noise and jet noise do not interact: the CONOCHAIN itself uses this assumption, computing combustion noise alone and adding it to jet noise. The present chapter, using LES for the jet itself, allows to check the validity of this assumption and shows that: combustion noise forcing not only produces noise which propagates downstream, but it also changes the flow itself at the nozzle exit, thereby modifying jet noise. This important result indicates that we may have to revisit classical noise computation methods where combustion noise and jet noise are supposed to be independent (Fig. 8.1).

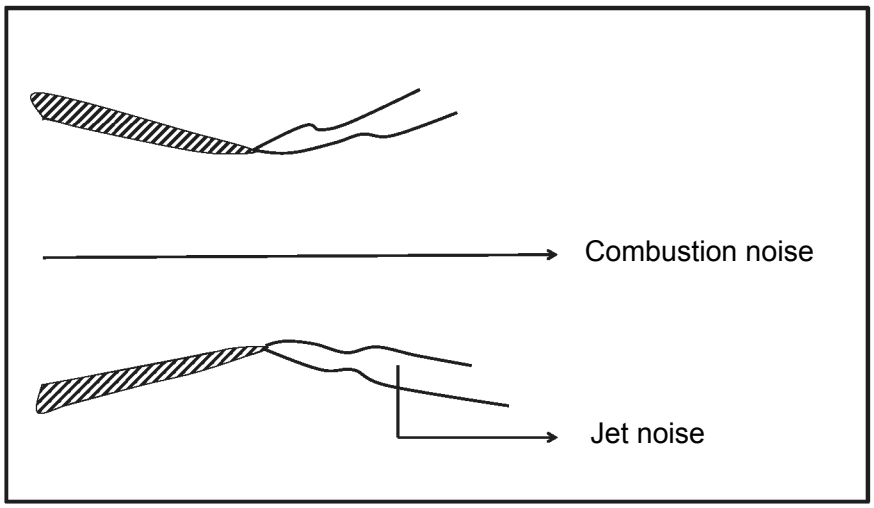

(a)

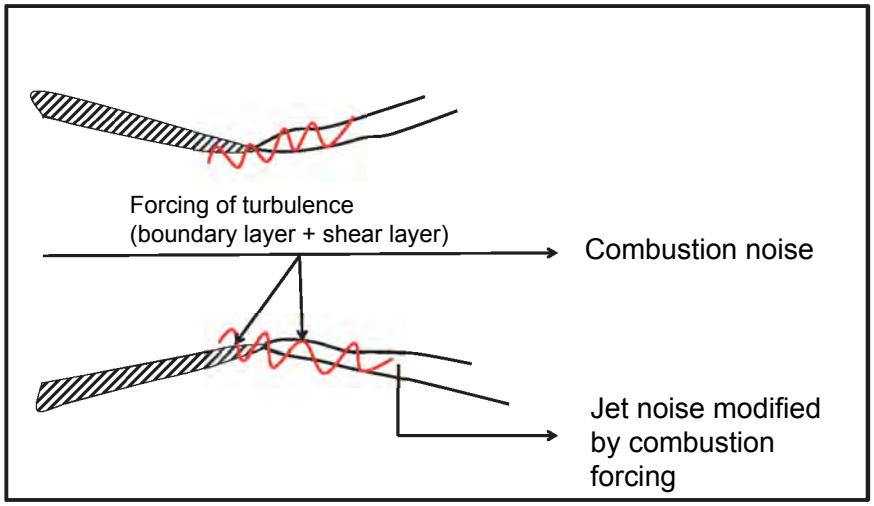

(b)

Figure 8.1: a) Classical view to compute total noise: combustion noise and jet noise are uncorrelated. b) Proposed view obtained from LES of forced and unforced jet noise.

8.1 Simulations of a double stream jet in a complex configuration

8.1.1 Jet flow characteristics

The characteristics of the double stream jet flow are summarized in Table 8.1 for the two computed operating points. All geometrical dimensions have been scaled

	Low power	High power
Mach number primary jet ($M_p = U_p/c_p$)	0.07	0.42
Mach number secondary jet ($M_s = U_s/c_s$)	0.17	0.9
Reynolds number primary jet ($Re = UD/\nu$)	244 425	1 985 545
Reynolds number secondary jet	3 495 500	18 045 790
LES Reynolds number primary jet ($Re/10$)	24 442	198 554
LES Reynolds number secondary jet	349 550	1 804 579
Inlet temperature ratio (T_p/T_s)	3.03	3.04

Table 8.1: Simulation parameters of the double stream jet

by a factor 1/10 to obtain Reynolds numbers based on the jet diameter that can be resolved by LES at a reasonable computational cost. The flow conditions such as temperature, pressure and Mach number have been conserved to be as close as possible to the real conditions and to have the good acoustic propagation in free field.

8.1.2 Numerical parameters

As for the numerical simulations of the combustion chamber, the unstructured parallel compressible LES solver AVBP is used for the computations of jet flow. Contrary to the former combustion simulations, the selected numerical scheme is TTG4A, third order accurate in space and fourth order accurate in time (Donea 1984). This scheme is chosen for its better behavior with hybrid meshes. It does not exhibit spurious aliasing noise at high frequency as TTGC (Selmin 1987).

Colin's artificial viscosity sensor (Colin et al. 2000) is used to reduce numerical instability in zones with strong gradients. Indeed, strong thermal and velocity gradients exist in the shear layers. Moreover, the Sigma sub-grid scale model (Nicoud et al. 2011) is used to close the LES equations as it has a correct asymptotic behavior for both wall-bounded flows and free stream flows.

8.1.3 Mesh and boundary conditions

8.1.3.1 Mesh

The computational domain is axisymmetric but a full 3D mesh is used. Denoting

with D_s the diameter of the secondary nozzle exit, the computational domain has a radius of 14 D_s and a length in the streamwise direction of 40 D_s. Primary and secondary nozzles are fully computed as shown in Fig. 8.2.

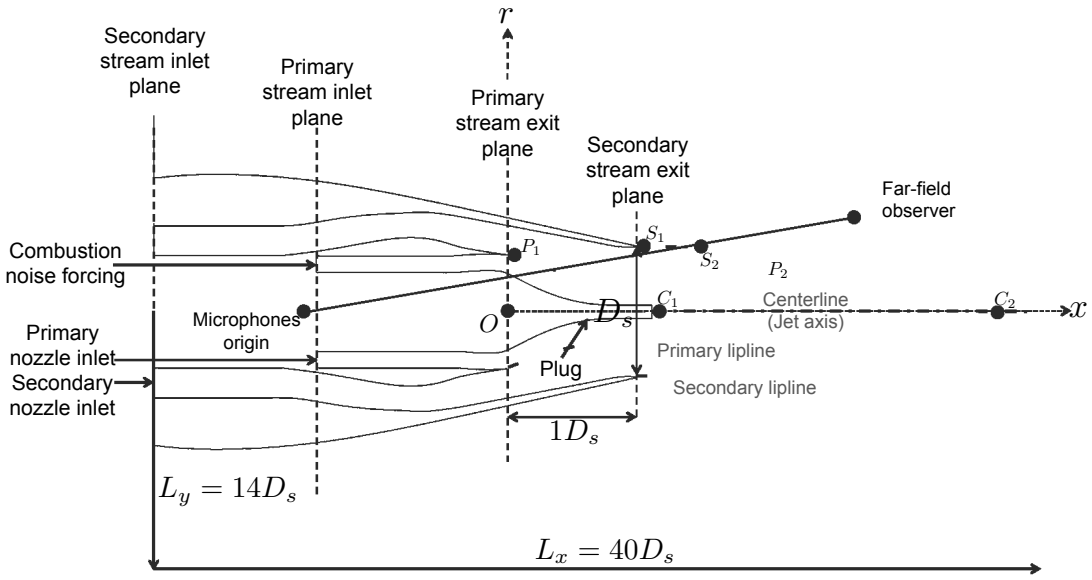

Figure 8.2: Illustration of the computational jet domain and different planes used in the simulations and in the results analysis.

The geometry is discretized with an hybrid mesh, tetrahedra and prisms, in order to accurately capture both the jet flow features and the acoustic waves in the far field (Fig. 8.3). Hence, a fine discretization is required in the boundary layers and in the mixing layers (Fig. 8.4). At the nozzle walls, boundary layers are solved with prismatic layers. The maximum aspect ratio (ratio between the prism width and its height) is 20, in order to have a good prediction of the velocity profiles and of the Mach numbers. The main sources of jet noise are located in the mixing layers, therefore more points are needed in these zones to accurately predict the acoustic sources of jet noise. Prior RANS simulations have been used to focus on zones where more points are required. In accordance with previous simulation of coaxial jet noise (Sanjose et al. 2014), the characteristic cell size is about 0.006 D_s near the nozzle lips and 0.01 D_s in the main acoustic source region ($x < 9$ D_s). A finer mesh is also used for the simulations in which the characteristic tetrahedral cells size is divided by a factor 1.3, leading to a cell size of 0.0046 D_s near the nozzle lips and 0.008 D_s in the main acoustic source region. These meshes allow to reach a wall y^+ of 10 and 30 at low power and high power conditions in the first mesh M_1, while a maximum y^+ of 3 and 15 is reached in the second finer mesh M_2.

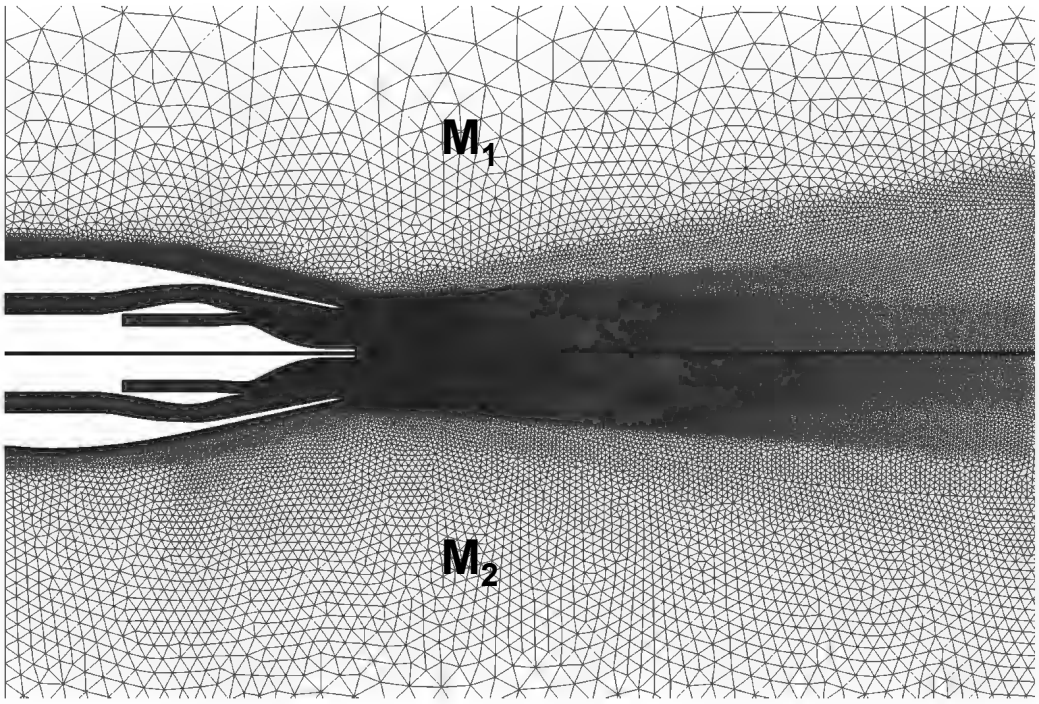

Figure 8.3: View of the mesh refinement in the main acoustic zone for M_1 and M_2.

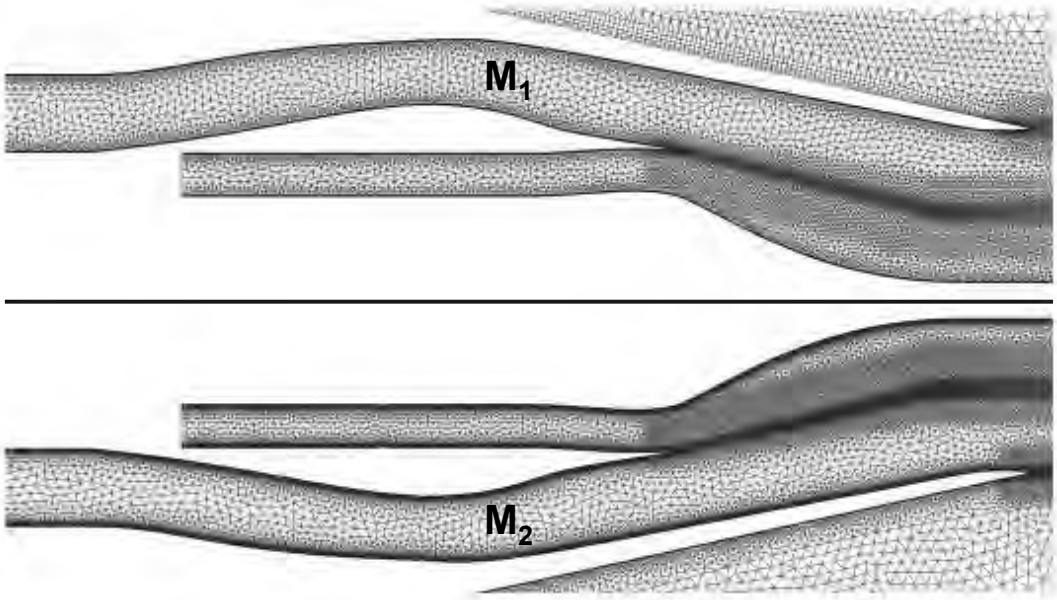

Figure 8.4: Detailed view of the mesh refinement in the nozzle vanes for M_1 and M_2.

On the finer mesh, roughness structures are introduced to trigger turbulence. These small bumps are added 0.5 D_s before the primary nozzle exit and 1.5 D_s before the secondary nozzle exit, to enhance the turbulence development of the external mixing layers, Fig. 8.5. The height of the tripping structure is chosen as function of the thickness of the local boundary layer obtained by the resolved RANS (Sanjose et al. 2014). The height of the structure has arbitrarily been chosen as 0.5% of D_s.

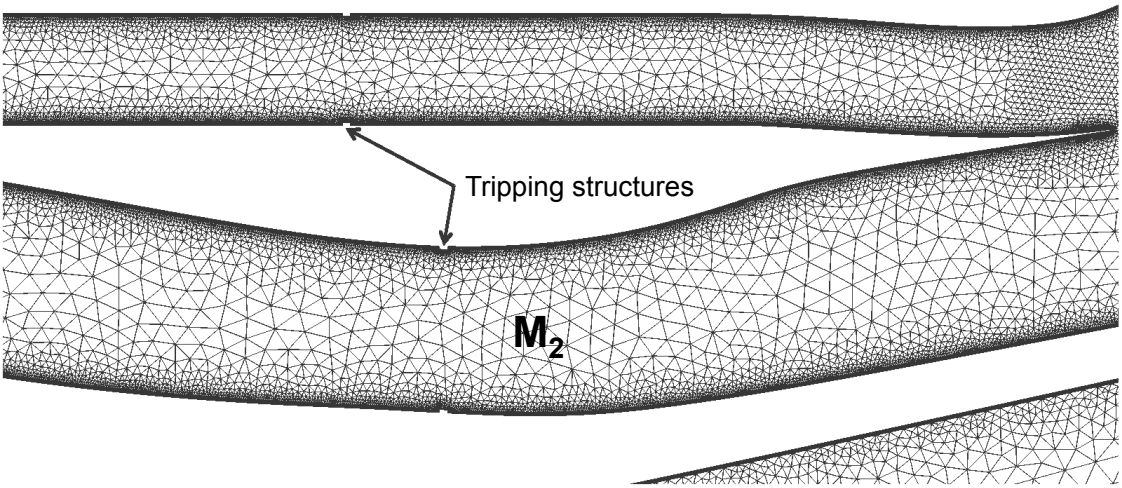

Figure 8.5: Tripping structures added in the nozzles vanes, M_2.

The mesh characteristics are summarized in Table 8.2.

	M_1	M_2
Prismatic elements	4.8 M	72.4 M
Prismatic layers	5	7
Tetrahedral elements	34.3 M	135.6 M
Total number of elements	39 M	208 M

Table 8.2: Mesh characteristics, M stands for millions.

8.1.3.2 Boundary conditions

Primary hot air is injected through a NSCBC inlet which is non-reflective at the frequencies of interest ($K_{prim} = 10000$, i.e a cut-off frequency of about 80 Hz Selle et al. 2004b). Relaxation coefficients are necessary to correctly control mean flow and to avoid mean flow values to drift. In the same way, a non-reflective NSCBC inlet is used for the secondary cold flow with a relaxation coefficient on the stagnation pressure ($K_{sec} = 1000$). A little co-flow is added to avoid recirculation zone on the external wall of the secondary nozzle as in Sanjosé et al. [2011]. Non-reflecting NSCBC outlet boundary conditions are used, imposing a static pressure equal to the atmospheric pressure. A sponge layer is added at the end of the domain (20 D_s downstream of the primary nozzle exit) to avoid acoustic reflections. The nozzles walls are treated as no-slip adiabatic walls, without wall-law model as $y^+ < 40$.

The initial conditions of the simulations and the target variables of all the boundary conditions have been set using axi-symmetric RANS simulations with the ANSYS-Fluent solver. These RANS simulations have been performed on a hybrid mesh resolving the boundary layers in the nozzle with a maximum y^+ value of about 3. A standard k - ϵ turbulent model and a first order upwind numerical scheme for the turbulent variables have been used. A 2^{nd} order high resolution scheme is chosen for all conservative variables as in Fosso-Pouangué et al. [June 4-6 2012]; Sanjose et al. [2014]. The LES simulations have been converged on a sufficient sampling time of at least 400 τ_c (with the convection time τ_c defined as $\tau_c = t^* U_j / D_j$) to converge in terms of acoustic and turbulence statistics, using a CFL number of 0.7. The LES simulations on mesh M_2 have been initialized from the last solutions of the converged runs with M_1.

8.1.3.3 Impact of the plug exit boundary condition on jet flow simulations

In a first simulation, the plug exit (Fig. 8.6) was defined as a wall, so that it was acting like a non profiled bluff-body, surrounded by the primary hot stream. Due to this bluff-body, a recirculation zone was created, and a Von Karman alley was observed in Fig. 8.6. This instability is characterized by a regular release of alternating vorticity vortices of opposite sign at the frequency f_0 corresponding to a Strouhal number of 0.2 ($St = f D_{plug}/U$), on either side of the plug. The vortex shedding was creating an acoustic excitation at the frequency f_0 as shown in the upper part of Fig. 8.7(a). This frequency was exciting the instability frequency of the secondary mixing layer which corresponds to $f_i = f_0/2$ (upper part of Fig. 8.7(b)). Consequently, all the acoustics of the system was driven by these Von Karman vortices.

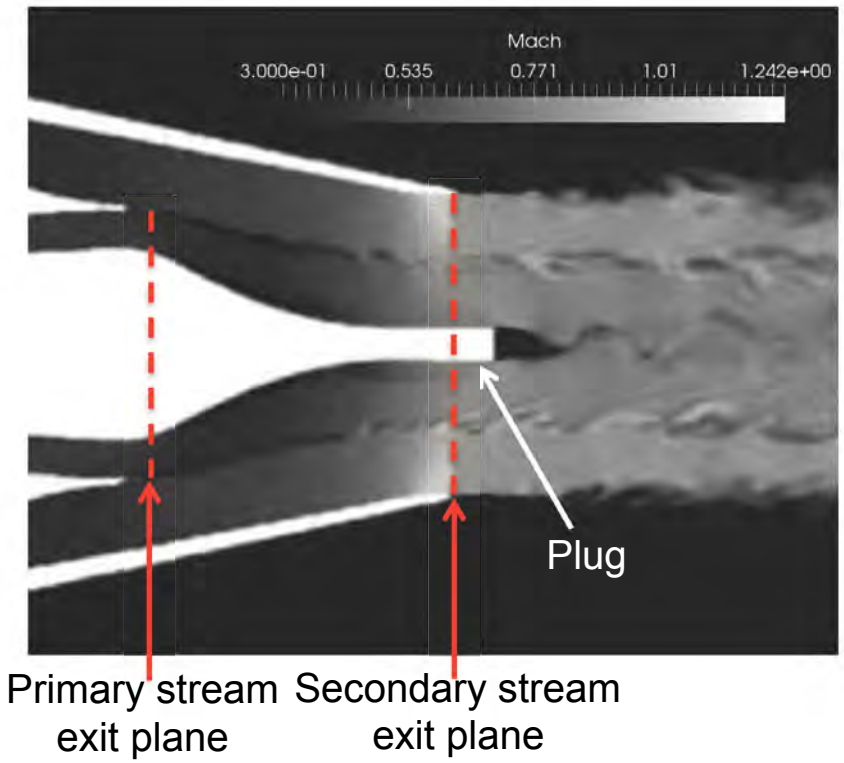

Figure 8.6: Instantaneous Mach number field with Von Karman alley at the plug exit, at high power.

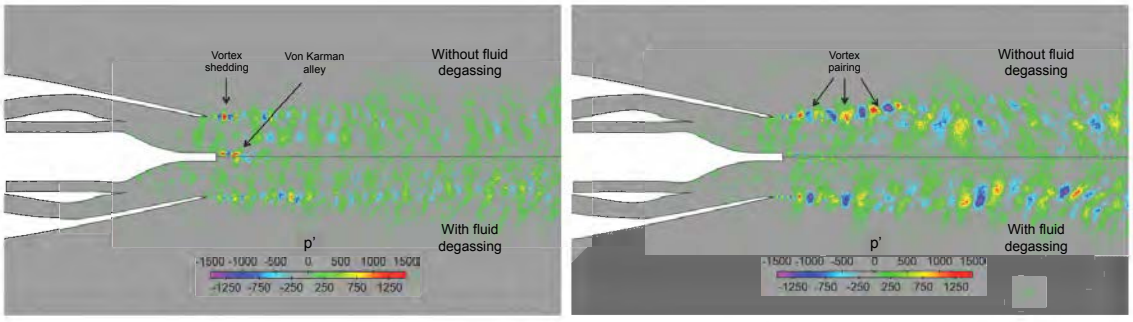

(a) $St = 0.2$ (b) $St = 0.1$

Figure 8.7: Comparison of instantaneous pressure fluctuation fields reconstructed from pressure module and phase at a) $St = 0.2$ and b) $St = 0.1$, between a closed plug (upper part) and a plug with a fluid degassing (lower part).

To solve this problem, the degassing of fluids is taken into account at the outlet of the plug. The temperature of ejection is assumed to be the mixing temperature

at the outlet of the nozzle (Fig. 8.8(a)). This temperature is computed as:

$$T_{mix} = \frac{\dot{m}_1 T_1 + \dot{m}_2 T_2}{\dot{m}_1 + \dot{m}_2}, \tag{8.1}$$

where T_1 and $\dot{m}_1$ stand for the temperature and the mass-flow rate of the primary hot flow and T_2, $\dot{m}_2$ stand for the temperature and the mass-flow rate of the secondary cold flow.

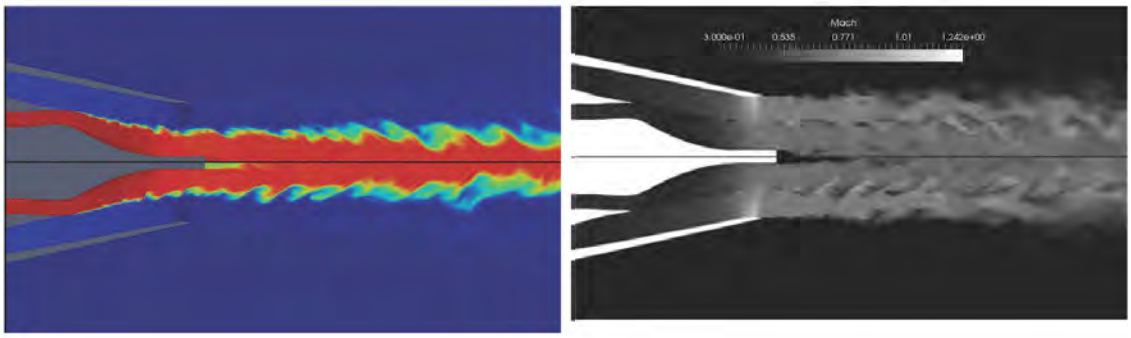

(a) Instantaneous temperature field (b) Instantaneous Mach number field

Figure 8.8: Comparison of instantaneous fields between a closed plug (upper part) and a plug with a fluid degassing (lower part).

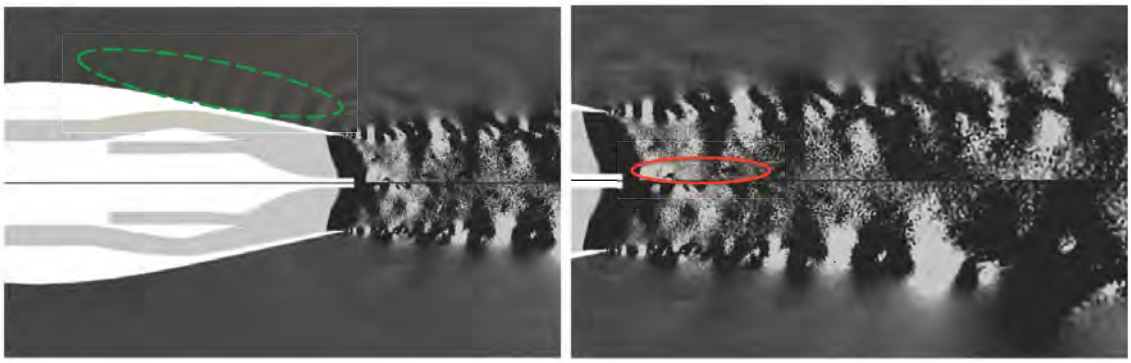

(a) Around the nozzles (b) In the jet flow

Figure 8.9: Comparison of pressure-fluctuations fields between a closed plug (upper part) and a plug with a fluid degassing (lower part).

This allows to attenuate the Von Karman alley that was observed at high frequency in former computations by blowing the recirculation zone, as shown in Figs. 8.8(b) and 8.7(a). Therefore, the mixing layers are no longer excited by this phenomenon (Figs. 8.7(b) and 8.9(b)). The upstream acoustic activity observed around the nozzle is also attenuated (Fig. 8.9(a)). The attenuation of the Von Karman signature can be evaluated more quantitatively by looking at the power spectral density of the radial velocity, on a probe localized just behind the plug (Fig. 8.10). The amplitude of the radial velocity fluctuations behind the plug decreases by a factor 1000.

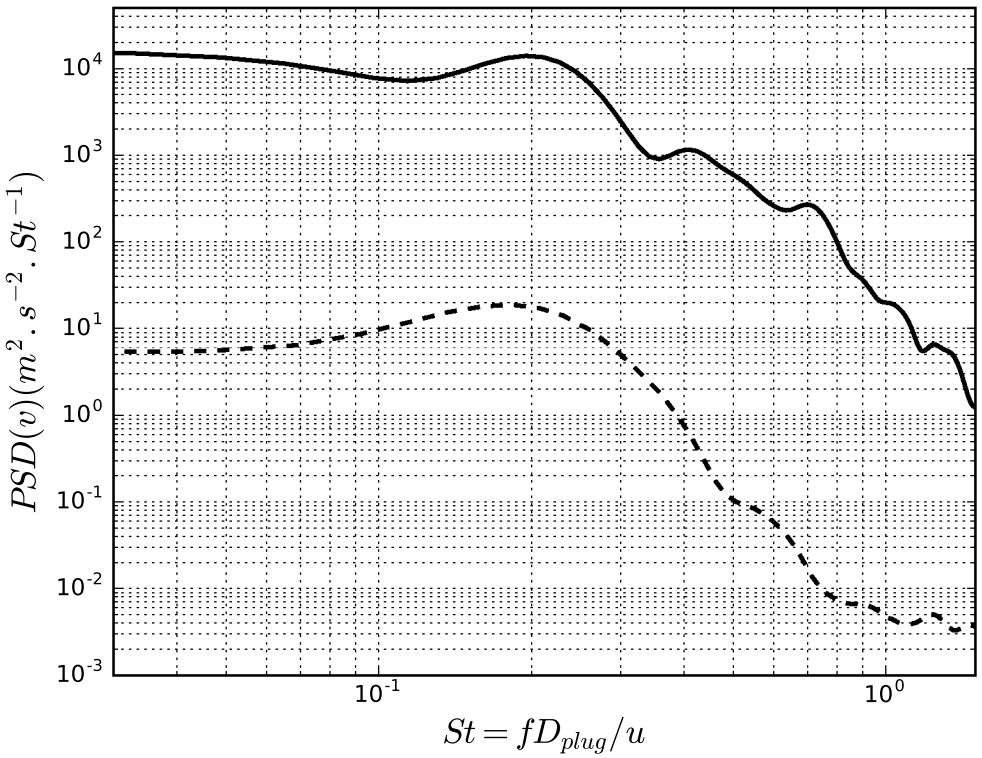

Figure 8.10: Power spectral density of the radial velocity at the plug exit (C_1 in Fig. 8.2), without fluid degassing (–), with fluid degassing (- -).

8.1.4 Aerodynamical features

8.1.4.1 Validation of the nozzle exit conditions

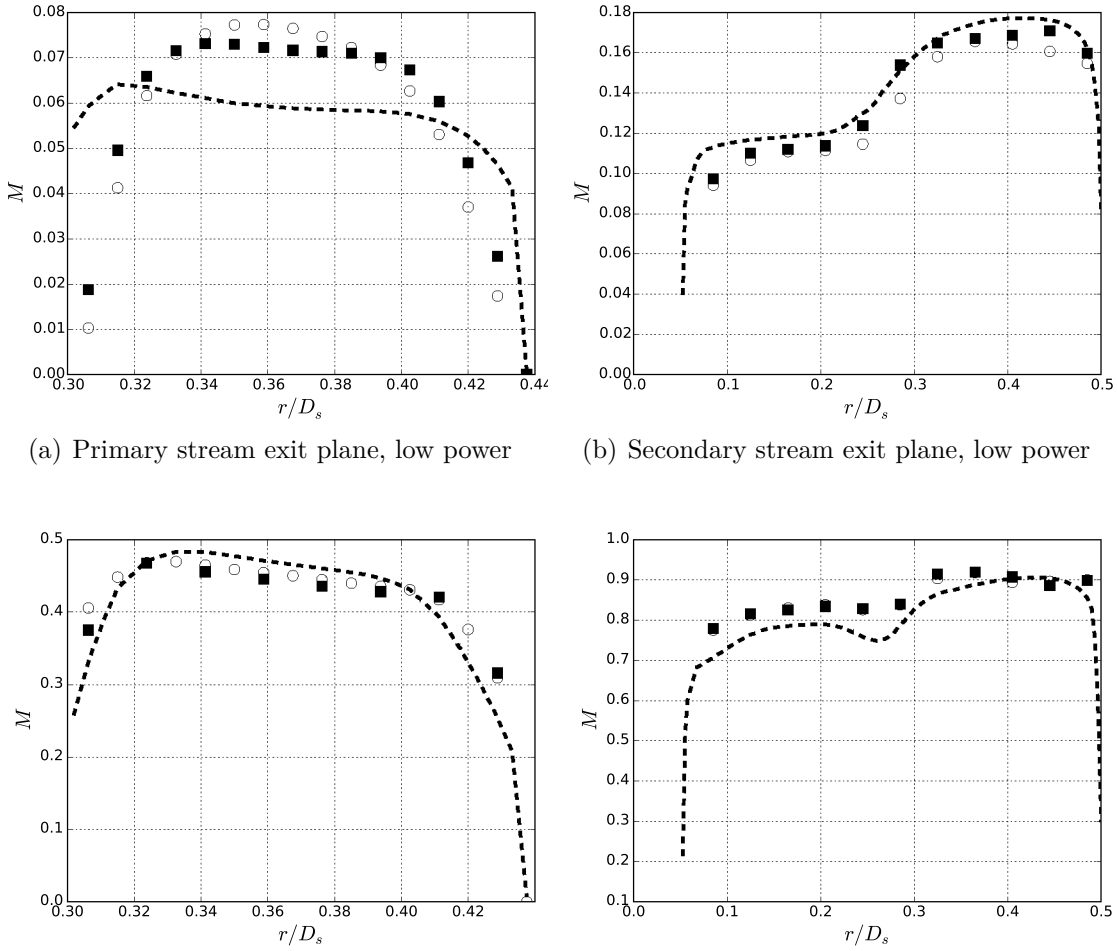

(a) Primary stream exit plane, low power

(b) Secondary stream exit plane, low power

(c) Primary stream exit plane, high power

(d) Secondary stream exit plane, high power

Figure 8.11: Mach profiles at the primary and secondary stream exits (Figs. 8.2 and 8.6), RANS Init (- -), M_1 (■) and M_2 (○).

Fig. 8.11 shows the mean Mach number profiles plotted at the exit of the primary and secondary nozzles, and compared with the initial RANS simulation that provides the boundary condition for the nozzle inlets. From bench data at low power, it is known that the outlet Mach number should be about 0.07 at the primary exit plane and about 0.17 at the secondary exit plane (Tab. 8.1). LES are able to reach these target values (Figs. 8.11(a) and 8.11(b)), contrarily

to the RANS simulation, that does not give the good bulk value for the primary exit plane. No conclusion on the profile shape can be obtained since no more information is available, but a recirculation zone appears around the plug, mostly due to its strong curvature, a weak flow velocity and to an insufficient discretization in this zone.

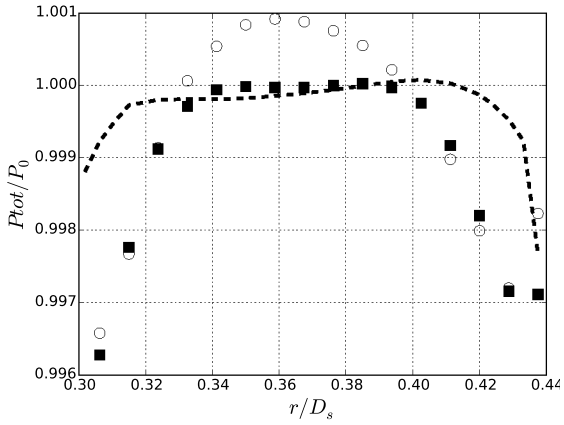

(a) Primary stream exit plane, low power

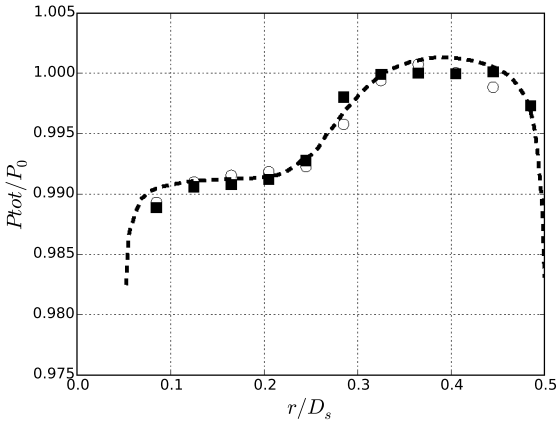

(b) Secondary stream exit plane, low power

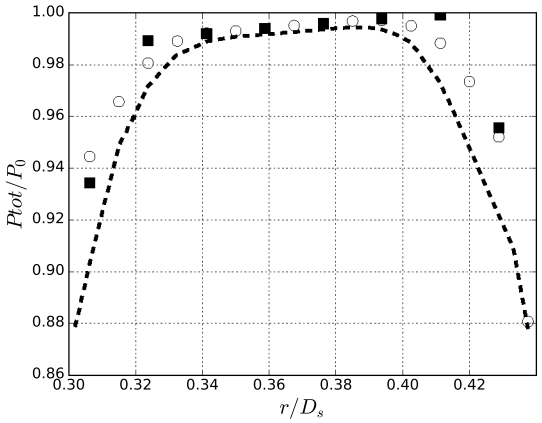

(c) Primary stream exit plane, high power

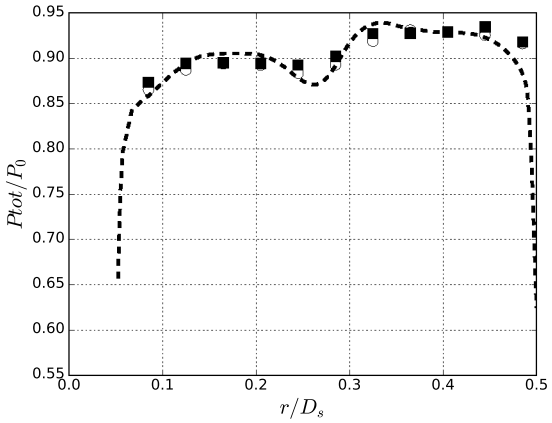

(d) Secondary stream exit plane, high power

Figure 8.12: Total pressure ratio profiles at the primary and secondary stream exits (Figs. 8.2 and 8.6), RANS Init (- -), M_1 (■) and M_2 (○).

At the secondary exit (Fig. 8.11(b)), both simulations with M_1 and M_2 exhibit similar Mach profiles. The shape of the profiles agrees with the profile obtained by RANS simulation.

For the high power case, all simulations are in agreement in terms of shape and mean Mach number value, 0.48 for the primary nozzle exit (Fig. 8.11(c)) and 0.9 for the secondary nozzle exit (Fig. 8.11(d)). This confirms the capacity of the LES code to predict the good levels and profiles of Mach number with prismatic layers as in Sanjose et al. [2014].

By looking at the total pressure levels at the primary and secondary nozzles exit planes for the low power case (Figs. 8.12(a) and 8.12(b)), it can be noted that the levels are similar between the initial RANS simulation and both LES with M_1 and M_2. Moreover, the profile shape is recovered at the secondary stream exit plane (Fig. 8.12(b)), meaning that the pressure loss inside the nozzle is well-estimated according to the RANS simulation. On the contrary, at the primary nozzle exit (Fig. 8.12(a)), the pressure gradients that develop near the plug due to the strong curvature are over-estimated as it was observed in the EXEJET simulations (Sanjose et al. 2014). More grid refinement is required.

For the high power case (Figs. 8.12(c) and 8.12(d)), once again the total pressure profiles agree in shape and magnitude meaning that the boundary layers are well resolved. Moreover, in Fig. 8.12(c) both LES predict less pressure loss than the RANS simulation for the primary nozzle exit plane close to the walls.

8.1.4.2 Jet flow development analysis

As no experimental data is available to validate the jet flow development, only a descriptive analysis can be done. The mean flow field is evaluated along a longitudinal plane.

The mean velocity fields extracted on the longitudinal plane for the two grids M_1 and M_2 are compared for both operating points in Fig. 8.13. The mean velocity field $\bar{U}$ is non-dimensionalized by the bulk velocity of the secondary stream at the exhaust plane, $\bar{U}_s$. The flow behavior can be described as a dual stream jet with two separated jets as described in Ko and Kwan [1976]. Because of the plug, a recirculation zone appears behind it (**A**). For both operating points, its size is smaller with the grid M_2. In Fig. 8.13(a), another recirculation zone develops around the plug at the end of the primary nozzle (**B**). This zone is reduced at the high power operating point (Fig. 8.13(b)) as the exhaust velocity is higher.

By comparing the low power case to the high power case, similar development of the jet can be observed. The speed of the central primary jet U_p is higher than that of the secondary annular jet U_s. However, in Fig. 8.13(b) a weak shock can be observed just before the outlet of the secondary nozzle for the high power case, as it was already shown in Fig. 8.6. This weak shock is located between the secondary

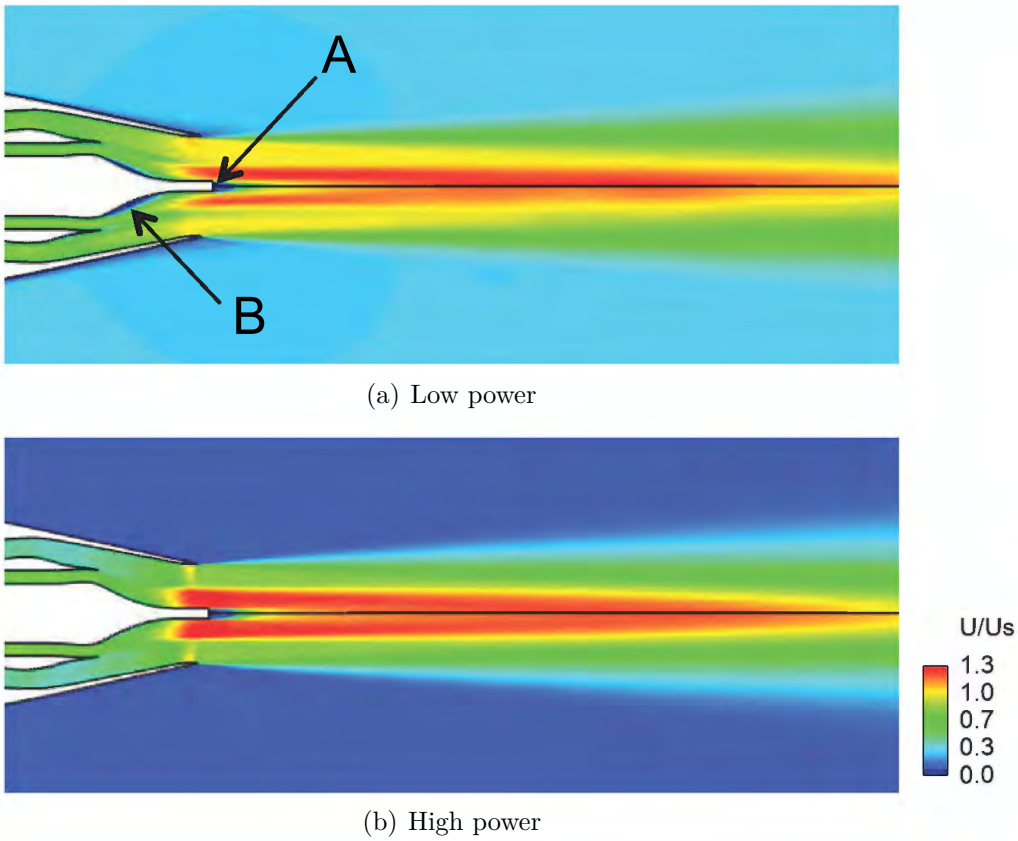

(a) Low power

(b) High power

Figure 8.13: Dimensionless mean velocity fields up to $x/D_s = 8.1$, $U/\bar{U}_s$, M_1 (upper part) and M_2 (lower part).

nozzle and the internal mixing layer. For the low power case in Fig. 8.13(a), the development of the secondary stream is totally different. The jet is strongly accelerated just before the secondary nozzle exit and then it is decelerated in the external mixing layer with the entrainment of ambient air in the jet.

The primary jet core length (zone delimited by the internal mixing layer in Fig. 3.5) seems a little longer with the M_2 mesh for both operating points. This suggests a vortex pairing in the internal mixing layer with M_1. The jet core length can be verified by looking at profiles of the mean velocity and the axial turbulent velocity extracted on the jet axis in Figs. 8.14(a) and 8.14(c). The mean velocity level is of the same order of magnitude for both meshes. With a finer resolution of the boundary layers and mixing layers with M_2, as well as the tripping, the primary jet core length is a little longer, but not significantly. This indicates that the tripping is probably not enough efficient. The jet core length L_c is characterized by the axial coordinate where the axial mean velocity $\bar{U}_c$ equals 95% of the bulk

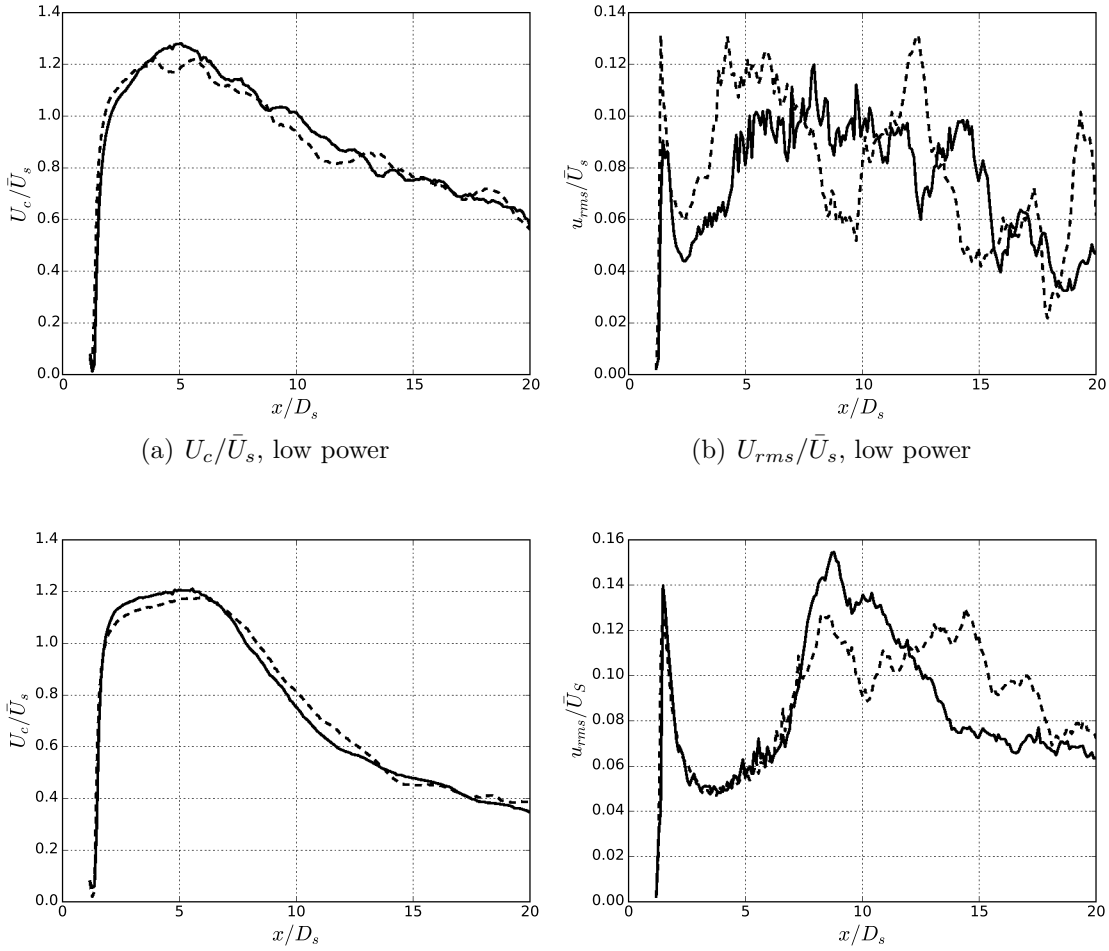

(a) $U_c/\bar{U}_s$, low power

(b) $U_{rms}/\bar{U}_s$, low power

(c) $U_c/\bar{U}_s$, high power

(d) $U_{rms}/\bar{U}_s$, high power

Figure 8.14: Profiles of the axial velocity $U_c/\bar{U}_s$ and the axial fluctuating velocity $U_{rms}/\bar{U}_s$ on the centerline from the primary nozzle exit (Fig. 8.2). M_1 (–) and M_2 (- -).

velocity at the secondary nozzle exit plane $\bar{U}_s$. Using this relation, the low power case exhibits a jet core length of about 10 D_s (Fig. 8.14(a)), while in the high power case the jet core length is about 8 D_s (Fig. 8.14(c)).

In Fig. 8.14(d), a peak at about 1.5 D_s can be observed in the axial fluctuating velocity profiles, corresponding to the recirculation zone just behind the plug. After this peak, the fluctuating levels strongly decrease, from 14 % to 5 % for the high power case. At the end of the primary jet core length, the fluctuating levels rapidly increase and reach a quasi-constant level of 14 % for M_1 and 12 % for M_2.

The fluctuating velocity levels are finally attenuated after 12 D_s for M_1 and 15 D_s for M_2. In Fig. 8.14(b), the same observations can be made for the low power case but with lower amplitudes of fluctuating velocity, which stabilize around 10 %. After 10 D_s, several peaks are observed due to the lack of convergence in time.

For a double stream jet (Fig. 8.15), the 1D profiles $r_{0.5}$ can be obtained by defining a line crossing the secondary jet core (zone between the internal and the external mixing layers). These profiles represent the radius where at the same axial position the velocity equals half of the secondary jet core velocity. The radial jet expansion is similar with both meshes whatever the operating point. In Fig. 8.15(a) at low power, a smooth and linear growth of the external mixing layer can be observed with a slope of 0.1. For the high power case (Fig. 8.15(b)), a transition zone where the thickness varies little is observed, up to 4 D_s. After this point, a quasi-linear radial expansion is observed with a slope of 0.11. In both cases, these values correspond to the rate of enlargement of single jets (Daviller 2010).

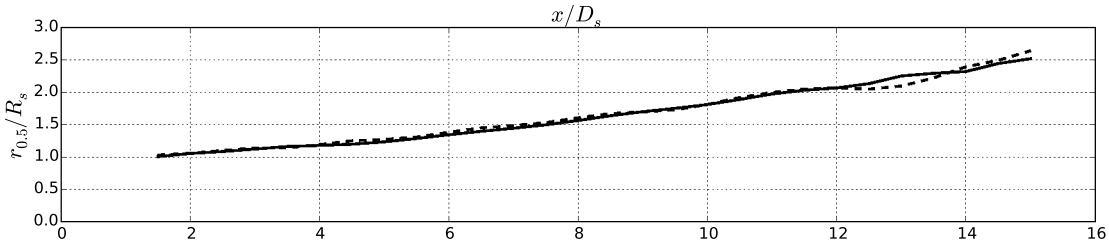

(a) Low power

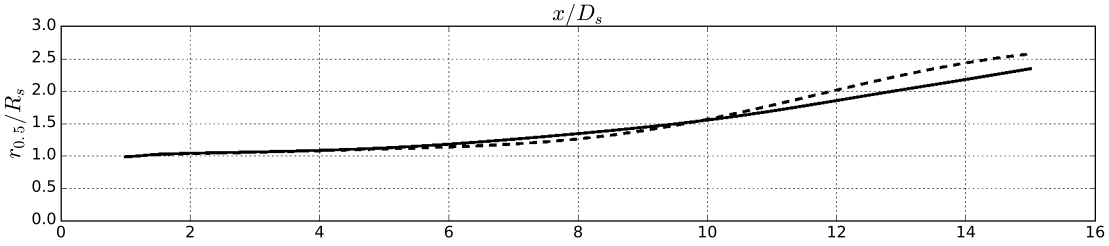

(b) High power

Figure 8.15: Profiles of $r_{0.5}$ of the external shear layer. M_1 (–) and M_2 (- -).

Fig 8.16 shows the mean temperature $\bar{T}$ fields, normalized by the bulk temperature at the inlet of the primary stream $\bar{T}_{p,0}$. A hot central zone can be seen, corresponding to the primary jet core. Radially, the temperature decreases when the hot primary jet interacts with the secondary cold one, in the so-called internal mixing layer. At high power (Fig. 8.16(b)), the primary jet core cools down faster than at low power (Fig. 8.16(a)), as a sign of higher mixing.

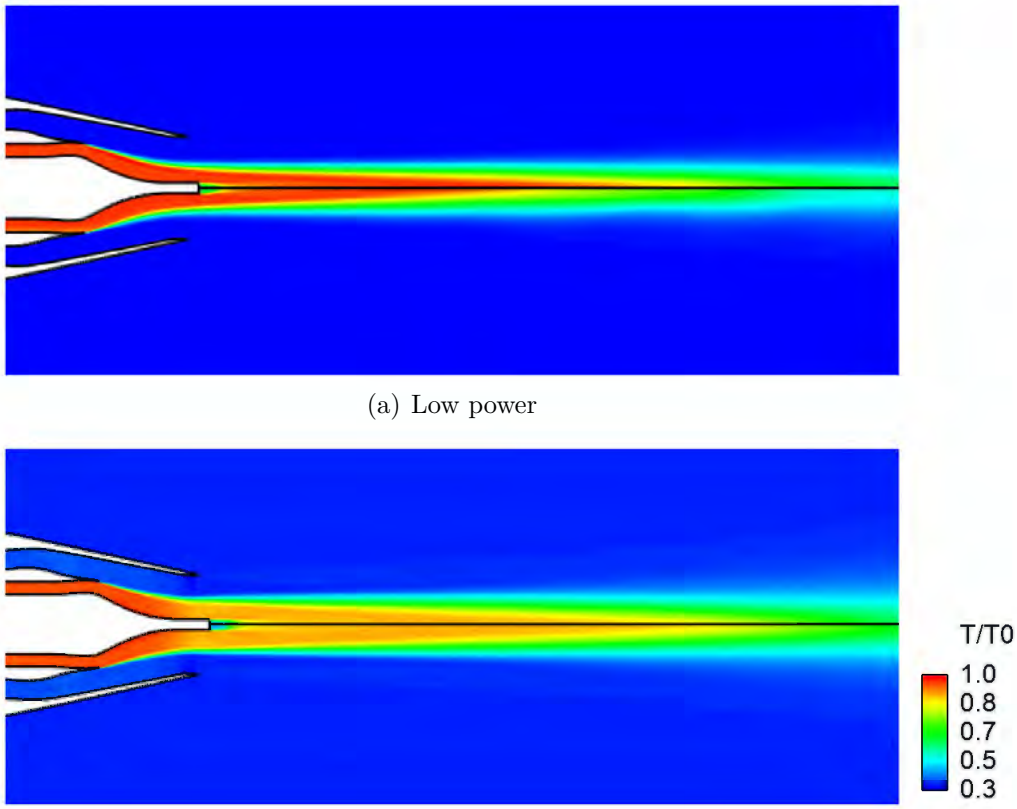

(a) Low power

(b) High power

Figure 8.16: Dimensionless mean temperature fields up to $x/D_s = 8.1$, $T/\bar{T}_{p,0}$, M_1 (upper part) and M_2 (lower part)

The turbulent kinetic energy fields (Fig. 8.17) show that the turbulent transition of the internal and external mixing layers occurs at the end of the nozzle lips for both meshes and both operating points. However, some differences can be noted. In Fig. 8.17(a), for the M_1 mesh, high levels of turbulent kinetic energy are observed at the end of the secondary nozzle lips and at the end of the primary jet core. The area of these zones is reduced by using the finer mesh M_2 as expected. Due to the finer resolution close to the nozzle walls and the tripping structures with the M_2 grid (lower part of Fig. 8.17(a)), the turbulence transition is triggered sooner in the nozzles than for the M_1 mesh, particularly in the secondary nozzle. The low power case exhibits a longer and wider area with high levels of turbulent kinetic energy just behind the secondary nozzle lip compared with the high power case. In Fig. 8.17(b), the junction between the internal and the external mixing layers occurs farther in the development of the jet leading to a longer secondary jet core for the M_2 mesh as confirmed in Fig. 8.18 by looking at profile of the mean

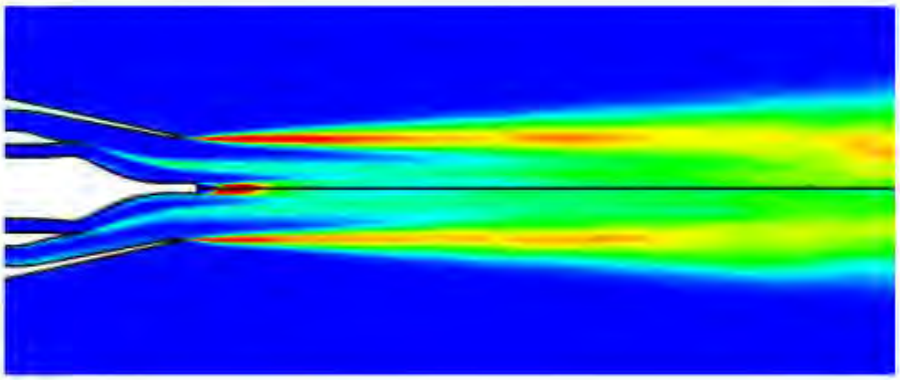

(a) Low power

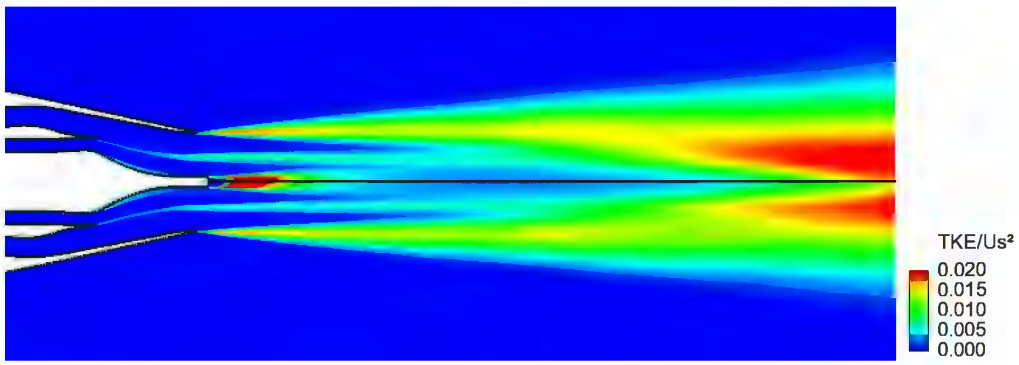

(b) High power

Figure 8.17: Dimensionless turbulent kinetic energy fields (k) up to $x/D_s = 9.5$, $k/\bar{U}_s^2$, M_1 (upper part) and M_2 (lower part)

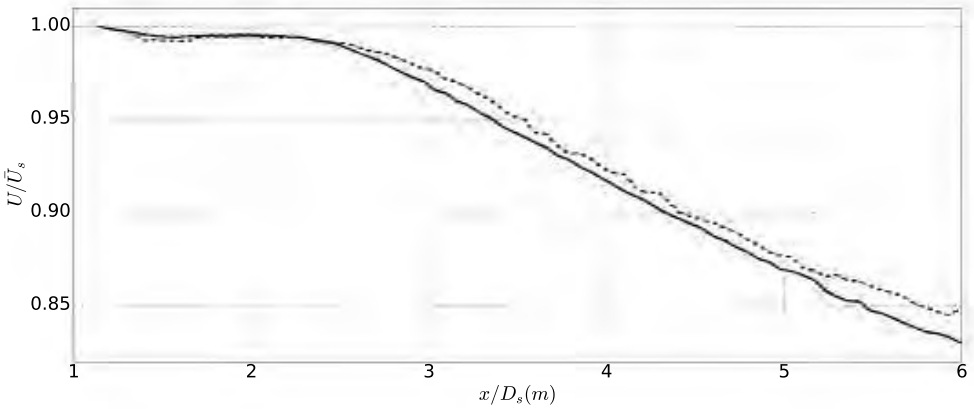

Figure 8.18: Profile of the mean velocity $U/\bar{U}_s$ on a line crossing the secondary jet core. M_1 (–) and M_2 (- -).

velocity extracted on a line crossing the secondary jet core.

8.1.4.3 Vortex tripping effects

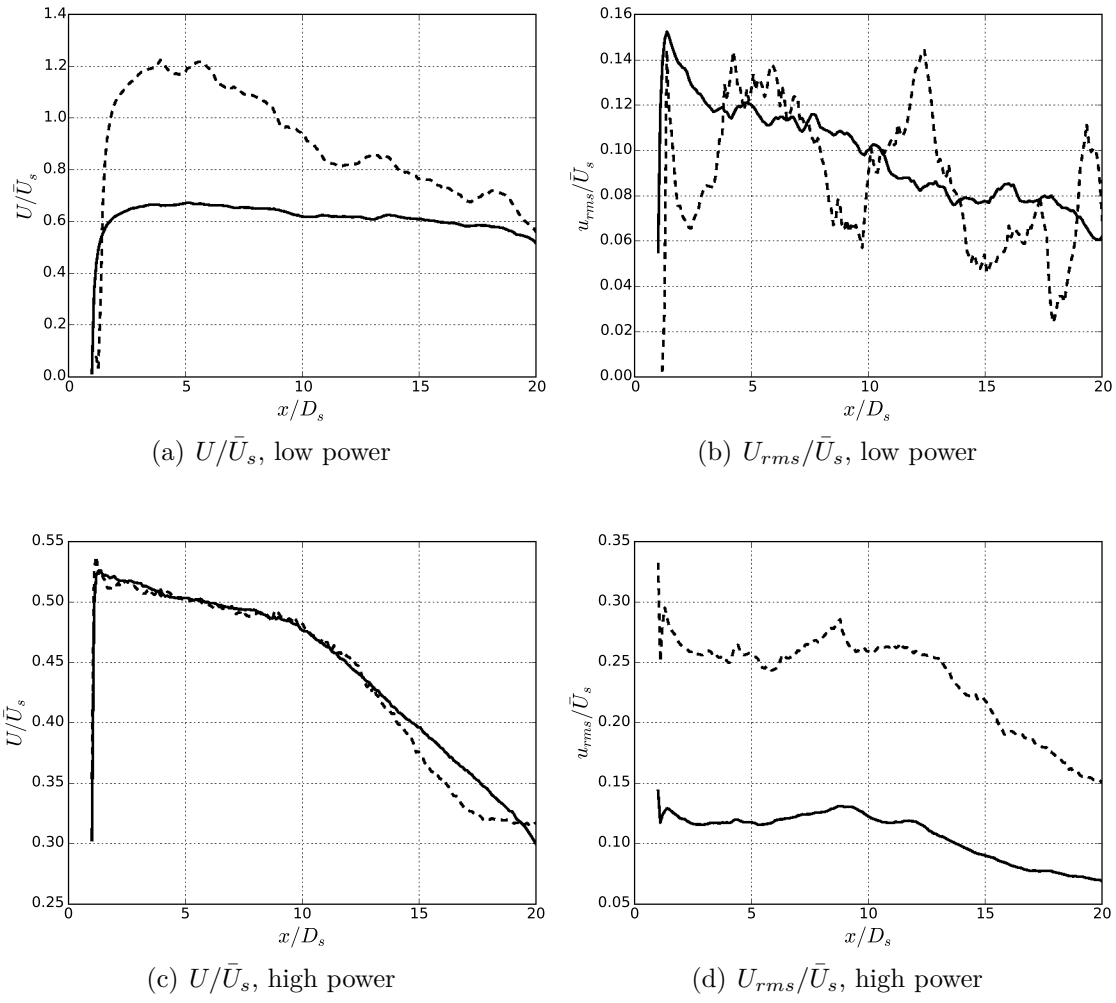

(a) $U/\bar{U}_s$, low power

(b) $U_{rms}/\bar{U}_s$, low power

(c) $U/\bar{U}_s$, high power

(d) $U_{rms}/\bar{U}_s$, high power

Figure 8.19: Profiles of the axial velocity $U/\bar{U}_s$ and the axial fluctuating velocity $U_{rms}/\bar{U}_s$ on the lip-line of the secondary stream (Fig. 8.2). With M_1 grid (–) and M_2 grid (- -).

In order to measure the efficiency of the tripping with the M_2 mesh, mean and axial turbulent velocity profiles on the lip-lines of the primary and secondary nozzle are plotted in Figs. 8.19 and 8.20. No conclusions will be drawn regarding the low power case as it is not sufficiently converged in time. For the high power

case, the mean velocity profiles on the lip-lines of the primary (Fig. 8.20(c)) and secondary (Fig. 8.19(c)) nozzles are similar between M_1 and M_2, meaning that the mean flow is well predicted with both meshes.

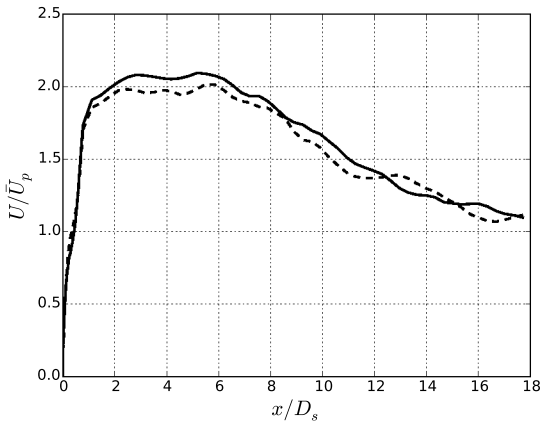

(a) $U/\bar{U}_p$, low power

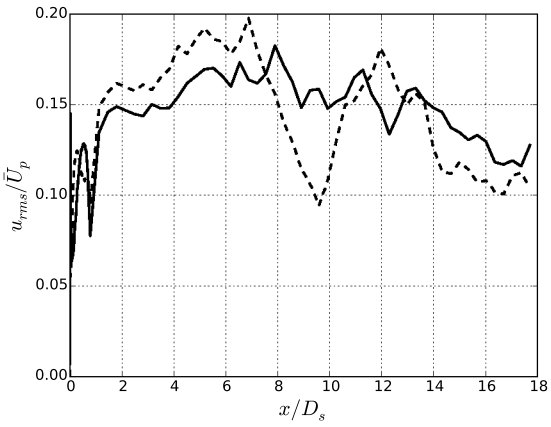

(b) $U_{rms}/\bar{U}_p$, low power

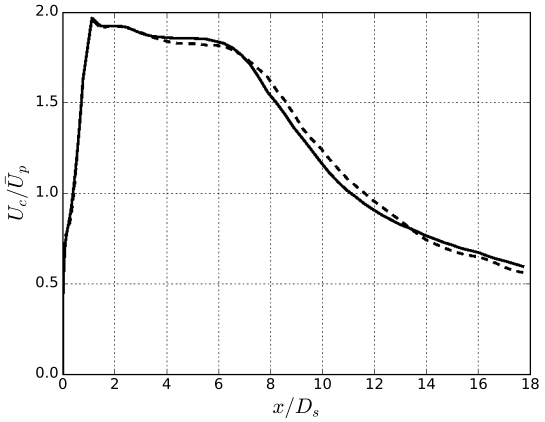

(c) $U/\bar{U}_p$, high power

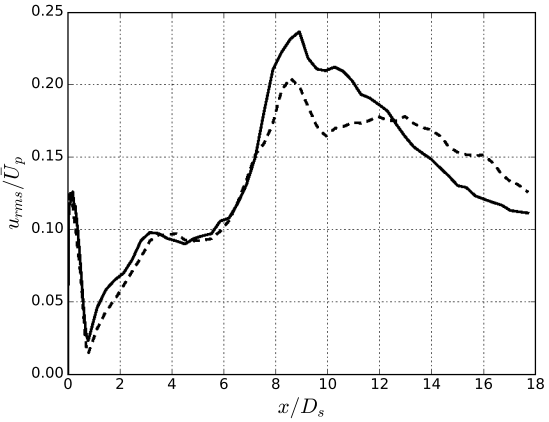

(d) $U_{rms}/\bar{U}_p$, high power

Figure 8.20: Profiles of the axial velocity $U/\bar{U}_p$ and the axial fluctuating velocity $U_{rms}\bar{U}_p$ on the lip-line of the primary stream (Fig. 8.2). With M_1 grid (–) and M_2 grid (- -).

In Fig. 8.19(d), with tripping, the levels of the axial turbulent velocity are highly amplified from 12% to 25% in the external mixing layer. The overshoot observed at the junction of the mixing layers on the primary lip-line (about 9 D_s in Fig. 8.20(d)) is attenuated and a maximum constant value of about 16% is reached from 10 to 14 D_s. To conclude, the tripping induces more turbulent fluctuations at end of

the secondary nozzle. This explains that the second jet core is longer with M_2 as shown in Fig. 8.17(b). The levels of turbulent velocity are not amplified on the primary lip-line meaning that the tripping is less efficient in the primary nozzle although the overshoot has been attenuated.

8.1.5 Noise source analysis

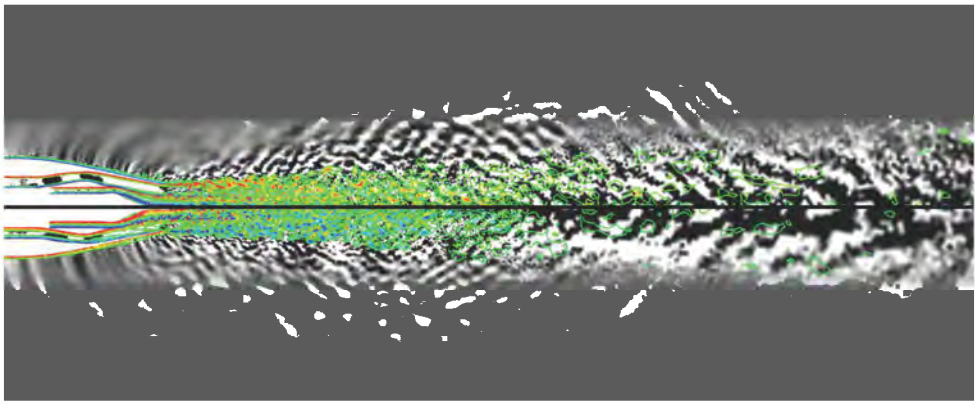

(a) In the jet flow up to $x/D_s = 21$

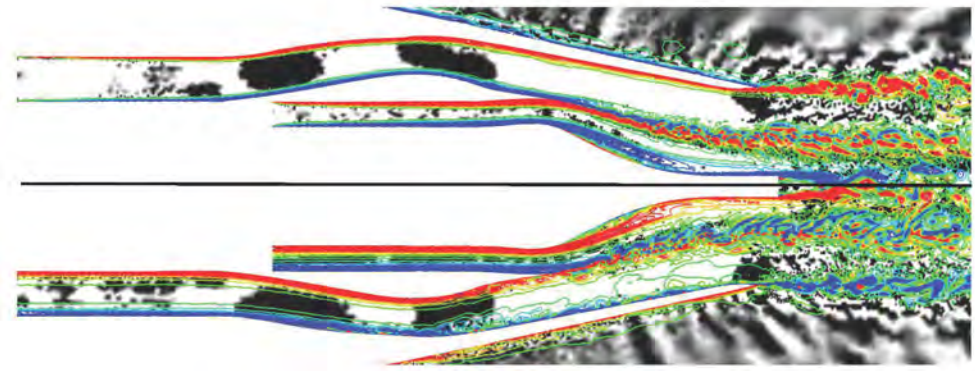

(b) Zoom in the nozzle vanes

Figure 8.21: Instantaneous dilatation field (gray-scale) with iso-contours of vorticity (color), M_1 (upper part) and M_2 (lower part) for the low power case.

Instantaneous dilatation fields (gray-scales) and vorticity iso-contours (color) are shown in Figs. 8.21 and 8.22 for both low power and high power conditions. For both meshes, the jet seems fully developed with a linear and smooth growth of the mixing layers as already shown in Fig. 8.15(a). The large turbulent structures, identified by the higher levels of vorticity, are mostly localized right behind the exit of the nozzle, where the jet is destabilized and transitions to turbulence. These

structures are responsible for the noise sources in the mixing layer and propagate in the downstream direction. This low frequency downstream propagation can be observed at low power in the dilatation field (Fig. 8.21(a)) and is stronger with the M_2 grid.

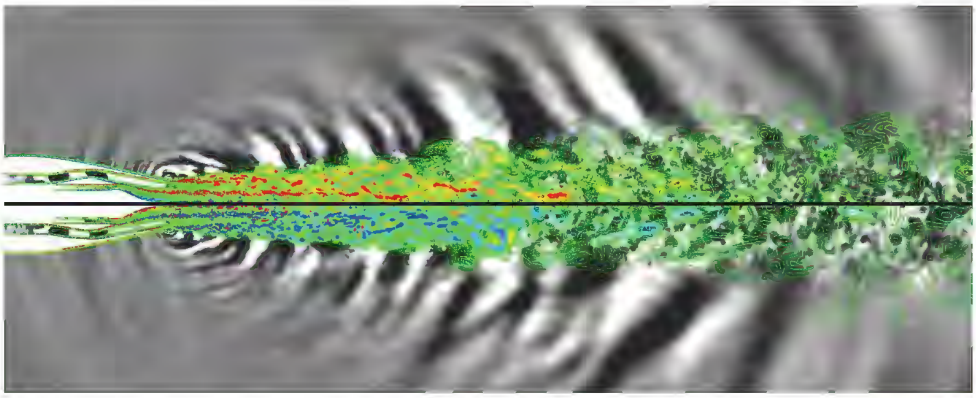

(a) In the jet flow up to $x/D_s = 21$

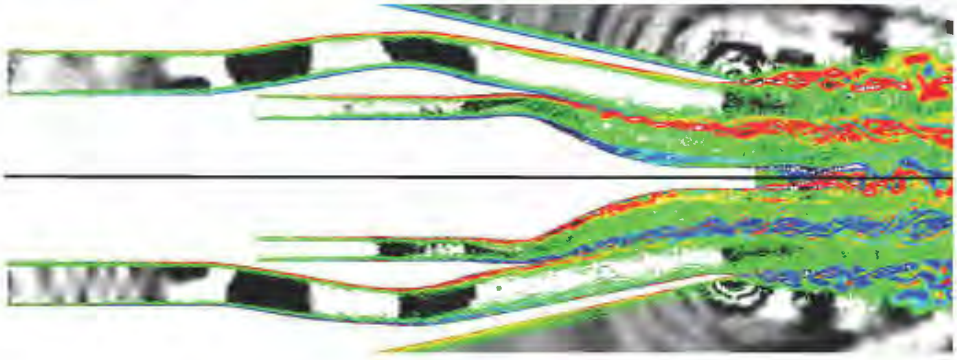

(b) Zoom in the nozzle vanes

Figure 8.22: Instantaneous dilatation field (gray-scale) with iso-contours of vorticity (color), M_1 (upper part) and M_2 (lower part) for the high power case.

For the low power case (Fig. 8.21(b)), the vorticity development inside the nozzle and at the nozzle lips is different, depending on the mesh used. The M_2 mesh exhibits a more developed turbulence. Indeed, there are more structures around the nozzle walls, particularly in the secondary nozzle, where the boundary layer transitions from laminar to turbulent earlier. More vorticity contours are also observed around the plug. The internal mixing layer transitions to turbulence more rapidly after the end of the primary nozzle lip. This is corroborated by the power spectral densities of the kinetic energy extracted at some probes (Fig. 8.2) in the internal and external mixing layers as shown in Figs. 8.23(a) and 8.23(b)).

Higher levels of kinetic energy are observed with M_2 at the nozzles lips (P_1 and S_1 in Fig. 8.2).

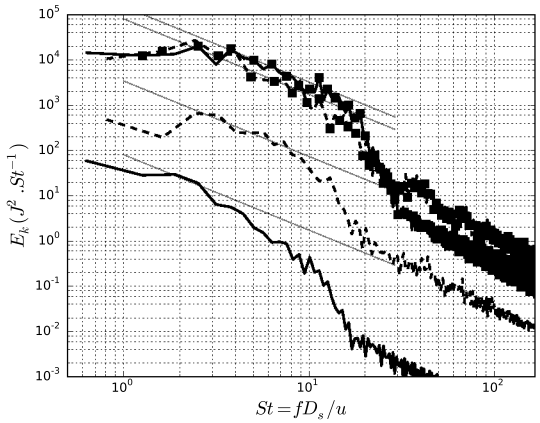

(a) Internal mixing layer, low power

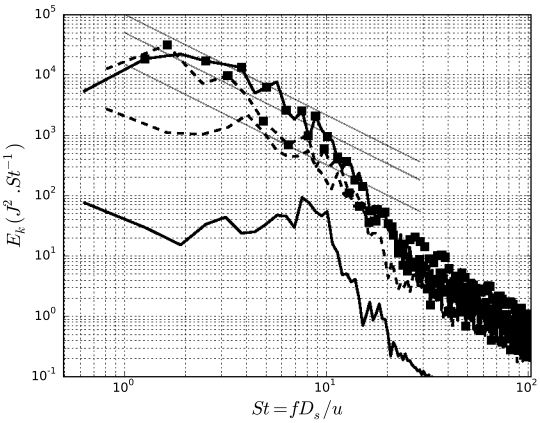

(b) External mixing layer, low power

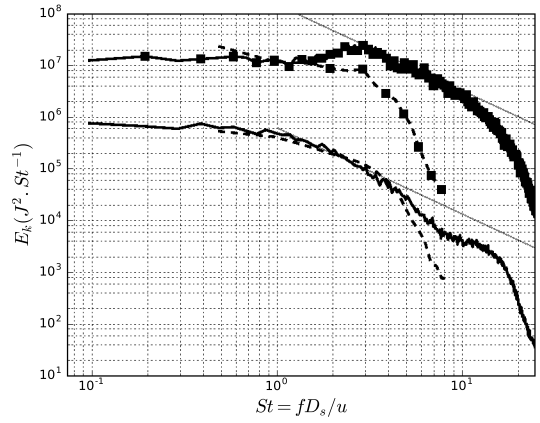

(c) Internal mixing layer, high power

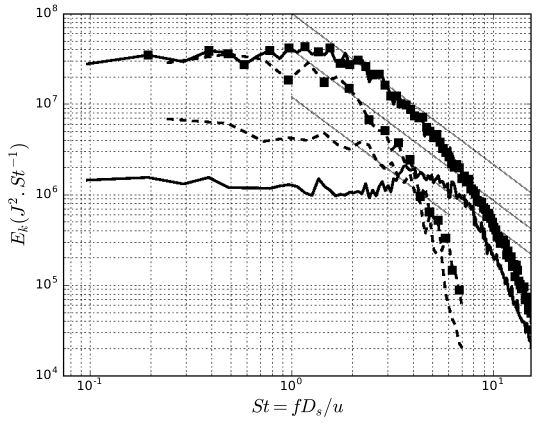

(d) External mixing layer, high power

Figure 8.23: PSD of kinetic energy k. With M_1 grid (–) and M_2 grid (- -). At the lips of the primary (internal mixing layer, P_1 in Fig. 8.2) and secondary (external mixing layer, S_1) nozzles (no symbol). At 2 D_s of the primary nozzle exit (P_2) in the internal mixing layer and at 0.45 D_s of the secondary nozzle exit (S_2) in the external mixing layer (■). $-5/3$ power law (–).

In Fig. 8.23(a), a wider inertial range is observed at the primary nozzle lip (P_1) with M_2 so that the mixing layer is more turbulent than with M_1. In the inertial range, the energy coming from the energy-containing eddies is in equilibrium with the energy cascading to smaller eddies where it is dissipated. Thus the slope of

the energy spectrum in this range remains constant. Kolmogorov [1941] showed that the slope is $-5/3$. A little further in the development of the mixing layers (P_2 and S_2 in Fig. 8.2), the kinetic energy levels are similar and the shapes of the spectra are equivalent. The internal mixing layer (Fig. 8.23(a)) is more turbulent as an inertial range is obtained over one decade.

Similar observations can be made for the high power case (Fig. 8.22(b)). Contrary to the low power case where the internal mixing layer is less turbulent at the nozzle lip (due to a small Reynolds number and a very low Mach number $M \approx 0.07$), the mixing layer seems more turbulent with a higher vorticity content. This is verified by looking at the PSD of the kinetic energy at the primary nozzle lip (P_1) in Fig. 8.23(c) where a wider inertial range is observed with M_1 than for the low power case (Fig. 8.23(a)). M_1 and M_2 give the same spectrum. A little further in the internal mixing layer development (at 2 D_s of the primary exit, P_2), a level discrepancy is observed at high frequency ($St > 2$). The turbulence at this point is less developed with the M_2 mesh, probably due to a lack of convective time. The external mixing layer is also turbulent with both meshes (Fig 8.23(d)). However, higher kinetic energy amplitudes levels are obtained with M_2 at the secondary nozzle lip (S_1).

In the near field in Fig. 8.22(a), the directivity of the jet noise is clearly visible at about 150°. By considering the dilatation field in the nozzle vanes (Fig. 8.22(b)), a strong mode can be observed propagating in the secondary stream and being diffracted at the end of the secondary nozzle lip. This mode was also present in the low power case.

8.2 Excitation of the primary hot jet with combustion noise sources

8.2.1 Acoustic forcing with combustion noise sources

8.2.1.1 Scaling of combustion noise sources

Acoustic waves due to combustion noise are injected in the primary hot gas flow by means of a velocity inlet NSCBC boundary condition. The injected wave is defined as introduced in chapter 4. A polyfrequential temporal signal describing the incident waves is built using the CHORUS exit. Each frequency is injected with a different phase shift.

As the computational domain has been scaled by a factor 1/10, the wavelengths of the acoustic waves obtained by CHORUS have to be scaled to be representative of the interaction of the waves with the geometry. This can be done by conserving

the Helmholtz number, He:

$$He \equiv kr = \frac{2\pi r}{\lambda}, \tag{8.2}$$

with r the outlet radius of the nozzle and λ the associated acoustic wavelength.

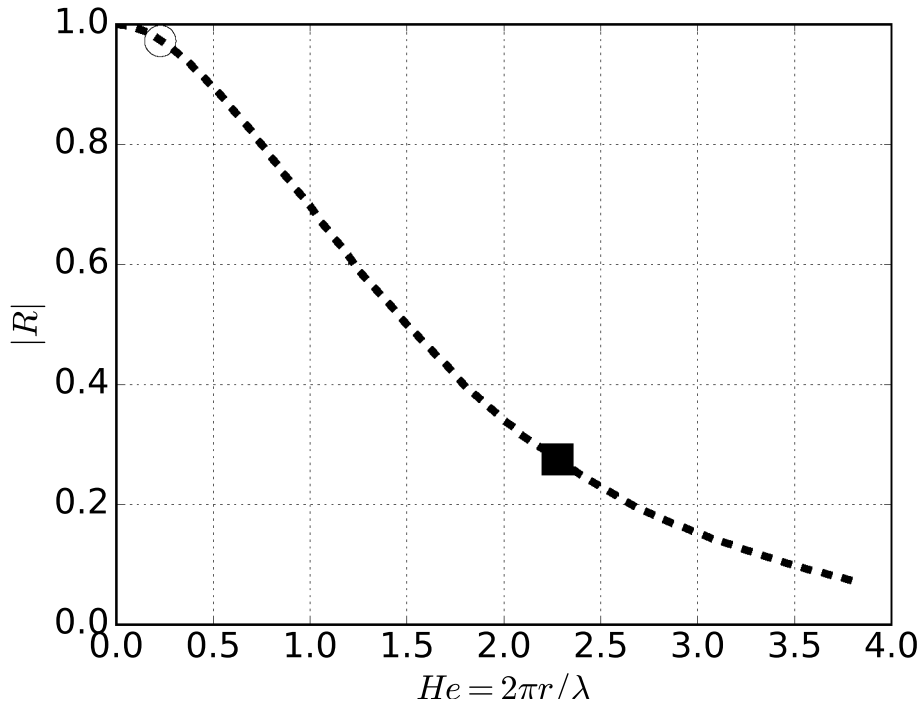

Figure 8.24: Magnitude of the reflection coefficient $|R|$ as a function of the Helmholtz number He (Levine and Schwinger 1948), at a fixed frequency of 260 Hz, without scaling (■) and with proper scaling (○).

Nearly complete reflection of a dominant mode sound wave occurs at the open end of a pipe of circular cross section, if the diameter is small compared to the wavelength. According to Levine and Schwinger [1948], the reflection coefficient R at the end of an unflanged circular pipe can be analytically obtained in function

of the Helmholtz number (Fig. 8.24):

$$|R| = \exp\left(-\frac{2He}{\pi}\int_0^{He}\frac{\tan^{-1}(-J_1(x)/N_1(x))}{x(He^2-x^2)^{1/2}}dx\right), \quad (8.3)$$

$$J_1(x) = \sum_{m=0}^{\infty}\frac{(-1)^m(x/2)^{2m+1}}{m!(m+1)!}, \quad (8.4)$$

$$N_1(x) = \frac{2}{\pi}\log\left(\frac{x}{2}\right)J_1(x) - \frac{2}{\pi x} - \frac{1}{\pi}J_1(x)\left(\psi(m+1)+\psi(m+2)\right), \quad (8.5)$$

$$\psi(m+1) = 1+\frac{1}{2}+...+\frac{1}{m}-\log\gamma,\ \log\gamma = 0.5772, \quad (8.6)$$

where J_1 and N_1 are first order cylinder Bessel functions of real and imaginary argument. At 260 Hz for instance, without scaling the Helmholtz number is 0.227 and the reflection coefficient is more than 0.9 whereas, with scaling, the He is 2.27 and the reflection coefficient is about 0.3. This has been verified by AVSP-f

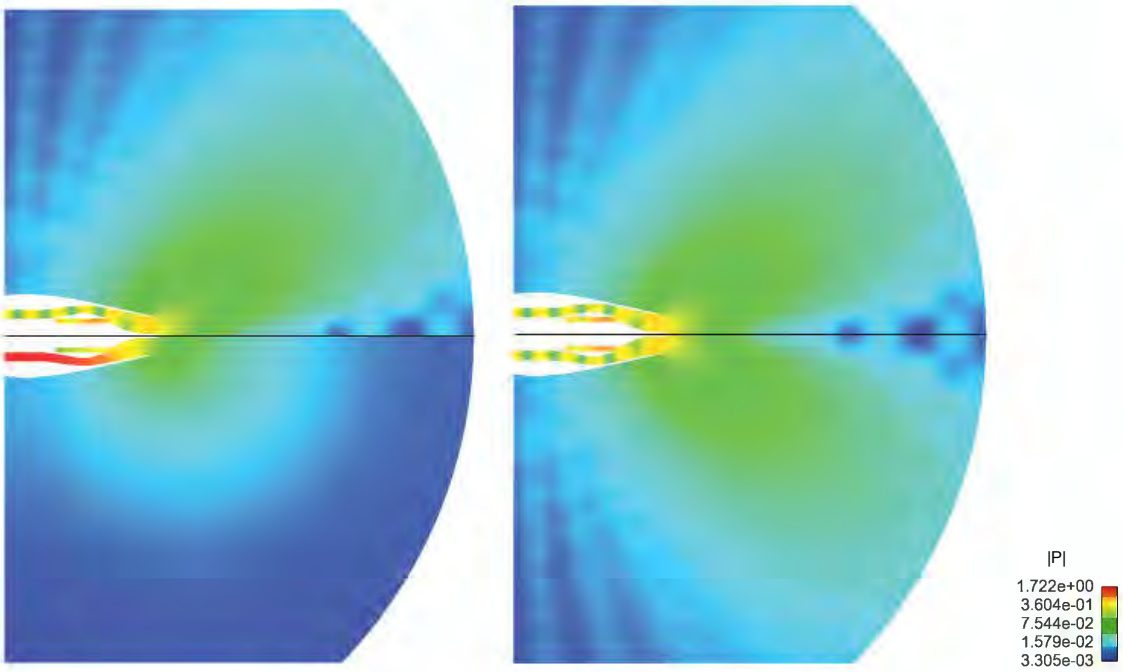

(a) Wavelengths 1:1 (b) Wavelengths 1:10

Figure 8.25: Comparison of the acoustic pressure module fields between the real dimension case (upper part) and the 1:10 scaled case (lower part) (a) without rescaling and (b) with proper rescaling.

computations with the same flow conditions as in the CONOCHAIN computations of the low power case (Fig. 6.59(a)). Acoustic waves with an amplitude of 1 Pa, have been injected in the scaled geometry. In the first case, the acoustic wavelengths have not been scaled, while in the second case the acoustic wavelengths have been scaled by a factor 1/10. Compared to the computations with the actual geometry, it can be seen that in the first case, at a frequency of 260 Hz, acoustics does not propagate to the far-field as the acoustic reflection coefficient is strong (Fig. 8.25(a)). In the second case, at a frequency of 2600 Hz, the acoustic pressure fields are completely identical. This means that by scaling the acoustic wavelength to fit with the scaled geometry, the interaction between the acoustics and the geometry represent well the real case (Fig. 8.25(b)).

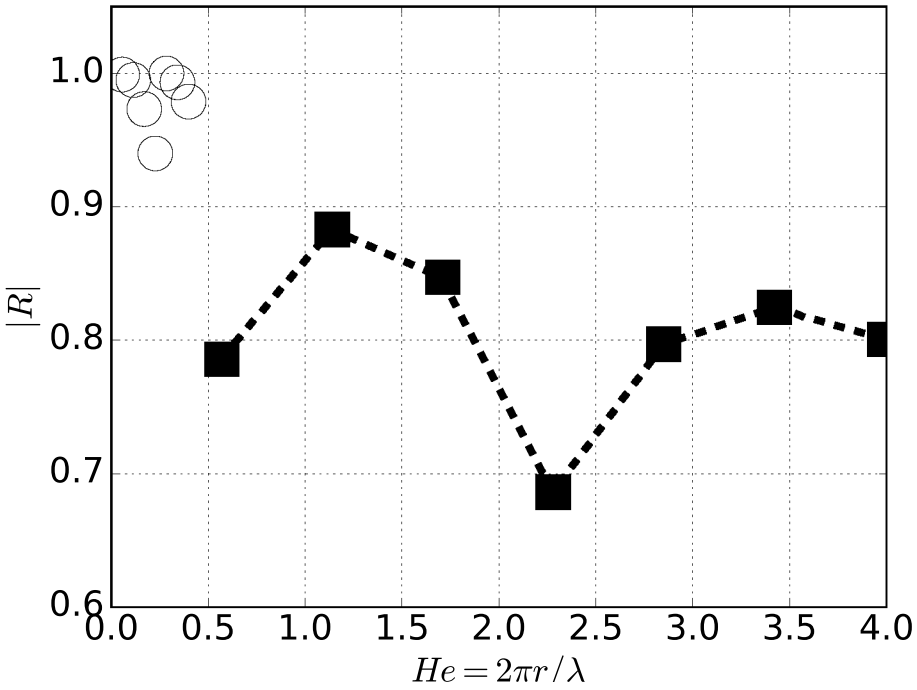

Figure 8.26: Magnitude of the reflection coefficient $|R|$ as a function of the Helmholtz number He at the scaled secondary stream exit plane (Fig. 8.2). Wavelengths with (■) and without scaling (○) and CONOCHAIN case (- -).

The actual reflection coefficient R has been computed for both geometries

(scaled and not scaled), at the secondary stream exit plane (Fig. 8.26):

$$R = \frac{Z-1}{Z+1}, \tag{8.7}$$

$$Z = \frac{\hat{p}}{\rho_0 c_0 \hat{u}}. \tag{8.8}$$

where Z is the acoustic impedance, ρ_0 and c_0 are the mean density and speed of sound. $\hat{p} = |p|e^{i\phi}$ and $\hat{u} = |u|e^{i\phi}$ are complex numbers extracted on a probe at the center of the exit plane coming from CONOCHAIN. Without scaling the reflection coefficient stay high $|R| > 0.93$. With proper He scaling the reflection coefficients match the coefficients given by CONOCHAIN for the actual geometry.

8.2.1.2 Acoustic forcing at the primary inlet plane

Considering this scaling in frequency to agree with the reduction of the computational domain, a temporal signal for the incident acoustic waves has been built. The power spectral density of this reconstructed signal is plotted in Fig. 8.27, as

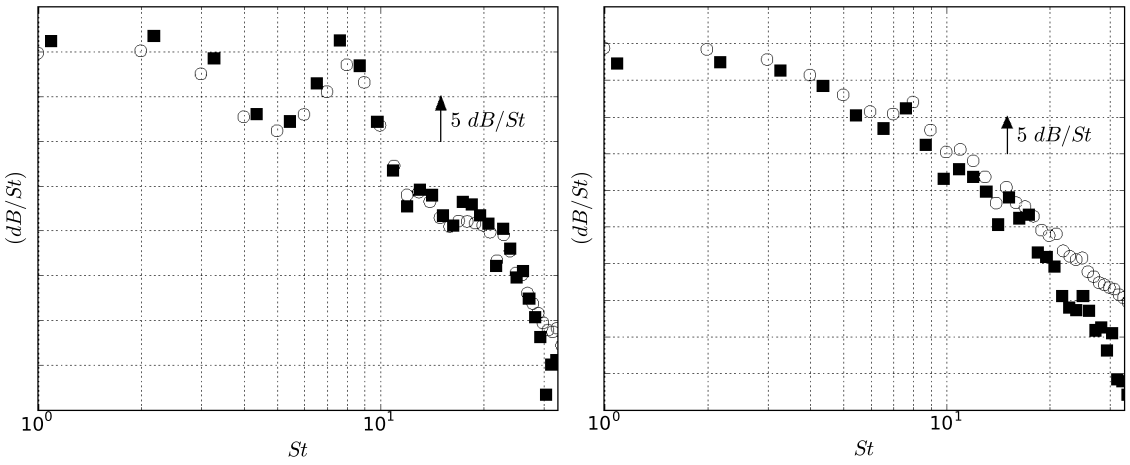

(a) Low power

(b) High power

Figure 8.27: Discrete power spectral density of the reconstructed forcing temporal signal (○), compared to the PSD of total noise from CHORUS data (■), at the turbine exit (position **S4** in Fig. 5.4)

a function of the Strouhal number, $St = fD_s/u_s$, to be comparable to the PSD obtained by CONOCHAIN with a geometry at scale 1:1. It can be noted that the amplitudes and the frequencies describing the incident acoustic waves given by CONOCHAIN at the turbine exit (position **S4** in Fig. 5.4) are well found.

The acoustic forcing is realized at the primary stream inlet plane (Fig. 8.2). In order to impose the target value of the boundary condition, a relaxation coefficient K is used, so that some reflections occur at the inlet, $A^{+,r}$: waves propagating back to the inlet (A^-) are partially reflected into $A^{+,r} = RA^-$. Therefore, the forcing signal $A^{+,f}$ cannot be directly obtained at the inlet since:

$$\begin{aligned} A^+ &= A^{+,r} + A^{+,f} \\ &= RA^- + A^{+,f} \end{aligned} \tag{8.9}$$

By computing the actual reflection coefficient of the inlet boundary condition (Selle et al. 2004b):

$$R(f) = \frac{1}{1 - i\dfrac{2\pi f}{K}}, \tag{8.10}$$

the acoustic wave $A^{+,f}$ induced by the forcing signal can be expressed as

$$A^{+,f}(f) = A^+(f) - R(f)A^-(f). \tag{8.11}$$

The temporal signal of $A^{+,f}$ can be found with an inverse Fourier transform:

$$A^{+,f}(t) = \int_f \left(A^+(f) - R(f)A^-(f)\right) \exp(i2\pi ft)df \tag{8.12}$$

and finally, the pressure fluctuation related to the forcing signal is written as

$$p'^f(t) = \gamma P A^{+,f}(t). \tag{8.13}$$

By retrieving the acoustic part due to the relaxation coefficient, $A^{+,r}$, from the downstream-propagating acoustic wave A^+, it can be seen that the forcing signal of the wave $A^{+,f}$ is well superposed with the given temporal signal at the primary inlet plane for both operating points (Fig. 8.28).

The impact of the relaxation coefficients on the acoustics has been evaluated in annex A. In a standard non-reflecting NSCBC boundary condition using an expression for inlet wave $L_1 = K(u^t - u)$, the actual reflection coefficient R at boundary is frequency-dependent on the relaxation coefficient K. It has been seen how acoustics is extremely sensitive to the reflection coefficient and how it is more complicated to control acoustic propagation when there are two inlets. As no more information has been given concerning the reflection coefficient at the inlet of the nozzles, the relaxation coefficients of the NSCBC have been chosen to give an acoustic pressure module field close to the one obtained with AVSP-f computations of Chapter 6. Therefore, $K_{sec} = 225000$ ($f_c \approx 1800$ Hz with $f_c = K/(4\pi)$ the cut-off frequency, i.e. $St = 3$ at low power and $St = 0.45$ at high power) at the secondary nozzle inlet and $K_{prim} = 10000$ ($f_c \approx 80\ Hz$ i.e. $St = 0.13$ at low power and $St = 0.02$ at high power) at the primary nozzle inlet have been imposed for all the forced simulations.

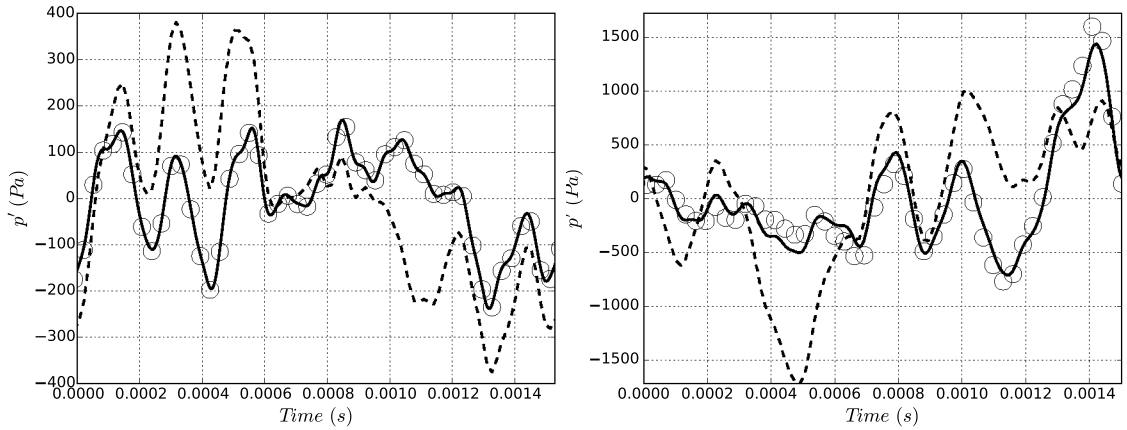

(a) Low power

(b) High power

Figure 8.28: Pressure fluctuation signal at the primary stream inlet plane (Fig. 8.2), total signal (- -), forcing signal (○), reconstructed signal from CHORUS data (–)

8.2.2 Aerodynamical mean features of the forced jet

8.2.2.1 Jet flow development analysis

Mean flow characteristics of the jet simulations forced with combustion noise are compared with the flow characteristics of the unforced jet simulations with the mesh M_1. As for the unforced jet simulations presented in the previous section 8.1.4, the dimensionless mean velocity $\bar{U}/U_s$, the mean temperature $\bar{T}/T_{p,0}$, and the turbulent kinetic energy k/U_s^2 are analyzed along longitudinal planes in Figs. 8.29, 8.31 and 8.32.

In Fig. 8.29, the mean velocity conditions inside the nozzle are similar for the forced and the unforced jet for both operating points and the prediction of the recirculation zone around the plug is the same. However, in the jet development more differences can be observed, particularly for the low power case with combustion noise forcing, where a smaller recirculation zone is generated at the outlet of the plug and the secondary jet core is smaller than without forcing.

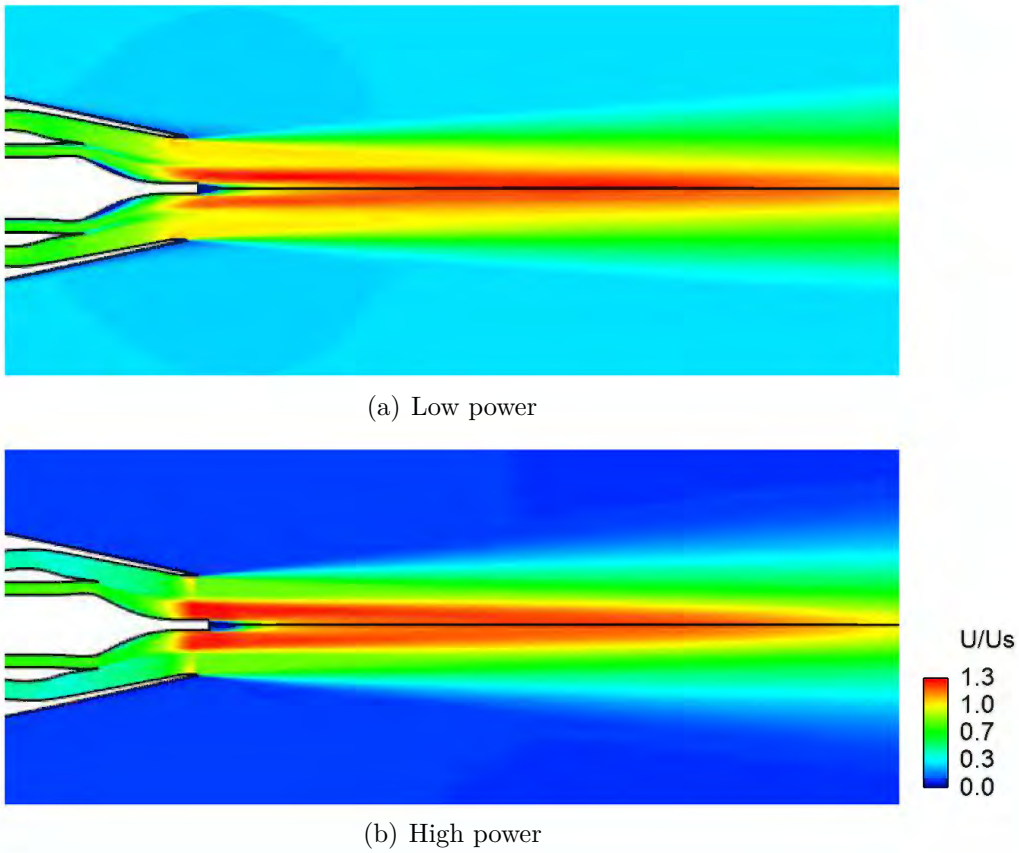

(a) Low power

(b) High power

Figure 8.29: Dimensionless mean velocity fields, $U/\bar{U}_s$ up to $x/D_s = 9.5$, no forcing (upper part) and combustion noise forcing (lower part).

Fig. 8.30 shows the 1D profiles $r_{0.5}$ defining the radius where at the same axial position the velocity equals half of the secondary jet core velocity. It can be shown that the radial expansion of the secondary mixing layer is similar between the forced and the unforced cases. This indicates that the development of the external mixing layer is weakly impacted by the combustion noise.

By looking at the temperature mean field (Fig. 8.31), the hot central zone is seen to be shorter in the case of the forced jet, however the temperature magnitude decrease in this zone is conserved.

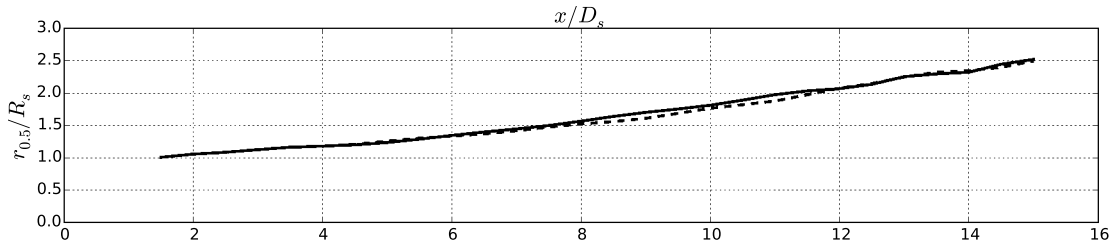

(a) Low power

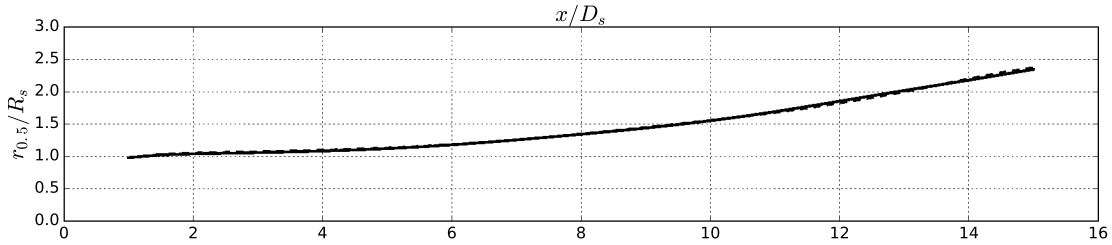

(b) High power

Figure 8.30: Profiles of $r_{0.5}$ of the external shear layer. Without (–) and with combustion noise forcing (- -).

In Fig. 8.32, a significant effect of the combustion noise forcing on the mean jet flow development can be seen on the repartition of the turbulent kinetic energy. The impact seems more important for the low power case as shown in Fig. 8.32(a). The turbulent kinetic energy is more distributed around the plug, this can be responsible of the reduction of the recirculation zone at the end of the plug as the separated flow is more turbulent and so the Von Karman alley is developing less. The development of the internal mixing layer is also strongly impacted resulting in a wider layer and a shorter secondary jet core (as shown in Fig. 8.33). The external mixing layer does not seem to be impacted, since same levels of turbulent kinetic energy and same development is observed at the end of the secondary nozzle lip. However, the axial zone where the magnitudes are higher is shorter and ends before the merging of the two mixing layers. This suggests an higher dissipation of the large turbulent structures.

In the forced high power case (Fig. 8.32(b)), the central core exhibits higher levels of turbulent kinetic energy than the unforced jet case. The area of higher levels is also bigger and begins before the fully merged zone. Therefore, it seems that the combustion noise interacts with the turbulent structures of the high Mach jet.

These observations can be further highlighted by examining turbulent velocity profiles at the centerline of the jet and at the nozzle lip-lines.

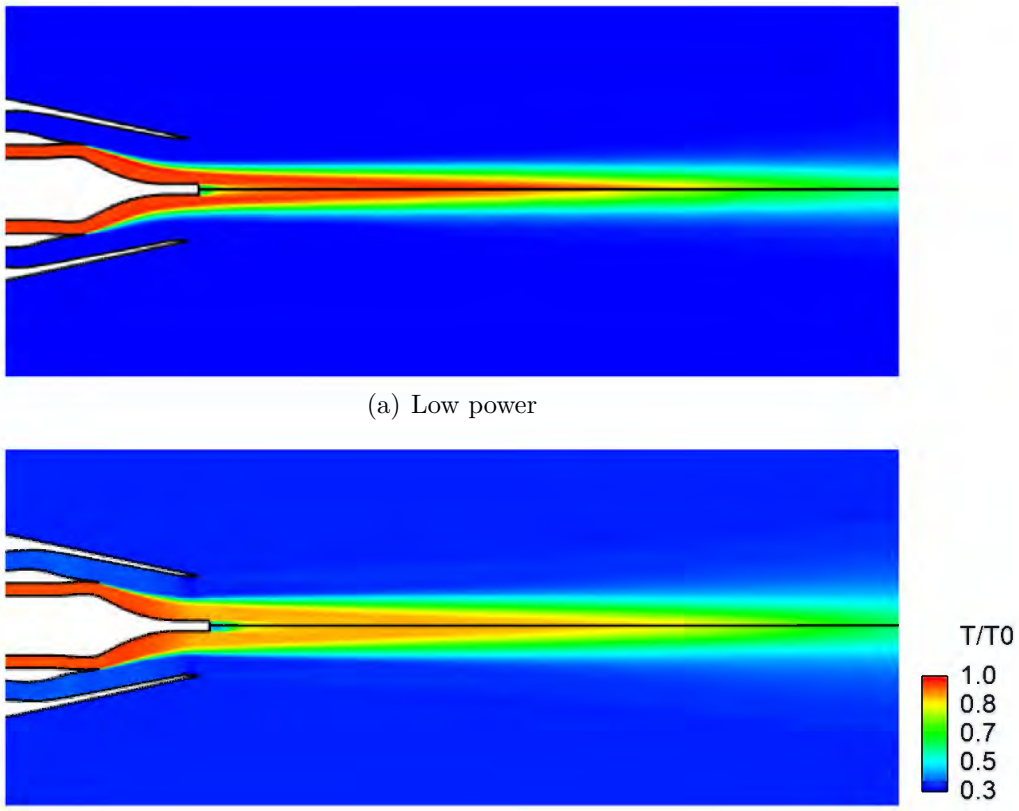

(a) Low power

(b) High power

Figure 8.31: Dimensionless mean temperature fields, $T/\bar{T}_{p,0}$ up to $x/D_s = 9.5$, no forcing (upper part) and combustion noise forcing (lower part)

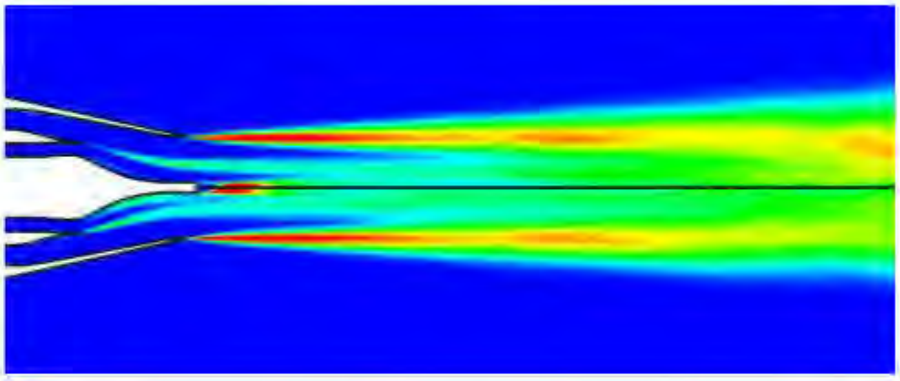

(a) Low power

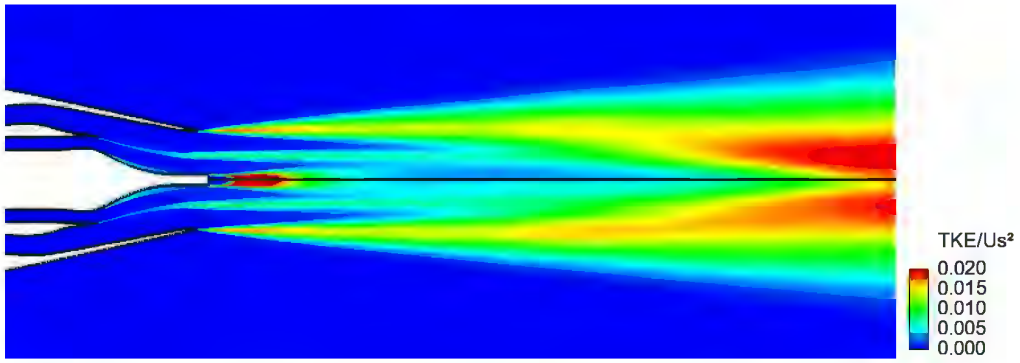

(b) High power

Figure 8.32: Dimensionless turbulent kinetic energy fields (k), $k/\bar{U}_s^2$ up to $x/D_s = 9.5$, no forcing (upper part) and combustion noise forcing (lower part)

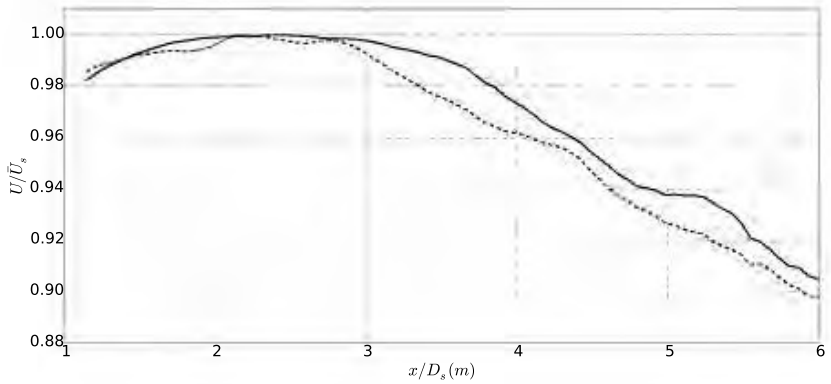

Figure 8.33: Profile of the mean velocity $U/\bar{U}_s$ on a line crossing the secondary jet core. no forcing (–) and combustion noise forcing (- -).

8.2.2.2 Analysis at the centerline of the jet and at the nozzle lips

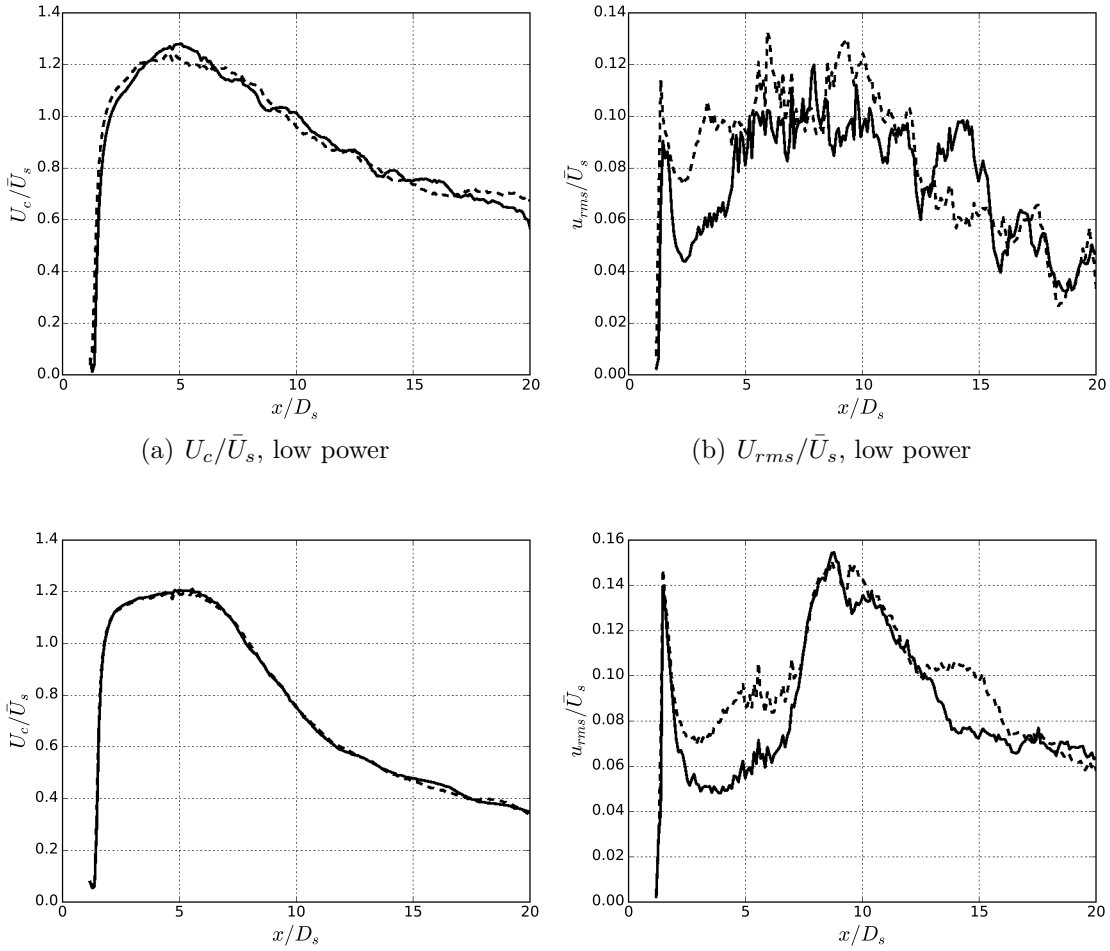

(a) $U_c/\bar{U}_s$, low power

(b) $U_{rms}/\bar{U}_s$, low power

(c) $U_c/\bar{U}_s$, high power

(d) $U_{rms}/\bar{U}_s$, high power

Figure 8.34: Profiles of the axial velocity $U_c/\bar{U}_s$ and the axial fluctuating velocity $U_{rms}/\bar{U}_s$ on the centerline at the plug exit (Fig. 8.2). Unforced jet (–) and forced jet (- -).

The mean flow characteristics at the centerline of the jet are equivalent for both unforced and forced simulations, whatever the operating point is (Figs. 8.34(a) and 8.34(c)). However, the turbulent axial velocity levels increase earlier on the centerline with the injection of the combustion noise sources (Figs. 8.34(b) and 8.34(d)). For the high power case, the turbulent velocity profile part where the levels are the highest in the unforced simulation is also conserved with the forced simulation.

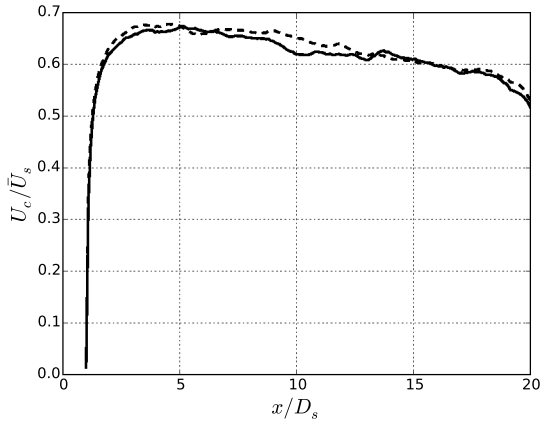

(a) $U/\bar{U}_s$, low power

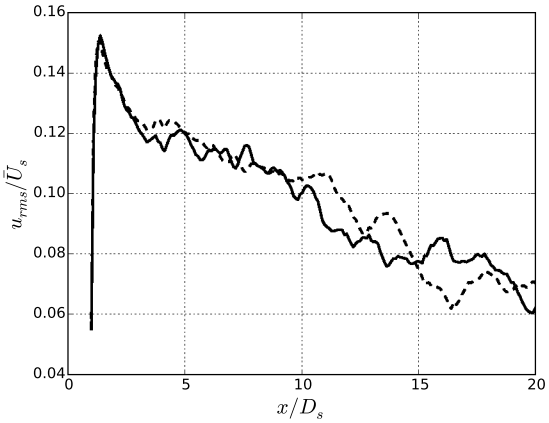

(b) $U_{rms}/\bar{U}_s$, low power

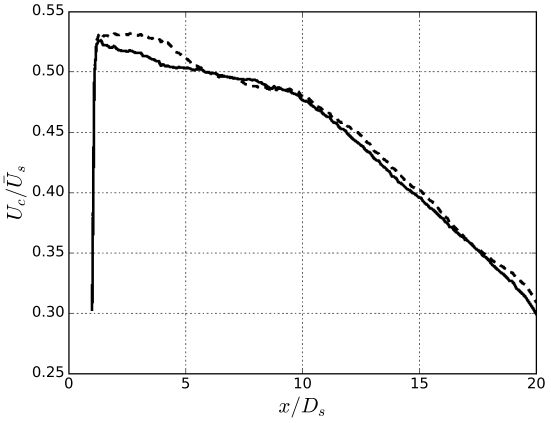

(c) $U/\bar{U}_s$, high power

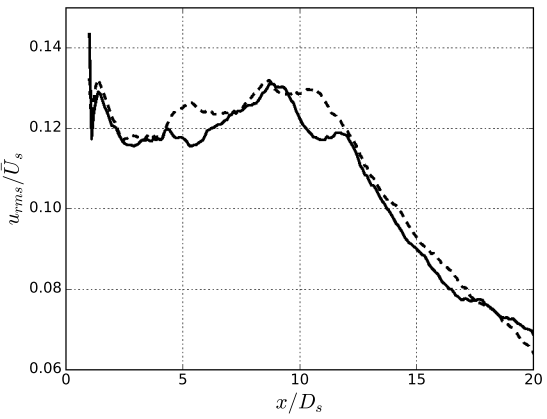

(d) $U_{rms}/\bar{U}_s$, high power

Figure 8.35: Profiles of the axial velocity $U/\bar{U}_s$ and the axial fluctuating velocity $U_{rms}/\bar{U}_s$ on the secondary stream lip-line (Fig. 8.2). Unforced jet (–) and forced jet (- -).

Again the development of the external mixing layer does not seem to be impacted by the forcing a lot (Fig. 8.35). The mean velocity-profile shape plotted on the secondary nozzle lip line is similar. Same conclusion can be made for the turbulent velocity profiles. However, the amplitudes of fluctuations are a little higher.

The internal mixing layer is clearly disturbed by the forcing (Fig. 8.36). Even if the profiles shape is conserved, the amplitudes levels are much higher. The turbulent axial velocity fluctuations are amplified by 5%. Therefore, the combustion

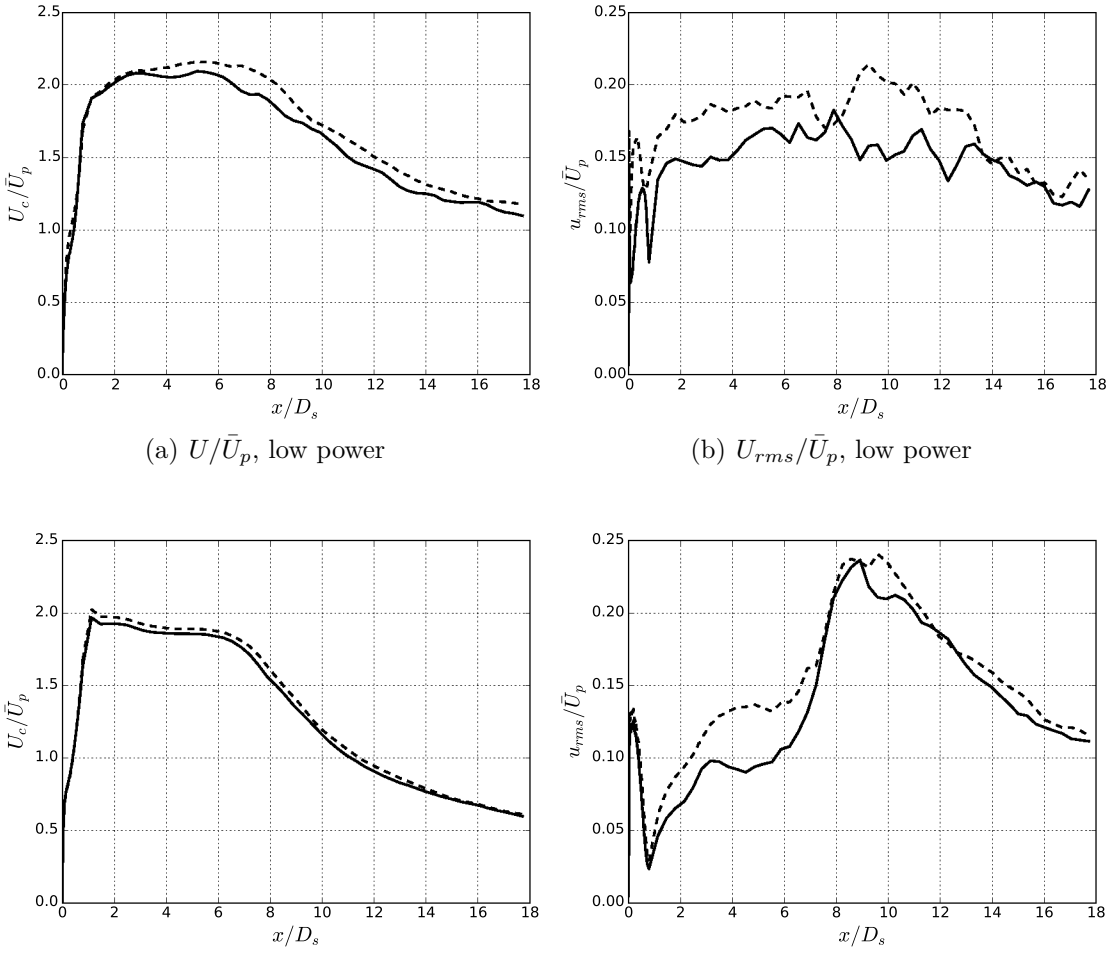

(a) $U/\bar{U}_p$, low power

(b) $U_{rms}/\bar{U}_p$, low power

(c) $U/\bar{U}_p$, high power

(d) $U_{rms}/\bar{U}_p$, high power

Figure 8.36: Profiles of the axial velocity $U/\bar{U}_p$ and the axial fluctuating velocity $U_{rms}/\bar{U}_p$ on the primary lip-line (Fig. 8.2). Unforced jet (–) and forced jet (- -).

noise forcing seems to mainly impact the turbulence in the jet core and in the internal mixing layer which separates the primary flow where the noise sources are introduced from the secondary flow.

To conclude, no major impact of the forcing with combustion noise has been observed on the secondary flow, whereas the forcing has an impact on the turbulence and on the primary flow.

8.2.3 Influence of combustion noise on the aerodynamic development and the acoustics of the jet

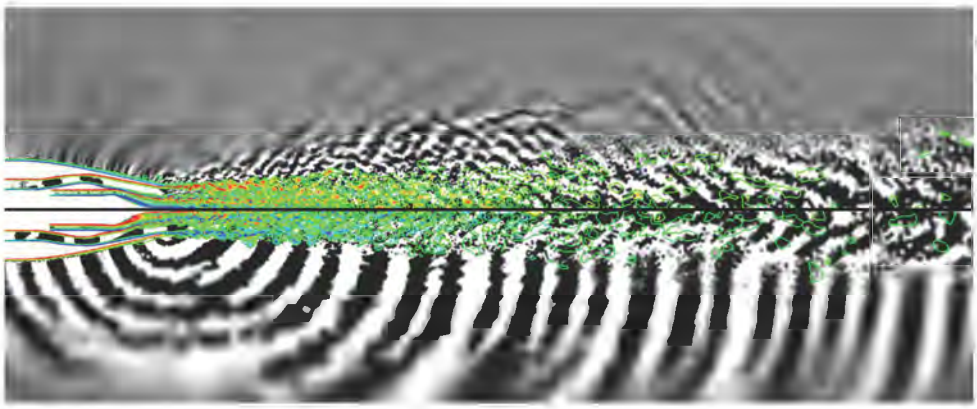

(a) In the jet flow up to $x/D_s = 21$

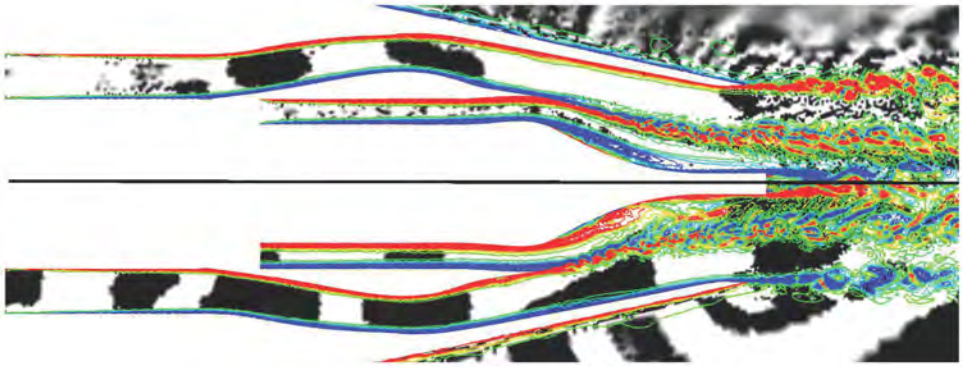

(b) Zoom in the nozzle vanes

Figure 8.37: Instantaneous dilatation field (gray-scale) with the iso-contours of the vorticity (color), no forcing (upper part) and combustion noise forcing (lower part) for the low power case.

Instantaneous dilatation fields (gray-scales) and vorticity iso-contours (color) are shown in Figs. 8.37 and 8.38 for both forced operating points and compared to the unforced simulations. From the dilatation fields in Fig. 8.37(a), at low power case where the jet noise is weak, it can be clearly seen that the low frequency combustion noise propagates and that it is the principal source of noise. It can also be noted that this noise from combustion sources propagates also towards the secondary nozzle inlet.

In the lower part of Fig. 8.38(b), the combustion noise source can be observed at the outlet of the secondary nozzle for the high power forced case. This low

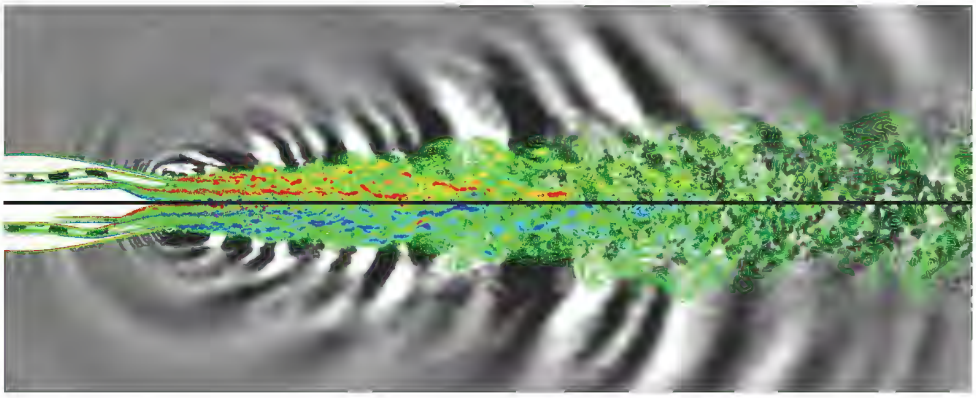

(a) In the jet flow up to $x/D_s = 21$

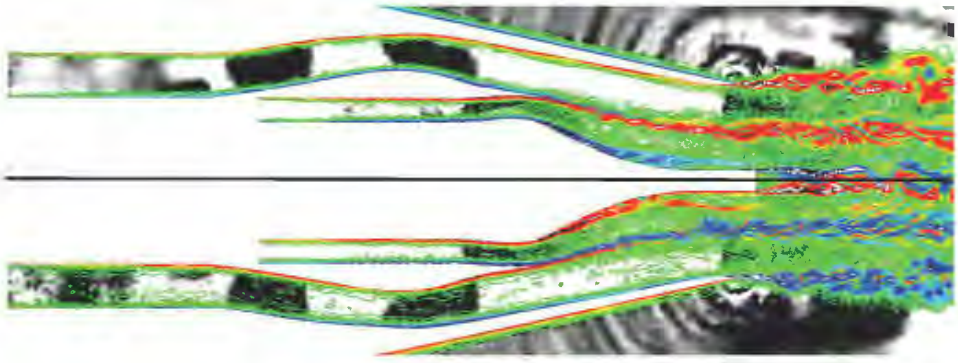

(b) Zoom in the nozzle vanes

Figure 8.38: Instantaneous dilatation field (gray-scale) with iso-contours of vorticity (color), no forcing (upper part) and combustion noise forcing (lower part) for the high power case.

frequency source does not exist in the case of the unforced simulation. By considering the near field in Fig. 8.38(a), it can be noticed that this source propagates at more upstream angles than the jet sources which propagate in a more downstream direction as already observed in the unforced case.

In terms of vorticity levels, it is important to notice that for the low power forced case (lower part of Fig. 8.37(b)) the forcing with the combustion noise sources triggers the turbulence transition earlier at the end of the primary nozzle lip. The vorticity content of the internal mixing layer is higher. The turbulence development is more important around the nozzle and between the mixing layers. In the jet flow development, the large turbulent scales seem to be dissipated more rapidly. This is in agreement with the shorter zone of high turbulent kinetic energy magnitude seen in the lower part of Fig. 8.32(a).

In the high power forced case (lower part of Fig. 8.38(b)) the boundary layer

of the primary nozzle but also of the secondary nozzle seems excited by the combustion noise sources injected in the primary nozzle inlet. This impacts the jet flow development since more turbulent structures can be observed in the internal mixing layer and close to the jet axis (lower part of Fig. 8.38(a)).

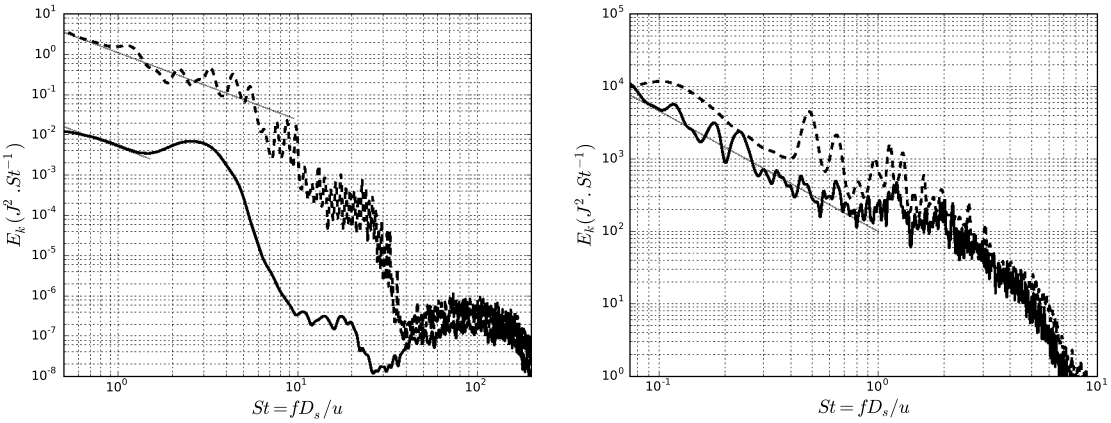

(a) Low power (b) High power

Figure 8.39: PSD of the kinetic energy k on the centerline of the jet at the plug exit (C_1 in Fig. 8.2). With M_1 grid, jet simulation without combustion noise introduction (–) and with combustion noise introduction (- -). $-5/3$ power law (–).

The development of the turbulence is investigated on the centerline of the jet (Figs. 8.39, 8.40 and 8.41). In Fig. 8.39(a) at low power, combustion noise induces more turbulent structures at the plug exit (C_1 in Fig. 8.2). An inertial range over one decade can be observed at $0.5 < St < 6$ with higher levels of turbulent kinetic energy for the jet simulation with combustion noise introduction. Some broadband peaks at the frequency of combustion noise are noticed as a sign of instability of the boundary layer of the plug at certain preferential frequencies. On the contrary, the jet simulation without combustion noise does not exhibit yet an inertial range at the plug exit. A broadband bump is seen at about $St = 3$. At high power (Fig. 8.39(b)), the combustion noise introduction amplifies the kinetic energy levels which are doubled. Several broadband peaks appear related to the combustion noise sources between $0.5 < St < 2$.

In Figs. 8.40(a) and 8.41(a) at low power case, further downstream in the centerline of the jet (3.8 D_s and 6.7 D_s), the turbulence development between the forced case and the unforced case is globally similar. However, it can be noticed that there is still a response at the first forcing frequency of combustion noise ($St \approx 1.2$).

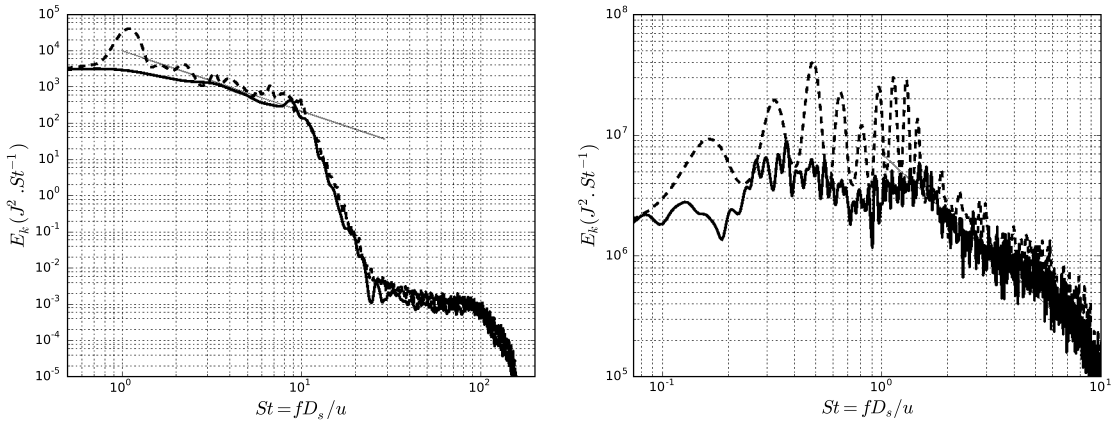

(a) Low power (b) High power

Figure 8.40: PSD of the kinetic energy k on the centerline of the jet at 3.8 D_s of the primary nozzle exit (C_2 in Fig. 8.2). With M_1 grid, jet simulation without combustion noise introduction (–) and with combustion noise introduction (- -). $-5/3$ power law (–).

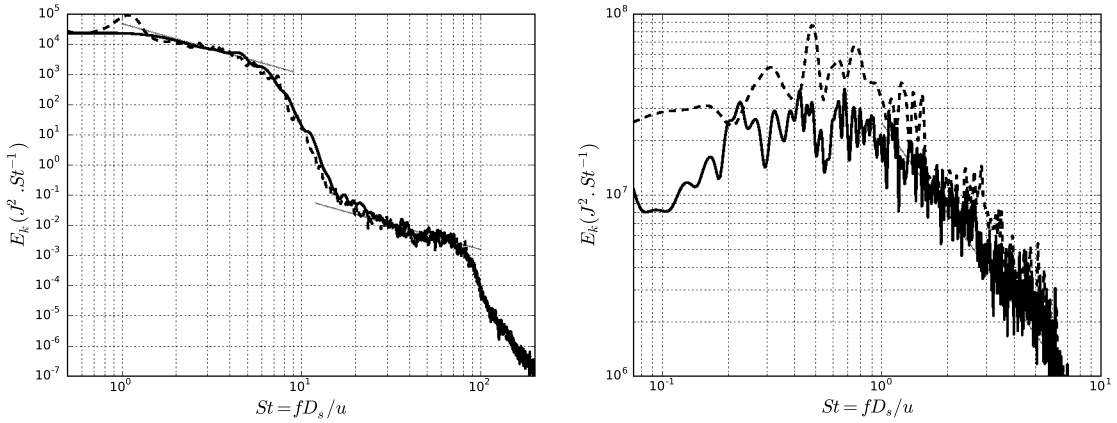

(a) Low power (b) High power

Figure 8.41: PSD of the kinetic energy k on the centerline of the jet at 6.7 D_s of the primary nozzle exit. With M_1 grid, jet simulation without combustion noise introduction (–) and with combustion noise introduction (- -). $-5/3$ power law (–).

At high power (Figs. 8.40(b) and 8.41(b)), the turbulent flow is strongly impacted by the combustion noise sources. Turbulence is modulated by the com-

bustion noise frequencies and the kinetic energy levels are multiplied by about three. At Strouhal numbers corresponding to the combustion noise frequencies ($0.1 < St < 2$), the distribution of the vortical structures is not sufficiently turbulent so that the flow is excited at the combustion noise frequencies.

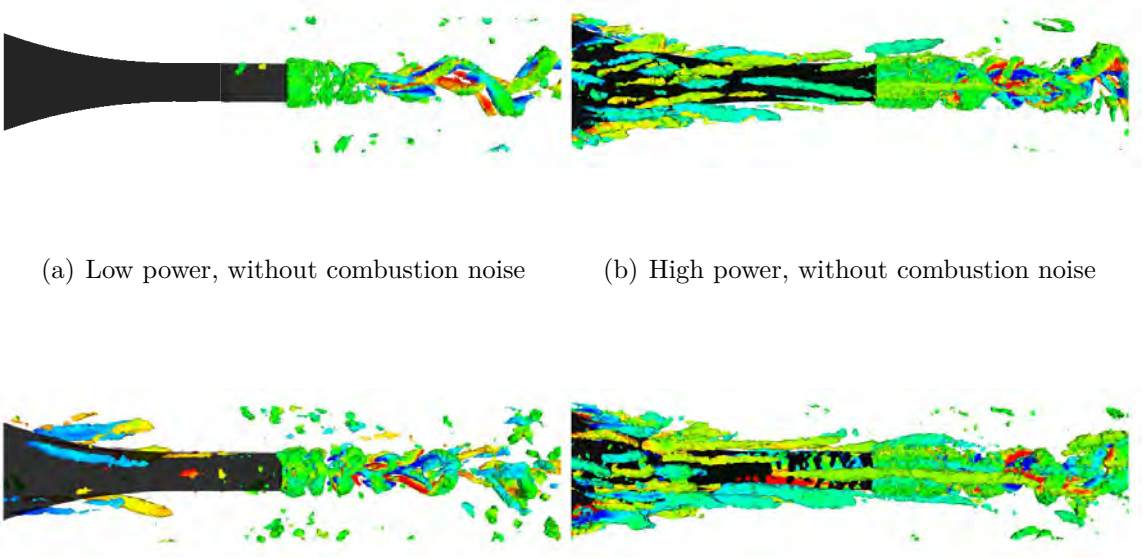

(a) Low power, without combustion noise (b) High power, without combustion noise

(c) Low power, with combustion noise forcing (d) High power, with combustion noise forcing

Figure 8.42: Iso-criterion Q colored by the vorticity in the plug region, left: low power ($Q = 1.5e + 7$), right: high power ($Q = 1e + 8$)

By looking at iso-criterion Q in the plug region (Fig. 8.42), it can be seen that with combustion noise introduction, roller structures appear around the plug end which trigger a Kelvin-Helmholtz instability at high power (Fig. 8.42(d)). More turbulent structures can also be observed at both operating points (Figs. 8.42(c) and 8.42(d)).

More details around the nozzle lips can be observed in Figs. 8.43 and 8.44. At low power (Fig. 8.43), with combustion noise forcing, the boundary layer of the primary nozzle becomes instable before the end of the nozzle lip. Three large turbulent structures appear just at the end of the lip which could be vortex pairing. This corroborates the shorter secondary jet core seen in the lower part of Fig. 8.29(a) and agrees with the PSD of the kinetic energy plotted in Fig. 8.45(a). At the primary nozzle lip (P_1 in Fig. 8.2), a more turbulent spectrum with higher

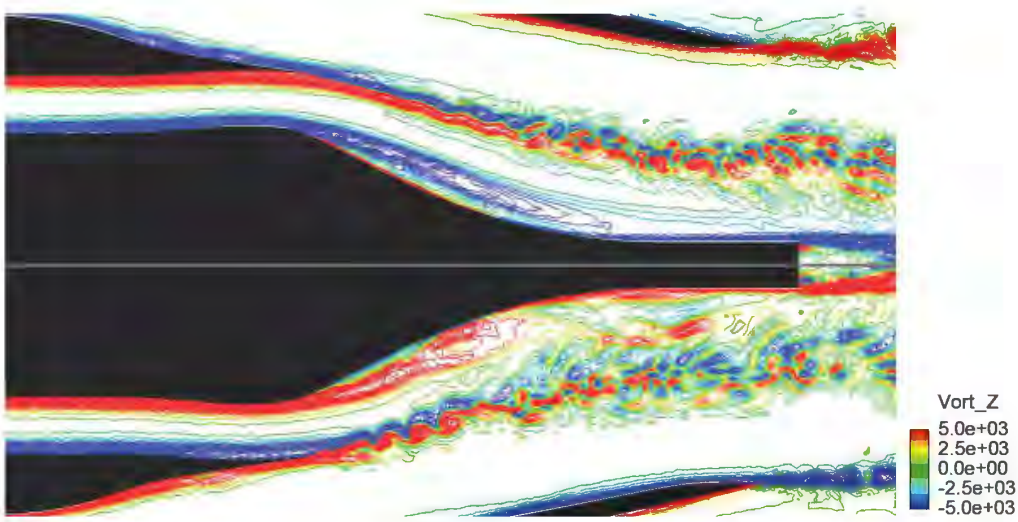

Figure 8.43: Vorticity iso-contours in the nozzle lips region, low power case, no forcing (upper part) and combustion noise forcing (lower part)

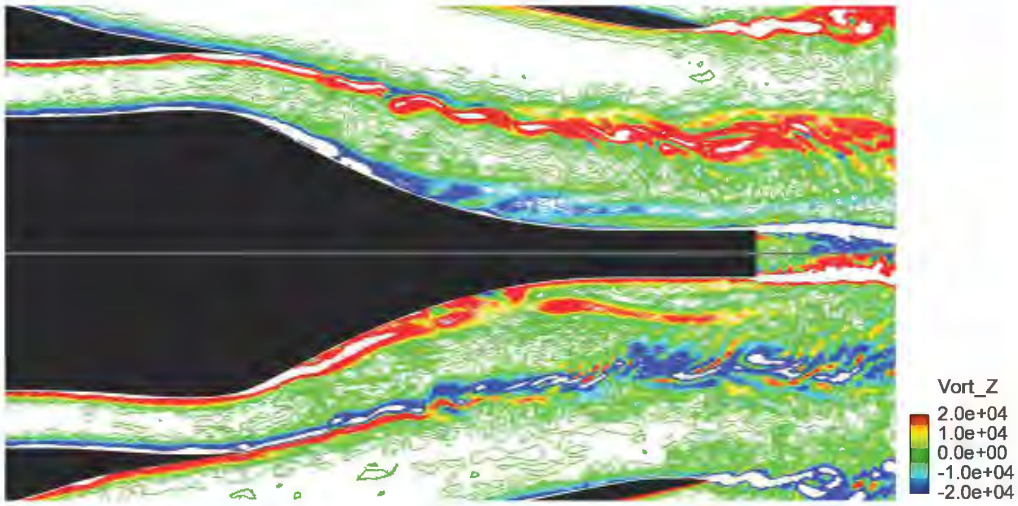

Figure 8.44: Vorticity iso-contours in the nozzle lips region, high power case, no forcing (upper part) and combustion noise forcing (lower part)

levels is obtained with the combustion noise introduction. The primary mixing layer responds at preferential frequencies of $St = 8$ with its harmonic at $St = 16$ (combustion noise frequencies). This could be assimilated to the vorticity structures observed in the lower part of Fig. 8.43 and that are therefore generated by the excitation of the primary mixing layer with the combustion noise. Further downstream in the development of the primary mixing layer (2 D_s, P_2 in Fig. 8.2), the

turbulent kinetic energy levels are equivalent and no further mixing layer response is observed.

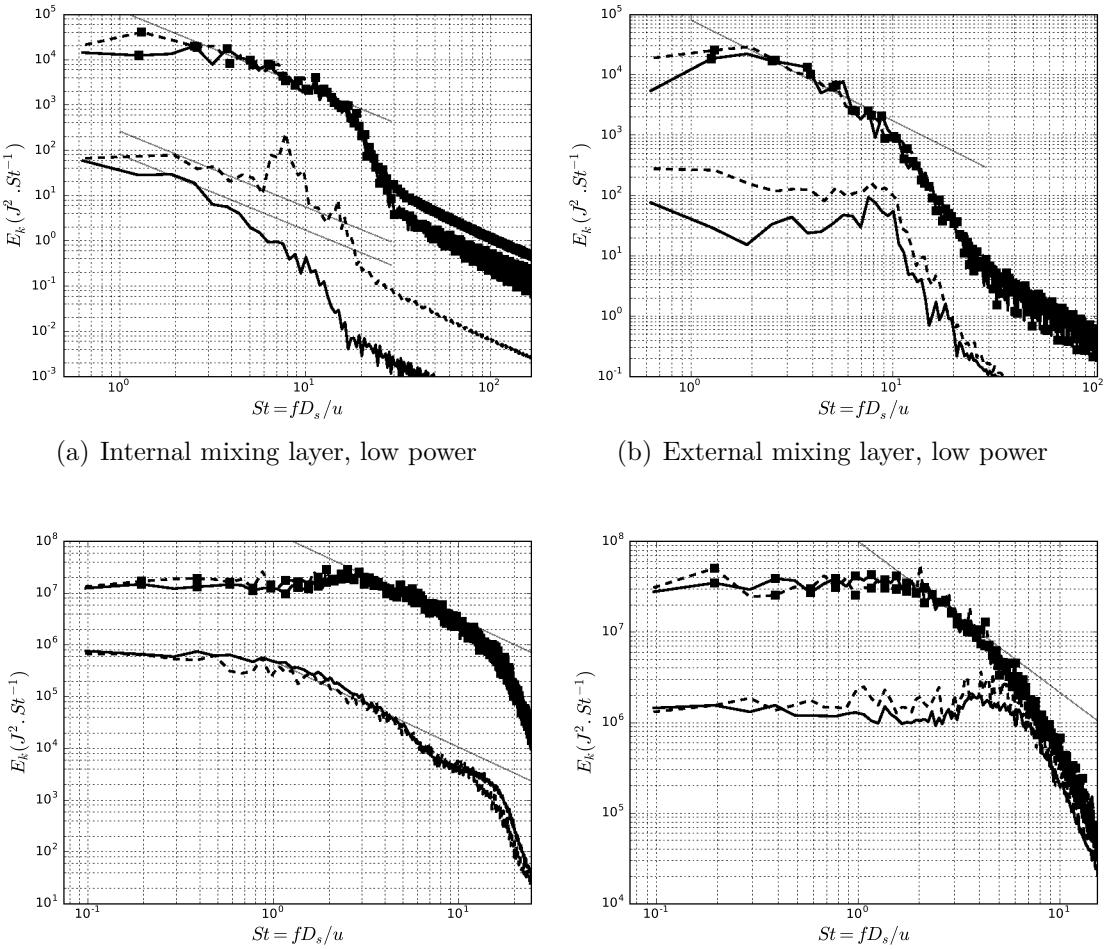

(a) Internal mixing layer, low power

(b) External mixing layer, low power

(c) Internal mixing layer, high power

(d) External mixing layer, high power

Figure 8.45: PSD of the kinetic energy k. With M_1 grid, jet simulation without combustion noise forcing (–) and with combustion noise forcing (- -). At the lips of the primary (P_1 in Fig. 8.2, internal mixing layer) and secondary (S_1, external mixing layer) nozzles (no symbol). At 2 D_s of the primary nozzle exit (P_2 in Fig. 8.2) in the internal mixing layer and at 0.45 D_s of the secondary nozzle exit (S_2) in the external mixing layer (■). $-5/3$ power law (–).

In Fig. 8.43, a lot of turbulent structures are generated between the internal mixing layer and the plug. It can also be noticed that the flow just behind the plug exit is much more turbulent (as shown in Figs. 8.39(a) and 8.42(c)). Almost

no difference can be observed in the external mixing layer at the secondary nozzle lip (S_1 in Fig. 8.2). Some large vorticity structures are observed at the secondary nozzle lip, that is in agreement with the peaks observed with the PSD of the kinetic energy in Fig. 8.45(b). However, the peaks are less pronounced with the combustion noise injection as the turbulent kinetic energy levels increase. A little further in the secondary mixing layer (S_2 in Fig. 8.2), the turbulence is more developed and is not impacted by the combustion noise.

At high power, vorticity in the secondary nozzle is more intense with the introduction of combustion noise (lower part of Fig. 8.44) even if the development of the mixing layers downstream seems similar in both cases. The PSD of the kinetic energy confirm this observation where the same kinetic energy repartition is observed in Figs. 8.45(c) and 8.45(d).

The development of the mixing layers does not seem to be impacted by the combustion noise when the flow is sufficiently turbulent. However, it seems that combustion noise has a strong interaction with the primary potential core, particularly at high power where strong response of the flow is observed at the combustion noise forcing frequencies. The noise linked to these turbulent structures should be different. Therefore, a far-field acoustic analysis is required in order to investigate how the combustion noise sources propagate and impact the far-field acoustic propagation of jet noise.

8.3 Far-field acoustic propagation using an acoustic analogy

In order to propagate the noise sources in the far-field at 45.72 m, the Ffowcs Williams and Hawkings acoustic analogy has been chosen (Brentner and Farassat 1998), using the advanced time formulation proposed by Casalino [2003]. The FWH acoustic analogy allows to take into account solid or moving surfaces. In this analogy, we consider a surface S in part included in the source region as shown in Fig. 8.46.

The surface S moves at the speed u^S. Its position is indicated by the function $f(x,t)$ which is zero for the points belonging to the surface, negative for the points inside the surface and positive for points outside. The Heaviside function $H(f)$ is introduced as:

$$H(f) = 0 \text{ for } f < 0, \tag{8.14}$$

$$H(f) = 1 \text{ for } f \geq 0. \tag{8.15}$$

By multiplying the conservation equations of mass and momentum by $H(f)$ and

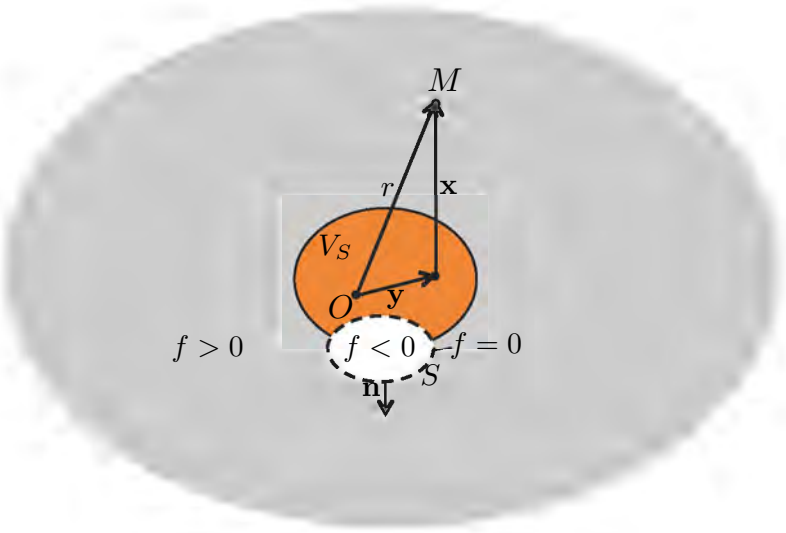

Figure 8.46: Representation of space according to the FWH acoustic analogy: the source region of volume V_S is orange, the propagation region in which is the observer M corresponds to the gray part, a surface S of normal n, defined by the function f, is partially included in the source region.

by combining them, we obtain the equation of the FWH acoustic analogy:

$$\frac{\partial^2}{\partial t^2}((\rho - \rho_0)H(f)) - c_0^2\nabla^2(\rho - \rho_0)H(f) = \tag{8.16}$$

$$\frac{\partial^2}{\partial x_i \partial x_j}(T_{i,j}H(f)) + \frac{\partial}{\partial x_i}(L_i\delta(f)) + \frac{\partial}{\partial t}(Q\delta(f)), \tag{8.17}$$

where $T_{i,j}$ is the Lighthill tensor defined as:

$$T_{i,j} = \rho u_i u_j + (p - c_0^2\rho)\delta_{i,j} - \tau_{i,j}. \tag{8.18}$$

The terms L_i and Q are given by:

$$L_i = -(\rho u_i(u_j - u_j^S) + (p - p_0)\delta_{i,j} - \tau_{i,j})n_j, \tag{8.19}$$

$$Q = (\rho(u_i - u_i^S) + \rho_0 u_i^S)n_i, \tag{8.20}$$

where $\mathbf{n}$ is the unit normal at the surface S directed towards the exterior. An equation for the fluctuations of $(\rho - \rho_0)H(f)$ is thus obtained. The formalism of

the Green's function allows to express the variations of the density by the relation:

$$
\begin{aligned}
4\pi c_0^2(\rho-\rho_0)H(f) &= \frac{\partial^2}{\partial x_i \partial x_j}\int_{f>0}\frac{1}{r|1-M_r|}T_{i,j}\left(\mathbf{y},t-\frac{r}{c_0}\right)d\mathbf{y} \\
&+ \frac{\partial}{\partial x_i}\int_{f=0}\frac{1}{r|1-M_r|}L_i\left(\mathbf{y},t-\frac{r}{c_0}\right)dS \\
&+ \frac{\partial}{\partial t}\int_{f=0}\frac{1}{r|1-M_r|}Q\left(\mathbf{y},t-\frac{r}{c_0}\right)dS,
\end{aligned}
\tag{8.21}
$$

where M_r is the Mach number defined as $M_r = (\mathbf{u}.r)/(rc_0)$. It can be noted that the variations of the density are expressed in Eq. 8.22 as the sum of three contributions. The first contribution, associated with the tensor $T_{i,j}$, corresponds to a quadrupole source term and is neglected. It includes all quadrupoles outside of the surface S. The second contribution, containing the term L_i, represents a dipolar component which corresponds to the stresses exerted on the surface S. Finally, the third contribution, associated with the term Q, is a monopolar component due to the passage of the fluid through the surface S.

	Low Mach	High Mach	Noise investigated	Code
Unforced jet LES, M_1 mesh	M1UL	M1UH	Jet noise	AVBP
Unforced jet LES, M_2 mesh	M2UL	M2UH	Jet noise	AVBP
Forced jet LES, M_1 mesh Pressure-NSCBC	M1FL	M1FH	Jet noise and combustion noise	AVBP
Forced jet LES, M_1 mesh Velocity-NSCBC	M1FLb	M1FHb	Jet noise and combustion noise	AVBP
CONOCHAIN	CONL	CONH	Combustion noise	AVSP-f

Table 8.3: Computations comparisons

The FWH acoustic analogy is applied to the unforced and forced jet LES. Table 8.3 summarizes the computations performed in this chapter and compared with the CONOCHAIN results of Chapter 6. From the unforced jet LES, jet noise is investigated whereas from the forced jet LES, the noise from jet flow with combustion noise forcing is obtained. Therefore the noise will be the contribution of jet noise and combustion noise as shown in Fig. 8.1. CONOCHAIN far-field propagation with AVSP-f propagates only combustion noise in an heterogeneous temperature field.

Thus, the jet flow field in the LES is enclosed by an integral surface. This surface is closed upstream and downstream with several surfaces, and have been placed in the area where the pressure amplitudes are still intense, before the mesh coarsening, Fig 8.47. The acoustic pressure levels are computed at 47.16 D_s from the configuration origin and compared with the experimental data.

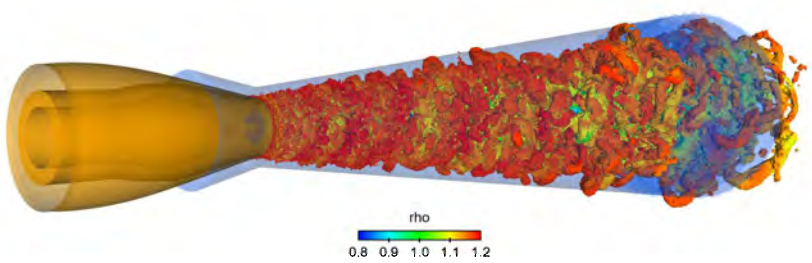

Figure 8.47: Integral surface used for the FWH analogy with an iso-contour of the Q criterion colored by the density in the high power case.

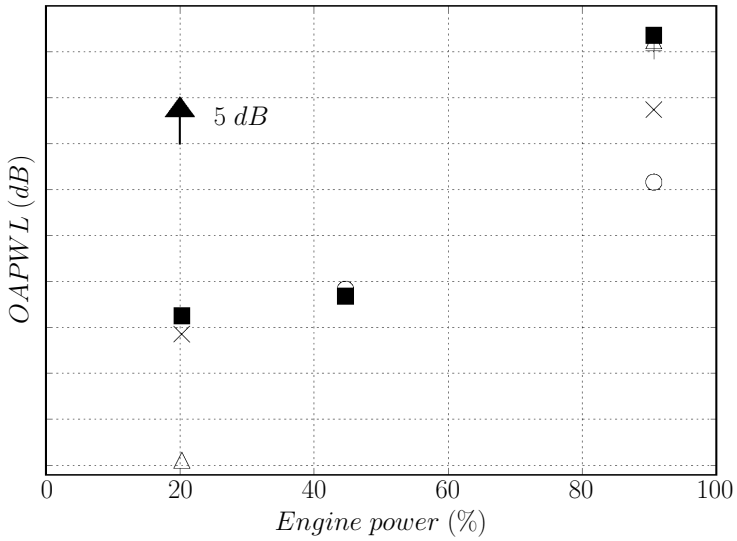

Figure 8.48: Over All Power Level (OAPWL) in far field (45.72 m). CONOCHAIN combustion noise (○), jet noise with M_1 (△) and with M_2 (+), jet noise and combustion noise from M1FL and M1FH in Table 8.3 (×), experimental OAPWL of downstream engine noise (■).

The OAPWL of the computed cases are presented in Fig. 8.48 and compared with the experimental and CONOCHAIN results. At low power case, it can be seen that jet noise is not the main contribution since its OAPWL is 15 dB lower than the one of the experimental data. On the contrary, when the contribution of combustion noise is added to the jet, the power is increased and is close to reach the experimental and CONOCHAIN levels within 1 dB. At high power case, it is confirmed that jet noise is the main contribution of the acoustic engine signature since its predicted power is only of about 1 dB lower than the total downstream acoustic engine noise. By adding the contribution of combustion noise, the noise power is attenuated by 6 dB, which means that the combustion noise in this investigated case strongly impacts the acoustic signature.

The acoustic behavior is investigated more precisely in the next sections for both operating points.

8.3.1 Flow field impacts on far-field combustion noise radiation at low Mach number (AVSP-f versus LES)

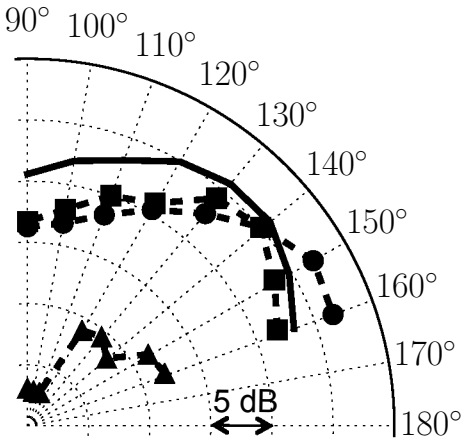

Figure 8.49: Over All Sound Pressure Level (OASPL) in far field (45.72 m) of the low power case. Jet noise (M1UL in Tab. 8.3): (▲), Jet and Combustion noise (M1FL in Tab. 8.3): (■), Combustion noise predicted with CONOCHAIN (CONL in Tab. 8.3): (●) and total experimental OASPL (–).

At low power, the jet is characterized by a two-lobe directivity (Fig. 8.49). The first lobe at 130° is the acoustic diffraction at the nozzle lip end. The secondary lobe at 160° corresponds to the directivity of the large turbulent scales. By adding the contribution of combustion noise, the directivity obtained is closest to the

experimental directivity. Meaning that what is captured in the acoustic spectra is mainly the combustion contribution. The combustion noise mainly propagates at 140° whereas it propagates at 150° with AVSP-f. This corroborates the directivity obtained with Amiet's assumption to take into account the shear layer refraction (Fig. 6.69). Therefore, the jet flow has an impact on the directivity even if the jet velocity is low and considering the temperature inhomogeneities with AVSP-f is already a good step but not enough. Up to 110° the LES levels corroborates the AVSP-f ones. However, after this angle, the levels are lower.

To better understand the reason of this level decrease, the acoustic spectra are presented in Fig. 8.50. For several angles as defined in Fig. 5.2, both acoustic sources can be distinguished. Jet noise obtained from the unforced jet LES (M1UL in Tab. 8.3) is a very low frequency noise, $0.1 < St < 0.8$. At these frequencies, the jet noise levels reach the experimental level spectra and rapidly decrease at much higher frequency. The first bump observed around $St = 0.1$ is due to convergence. More simulation time is required to solve these very low frequencies. According to Tam et al. [2008], the fine turbulent scales of a jet (high frequencies) propagate mainly at 90° whereas, the large turbulent scales (low frequencies) propagate at more downstream angles. It can be observed that the jet noise levels at high frequencies ($St > 6$) are more important in the radial direction (90°). On the contrary, the low frequency noise ($St < 0.8$) is more important at 160°. The cut-off frequency is observed around $St = 30$.

The jet LES simulation forced with combustion noise in Fig. 8.28(a) (M1FL in Tab. 8.3) exhibits a rich acoustic spectrum as shown in Fig. 8.50. The first bump is due to time convergence. In terms of noise levels, the spectra globally agree with the experimental data and the CONOCHAIN results with AVSP-f. Meaning that at low power case, with low Mach number jet, CONOCHAIN is sufficient to obtain a good estimate of the combustion noise in terms of OAPWL and acoustic spectra. A very noisy signal with many pseudo discrete tones is obtained. And these large tones seem to reproduce the acoustic signature of the experimental data: these tones observed in the experimental data at low frequency are very characteristic of the combustion noise. However, at some angles (130° in Fig. 8.50(b) and 140° in Fig. 8.50(c)) and at certain frequencies ($2 < St < 3$), a strong loss of power levels can be observed. This acoustic loss was not observed with the AVSP-f computations. Two causes can be considered by listing the differences between the two computations: the jet flow and the boundary conditions. As the jet noise is very low at these frequencies, it is probably not the cause of this attenuation. One possible cause could be the boundary conditions. Indeed, it is explained in Annex A that low frequencies are strongly reflected due to the relaxation coefficient at the primary nozzle inlet. This induces destructive interferences in the far-field when it is coupled with a negative reflection coefficient at the secondary nozzle

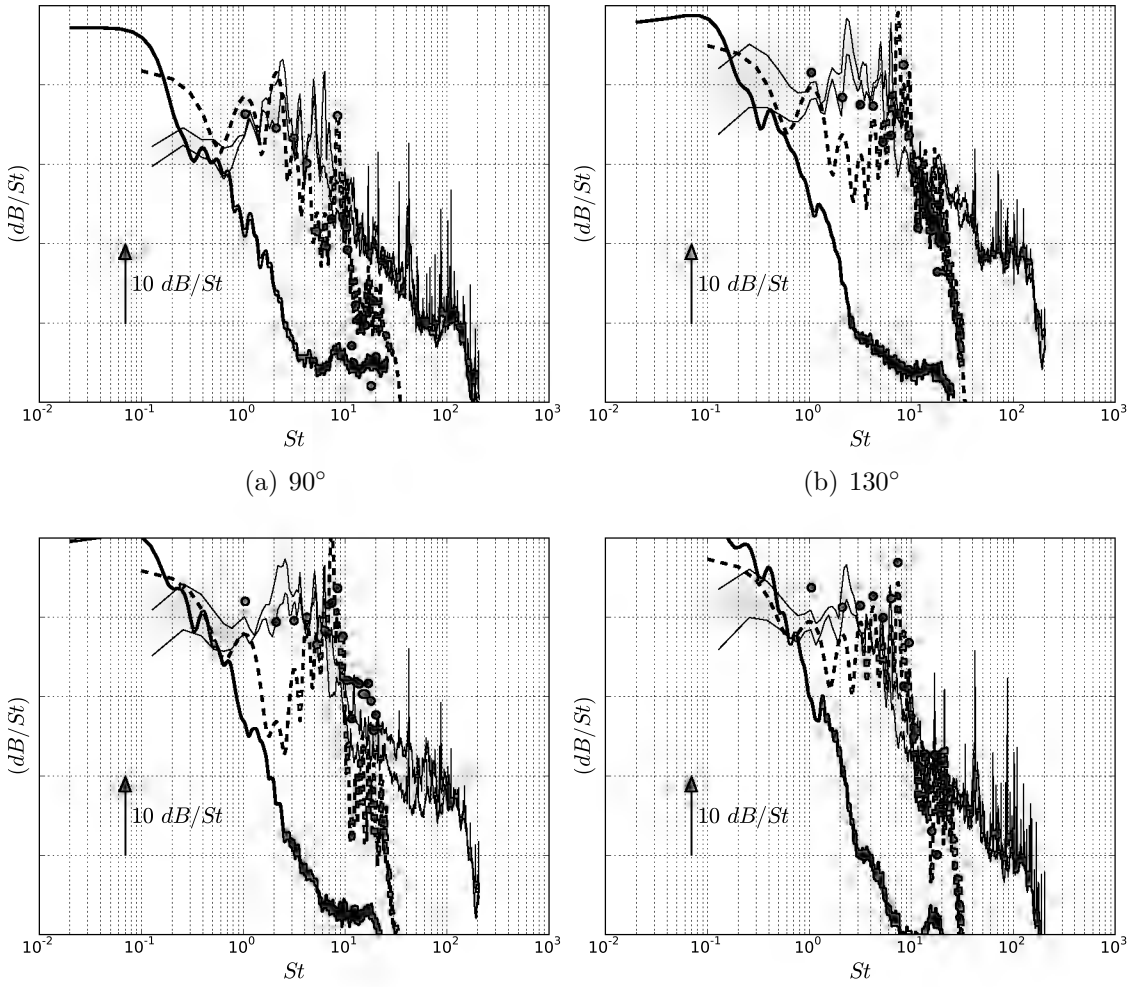

(a) 90° (b) 130°

(c) 140° (d) 160°

Figure 8.50: Combustion noise propagated through a low Mach number jet flow in far field (45.72 m) with a pressure condition imposed at the secondary stream inlet. Jet noise (M1UL in Tab. 8.3): (–), Jet and Combustion noise (M1FL in Tab. 8.3): (- -), Combustion noise predicted with CONOCHAIN (CONL in Tab. 8.3): (●) and total experimental PSD (gray area).

inlet (total pressure imposed). These attenuations can be limited by decreasing the relaxation coefficient value at the primary nozzle inlet, so that the reflection coefficient is lower. However, these destructive interferences still exist, even if their amplitudes are less important.

In Fig. 8.51, if the boundary condition at the secondary nozzle inlet is replaced by a velocity condition (M1FLb in Tab. 8.3), then the reflection coefficient becomes

positive. With the same relaxation coefficient than for the pressure condition, the reflection coefficient module is the same. However, the acoustic waves interaction changes due to a different phase. There are no more destructive interferences observed in far-field and the spectra obtained are more similar to the experimental ones as shown in Fig. 8.51.

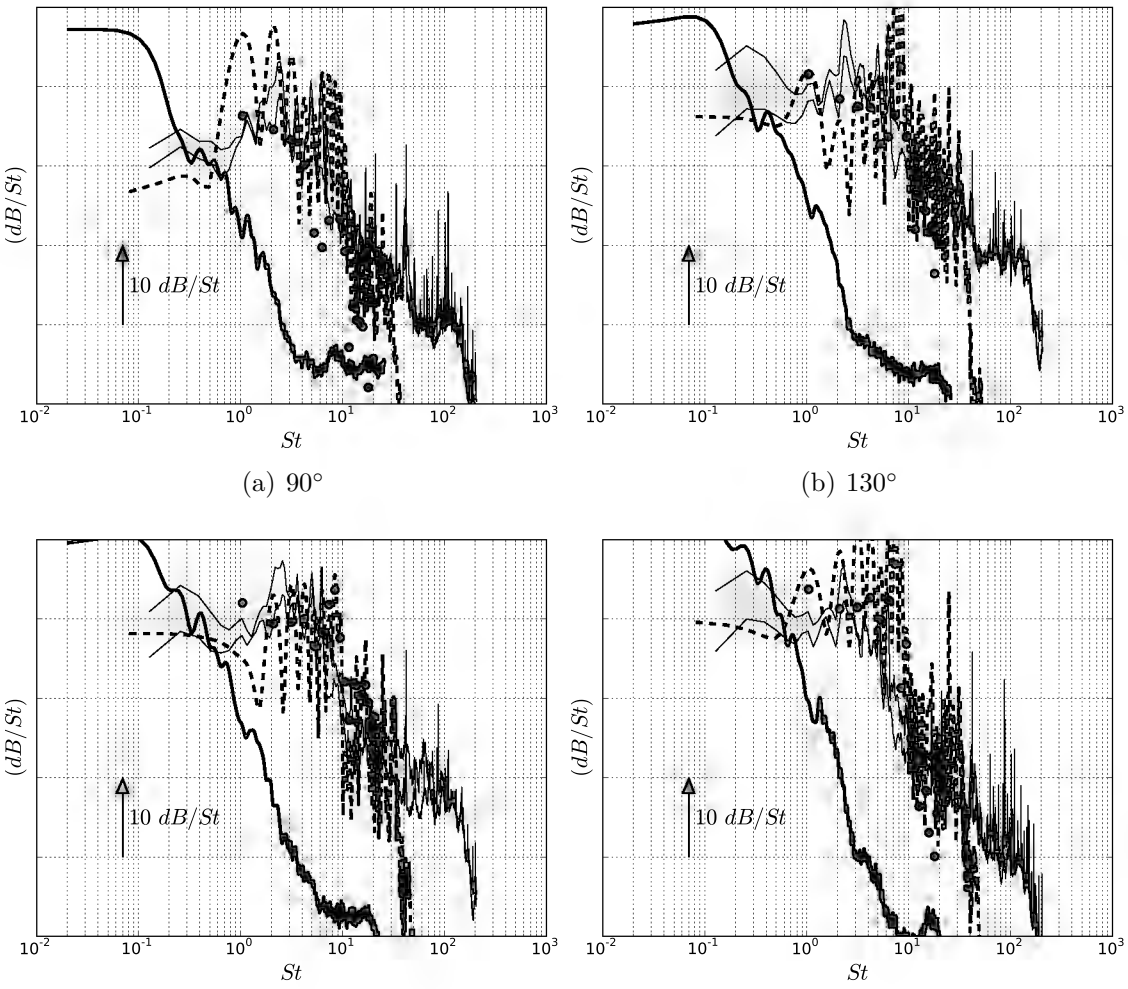

(a) 90° (b) 130°

(c) 140° (d) 160°

Figure 8.51: Combustion noise propagated through a low Mach number jet flow in far field (45.72 m) with a velocity condition imposed at the secondary stream inlet. Jet noise (M1UL in Tab. 8.3): (–), Jet and Combustion noise (M1FLb in Tab. 8.3): (- -), Combustion noise predicted with CONOCHAIN (CONL in Tab. 8.3): (●) and total experimental PSD (gray area).

None of these boundary conditions give false results: the same mean jet flow

characteristics are obtained. Acoustics is extremely dependent on the impedance conditions at the nozzle inlets which are an important parameter to know when acoustic forcing is performed. Moreover, the choice between a pressure or a velocity condition (described in section A) seems determinant for acoustics computation as the phase contribution will depend on this as shown with AVSP-f. Knowing which boundary condition to impose with the correct impedance at each nozzle inlet is required to correctly propagate the acoustics at the desired operating point.

8.3.2 Contribution of combustion noise and subsonic jet noise at high Mach number

In Fig. 8.52, both LES jet computations without combustion noise forcing (M1UH and M2UH in Tab. 8.3) give a maximum directivity at 160° as in the experimental data (Fig. 8.52). The directivity of the OASPL is not well predicted at angles from 90° to 120°, the pressure levels differ from the experimental one with a discrepancy of about 2 dB. On the contrary, between 130° and 160°, the evolution of the levels is similar. This slight difference in the directivity shape could be explained by the difference of geometry between the simulations and the bench data.

The OASPL of the forced jet simulation (M1FH in Tab. 8.3) exhibits a maximum directivity at 160°. As seen before, this directivity corresponds to the propagation direction of the large turbulent scale of the jet, while the pressure fluctuations from the engine core are refracted and more intense at 140°. However, the pressure level at 160° is about 10 dB lower than the experimental level. Either the combustion noise strongly affects the jet noise generating mechanisms or once again it is due to the boundary conditions. In the first case, the combustion noise sources excite the boundary layer. As the latter is not enough turbulent, its fluctuations are completely controlled by the excitation. This would lead to a different boundary-layer thickness and so to a different development of turbulence. So that the jet will not be the same as the one obtained with an unforced simulation. A turbulent forcing at the outlet of the nozzle would be required to keep the same boundary layer thickness and so to propagate the combustion noise in the same jet development. In the second case, it could be possible that due to the total pressure condition at the secondary nozzle inlet, the phase contribution would not be necessarily the same as in the experimental condition. However, it has been seen that the differences induced by a total pressure condition concern mainly the low frequency (section A). At 90°, the pressure level is quite close to the experimental one. However, it is 2 dB lower than the one obtained with the M_1 unforced jet simulation (M1UH in Tab. 8.3).

The PSD of pressure (Fig. 8.53) show that jet noise predicted with unforced jet LES (M1UH in Tab. 8.3) is in good agreement with the experimental one, both

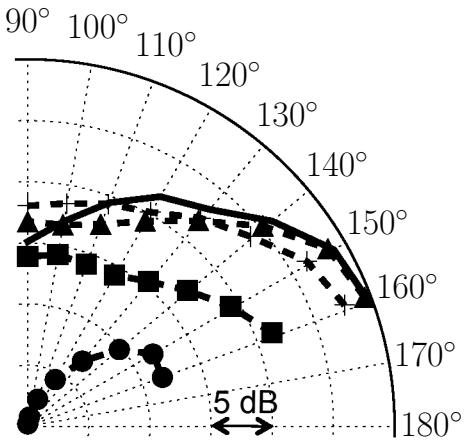

Figure 8.52: Over All Sound Pressure Level (OASPL) in far field (45.72 m) of the high power case. Jet noise with M1UH in Tab. 8.3: (▲) and M2UH in Tab. 8.3: (+), Jet and Combustion noise (M1FH in Tab. 8.3): (■), Combustion noise predicted with CONOCHAIN (CONH in Tab. 8.3): (●) and total experimental OASPL (–).

in terms of shape and noise levels. At high frequency ($St > 1$), the jet-noise slope differs from the experiment. Once again, it could be supposed that a lobe mixer will give more noise levels at high frequency due to an enhanced mixing as seen in the LES simulations of a dual stream jet with an internal lobed mixer (Pouangué et al. 2014). At 90° (Fig. 8.53(a)), three bumps can be observed. The first one around $St = 0.03$ is due to time convergence. The second one seen at $St = 0.6$ would be vortex shedding, that could be observed in temporal movie. The last one at $St = 0.3$ could be associated with vortex pairing. Its frequency corresponds to the frequency of the vortex shedding divided by two. These phenomena are attenuated with the M_2 mesh (M2UH in Tab. 8.3) but are still persistent.

The forced jet simulation (M1FH in Tab. 8.3) exhibits a different behavior compared with the unforced jet simulations. At high frequency, $St > 0.7$, the noise levels are close to the combustion noise levels. Therefore the turbulence has changed. This seems to be more in agreement with a jet development entirely controlled by the combustion noise due to not enough turbulent boundary layers. However, more investigations are needed to know if the jet noise generation mechanisms have been modified. Otherwise the level attenuation could be due to a destructive contribution between the acoustics coming from combustion and the acoustics coming from the jet turbulence. At low frequency, $St < 0.1$, the noise levels reach the jet noise ones. It seems that the spectra are less impacted at 90° and 130° (Figs. 8.53(a) and 8.53(b)). At 90°, the vortex pairing frequency

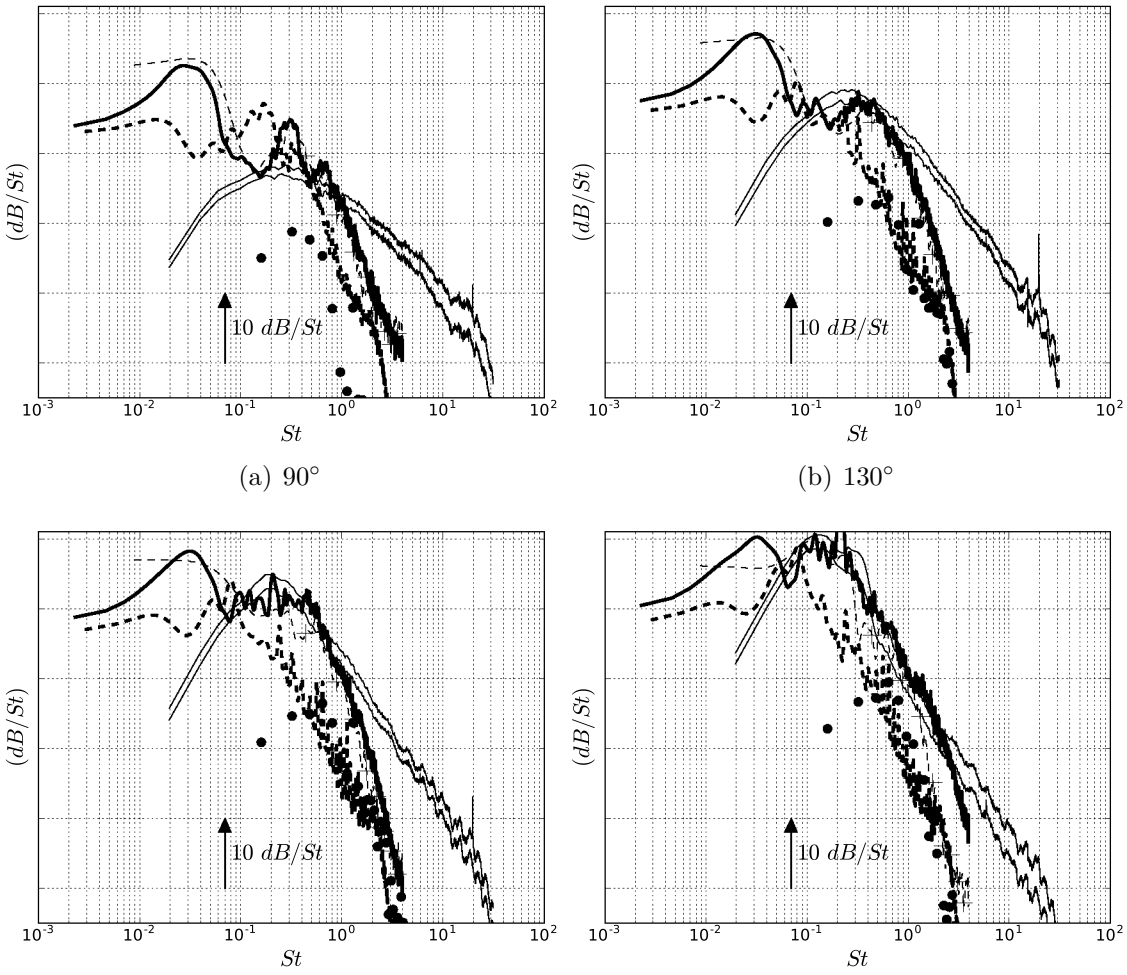

(a) 90° (b) 130°

(c) 140° (d) 160°

Figure 8.53: Combustion noise propagated through a high Mach number jet flow in far field (45.72 m). Jet noise with M1UH in Tab. 8.3: (–) and with M2UH in Tab. 8.3: (– + –), Jet and Combustion noise (M1FH in Tab. 8.3): (- -), Combustion noise predicted with CONOCHAIN (CONH in Tab. 8.3): (●) and total experimental PSD (gray area).

has been decreased from $St = 0.3$ to $St = 0.15$ which corresponds to the first combustion noise forcing frequency. It is also observed with the vortex shedding frequency which has been shifted from $St = 0.6$ to $St = 0.3$. This tends to be in agreement with a modification of the boundary layer at the nozzle lips ends due to an acoustic excitation. It has to be noticed that all peaks observed are harmonics of $St = 0.15$. In order to understand which mechanisms control these

peaks, reconstructed instantaneous pressure fluctuation fields are obtained from two-dimensional Discrete Fourier Transform (DFT).

Pressure fluctuation fields at $St = 0.15$ and $St = 0.3$ are shown in Figs. 8.54(a) and 8.54(b). At $St = 0.15$ (first combustion noise forcing frequency), strong coherent pressure oscillations can be observed in the near-acoustic field and appear as a train of puffs. These intermittent turbulent structures leak a relatively small fraction of their energy to the far-field but are nonetheless acoustically important (Jordan and Colonius 2013). The amount of leakage depends on the envelope of the coherent pressure oscillation which can lead to a super-directive radiation with certain forms (Crighton and Huerre 1990). These oscillations are more intense with the combustion noise introduction (M1FH in Tab. 8.3). This phenomenon was already existing in the unforced simulation (M1UH in Tab. 8.3) but it is amplified with the forcing at this frequency and more spread over the radial direction. Combustion noise has energized the big turbulent structures of the external mixing layer.

At $St = 0.3$ in Fig. 8.54(b), a strong pressure oscillation is observed at the end of the secondary nozzle which releases acoustic waves radially propagating in the unforced simulation. The turbulent structures which are released at the end of the secondary nozzle are convected through the external mixing layer and then gather together to form bigger structures. These phenomena are captured by the FWH surface of integration. The position of this surface could have an impact on the acoustic results. With the introduction of combustion noise, the internal mixing layer is excited at the combustion noise frequency forcing and smaller structures are observed at the centerline of the jet (**A**). The coherent pressure oscillations in the external mixing layer are also more regular and less spread over the radial direction (**B**). Wei and Freund [2006] showed that more regular coherent structures are quieter than those with spatial modulation. This explains the attenuation of the peak at $St = 0.3$ in the case with combustion noise introduction.

At $St = 0.6$ in Fig. 8.55(a), different instantaneous pressure fields are observed. In the unforced case (upper part), downstream-propagating acoustic waves can be observed in the far-field (**C**). These acoustic waves are probably related with large turbulent scales of the jet. On the contrary, with the combustion noise forcing (lower part), these acoustic waves have disappeared. This corroborates a modification of the turbulence with the combustion noise introduction leading to a different acoustics and thus an attenuation of the noise levels at this Strouhal number as shown in Fig. 8.53. However, these conclusions concern a jet with non-fully turbulent boundary layers and a proper turbulent forcing with a particular attention on the boundary conditions should be considered for future simulations.

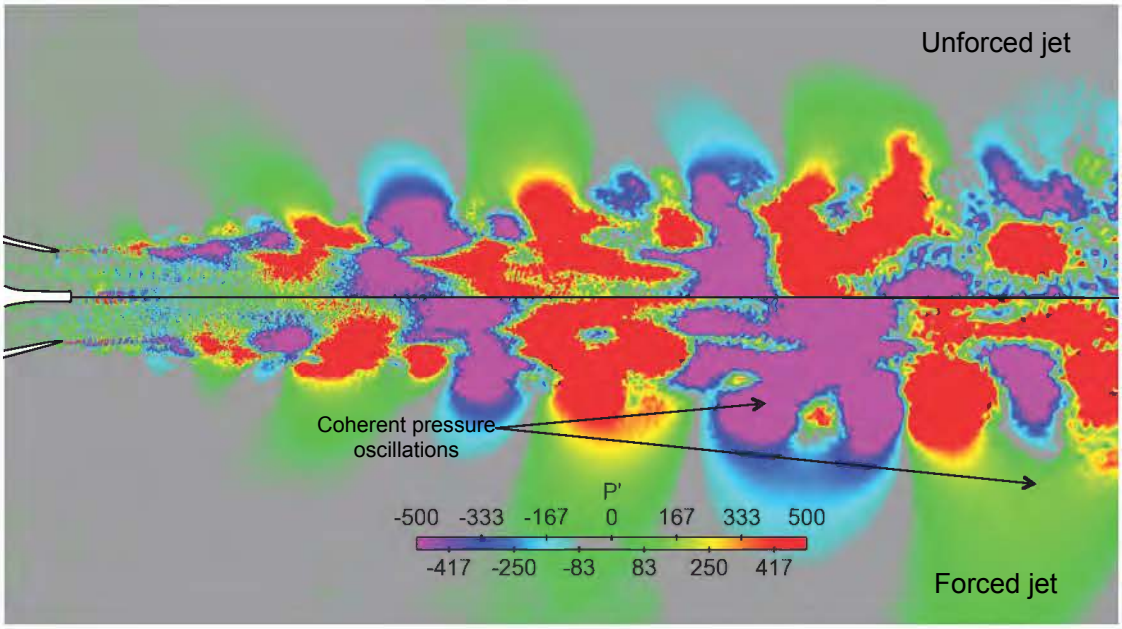

(a) $St = 0.15$

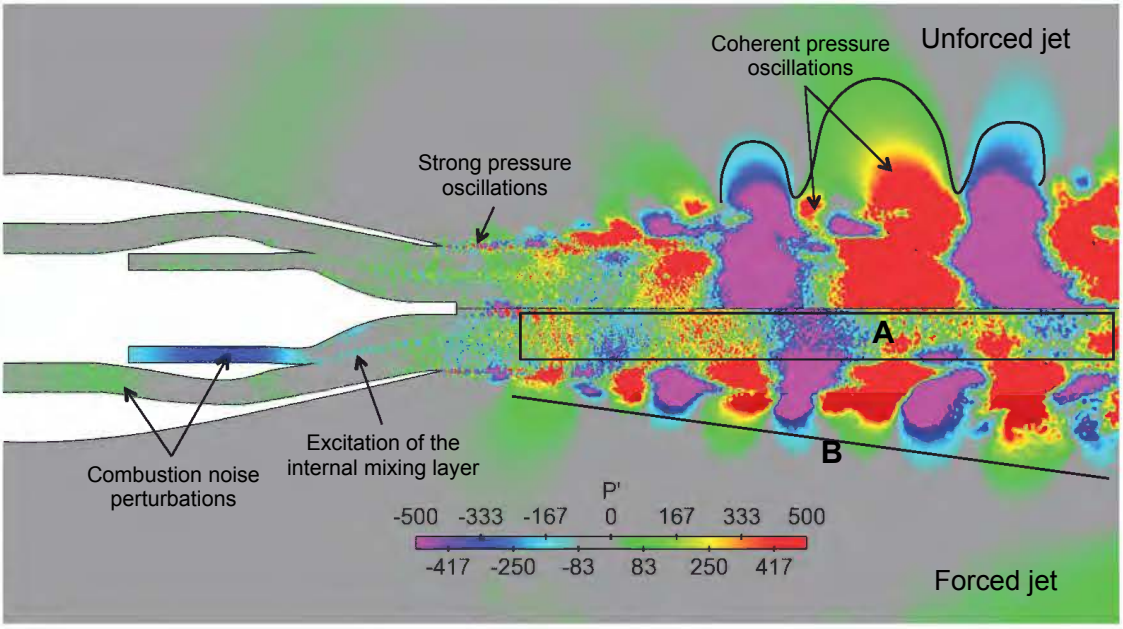

(b) $St = 0.3$

Figure 8.54: Instantaneous pressure fields for unforced jet (upper part) and forced jet (lower part).

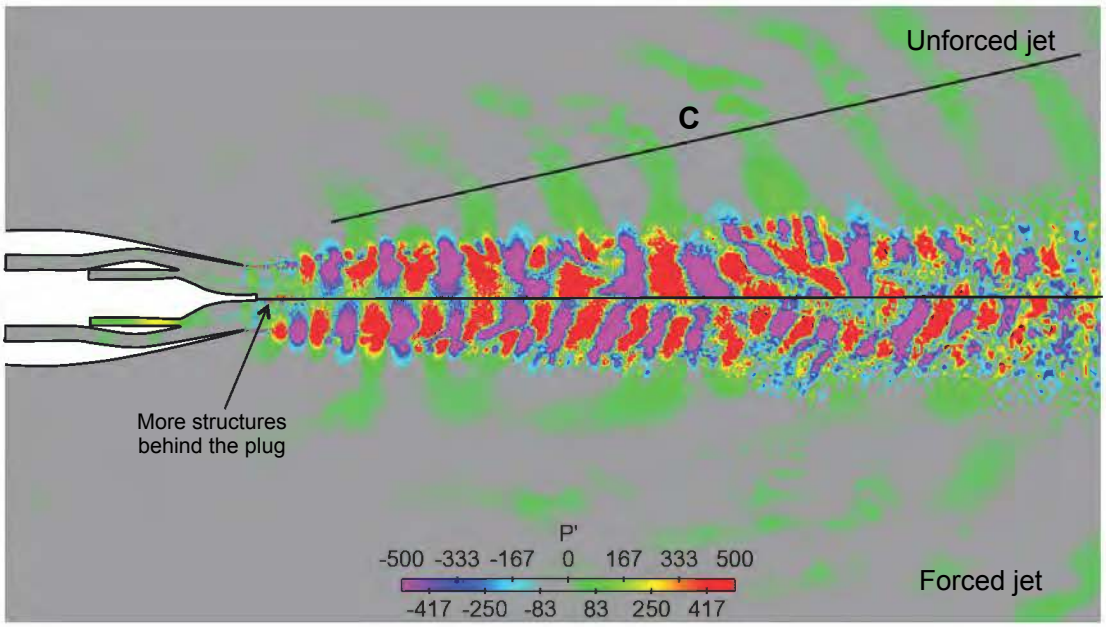

(a) $St = 0.6$

Figure 8.55: Instantaneous pressure fields for unforced jet (upper part) and forced jet (lower part).

To conclude, numerical simulations of a double stream jet, acoustically forced with the combustion noise predicted by CONOCHAIN, have been performed. Two different operating points have been computed, at low and high engine power conditions. The overall behavior of the jet in terms of mean fields has been found to be quite insensitive to the acoustic forcing. However, noticeable differences in the turbulence spectra have been observed particularly at high power conditions, leading to a change in the noise generating mechanisms. This has been found to be probably due to an insufficient turbulence of the boundary layer in the unforced jet, which is so subject to a stronger influence on the forcing frequency. This causes differences also in the propagation of noise to the far field and to a change in the overall noise spectra. The acoustic treatment of the boundary conditions has been found to be crucial in order to correctly control the incoming and outcoming acoustic waves in the computational domain. In particular, it has been highlighted that the knowledge of the nozzle impedances is of primary importance if a forced jet simulation is to be performed. Moreover, the choice of imposing a velocity or pressure node boundary condition at inlets implies differences in the phase shift between the incoming and outcoming waves, leading to a completely different acoustic propagation. This has been noticed mostly in the low power case, where destructive contributions have been observed at low frequencies.

General conclusion

Predicting combustion noise is not an easy task due to the multiple physical interactions involved during the combustion processes. Many experiments exist to evaluate the combustion noise from flames or combustion test rig. However, only a few include the complete propagation path of combustion noise within an engine device as it is difficult to isolate this acoustic source from the noise of the other engine modules. Empirical methods based on extrapolations and simplifications are often used for the prediction of combustion noise within modern aero-engines. However, these methods do not consider the combustion noise problem in its complexity and many physical processes are not captured. To overcome the limitation of such methods and capture more physics, a fully deterministic simulation chain can be envisaged. However, this challenge remains difficult as it requires to accurately capture the unsteadiness responsible for direct and indirect combustion noise, to correctly identify the acoustic role of each engine component from the combustion chamber to the turbine exit and to have the good far-field noise propagation. Such a numerical method exists and has proved its feasibility with the TEENI database (Livebardon 2015).

The numerical tool CONOCHAIN was chosen to investigate the combustion noise of a real turbofan engine. Several operating points are computed to evaluate the evolution of combustion noise levels with an increase in engine power. The turbofan engine is composed of an 18 injectors combustion chamber, an high pressurized axial turbine followed by a low pressurized axial turbine. The engine ends with a double stream nozzle having a plug. Each component of the engine is treated with a specific part of CONOCHAIN. LES of combustion chamber are first used to provide high-fidelity predictions of the unsteadiness of the flow and extract acoustic (direct noise) and entropy as well vorticity waves (indirect noise) at the combustor exit. LES are then coupled with an actuator disk theory named CHORUS to propagate the acoustic and convective (entropy, vorticity) waves in the stator/rotor stages. The acoustic waves are finally propagated from the turbine exit to the far-field using the acoustic solver AVSP-f.

Performing LES of combustion in a single sector chamber for three operating points: low power, intermediate power and high power, mechanisms responsible for combustion noise have been highlighted. As there is no acceleration of entropy or vorticity waves in the chamber, direct noise is the main source of noise. The turbulence interaction with the flame induces hot and cold spots, however, most of the entropy noise sources are generated by the interaction of the cold flow (dilution holes) with the burnt gases. It has been seen that for similar flow characteristics and flame shape (low and high power), similar shape of direct noise spectra at the outlet of the combustor are found. On the contrary, the intermediate case has shown a different flame shape and a spectrum for direct noise.

By introducing these acoustic, entropy and vorticity waves in the turbines, the acoustic behavior of the successive blade rows has been analyzed. It has been found that an increase in engine power leads to a higher transmission of noise through the turbines. Vorticity noise is negligible as it is strongly damped in the successive turbine stages. However, it could be necessary to consider azimuthal modes and other vorticity interactions. The other source of indirect noise (entropy noise) in the turbines stages has been demonstrated to be important, as the effect of the acceleration of hot and cold spots. Due to higher velocity gradients with an increase in engine power, more indirect noise is generated. Moreover, it has been noticed how, for high engine powers, indirect noise is generated also in the subsequent turbine stages. All propagation analysis have been done with the entropy planar mode filter proposed by Livebardon et al. [2015]. This filter was developed to overcome the periodicity assumption used for single sector simulations. Indeed, due to this assumption the entropy planar modes of each sector are assumed to be in phase. Therefore a correction is done to consider a random phase-shift of the modes to mimic a 360° full annular combustion chamber. This correction considerably attenuated the entropy noise levels. The limits of this filter are questionable for a thermoacoustic instability as it would induce coherence between the fluctuating signals. A 360° full annular simulation at this operating condition should be considered to verify the validity of the filter.

Far-field propagation of the combustion noise sources have been performed with AVSP-f. The double stream nozzle and its plug have been considered. The mean temperature field has been extracted from numerical simulations to provide accurate mean temperature gradients. It has been confirmed by looking at OAPWL that combustion noise is the dominant noise source at low engine regimes (low power and high power case) and that the overall combustion noise increases with an increase in engine power. The far-field propagation shows a noise directivity at nearly 140°. By considering monopolar acoustic sources, the far-field noise levels are obtained by scaling the acoustic pressure from the acoustic domain boundaries and can be impacted. Finally, the absence of azimuthal acoustic modes in the

acoustic forcing at the turbine exit is also a significant bias introduced in these noise computations.

In the acoustic solver AVSP-f, the absence of mean velocity field is the major assumption which can alter acoustic propagation even if the turbofan engine exhaust flow is low-Mach number (at low and intermediate power). Another acoustic analogy allowing to consider flow effects on the acoustic propagation could be considered (for instance Möhring et al. 1983; Mohring 2010). To investigate this point, a full LES of the jet itself was performed.

In order to consider the full engine-core flow path to take into account the effects of core noise on the far field radiation, a forcing method has been implemented in LES to check the effects of combustion forcing. Acoustic sources predicted by CHORUS have been introduced in LES jet noise simulation to force the flow and propagate to the far-field. To do so, LES of a double stream jet, acoustically forced with the combustion noise predicted by CONOCHAIN, have been performed. Two different operating points have been computed, at low and high engine power conditions. At low power, it is known that jet noise is negligible due to low exhaust velocity. However, at high power, jet noise is the preponderant source of noise. In terms of mean fields characteristics, it has been found that jet flow is not very sensitive to the acoustic forcing. However, noticeable differences in the turbulence spectra have been observed particularly at high power conditions in the primary jet core length. This forcing of the jet by combustion noise leads to a change in the noise generating mechanisms. However, it has been found to be probably due to an insufficient turbulence of the boundary layer in the unforced jet, which is so subject to a stronger influence on the forcing frequency. This causes differences also in the propagation of noise to the far field and so to a change in the overall noise spectra. Acoustic forcing to obtain sufficient turbulence levels at the outlet of the nozzle could be envisaged to perform the combustion noise forcing and avoid the generation of structures excited at the combustion noise frequencies. A broadband combustion noise forcing should also be considered to overcome the excitation due to tonal forcing. The acoustic treatment of the boundary conditions has been found to be crucial in order to correctly control the incoming and outcoming acoustic waves in the computational domain. In particular, the knowledge of the nozzle impedances is of primary importance for forced jet simulations. Moreover, the choice of imposing a velocity or pressure node boundary condition at inlets implies differences in the phase shift between the incoming and outcoming waves, leading to a completely different acoustic propagation. This has been noticed mostly in the low power case, where destructive contributions have been observed at low frequencies.

The results obtained at low power condition are rather encouraging and the method could be used at higher operating condition where jet noise is present but

not dominant to better understand how the far-field noise is impacted.

Appendices

Appendix A

Impact of the inlet boundary conditions on the acoustic propagation

Numerical simulations of compressible flows are very sensitive to the treatment of the boundary conditions. This is particularly true for aeroacoustic simulations where reflection coefficients at boundary conditions are highly decisive for the acoustic propagation (Bogey and Bailly 2002). Even if mean flow quantities are well predicted, acoustics can be completely different depending on these reflection coefficients. With an NSCBC formalism, the acoustics entering or leaving a domain can be properly dealt. In a standard non-reflecting NSCBC boundary condition using an expression for inlet wave $L_1 = K(u^t - u)$, the actual reflection coefficient R at boundary is frequency-dependent on the relaxation coefficient K. The value of this relaxation coefficient must be high enough to allow a perfect control of the mean flow, acting so as a low pass filter. High frequencies will easily leave the computational domain whereas low frequencies will be strongly reflected , i.e. the frequencies below a certain cut-off frequency f_c. This cut-off frequency (Selle et al. 2004b) can be defined as

$$f_c = \frac{K}{4\pi}. \tag{A.1}$$

Another critical point to consider is the dependence of the reflection coefficients on the boundary condition type. For instance if the pressure is imposed, the reflection coefficient is negative. On the contrary, if the velocity is imposed, the reflection coefficient is positive (Poinsot and Veynante 2011). This comes from the definition of the reflection coefficient for an inlet:

$$R = \frac{Z+1}{Z-1}, \text{ with } Z = \frac{\hat{p}}{\rho_0 c_0 \hat{u}}. \tag{A.2}$$

Assuming harmonic waves, spatial and temporal variations may be written as:

$$p' = \Re(\hat{p}e^{-i\omega t}), \tag{A.3}$$
$$u' = \Re(\hat{u}e^{-i\omega t}), \tag{A.4}$$

where $\hat{p}$ and $\hat{u}$ are complex numbers and $\Re$ designates the real part of a complex number. For a fully reflective pressure condition, $p' = 0$ so that $Z = 0$ leading to $R = -1$. For a fully reflective velocity condition, $u' = 0$ so that Z tends to infinity leading to $R = 1$. Therefore, it is important to investigate the influence of both the relaxation coefficient K and the boundary condition type on the acoustics.

To better understand the differences implied by a pressure or a velocity condition, AVSP-f computations have been performed with the scaled setup of the CONOCHAIN case. In the first case, the inlet boundary conditions are: a non-reflective primary nozzle inlet ($R = 0$) and a fully reflective secondary nozzle inlet. The fully reflective condition is assimilated to a wall ($\vec{u}.\vec{n} = 0$) so that $R = 1$ at the secondary nozzle inlet. In the second case, the reflective velocity condition ($R = 1$) has been replaced by a pressure one ($R = -1$). The outlet condition is non-reflective in both cases. As initial condition, pressure and temperature have been fixed at 101325 Pa and 300 K in the whole domain. Scaled acoustic waves coming from the CONOCHAIN results at the outlet of the turbine have been introduced through the non-reflective inlet in the scaled geometry. The acoustic pressure module is compared for both cases at low and high frequencies. Comparisons are presented as examples at $St = 4.34$ and $St = 26$ in Fig. A.1. It has to be reminded that $St = fD_s/u$ and that all the forcing frequencies have been multiplied by 10 to correspond to the scaled geometry. Therefore, for instance $St = 4.34$ is equivalent to f=260 Hz in the real case. All frequencies will be presented with their equivalent in the real dimension case not to be confusing.

At low frequency ($St = 4.34$ in Fig. A.1(a)), the boundary condition (pressure or velocity) has more impact on the acoustic propagation than at high frequency ($St = 26$, i.e. 1700 Hz). A shift on the pressure nodes location and more saturated pressure module levels can be observed in the secondary nozzle. This is the consequence of a different acoustic wave phasing implied by an opposite reflective coefficient as shown in Fig. A.1(b). It can also be noticed that the reflection coefficient is consequently different at both nozzles exits, with a more stretched acoustic pattern in the near field.

At high frequency, the condition type does not seem to have a major impact on the acoustic propagation (Fig. A.1(c)). The acoustic pattern is quite similar in both cases. The phase distribution is also alike, even if some pressure nodes are observed in the near field silent zone, when a velocity condition is used, lower part of Fig. A.1(d). At this frequency, diffraction at the secondary nozzle lip can be observed, while it is not observable at low frequency.

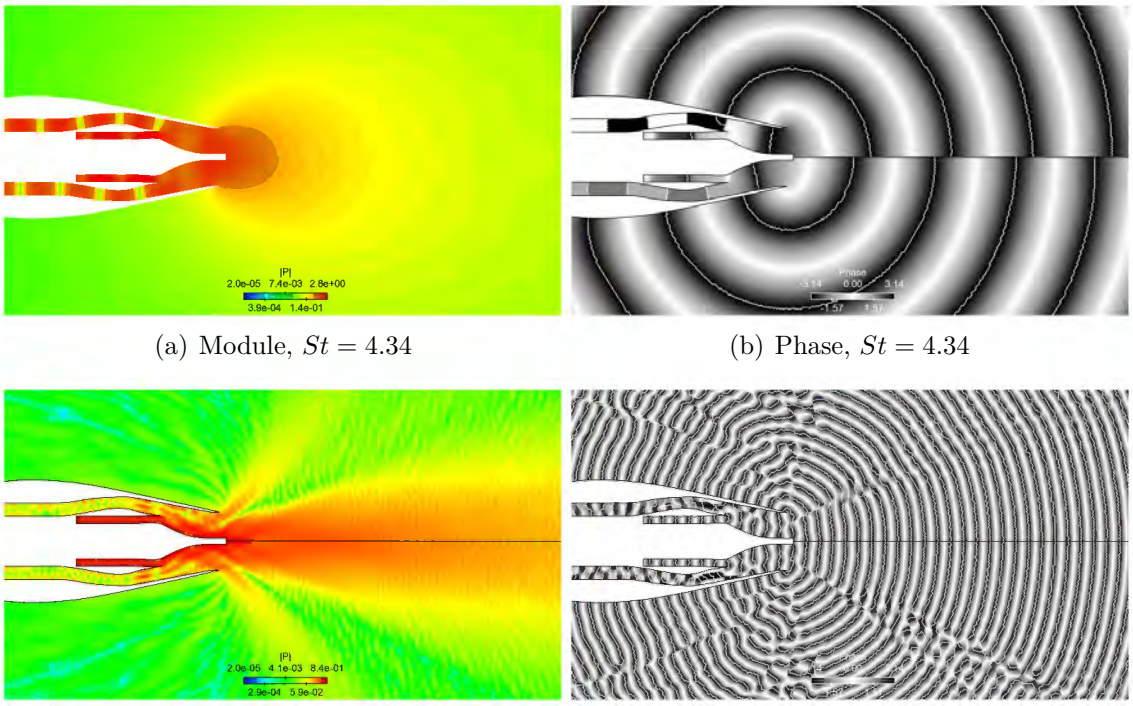

(a) Module, $St = 4.34$ (b) Phase, $St = 4.34$

(c) Module, $St = 26$ (d) Phase, $St = 26$

Figure A.1: Comparison of the acoustic pressure module and phase fields between a pressure condition (upper part) and a velocity condition imposed at the secondary nozzle inlet (lower part).

To measure the impact of the relaxation coefficient K on the acoustic propagation, forced LES computations have been performed to be compared to the AVSP-f computations. The forced LES boundary conditions are the same as those used for the jet simulations without combustion noise forcing. The no forced simulations were performed and initialized before this parametric investigation. The boundary conditions were chosen only using the available mean data (no acoustic data was available, i.e. impedances) to converge the simulations. Therefore, the acoustic behavior of the boundary conditions was not considered and should have an important role in the acoustic generation and propagation. The inlet boundary conditions are: the total pressure at the secondary nozzle inlet ($R < 0$) and the velocity components at the primary nozzle inlet ($R > 0$).

As the boundary condition influence on the acoustic propagation has been highlighted, the AVSP-f computations with a reflective pressure condition at the secondary nozzle inlet will be chosen as the reference case. At the primary nozzle inlet, the AVSP-f boundary condition is perfectly non-reflective so that the choice of the variable to impose does not have any importance. To compare both simu-

lations (AVBP/AVSP-f) respecting as much as possible all the hypotheses made, a quiescent flow ($U = 0$) is imposed in the LES. The same acoustic sources are injected through the velocity inlet NSCBC in the primary nozzle. The acoustic waves are introduced by the forcing signal described in Fig. 8.28(a) which gives the same acoustic contents as the CONOCHAIN results (Fig. 8.27(a)). The influence of the reflection coefficient at the secondary nozzle inlet is investigated by imposing different values of the relaxation coefficient K_{sec}. The reflection coefficient at the primary nozzle inlet is conserved as for the jet simulations without forcing, with $K_{prim} = 10000$, i.e. $f_c = 80$ Hz.

The module and the phase of the reflection coefficient can be analytically obtained in function of the relaxation coefficient K_{sec} imposed at the secondary nozzle inlet (Fig. A.2). If the relaxation coefficient is low ($K_{sec} = 1000$, i.e. $f_c = 8$ Hz),

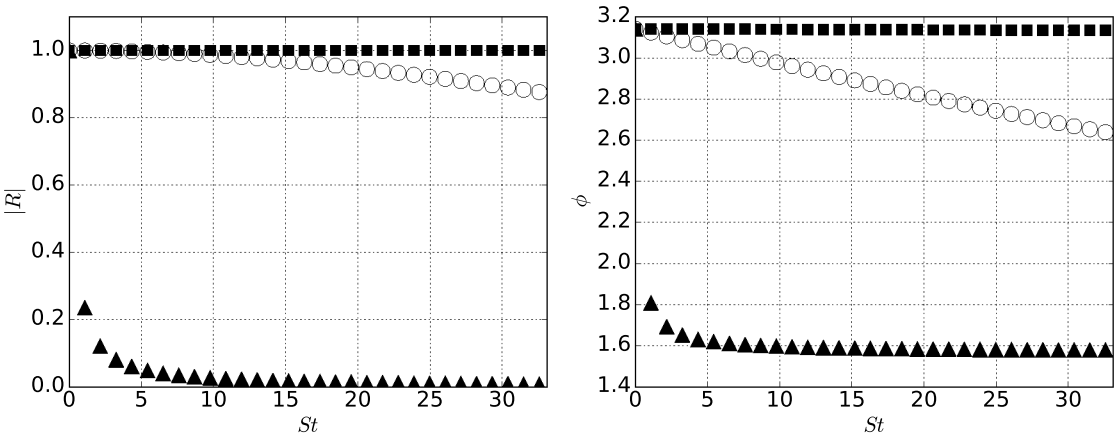

(a) Module (b) Phase

Figure A.2: Theoretical coefficient reflection modulus a) and phase b), in function of the Strouhal number for several relaxation coefficient values, $K_{sec} = 1000$ (▲), $K_{sec} = 225000$ (○) and $K_{sec} = 1550000$ (■).

the boundary condition is almost non-reflective. Otherwise, if the relaxation coefficient is high ($K = 1550000$, i.e. $f_c \approx 12300$ Hz), the boundary condition is fully reflective. Hence, three cases have been tested and are presented in the next sections: an almost non-reflective secondary stream inlet, a fully reflective secondary stream inlet and a partially reflective secondary stream inlet. By means of Discrete Fourier Transform (DFT), the fields of the acoustic pressure module are compared with the AVSP-f reference case. Only the mode at $St = 4.34$ (260 Hz) is presented as an example.

A.1 Quasi non-reflective secondary stream inlet

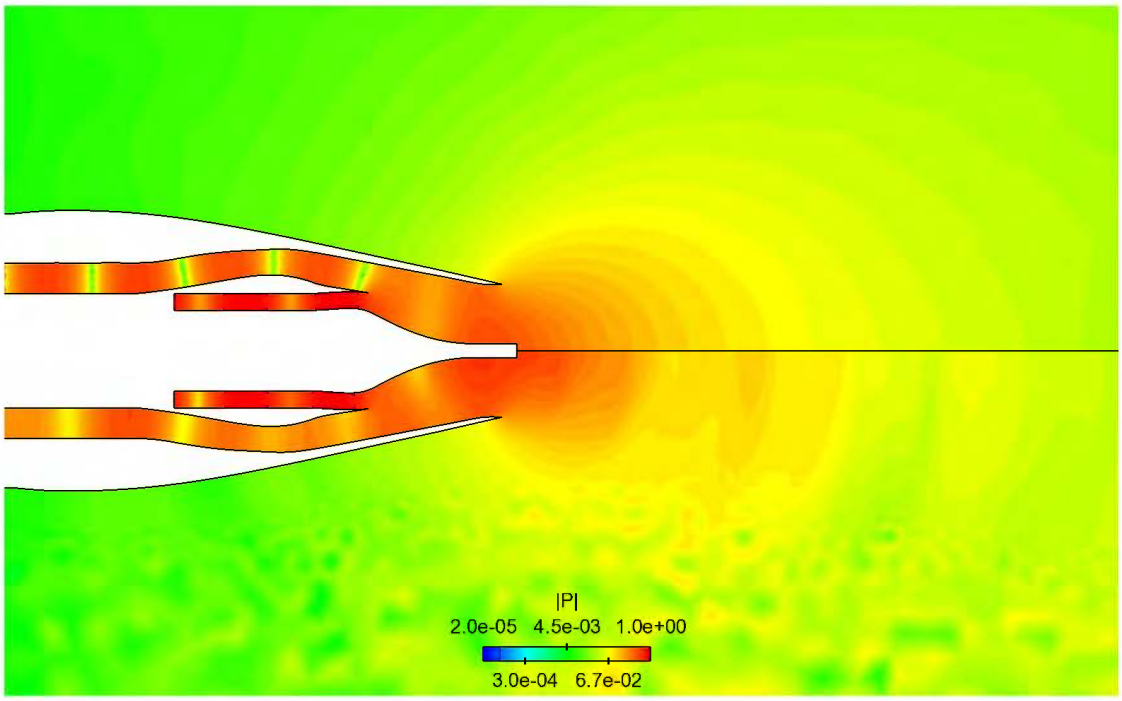

(a) $K_{sec} = 1\ 000$, $f_c = 8$ Hz and $K_{prim} = 10000$, $f_c = 80$ Hz

Figure A.3: Comparison of the acoustic pressure module fields between the AVSP-f case (upper part) and the AVBP case (lower part) with a non-reflective secondary inlet condition and a partially reflective primary nozzle inlet.

No forced jet simulations have been converged with an almost non-reflective secondary nozzle inlet ($K_{sec} = 1000$, $f_c = 8$ Hz), so that, the same boundary conditions are imposed in the forced jet simulations. In the case of a low Mach number flow ($M < 0.3$), part of the forced acoustic waves (coming from the inlet of the primary stream) propagates towards the inlet of the secondary nozzle. If the condition is almost non-reflective, most of the waves simply go out through the nozzle.

In the secondary nozzle, the acoustic pattern differs from the AVSP-f case as shown in Fig. A.3. Indeed, only some pressure nodes, mostly attenuated, are observed and the acoustic pressure amplitudes in the rest of the nozzle are also lower. The repartition of the acoustic pressure amplitudes differs at the outlet of the nozzles. The levels are more saturated at the secondary nozzle exit and more concentrated around the centerline. It can be noted that the quality of the acoustic resolution is deteriorated in the radial direction of the domain as there is

less mesh resolution. Indeed, it has been chosen to have a good mesh resolution up to the limits of the integration domain used for the far-field propagation.

A.2 Fully reflective secondary stream inlet

If a fully reflective secondary stream inlet ($K_{sec} = 1550000$, i.e. $f_c \approx 12300$ Hz) is used, a similar acoustic behavior than the one predicted with AVSP-f is expected. However, the acoustic propagation is completely different as shown in Fig. A.4. The acoustic pressure amplitudes are strongly attenuated. With the same reflection coefficient module than the one in AVSP-f, all the acoustic waves are reflected.

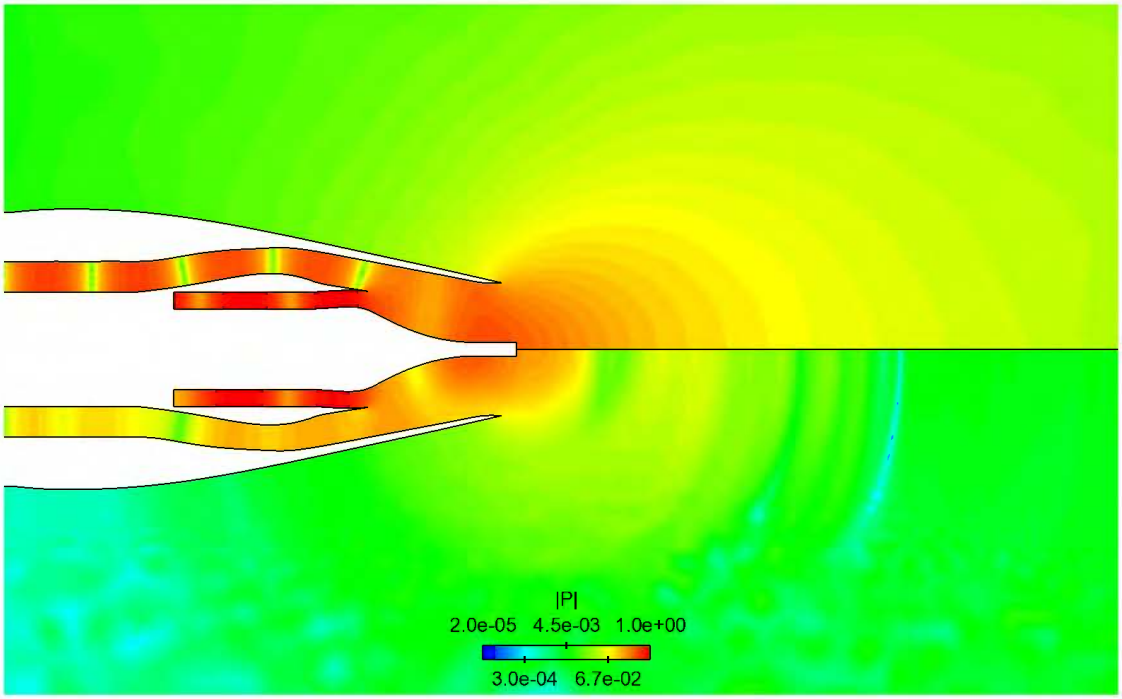

(a) $K_{sec} = 1\ 550\ 000$, $f_c = 12300$ Hz and $K_{prim} = 10000$, $f_c = 80$ Hz

Figure A.4: Comparison of the acoustic pressure module fields between the AVSP-f case (upper part) and the AVBP case (lower part) with a fully reflective secondary inlet condition and a partially reflective primary nozzle inlet.

In AVSP-f computations, the acoustic forcing is performed through a perfectly non-reflecting inlet boundary condition. However, with AVBP, it is not advisable to impose a perfectly non-reflecting inlet boundary condition. This would lead to a diverging solution, and eventually to a numerical instability. The value of the

relaxation coefficient ($K_{prim} = 10000$) tested at the primary nozzle inlet has a cut-off frequency of about 80 Hz. However, it can be seen that it implies a reflection of more than 30 % at low frequencies ($St < 10$, i.e. $f < 600$ Hz) and less than 10 % at high frequencies, which is not negligible for acoustics (Fig. A.5). Moreover, it must be kept in mind, that combustion noise propagates in a frequency range going from 100 Hz to 1500 Hz. These acoustic reflections at low frequency are

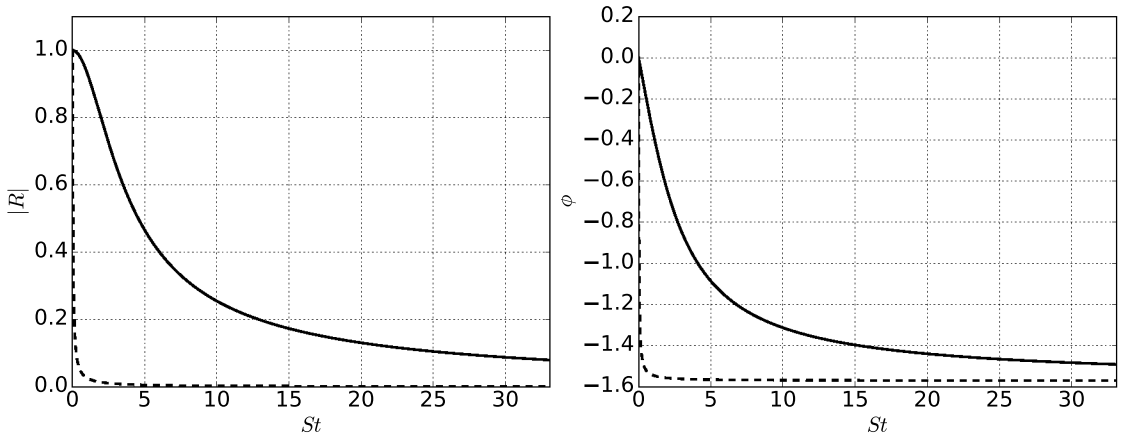

(a) Module (b) Phase

Figure A.5: Theoretical coefficient reflection modulus (Selle et al. 2004b) a) and phase b) of the primary nozzle inlet, $K = 10000$ (–) and $K = 100$ (- -)

sufficiently strong to modify the acoustic propagation. The interaction between the two nozzles induces destructive interferences.

By reducing the value of the relaxation coefficient to $K_{prim} = 100$ (i.e. $f \approx 0$ Hz), less than 1% of reflection occurs at $St < 5$ (i.e. $f < 300$ Hz). Modifications on the acoustic pressure field can be observed in Fig. A.6. Indeed, the acoustic pattern is more in agreement with AVSP-f. The pressure nodes location is well predicted in the secondary and in the primary nozzles. However, one of the pressure nodes in the secondary nozzle is more attenuated, while one of the pressure nodes in the primary nozzle is more amplified. The pressure levels are also more saturated at the secondary nozzle exit.

Another critical point to remember is that AVSP-f solves the Helmholtz wave equation which is linear whereas AVBP solves the Navier-Stokes equations which are non-linear. Moreover, different numerical schemes induce different dispersion and dissipation properties.

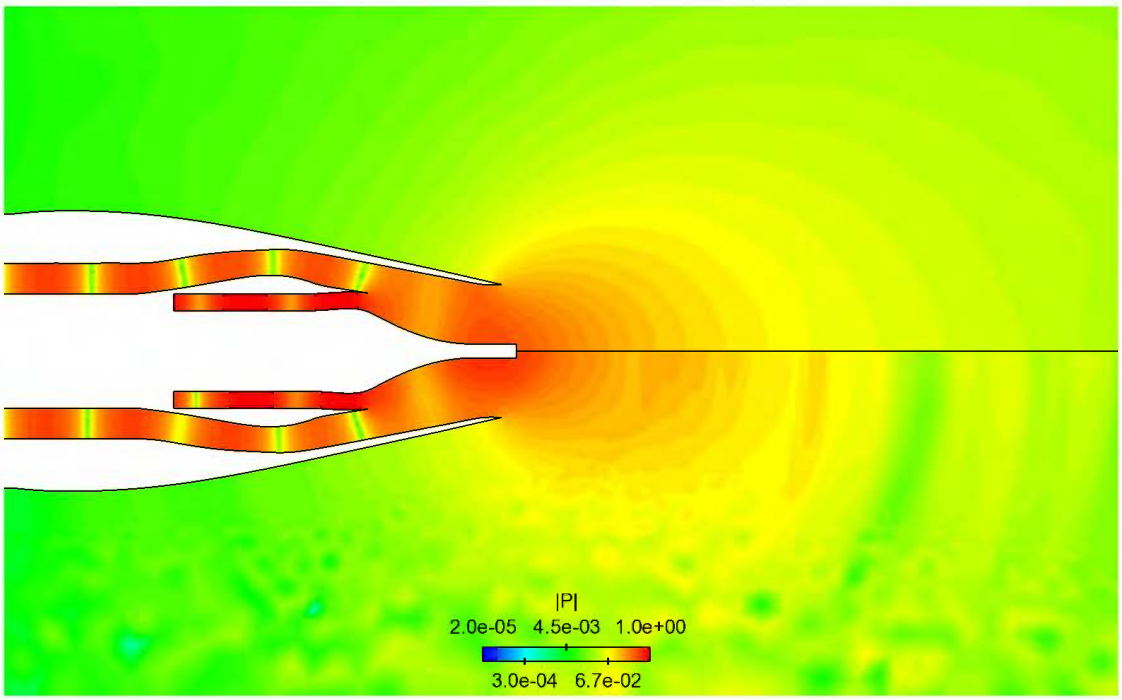

(a) $K_{sec} = 1\ 550\ 000$, $f_c = 12300$ Hz and $K_{prim} = 100$, $f_c = 0.8$ Hz

Figure A.6: Comparison of the acoustic pressure module fields between the AVSP-f case (upper part) and the AVBP case (lower part) with a fully reflective secondary inlet condition and a quasi non-reflective primary nozzle inlet.

A.3 Partially reflective secondary stream inlet

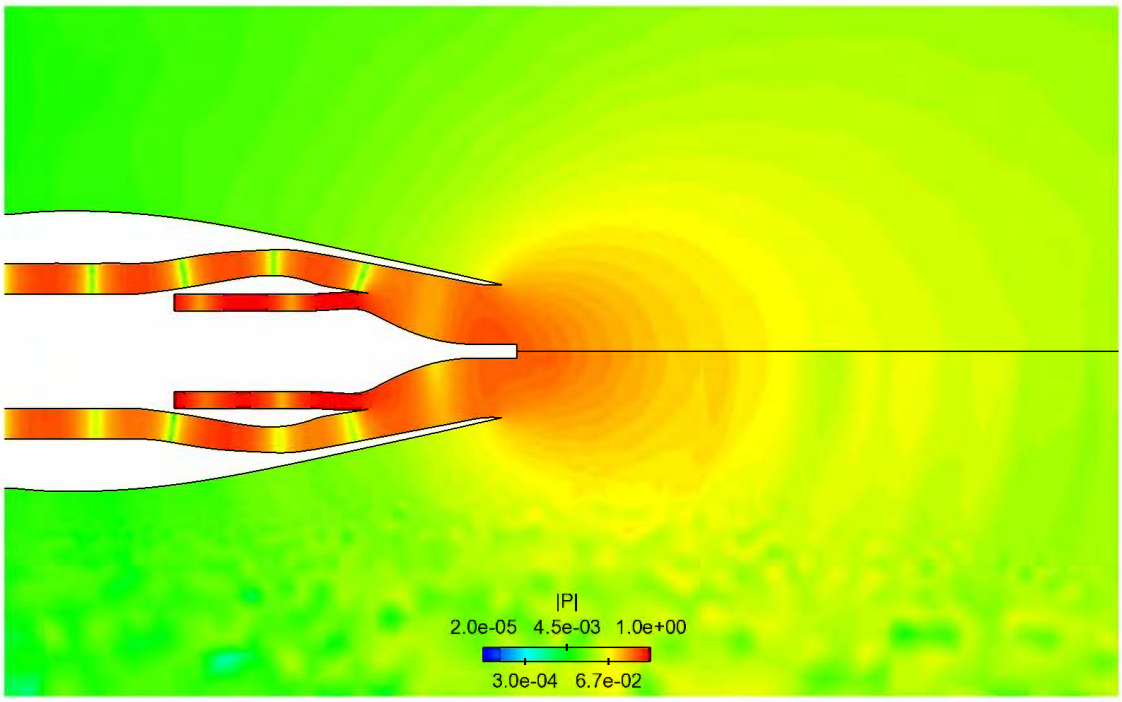

(a) K_{sec} = 225 000, f_c = 1800 Hz and K_{prim} = 10000, f_c=80 Hz

Figure A.7: Comparison of the acoustic pressure module fields between the AVSP-f case (upper part) and the AVBP case (lower part) with a partially reflective secondary inlet condition and a partially reflective primary nozzle inlet.

Another solution is to consider a partially reflective secondary stream inlet with $K_{sec} = 225000$, i.e. $f_c \approx 1800$ Hz. This allows to have more than 95% of reflection at $St < 18$ (i.e. $f < 1100$ Hz) and still more than 85% of reflection beyond this Strouhal value (Fig. A.2). The acoustic pressure field obtained is illustrated in Fig. A.7 and compared with the AVSP-f reference case. The predicted field is quite similar to the AVSP-f one. In the secondary nozzle, the pressure nodes are consistent with the the pressure nodes found by AVSP-f. At this frequency ($St = 4.34$, i.e. $f = 260$ Hz), the secondary inlet boundary condition is still strongly reflective ($> 95\%$) as shown in Fig. A.2(a). However, the phase is not exactly of π as seen in Fig. A.2(b). It seems that this slight phase-shift allows to obtain the same acoustic pattern in the secondary nozzle than for the AVSP-f case, considering a reflective primary nozzle inlet ($K_{prim} = 10000$, i.e. $f_c \approx 80$ Hz) instead of a perfectly non-reflective one ($K_{prim} = 100$, i.e. $f_c \approx 0$ Hz).

However, the acoustic levels are less saturated than the one obtained with AVSP-f. This can be explained by the phase-shift between the two cases. Indeed, the contribution of the reflective waves is added to the other acoustic waves. However, this contribution is dependent on the phase and can be positive or negative, so that, the acoustic levels can be lower at some points. The acoustic activity in the primary nozzle seems to be the same and the propagation pattern in the near field is quite close to the propagation pattern given by AVSP-f.

A.4 Acoustic propagation analysis

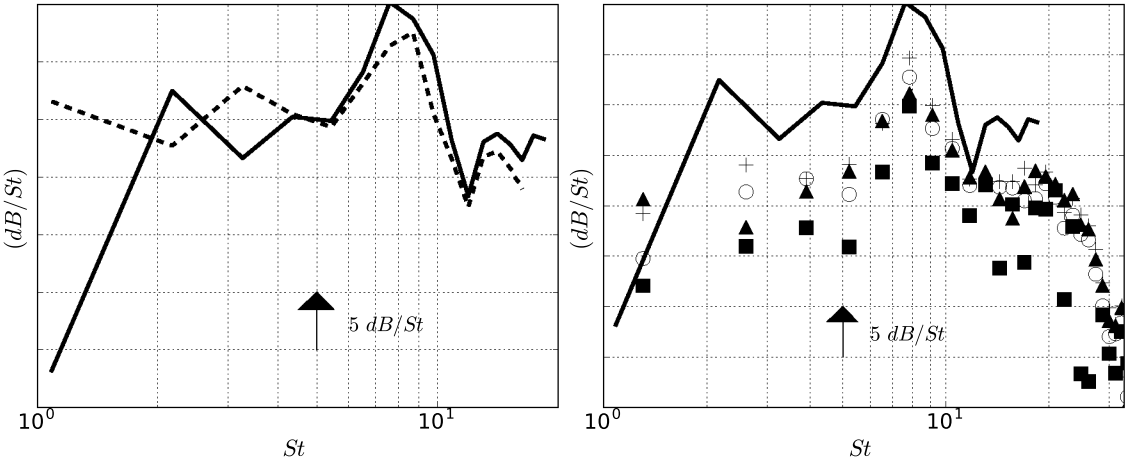

Figure A.8: PSD of a pressure probe localized at 4 D_s in the jet axis. AVSP-f results with a velocity condition (- -) and with a pressure condition (–). LES results with $K_{sec} = 1000$ (▲), $K_{sec} = 225000$ (○), $K_{sec} = 1550000$ (■) and $K_{sec} = 1550000$ with $K_{prim} = 100$ (+).

The inlet boundary-condition impact on the acoustic propagation has been highlighted for different boundary-condition types (pressure or velocity) and different reflection characteristics (non-reflective, partially reflective and fully reflective). It has been seen how acoustics is extremely sensitive to the reflection coefficient and how it is more complicated to control acoustic propagation when there are two inlets. Moreover, it has been seen that a different phasing of the waves occurs for different boundary-condition type.

The influence of the boundary conditions on the acoustic propagation can be investigated more precisely with probes analysis. Power spectral density of pressure has been analyzed on a probe localized in the jet axis at 4 D_s of the primary nozzle

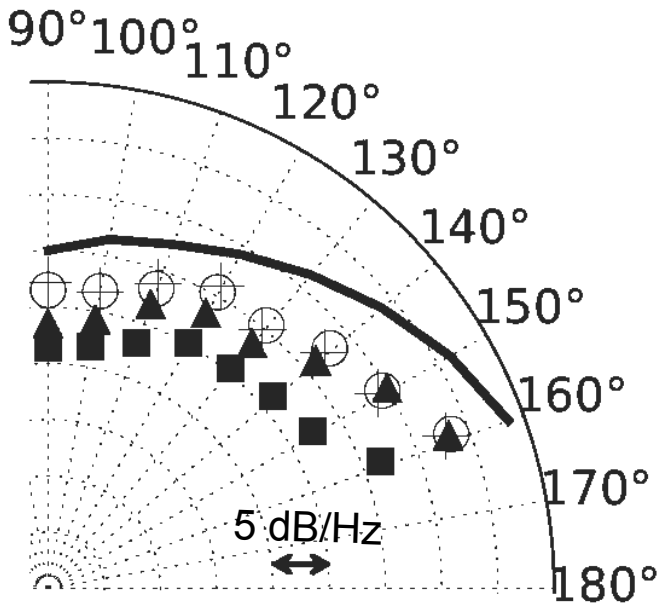

Figure A.9: Over All Sound Pressure Level (OASPL) of combustion noise in the near field (5 m) compared with the AVSP-f results (–), $K_{sec} = 1000$ (▲), $K_{sec} = 225000$ (○), $K_{sec} = 1550000$ (■) and $K_{sec} = 1550000$ with $K_{prim} = 100$ (+).

exit. In the case of a different boundary-condition type imposed at the secondary nozzle inlet, AVSP-f comparison between velocity and pressure boundary conditions shows that a pressure condition at the secondary nozzle inlet gives higher levels of noise (+ 3 dB) than a velocity condition at high frequency (Fig. A.8(a)). The noise levels at low frequency are globally attenuated, particularly at very low frequency ($St < 2$, i.e. $f_c < 120$ Hz) where the strongest discrepancy is observed (-20 dB). The only difference in the simulations parameters is the phase of the reflection coefficient at the secondary nozzle inlet. The phase is π in the case of a pressure condition, meaning that the reflected acoustic wave is in phase opposition with the upstream acoustic wave. On the contrary, the phase is null with a velocity condition, meaning that the reflected acoustic wave is perfectly superposed with the upstream acoustic wave. The phase-shift is enough to change the acoustic propagation specially at low frequency.

To measure the impact of the reflection coefficient on the acoustic propagation, LES results are compared with the AVSP-f reference case (pressure condition) in Fig. A.8(b). The spectral shape obtained for the different relaxation coefficients is comparable with the AVSP-f results. However, in terms of magnitude, a discrepancy of about 5 dB is observed for the closest case ($K_{sec} = 1550000$, i.e.

$f_c \approx 12300$ Hz, with $K_{prim} = 100$, i.e. $f_c \approx 0$ Hz). The case with $K_{sec} = 225000$ ($f_c \approx 1800$ Hz) gives similar results. This is the result of a different phasing related to a different combination of the reflection coefficients chosen at both nozzle inlets. At low frequency, more important acoustic level loss ($> 10\ dB$) occurs for $K_{sec} = 1550000$ ($f_c \approx 12300$ Hz) and $K_{sec} = 1000$ ($f_c = 8$ Hz) with a partially reflective primary nozzle inlet ($K_{prim} = 10000$, i.e. $f_c = 80$ Hz). Indeed, it must be reminded that the primary nozzle inlet generates more than 30% of reflection at low frequency. So that, the contribution at low frequency will be surely different that the one in the AVSP-f case. To be comparable at all frequencies with AVSP-f, more development would be necessary to implement an acoustic forcing with a frequency dependent reflective coefficient in AVSP-f.

By looking at the directivity of acoustics in Fig. A.9, all AVBP cases exhibit more acoustic emissions at 160°. The acoustic propagation has been obtained at 5 D_s using the FWH acoustic analogy presented in section 8.3. The same directivity of the OASPL is predicted with the AVSP-f case. A small peak is observed at 120°, which corresponds to the acoustic diffraction at the nozzle lip occurring at high frequency as observed in Fig. A.1(c). By choosing reflection coefficients close to the AVSP-f one ($K_{sec} = 1550000$ i.e. $f_c \approx 12300$ Hz with $K_{prim} = 100$ i.e. $f_c \approx 0$ Hz), the LES results are in good agreement with the acoustic pressure field prediction. This has also been verified by means of probe analysis by looking at the PSD and the directivity. The discrepancies in terms of noise levels could be explained by the acoustic dissipation due to viscosity. Indeed, viscosity effects are considered in the LES while no viscosity is taken into account in AVSP-f. An Euler simulation could be considered to validate or invalidate this assumption. The non-linearity effects could also have a part in the differences observed in the acoustic propagation pattern and the PSD.

In spite of these differences in acoustic pressure amplitude, the results are rather convincing. As no more information has been given concerning the reflection coefficient at the inlet of the nozzles, the relaxation coefficients of the NSCBC have been chosen to give an acoustic propagation pattern close to the one obtained with AVSP-f computations. Therefore, $K_{sec} = 225000$ ($f_c \approx 1800$ Hz) with $K_{prim} = 10000$ ($f_c \approx 80\ Hz$) has been imposed for all the forced simulations.

Appendix B

Vortex sound theory

The vortex sound theory Rienstra and Hirschberg [2003] is known as a variant of Lighthill's analogy and is based on the absence of external forces and source of mass. This theory was first developed by Powell Powell [1964] for low Mach number flows in free-field conditions. It follows the same way as the approach of Lighthill, by reorganizing the equations of fluid mechanics in a single inhomogeneous wave equation. But the difference stands in the introduction of the vorticity. Indeed the study of the motion of vortices corresponds to a kinematic problem which is easier than the solution of the dynamical problem and more intuitive. Here the formulation of interest will be the Möhring's one Mohring [2010], which follow a path used by Howe. Howe proposed a generalized formulation of Powell's analogy, based on the use of total enthalpy (B) as acoustic variable. He considered a steady homentropic, irrotational flow instead of the uniform and quiescent medium chosen as propagation region by Lighthill. Bernoulli's equation states that the stagnation enthalpy differs from the potential only by a sign and by a time derivative. Thus this stagnation enthalpy can be used as acoustic variable instead of the potential.

B.1 Möhring's analogy

From thermodynamics laws it can be established that :

$$dh = Tds + \frac{dp}{\rho}. \tag{B.1}$$

The stagnation enthalpy being $B = h + \frac{u^2}{2}$, the momentum equation can be rewritten for non-homentropic flow as :

$$\begin{aligned} \frac{Du}{Dt} &= -\frac{\nabla p}{\rho} \\ &= -\nabla h + T\nabla s. \end{aligned} \tag{B.2}$$

Using the vectorial identity :

$$(u.\nabla)u = \frac{1}{2}\nabla u^2 + w \times u, \text{ where } \mathbf{w} = curl\ \mathbf{u} \text{ denotes the vorticity,} \tag{B.3}$$

Eq. (B.2) becomes as Crocco's form :

$$\frac{\partial u}{\partial t} = -\nabla B - (\mathbf{w} \times \mathbf{u}) + T\nabla s. \tag{B.4}$$

Taking the energy conservation equation :

$$\rho\frac{DB}{Dt} - \frac{\partial p}{\partial t} = \frac{\partial q_j}{\partial x_j} - \frac{\partial u_i \sigma_{ij}}{\partial x_j} \tag{B.5}$$

and assuming that power dissipated by viscous forces and heat is neglected :

$$\rho\frac{DB}{Dt} = \frac{\partial p}{\partial t} \tag{B.6}$$

From the state law $\rho(p, s)$, it is found that :

$$\begin{aligned} \frac{\partial \rho}{\partial t} &= \frac{1}{c^2}\frac{\partial p}{\partial t} + \left(\frac{\partial \rho}{\partial s}\right)_p \frac{\partial s}{\partial t} \\ &= \frac{\rho}{c^2}\frac{DB}{Dt} + \left(\frac{\partial \rho}{\partial s}\right)_p \frac{\partial s}{\partial t} \end{aligned} \tag{B.7}$$

with $c^2 = \left(\frac{\partial p}{\partial \rho}\right)_s$ for an isentropic flow.
Then it can be deduced that :

$$\begin{aligned} \rho\frac{\partial u}{\partial t} &= \frac{\partial \rho u}{\partial t} - u\frac{\partial \rho}{\partial t} \\ &= \frac{\partial \rho u}{\partial t} - \frac{\rho u}{c^2}\frac{DB}{Dt} - \left(\frac{\partial \rho}{\partial s}\right)_p u\frac{\partial s}{\partial t} \end{aligned} \tag{B.8}$$

Therefore Eq. (B.4) multiplied by ρ can be rearranged as :

$$\begin{aligned} \frac{\partial \rho u}{\partial t} - \frac{\rho u}{c^2}\frac{DB}{Dt} - \left(\frac{\partial \rho}{\partial s}\right)_p u\frac{\partial s}{\partial t} + \rho\nabla B \\ = \rho(\mathbf{u} \times \mathbf{w}) + \rho T\nabla s \end{aligned} \tag{B.9}$$

and the mass conservation is rewritten as :

$$\frac{\rho}{c^2}\frac{DB}{Dt} + \nabla.(\rho u) = -\left(\frac{\partial \rho}{\partial s}\right)_p \frac{\partial s}{\partial t} \tag{B.10}$$

Finally, by considering a scaled enthalpy (b) defined as :

$$\frac{Db}{Dt} = \rho_T \frac{DB}{Dt}, \quad \rho_T \text{ being the total density,} \tag{B.11}$$

Möhring's analogy is obtained by $\frac{\partial}{\partial t}\left(\frac{1}{\rho_T}(B.10)\right) - \nabla.\left(\frac{1}{\rho_T}(B.9)\right)$:

$$\frac{\partial}{\partial t}\left[\frac{\rho}{\rho_T^2 c^2}\frac{Db}{Dt}\right] + \nabla.\left[\frac{\rho u}{\rho_T^2 c^2}\left(\frac{Db}{Dt}\right) - \frac{\rho}{\rho_T^2}\nabla b\right] = R \tag{B.12}$$

where R is Möhring 's source term and represents only noise sources :

$$R = \underbrace{-\nabla.\left[\frac{\rho}{\rho_T}(\mathbf{u}\times\mathbf{w})\right]}_{\text{Turbulent noise}} \tag{B.13}$$

$$\underbrace{+\nabla.\left[\frac{u}{\rho_T}\left(\frac{\partial\rho}{\partial s}\right)_p\frac{\partial s}{\partial t} - \frac{\rho}{\rho_T}T\nabla s\right] + \frac{\partial}{\partial t}\left[\frac{1}{\rho_T}\left(\frac{\partial\rho}{\partial s}\right)_p\frac{\partial s}{\partial t}\right]}_{\text{Combustion noise}}$$

It can be seen that the second term of the LHS of Eq. (B.12) takes into account sound speed heterogeneities and velocity. Thus a part of flow effects on acoustic is contained in the wave operator, this allows to consider convection and refraction effects on the propagation in inhomogeneous media.

If Eq. (B.12) is rewritten in frequency domain, it gives :

$$-\omega^2\frac{\rho b}{\rho_T^2 c^2} + i\omega\frac{\rho u}{\rho_T^2 c^2}\nabla b + \nabla.\left[i\omega\frac{\rho u b}{\rho_T^2 c^2} + \frac{\rho u_i u_j}{\rho_T^2 c^2}\nabla b - \frac{\rho}{\rho_T^2}\nabla b\right] = FT[R] \tag{B.14}$$

where the sources are replaced by their Fourier Transform (FT).

Appendix C

Analytical model for combustion noise directivity

To explain how the maximum angle of directivity is controlled by the temperature field, a simplified 2D free subsonic jet is considered. To simplify the configuration, only the potential core with hot gas is kept and the jet shear layers are assumed infinitely thin. The plane wave arriving at the interface between the potential core and the atmosphere (fresh gas) is refracted (cf Fig. C.1), similar to Fermat's principle ($k_1.\sin(i_1) = k_2.\sin(i_2)$) which implies the conservation of tangential wavenumbers.

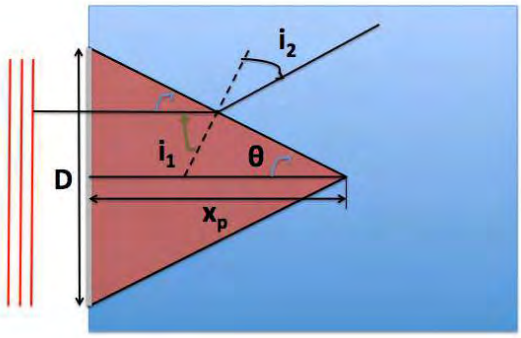

Figure C.1: Interface potential core - atmosphere

The various angles in Fig. C.1 are defined as :

$$\theta = \tan^{-1}\left(\frac{D/2}{x_p}\right), \tag{C.1}$$

where x_p is the length of the potential core.

$$\begin{aligned} i_1 &= \frac{\pi}{2} - \theta \\ &= \frac{\pi}{2} - \tan^{-1}\left(\frac{D/2}{x_p}\right) \end{aligned} \tag{C.2}$$

From Fermat principle we can deduce :

$$\begin{aligned} i_2 &= \sin^{-1}\left[\frac{n_1}{n_2}\sin\left(\frac{\pi}{2} - \tan^{-1}\left(\frac{D/2}{x_p}\right)\right)\right] \\ &= \sin^{-1}\left[\frac{n_1}{n_2}\cos\left(\tan^{-1}\left(\frac{D/2}{x_p}\right)\right)\right] \end{aligned} \tag{C.3}$$

Knowing that :

$$k_1 = \frac{\omega}{c_1}\ et\ k_2 = \frac{\omega}{c_2} \tag{C.4}$$

Finally we find that :

$$\begin{aligned} \theta_{dev} &= \frac{\pi}{2} + \theta + i_2 \\ &= \frac{\pi}{2} + \tan^{-1}\left(\frac{D}{2x_p}\right) + \sin^{-1}\left[\frac{c_2}{c_1}\cos\left(\tan^{-1}\left(\frac{D}{2x_p}\right)\right)\right] \end{aligned} \tag{C.5}$$

Bibliography

ACARE. Flightpath 2050: Europe's vision for aviation. Technical report, European Commission, 2011. 5, 8

R.K. Amiet. Refraction of sound by a shear layer. Journal of Sound and Vibration, 58(4):467–482, 1978. 158

C. Angelberger, D. Veynante, F. Egolfopoulos, and T. Poinsot. Large eddy simulations of combustion instabilities in premixed flames. In Proc. of the Summer Program , pages 61–82. Center for Turbulence Research, NASA Ames/Stanford Univ., 1998. 37

C. Bailly, C. Bogey, and S. Candel. Modelling of sound generation by turbulent reacting flows. International Journal of Aeroacoustics, 9(4):461–490, 2010. 12

F. Bake, C. Richter, B. Muhlbauer, N. Kings, I. Rohle, F. Thiele, and B. Noll. The entropy wave generator (ewg): a reference case on entropy noise. J. Sound Vib. , pages 574–598, 2009. 9, 13, 15

F. Bake, P. Gaetani, G. Persico, L. Neuhaus, and K. Knobloch. Indirect noise generation in a high pressure turbine stage. In Proceedings of the 22nd AIAA/CEAS Aeroacoustics Conference, Lyon, France, volume 30, 2016. 9, 14

M. Bauerheim, I. Duran, T. Livebardon, G. Wang, S. Moreau, and T. Poinsot. Transmission and reflection of acoustic and entropy waves through a stator–rotor stage. Journal of Sound and Vibration, 374:260–278, 2016. 15, 51, 52, 53, 54

C. Becerril. Simulation of noise emitted by a reactive flow. PhD thesis, 2017. 50, 75, 137

C. Becerril, S. Moreau, M. Bauerheim, L. Gicquel, and T. Poinsot. Numerical investigation of combustion noise: The entropy wave generator. In Proceedings

of the 22nd AIAA/CEAS Aeroacoustics Conference, Lyon, France, page 2830, 2016. 15

D.W. Bechert and E. Pfizenmaier. On the amplification of broad band jet noise by a pure tone excitation. J. Sound Vibration, 43:581–587, 1977. 20

M. Boger, D. Veynante, H. Boughanem, and A. Trouvé. Direct numerical simulation analysis of flame surface density concept for large eddy simulation of turbulent premixed combustion. In 27th Symp. (Int.) on Combustion, pages 917–927, Boulder, 1998. The Combustion Institute, Pittsburgh. 37

C. Bogey and C. Bailly. Three-dimensional non-reflective boundary conditions for acoustic simulations: far field formulation and validation test cases. Acta Acustica united with Acustica, 88(4):463–471, 2002. 232

C. Bogey and O. Marsden. Identification of the effects of the nozzle-exit boundary-layer thickness and its corresponding reynolds number in initially highly disturbed subsonic jets. Physics of Fluids, 25(5):055106, 2013. 19

C. Bogey, O. Marsden, and C. Bailly. Influence of initial turbulence level on the flow and sound fields of a subsonic jet at a diameter-based reynolds number of 10 5. Journal of Fluid Mechanics, 701:352–385, 2012. 18, 19

M.S. Bohn. Response of a subsonic nozzle to acoustic and entropy disturbances. J. Sound Vib., 52(2):283 – 297, 1977. ISSN 0022-460X. doi: 10.1016/0022-460X(77)90647-2. URL http://www.sciencedirect.com/science/article/pii/0022460X77906472. 14

E.J.L. Bouty, A. Dravet, D.T.J.A. Le, G.J.X. Riou, and T.A.C. Vincent. Corps central de tuyère de turboréacteur, October 10 2007. URL https://www.google.com/patents/EP1843032A1?cl=fr. EP Patent App. EP20,070,290,363. 96

S. Bragg. Combustion noise. J. Inst. of Fuel, 36:12–16, 1963. 10

K.S Brentner and F. Farassat. Analytical comparison of the acoustic analogy and kirchhoff formulation for moving surfaces. AIAA journal, pages 1379–1386, 1998. 213

F. P. Bretherton and C. J. R. Garrett. Wavetrains in inhomogeneous moving media. Proceedings of the Royal Society of London, 302(1471):529–554, 1968. 59

J.E Bridges and A.K.M.F. Hussain. Roles of initial condition and vortex pairing in jet noise. J. Sound Vibration, 117:289–311, 1984. 17

G. L. Brown and A. Roshko. On density effect on large structure in turbulent mixing layer. J. Fluid Mech. , 64(Part 4):775–816, 1974. 16

T. D. Butler and P. J. O'Rourke. A numerical method for two-dimensional unsteady reacting flows. Proc. Combust. Inst. , 16(1):1503 – 1515, 1977. 37

S. Candel. Analytical studies of some acoustic problems of jet engines. PhD thesis, California Institute of Technology, 1972. 13

S. Candel, D. Durox, and T. Schuller. Flame interactions as a source of noise and combustion instabilities. In 10th AIAA/CEAS Aeroacoustics Conference - Manchester, Great Britain, page 2928, 2004. 12

S. Candel, D. Durox, S. Ducruix, A.L. Birbaud, N. Noiray, and T. Schuller. Flame dynamics and combustion noise : progress and challenges. Int. J. Acoust. , 8: 1–56, 2009. 9

S. Candel, D. Durox, T. Schuller, J.F. Bourgouin, and J. P Moeck. Dynamics of Swirling Flames. Ann. Rev. Fluid Mech. , 46(1):147–173, January 2014. 93

D. Casalino. An advanced time approach for acoustic analogy predictions. Journal of Sound and Vibration, 261(4):583–612, 2003. 213

C.T. Chang, C.M. Lee, J.T. Herbon, and S.K. Kramer. Nasa environmentally responsible aviation project develops next-generation low-emissions combustor technologies (phase i). J. Aeronaut. Aerospace Eng., (2:1000116), 2013. 8

H.H. Chiu and M. Summerfield. Theory of combustion noise. Acta Astronautica , 1:967–984, 1974. 68

B.T. Chu and L.S.G. Kovásznay. Non-linear interactions in a viscous heat-conducting compressible gas. Journal of Fluid Mechanics, 3(05):494–514, 1958. 16

O. Colin and M. Rudgyard. Development of high-order taylor-galerkin schemes for unsteady calculations. J. Comput. Phys. , 162(2):338–371, 2000. 38, 99

O. Colin, F. Ducros, D. Veynante, and T. Poinsot. A thickened flame model for large eddy simulations of turbulent premixed combustion. Phys. Fluids , 12(7): 1843–1863, 2000. 37, 99, 100, 171

A. W. Cook and J. J. Riley. A subgrid model for equilibrium chemistry in turbulent flows. Phys. Fluids A, 6(8):2868 – 2870, 1994. 37

D. G. Crighton and P. Huerre. Shear-layer pressure fluctuations and superdirective acoustic sources. J. Fluid Mech, 220(355-368), 1990. 224

D. G. Crighton, A. P. Dowling, J. E. Ffowcs Williams, M. Heckl, and F. Leppington. Modern methods in analytical acoustics. Lecture Notes. Springer Verlag, New-York, 1992. 11

L. Crocco. Supercritical gaseous discharge with high frequency oscillations. Aerotecnica, 33, 1953. 13

S. C. Crow and F.H. Champagne. Ordely structure in jet turbulence. J. Fluid Mech, 48:547–591, 1971. 16, 20

N. A. Cumpsty and F. E. Marble. The interaction of entropy fluctuations with turbine blade rows; a mechanism of turbojet engine noise. Proc. R. Soc. Lond. A , 357:323–344, 1977. 14, 22, 40, 41, 45, 50, 53, 60, 65, 160

G. Daviller. Étude numérique des effets de température dans les jets simples et coaxiaux. PhD thesis, ISAE-ENSMA Ecole Nationale Supérieure de Mécanique et d'Aérotechique-Poitiers, 2010. 184

P.E. Doak. Analysis of internally generated sound in continuous materials: 2. a critical review of the conceptual adequacy and physical scope of existing theories of aerodynamic noise, with special reference to supersonic jet noise. Journal of Sound and Vibration, 25(2):263–335, 1972. 72

J. Donea. Taylor-galerkin method for convective transport problems. Int. J. Numer. Meth. Fluids , 20(1):101–119, 1984. 171

A. P. Dowling. The calculation of thermoacoustic oscillations. J. Sound Vib. , 180(4):557–581, 1995. 40

A. P. Dowling and J.E. Ffowcs Williams. Sound and sources of sound. Horwood, 1983. 11

A.P. Dowling and Y. Mahmoudi. Combustion noise. Proceedings of the Combustion Institute, 35(1):65–100, 2015. 9, 10, 119

I. Duran and S. Moreau. Analytical and numerical study of the entropy wave generator experiment on indirect combustion noise. In 17th AIAA/CEAS Aeroacoustics Conference - AIAA-2011-2829, Portland, Oregon, 2011. 50, 51, 53, 54

I. Duran and S. Moreau. Study of the attenuation of waves propagating through fixed and rotating turbine blades. In 18th AIAA/CEAS Aeroacoustics Conference (33rd AIAA Aeroacoustics Conference), number AIAA2012-2133 paper, Colorado Springs, USA, June 4-6 2012. 58

I. Duran and S. Moreau. Solution of the quasi-one-dimensional linearized euler equations using flow invariants and the magnus expansion. J. Fluid Mech., 723:190–231, 4 2013. ISSN 1469-7645. doi: 10.1017/jfm.2013.118. 15, 40

I. Duran and A. S. Morgans. On the reflection and transmission of circumferential waves through nozzles. J. Fluid Mech., 773:137–153, 2015. doi: 10.1017/jfm.2015.247. 15, 40, 138

I. Duran, M. Leyko, S. Moreau, F. Nicoud, and T. Poinsot. Computing combustion noise by combining Large Eddy Simulations with analytical models for the propagation of waves through turbine blades. C. R. Acad. Sci. - Mecanique, 341(1-2):131–140, January 2013a. 20, 22

I. Duran, S. Moreau, and T. Poinsot. Analytical and numerical study of combustion noise through a subsonic nozzle. AIAA Journal, 51(1):42–52, 2013b. 15

M.J. Fisher, G.A. Preston, and C.J. Mead. A modelling of the noise from simple coaxial jets, part ii: with heated primary flow. Journal of Sound and Vibration, 209(3):405–417, 1998. 158

F. Flemming, A. Sadiki, and J. Janicka. Investigation of combustion noise using a les/caa hybrid approach. In Proc. Combust. Inst., volume 31, pages 3189–3196, 2007. 13

A. Fosso-Pouangué, M. Sanjosé, and S. Moreau. Jet noise simulation with realistic nozzle geometries using fully unstructured les solver. In 18th AIAA/CEAS Aeroacoustics Conference (33rd AIAA Aeroacoustics Conference) - Colorado Springs, USA, page 2190, June 4-6 2012. 18, 148, 175

B. Franzelli, E. Riber, M. Sanjosé, and T. Poinsot. A two-step chemical scheme for Large-Eddy Simulation of kerosene-air flames. Combust. Flame, 157(7): 1364–1373, 2010. 100

C. Fureby and C. Løfstrøm. Large eddy simulations of bluff body stabilized flames. In 25th Symp. (Int.) on Combustion, pages 1257 – 1264. The Combustion Institute, Pittsburgh, 1994. 37

M. Germano, U. Piomelli, P. Moin, and W. Cabot. A dynamic subgrid-scale eddy viscosity model. Phys. Fluids, 3(7):1760–1765, 1991. 35

A. Giauque, M. Huet, and F. Clero. Analytical analysis of indirect combustion noise in subcritical nozzles. J. Eng. Gas Turbines Power, 134(11):111202, 2012. 15, 40

A. Giauque, M. Huet, F. Clero, F. Richecoeur, and S. Ducruix. Thermoacoustic shape optimization of a subsonic nozzle. J. Eng. Gas Turb. and Power , 135 (10):102601, 2013. 40

P. Gliebe, R. Mani, H. Shin, B. Mitchell, G. Ashford, S. Salamah, S. Connell, and D. Huff. Aeroacoustic prediction codes. Technical report, General Electric Co. Aircraft Engines - Cincinnati, OH United States, 2000. 7

C.S. Goh and A.S. Morgans. Phase prediction of the response of choked nozzles to entropy and acoustic disturbances. Journal of Sound and Vibration, pages 1–15, June 2011. ISSN 0022460X. doi: 10.1016/j.jsv.2011.05.016. URL http://linkinghub.elsevier.com/retrieve/pii/S0022460X11004019. 40

M. Harper-Bourne. Jet noise measurements: past and present. Int. Journal Aeroacoustics, 2010. 17

J. O. Hirschfelder, C. F. Curtiss, and R. B. Bird. Molecular theory of gases and liquids. John Wiley & Sons, New York, 1969. 32

R.G. Hoch, J.P. Duponchel, B.J. Cocking, and W.D. Bryce. Studies of the influence of density on jet noise. Journal of Sound and Vibration, 28(4):649–668, 1973. 19

M. S. Howe. Indirect combustion noise. J. Fluid Mech. , 659:267–288, 8 2010. ISSN 1469-7645. doi: 10.1017/S0022112010002466. URL http://journals.cambridge.org/article_S0022112010002466. 15

M. Huet and A. Giauque. A nonlinear model for indirect combustion noise through a compact nozzle. J. Fluid Mech. , 733:268–301, September 2013. 14

L.S. Hultgren. Core noise: Implications of emerging N+3 designs and acoustic technology needs. Acoustics Technical Working Group - Cleveland, OH, United States, 21-22 Apr. 2011. 7

I. R. Hurle, R. B. Price, T. M. Sugden, and A. Thomas. Sound emission from open turbulent premixed flames. Proc. R. Soc. Lond. A , 303(409), 1968. 11

Z.D. Husain and A.K.M.F. Hussain. Axisymmetric mixing layer: influence of the initial and boundary conditions. AIAA Journal, 17(1):48–55, 1979. 17

A.K.M.F. Hussain and M.A.Z. Hasan. Turbulence suppression in free turbulent shear flows under controlled excitation. part 2. jet-noise reduction. Journal of Fluid Mechanics, 150:159–168, 1985. 20

A.K.M.F. Hussain and M.F. Zedan. Effects of the initial condition on the axisymmetric free shear layer: Effects of the initial momentum thickness. Phys. Fluids, 21:1100–1112, 1978. 17

ICAO. Annex 16 to the convention on international civil aviation - environmental protection - aircraft noise, 2006. 5

M. Ihme. Combustion and engine-core noise. Fluid. Mech, 49:1–35, Annu. Rev. 2017. 9, 10, 16

M. Ihme and H. Pitsch. On the generation of direct combustion noise in turbulent non-premixed flames. International Journal of Aeroacoustics, 11(1):25–78, 2012. URL http://www-personal.umich.edu/~mihme/Site/Publications_files/IntJAeroAcoustics.pdf. 13

M. Ihme, M. Kaltenbacher, and H. Pitsch. Numerical simulation of flow- and combustion-induced sound using a hybrid LES/CAA approach. In Proc. of the Summer Program , pages 497–510. Center for Turbulence Research, NASA Ames/Stanford Univ., 2006. 69

M. Ihme, H. Pitsch, and H. Bodony. Radiation of noise in turbulent flames. Proc. Combust. Inst. , 32:1545–1554, 2009. 13

P. Jordan and T. Colonius. Wave packets and turbulent jet noise. Annu. Rev. Fluid Mech., 45(1):173–195, 2013. 224

B. Jubelin. New experimental studies on jet noise amplification. In 6th Aeroacoustics Conference - Hartford, Conn., page 961, June 4-6 1980. 20

A.M. Karchmer. Acoustic modal analysis of annular combustor. 8th Aeroacoustics Conference - Atlanta, GA, USA, 1983. 120

A. Kaufmann, F. Nicoud, and T. Poinsot. Flow forcing techniques for numerical simulation of combustion instabilities. Combust. Flame , 131:371–385, 2002. 76

A. R. Kerstein, W. Ashurst, and F. A. Williams. Field equation for interface propagation in an unsteady homogeneous flow field. Phys. Rev. A, 37(7):2728–2731, 1988. 37

V. Kibens. Discrete noise spectrum generated by acoustically excited jet. AIAA Journal, 18(4):434–441, 1980. 20

J.K. Kilham and N. Kirmani. The effect of turbulence on premixed flame noise. In Proc. Combust. Inst., volume 17, pages 327–336, 1979. 12

N.W.M. Ko and A.S.H. Kwan. The initial region of subsonic coaxial jets. Journal of Fluid Mechanics, 73(02):305–332, 1976. 71, 181

A. N. Kolmogorov. The local structure of turbulence in incompressible viscous fluid for very large reynolds numbers. C. R. Acad. Sci. , USSR, 30:301, 1941. 34, 192

S. Kotake. On combustion noise related to chemical reactions. J. Sound Vib. , 42:399–410, 1975. 68

S. Kotake and K. Takamoto. Combustion noise: Effects of the shape and size of burner nozzle. J. Sound Vib. , 112:345–354, 1987. 12, 163

S. Kotake and K. Takamoto. Combustion noise: effects of the velocity turbulence of unburned mixture. Journal of Sound and Vibration, 139(1):9–20, 1990. 12, 163

C. Kraus, L. Selle, T. Poinsot, C.M. Arndt, and H. Bockhorn. Influence of heat transfer and material temperature on combustion instabilities in a swirl burner. Journal of Engineering for Gas Turbines and Power, 139(5):051503, 2017. 155

R.N. Kumar. Further experimental results on the structure and acoustics of turbulent jet flames. In AIAA Paper 75-523, 1976. 12

A.S.H. Kwan and N.W.M. Ko. The initial region of subsonic coaxial jets. part 2. Journal of Fluid Mechanics, 82(02):273–287, 1977. 71

N. Lamarque. Schémas numériques et conditions limites pour la simulation aux grandes échelles de la combustion diphasique dans les foyers d'hélicoptère. Phd thesis, INP Toulouse, 2007. 102

J.-Ph. Légier, T. Poinsot, and D. Veynante. Dynamically thickened flame LES model for premixed and non-premixed turbulent combustion. In Proc. of the Summer Program , pages 157–168. Center for Turbulence Research, NASA Ames/Stanford Univ., 2000. 38

D.C. Leslie and G.L. Quarini. The application of turbulence theory to the formulation of subgrid modelling procedures. Journal of fluid mechanics, 91(1):65–91, 1979. 34

H. Levine and J. Schwinger. On the radiation of sound from an unflanged circular pipe. Physical review, 73(4):383, 1948. xvii, 193

M. Leyko, F. Nicoud, and T. Poinsot. Comparison of direct and indirect combustion noise mechanisms in a model combustor. AIAA Journal , 47(11):2709–2716, 2009. 14

M. Leyko, S. Moreau, F. Nicoud, and T. Poinsot. Waves transmission and generation in turbine stages in a combustion-noise framework. In 16th AIAA/CEAS AeroAcoustics Conference - Stockholm, Sweden, 2010. 40, 50, 51, 53, 54

M. Leyko, S. Moreau, F. Nicoud, and T. Poinsot. Numerical and analytical modelling of entropy noise in a supersonic nozzle with a shock. J. Sound Vib. , 330 (16, 1):3944–3958, 2011. 15

M. Leyko, I. Duran, S. Moreau, F. Nicoud, and T. Poinsot. Simulation and modelling of the waves transmission and generation in a stator blade row in a combustion-noise framework. J. Sound Vib. , 333(23):6090–6106, November 2014. xiv, 15, 50, 54, 128, 145, 146

T. Lieuwen. Analysis of acoustic wave interactions with turbulent premixed flames. Proc. Combust. Inst. , 29:1817–1824, 2002. 12

T. Lieuwen. Modeling premixed combustion-acoustic wave interactions: A review. J. Prop. Power , 19(5):765–781, 2003. 12

T. Lieuwen and V. Yang. Combustion instabilities in gas turbine engines. operational experience, fundamental mechanisms and modeling. 2005. 10

M. J. Lighthill. On sound generated aerodynamically. i. general theory. Proc. R. Soc. Lond. A , Mathematical and Physical Sciences, 211(1107):564–587, 1952. 11, 166

M. J. Lighthill. On sound generated aerodynamically: Ii. turbulence as a source of sound. Proc. R. Soc. Lond. , 222:1–32, 1954. 166, 167

G. M. Lilley. The generation and radiation of supersonic jet noise vol iv - theory of turbulence generated jet noise, noise radiation from upstream sources, and combustion noise. part ii: Generation of sound in a mixing region. Afapl-tr-72-53, Air Force Aero Propulsion Laboratory, 1972. 12

G. M. Lilley. On the noise from jets. Agard cp-131, 1974. 72

D. K. Lilly. The representation of small-scale turbulence in numerical simulation experiments. In Proceedings of the IBM Scientific Computing Symposium on Environmental Sciences, Yorktown Heights, USA, 1967. 35

T. Livebardon. Modeling of combustion noise in helicopter engines. PhD thesis, 2015. 22, 121, 138, 227

T. Livebardon, S. Moreau, T. Poinsot, and E. Bouty. Numerical investigation of combustion noise generation in a full annular combustion chamber. In 21th AIAA/CEAS Aeroacoustics Conference (36rd AIAA Aeroacoustics Conference), number AIAA2015-2971 paper, Dallas, USA, June 22-26 2015. 15, 40, 51, 53, 54, 64, 69, 70, 89, 228

T. Livebardon, S. Moreau, L. Gicquel, T. Poinsot, and E. Bouty. Combining les of combustion chamber and an actuator disk theory to predict combustion noise in a helicopter engine. In Combustion and Flames, volume accepted, 2016. 20, 22, 65, 141, 154

L. Magri, J. O'Brien, and M. Ihme. Compositional inhomogeneities as a source of indirect combustion noise. Journal of Fluid Mechanics, 799:R4, 2016. 16

J.R. Mahan and A. Karchmer. Combustion and core noise. Aeroacoustics of flight vehicles: theory and practice, 1:483–517, 1991. 163

F. E. Marble and S. Candel. Acoustic disturbances from gas nonuniformities convected through a nozzle. J. Sound Vib. , 55:225–243, 1977. 14, 16, 40, 44, 49

W. Meier, R. S. Barlow, Y.L Chen, and J.Y. Chen. Raman/rayleigh/lif measurements in a turbulent ch4/h2/n2 jet diffusion flame: Experimental techniques and turbulence-chemistry interaction. Combustion and Flame, 123:326–343, 2000. 12

S. Mendez and J. Eldredge. Acoustic modeling of perforated plates with bias flow for large-eddy simulations. J. Comput. Phys. , 228(13):4757–4772, 2009. URL http://www.cerfacs.fr/~cfdbib/repository/TR_CFD_09_8.pdf. 99

C. Meneveau and T. Poinsot. Stretching and quenching of flamelets in premixed turbulent combustion. Combust. Flame , 86:311–332, 1991. 37

J.H. Miles. Time delay analysis of turbofan engine direct and indirect combustion noise sources. Journal of Propulsion and Power, 25(1):218, 2009. 14, 145

Ashish Mishra and Daniel J. Bodony. Evaluation of actuator disk theory for predicting indirect combustion noise. /jsv, 332(4):821–838, February 2013. 40

W.H. Moase, M.J. Brear, and C. Manzie. The forced response of choked nozzles and supersonic diffusers. Journal of Fluid Mechanics, 585:281–304, 2007. ISSN 0022-1120. doi: 10.1017/S0022112007006647. URL http://journals.cambridge.org/abstract_S0022112007006647. 40

W. Mohring. A well posed acoustic analogy based on a moving acoustic medium. arXiv preprint arXiv:1009.3766, 2010. 68, 229, 244

W. Möhring, E.A. Müller, and F. Obermeier. Problems in flow acoustics. Reviews of modern physics, 55(3):707, 1983. 68, 229

E. Mollo-Christensen. Jet noise and shear flow instability seen from an experimenter's viewpoint. J. Appl. Mech, 34(1):1–7, 1967. 16

L. Mongeau, D. Huff, and B. Tester. In proceedings of meetings on acoustics. In Acoustic Society of America, volume 19, 2013. 8

C.J. Moore. The role of shear-layer instability waves in jet exhaust noise. Journal of Fluid Mechanics, 80(02):321–367, 1977. 20

C.L. Morfey. Amplification of aerodynamic noise by convected flow inhomogeneities. J. Sound Vib. , 31:391–397, 1973. 11

A.S. Morgans, C.S. Goh, and J.A. Dahan. The dissipation and shear dispersion of entropy waves in combustor thermoacoustics. J. Fluid Mech. , 733, September 2013. 54

A.S. S Morgans and I. Duran. Entropy noise: A review of theory, progress and challenges. International Journal of Spray and Combustion Dynamics, 8(4): 285–298, 2016. 9, 10

SA Mosier and RM Pierce. Advanced combustor systems for stationary gas turbine engines, phase i. review and preliminary evaluation, vol i. contract, pages 68–02, 1980. 91

E. Motheau, F. Nicoud, and T. Poinsot. Mixed acoustic - entropy combustion instabilities in gas turbines. J. Fluid Mech. , 749:542–576, 6 2014. ISSN 1469-7645. 14

F. Nicoud, H. Baya Toda, O. Cabrit, S. Bose, and J. Lee. Using singular values to build a subgrid-scale model for large eddy simulations. Phys. Fluids , 23 (8):085106, 2011. doi: 10.1063/1.3623274. URL http://link.aip.org/link/?PHF/23/085106/1. 35, 171

J.D. O'Brien, J. Kim, and M. Ihme. Investigation of the mechanisms of jet-engine core noise using large-eddy simulation. In 54th AIAA Aerospace Sciences Meeting - San Diego, California, USA, page 0761, 2016. 20

P. Palies, D. Durox, T. Schuller, and S. Candel. Acoustic and convective mode conversion in an aerofoil cascade. J. Fluid Mech. , 672:545–569, 2011. 138

Di. Papadogiannis, G. Wang, S. Moreau, F. Duchaine, L. Gicquel, and F. Nicoud. Assessment of the indirect combustion noise generated in a transonic high-pressure turbine stage. Journal of Engineering for Gas Turbines and Power, 138(4):041503, 2016. 15, 75

W.W. Peng. Fundamentals of turbomachinery. John Wiley & Sons, 2008. 50

O. M. Phillips. On the generation of sound by supersonic turbulent shear layers. J. Fluid Mech. , 9:1–28, 1960. 12, 67

C. D. Pierce and P. Moin. A dynamic model for subgrid scale variance and dissipation rate of a conserved scalar. Phys. Fluids , 10(12):3041–3044, 1998. 37

H. Pitsch. Large eddy simulation of turbulent combustion. Ann. Rev. Fluid Mech. , 38:453–482, 2006. 37

T. Poinsot. Prediction and control of combustion instabilities in real engines. Proc. Combust. Inst. , pages 1–29, 2017. ISSN 1540-7489. doi: http://dx.doi.org/10.1016/j.proci.2016.05.007. URL http://www.sciencedirect.com/science/article/pii/S1540748916300074. 10

T. Poinsot and S. Lele. Boundary conditions for direct simulations of compressible viscous flows. J. Comput. Phys. , 101(1):104–129, 1992. doi: 10.1016/0021-9991(92)90046-2. 76, 99

T. Poinsot and D. Veynante. Theoretical and Numerical Combustion. Third Edition (www.cerfacs.fr/elearning), 2011. 32, 33, 37, 98, 100, 232

T. Poinsot, T. Echekki, and M. G. Mungal. A study of the laminar flame tip and implications for premixed turbulent combustion. Combust. Sci. Tech. , 81(1-3):45–73, 1992. 76

W. Polifke, A. Fischer, and T. Sattelmayer. Instability of a premix burner with nonmonotonic pressure drop characteristic. J. Eng. Gas Turb. Power, 125:20–27, 2003. 63, 121, 125

S. B. Pope. Turbulent flows. Cambridge University Press, 2000. 69

A.F. Pouangué, M. Sanjosé, and S. Moreau. Dual-stream jet noise simulations with realistic nozzle geometries using a fully unstructured les solver. In 20th AIAA/CEAS Aeroacoustics Conference, Atlanta, GA (June 16–20, 2014), number 2014-2756, 2014. 158, 222

A. Powell. Theory of vortex sound. J. Acous. Soc. Am. , 36(1):177–195, 1964. 244

R. Price, I. Hurle, and T. Sudgen. Optical studies of the generation of noise in turbulent flames. In 12th Symposium (International) on combustion., pages 1093–1102, Pittsburg, 1968. The Combustion Institute,. 11

D.C. Pridmore-Brown. Sound propagation in a fluid flowing through an attenuating duct. The Journal of the Acoustical Society of America, 30(7):670–670, 1958. 72

R. Rajaram and T. Lieuwen. Effect of approach flow turbulence characteristics on sound generation from premixed flames. 42nd AIAA Aerospace Sciences Meeting and Exhibit - Reno, Nevada, USA, 2004. 13

M. Reshotko and A. Karchmer. Core noise measurements on a small, general aviation class turbofan engine, 1980. 10

S.W. Rienstra and A. Hirschberg. An introduction to acoustics. Eindhoven University of Technology, 2003. 70, 244

C. Royalty and B. Schuster. Noise from a turbofan engine without a fan from the engine validation of noise and emission reduction technology (evnert) program. In 14th AIAA/CEAS Aeroacoustics Conference (29th AIAA Aeroacoustics Conference) - Vancouver, British Columbia, Canada, page 2810, 2008. 120

P. Sagaut. Large eddy simulation for incompressible flows. Springer, 2002. 35

P. Salas. Aspects numériques et physiques des instabilités de combustion dans les chambres de combustion annulaires. PhD thesis, Université Bordeaux - INRIA, 2013. 69

M. Sanjosé, S. Moreau, A. Najab-Yazdi, and A. Fosso-Pouangue. A comparison between garlerkin and compact schemes for jet noise simulations. AIAA Paper, 2833(AIAA 2011-2833):7–9, 17th AIAA/CEAS Aeroacoustics Conference, Portland, Oregon, USA 2011. 175

M. Sanjose, A. Fosso Pouangue, S. Moreau, G. Wang, and T. Padois. Unstructured les of the baseline exejet dual-stream jet. In 20th AIAA/CEAS Aeroacoustics Conference - Atlanta, GA, USA, page 3037, 2014. 18, 148, 172, 174, 175, 181

T. Sattelmayer. Influence of the combustor aerodynamics on combustion instabilities from equivalence ratio fluctuations. J. Eng. Gas Turb. and Power , 125: 11–19, 2003. 54

C. Schneider, A. Dreizler, J. Janicka, and E.P. Hassel. Flow field measurements of stable and locally extinguishing hydrocarbon-fueled jet flames. Combustion and Flame, 135:185–190, 2003. 12

T. Schuller, D. Durox, and S. Candel. Dynamics of and noise radiated by a perturbed impinging premixed jet flame. Combust. Flame , 128:88–110, 2002. 12

Y.C. See, G. Amini, C. Koh, and M. Ihme. Jet noise receptivity to nozzle-upstream perturbations in compressible heated jets. In 18th AIAA/CEAS Aeroacoustics Conference (33rd AIAA Aeroacoustics Conference) - Colorado Springs, CO, USA, page 2259, 2012. 20

L. Selle, G. Lartigue, T. Poinsot, R. Koch, K.-U. Schildmacher, W. Krebs, B. Prade, P. Kaufmann, and D. Veynante. Compressible large-eddy simulation of turbulent combustion in complex geometry on unstructured meshes. Combust. Flame , 137(4):489–505, 2004a. 100

L. Selle, F. Nicoud, and T. Poinsot. The actual impedance of non-reflecting boundary conditions: implications for the computation of resonators. AIAA Journal , 42(5):958–964, 2004b. xx, 76, 99, 175, 197, 232, 238

V. Selmin. Third order finite element schemes for the solution of hyperbolic problems. Technical Report INRIA Report, 707, INRIA. Sophia Antipolis, France, 1987. 171

B.N. Shivashankara, W.C. Strahle, and J.C. Handley. Evaluation of combustion noise scaling laws by an optical technique. AIAA journal, 13:623–627, 1974. 11

C. Silva. Numerical study of combustion noise in gas turbines. PhD thesis, 2010. 69

K.K. Singh, S.H. Frankel, and J.P. Gore. Effects of combustion on the sound pressure generated by circular jet flows. AIAA journal, 41(2):319–321, 2003. 12

J. Smagorinsky. General circulation experiments with the primitive equations: 1. the basic experiment. Mon. Weather Rev. , 91:99–164, 1963. 35, 99

T.J.B. Smith and J.K. Kilham. Noise generation by open turbulent flames. J. Acous. Soc. Am. , 35(5):715–724, 1963. 10, 12

S.R. Stow, A.P. Dowling, and TP Hynes. Reflection of circumferential modes in a choked nozzle. Journal of Fluid Mechanics, 467:215–239, 2002. ISSN 0022-1120. doi: 10.1017/S0022112002001428. URL http://journals.cambridge.org/abstract_S0022112002001428. 14

W.C. Strahle. On combustion generated noise. J. Fluid Mech. , 49:399–414, 1971. 9, 11

W.C. Strahle and M. Muthukrishnanf. Correlation of combustor rig sound power data and theoretical basis of results. AIAA Journal, 18(3), 1980. 14

D.R. Stull and H. Prophet. JANAF thermochemical tables, 2nd Edition. Technical Report NSRDS-NBS 37, US National Bureau of Standards, 1971. 36

C. Tam, N. Pastouchenko, J. Mendoza, and D. Brown. Combustion noise of auxiliary power units. In 11th AIAA/CEAS Aeroacoustics Conference - Monterey, California, USA, page 2829, 2005. 8, 13

C.K.W. Tam and S.A. Parrish. On the generation of indirect combustion noise. In AIAA Paper presented at the 20thAIAA/CEAS Aeroacoustics Conference - Atlanta, GA, USA, 2014. 13

C.K.W. Tam and S.A. Parrish. Noise of high-performance aircraft at afterburner. Journal of Sound and Vibration, 352:103–128, 2015. 15

C.K.W. Tam, K. Viswanathan, K.K. Ahuja, and J. Panda. The sources of jet noise: experimental evidence. J. Fluid Mech, 615:253–292, 2008. 13, 17, 218

C.K.W. Tam, Bake F., L.S. Hultgren, and T. Poinsot. Aircraft noise generation and assessment. CEAS Aeronautical Journal, 2017. 10, 12

C.K.W.KW Tam. The spectral shape of combustion noise. International Journal of Aeroacoustics, 14(3-4):431–456, 2015. 163

H.K. Tanna. An experimental study of jet noise part i: Turbulent mixing noise. Journal of sound and Vibration, 50(3):405–428, 1977. 19

A. Thomas and G. T. Williams. Flame noise: sound emmission from spark-ignited bubbles of combustible gas. Proc. R. Soc. Lond. A , 294:449–466, 1966. 10

H.S. Tsien. The transfer functions of rocket nozzles. J. American Rocket Society , 22(3):139–143, 1952. 13, 40

K. Viswanathan. Aeroacoustics of hot jet. J. Fluid Mech, 516:39–82, 2004. 19

G. Wang, M. Sanjose, S. Moreau, D. Papadogiannis, F. Duchaine, and L. Gicquel. Noise mechanisms in a transonic high-pressure turbine stage. International Journal of Aeroacoustics, 15(1-2):144–161, 2016. 15

M. Wei and J. Freund. A noise-controlled free shear flow. J. Fluid Mech, 546: 123–152, 2006. 224

K.B.M.Q. Zaman. Effect of initial condition on subsonic jet noise. AIAA journal, 23(9):1370–1373, 1985. 17, 18

K.B.M.Q. Zaman. Asymptotic spreading rate of initially compressible jets-experiment and analysis. In Phys. Fluids, pages 10(10):2652–2660, 1998. 69

K.B.M.Q. Zaman. Effect of initial boundary-layer state on sibsonic jet noise. AIAA journal, 50:1784–1795, 2012. 18

B.T. Zinn, W.A. Bell, B.R. Daniel, and A.J. Smith. Experimental determination of three-dimensional liquid rocket nozzle admittances. AIAA Journal , 11:267–272, 1973. 14

E.E. Zukoski and J.M. Auerbach. Experiments concerning the response of supersonic nozzles to fluctuating inlet conditions. ASME J. Eng. Power, 98(1):60–64, 1976. 14

Publications

- M. Férand, T. Livebardon, S. Moreau, C. Sensiau and T. Poinsot. Numerical investigation of combustion noise from aeronautical combustor to far-field. *22nd AIAA/CEAS Aeroacoustics conference*, Lyon, France, 2016.
- M. Férand, G. Daviller, S. Moreau, C. Sensiau and T. Poinsot. Using LES for combustion noise propagation to the far-field by considering the jet flow of a dual-stream nozzle. *24th AIAA/CEAS Aeroacoustics conference*, Atlanta, Georgia, USA, 2018. Submitted.